

STRUCTURAL EVOLUTION OF QUIESCENT GALAXIES FROM THE PEAK
OF THE COSMIC STAR FORMATION EPOCH

by

Ivana Damjanov

A thesis submitted in conformity with the requirements
for the degree of Doctor of Philosophy
Graduate Department of Astronomy and Astrophysics
University of Toronto

Copyright © 2011 by Ivana Damjanov

Abstract

Structural Evolution of Quiescent Galaxies from the Peak of the Cosmic Star
Formation Epoch

Ivana Damjanov

Doctor of Philosophy

Graduate Department of Astronomy and Astrophysics

University of Toronto

2011

The main focus of this thesis is the investigation of an interesting new population of massive passively evolving galaxies found at high redshifts. We use a sample of these galaxies at redshifts $1 \lesssim z \lesssim 2$ drawn from the Gemini Deep Deep Survey sample and measure their structural parameters based on the *Hubble Space Telescope* imaging in the rest frame visible and ultraviolet wavelength range. Our analysis shows that a fraction of these systems are very compact, with effective radii of $R_e < 1$ kpc, even when observed in rest frame visible light. The average size of these objects is 2 – 5 times smaller than the typical size of an early-type galaxy of similar mass found locally.

We combine the results from our morphological analysis with data from published spectroscopic samples of quiescent systems with known structural parameters. Analysis of these data for galaxies over the redshift range $0 < z \lesssim 2.5$ shows that passively evolving galaxies are continuously and gradually growing in size. We also find smooth evolution of the stellar mass density within the central kiloparsec of these systems. The stellar mass density grows by a factor of 3 from $z = 0$ to $z \sim 2.5$. None of the models proposed to drive the structural evolution of early-type objects can explain all the observed aspects of this process.

Because these massive compact galaxies have such small angular sizes, future studies of these systems will benefit from adaptive optics. In order to compile a large statistical sample of these objects suitable for adaptive optics follow-up, we first need to find a large

number of targets with nearby bright natural guide stars. As a first step in this process, we describe the properties of a set of one square degree regions of the sky we have located that have a rare combination of high stellar surface density and low levels of extinction. We demonstrate that the adaptive optics-related properties of these fields are in some cases orders of magnitude better than those of existing deep fields.

Dedication

To my Mother and my Husband

For believing in me

Always

*Go as far as you can see;
when you get there you'll be able to see farther.*

– Thomas Carlyle

Acknowledgements

This thesis would have never been completed without the continuous guidance, support, understanding and enthusiasms of my Ph.D. advisor Prof. Roberto Abraham. Bob, I will always be grateful to you for sharing brilliant ideas, immense and knowledgeable help in bringing them to life, and for being my friend over the past five years. I feel privileged for being able to work closely with Prof. Karl Glazebrook and Dr. Patrick McCarthy. Karl and Pat, thank you for your unconditional help and for everything you have taught me over the years.

I am thankful to the members of my Ph.D. committee, Prof. Howard Yee and Prof. Raymond Carlberg, for their advice and insightful discussions during the committee meetings. I appreciate thoughtful comments from Prof. Francine Marleau and my external examiner, Prof. Pieter van Dokkum.

In the course of years I have met many people at the Department and some of them have become great friends. For being there when I needed her the most, I am forever grateful to Daniela Gonçalves. I will always remember with a smile the fun I had and cherish the moments spent with Sherry Yeh, Laura Fissel, Richard Chou, Vjera Miović, Allen Attard, Alana Rivera-Ingraham, Santiago Gonzalez, Mirza Ahmić, Juan Diego Soler, Marija Stanković, Erin Mentuch, Marco Viero, Arabindo Roy, Elizabeth Harper-Clark, Anne-Marie Weijmans, Koraljka Mužić, and others.

Most importantly, I would like to thank my family for their everlasting support and confidence in my abilities. To my parents, Borislava Damjanov-Berbeč and Ivan Damjanov, and my brother, Borislav Damjanov: I love you and could not have achieved this without you. Mama,

Tata, Lane: hvala vam što ste verovali u mene. Volim vas.

Finally, to my loving husband Aleksandar Stajkić: I am blessed to have you holding my hand forever. Volim te.

Contents

1	Introduction	1
1.1	The Fundamental Plane of elliptical galaxies and its projections	3
1.2	Scaling relations at high redshifts	6
1.3	Driving mechanisms for the observed size evolution	10
1.3.1	Dissipationless major mergers	10
1.3.2	Adiabatic expansion and feedback	11
1.3.3	Minor mergers or late accretion of low density material	13
1.4	Thesis overview	19
2	Sample and Methodology	22
2.1	The Gemini Deep Deep Survey	22
2.2	2D Modeling of galaxy surface brightness profiles	25
3	Red Nuggets at $z \sim 1.5$	27
3.1	Abstract	27
3.2	Introduction	28
3.3	Description of the observations	31

3.3.1	Sample definition	31
3.3.2	NICMOS observations	35
3.4	Analysis	35
3.4.1	Surface brightness profiles	35
3.4.2	K-corrections and cosmological dimming	42
3.5	Results	42
3.5.1	Morphologies of passive galaxies at $z > 1.3$	42
3.5.2	Surface brightness profiles & sizes	43
3.5.3	The Kormendy relation to $z = 2$	45
3.5.4	The mass-size relation and the stellar mass Kormendy relation	47
3.6	Discussion	50
3.7	Conclusions	61
4	Structural Evolution of Quiescent Galaxies	63
4.1	Abstract	63
4.2	Introduction	64
4.3	Sample and data reduction	65
4.4	The size-mass relation	69
4.5	The size growth of quiescent galaxies	71
4.5.1	The size-redshift relation	71
4.5.2	Continuous size evolution with redshift	73
4.5.3	Size evolution with lookback time	74
4.6	Central mass density evolution	77

4.7	Summary and conclusions	79
5	Extragalactic Fields Optimized for Adaptive Optics	89
5.1	Abstract	89
5.2	Introduction	90
5.3	Desirable characteristics of extragalactic fields optimized for adaptive optics	95
5.3.1	Extinction	95
5.3.2	Field size	95
5.3.3	Guide star limitations	97
5.4	Identification of the suitable fields for Adaptive Optics . .	100
5.5	CFHT imaging results for a proposed ‘optimal’ field	104
5.6	Benefits of undertaking observations in AO-optimized fields	107
5.6.1	Figure of merit	110
5.6.2	MCAO observations in existing and proposed fields	111
5.6.3	The AODF in the era of upcoming methods and instruments	116
5.7	Summary and conclusions	118
5.8	Appendices	119
5.8.1	Properties of selected fields	119
5.8.2	The form of the figure of merit	121
6	Conclusions and Future Prospects	127
6.1	Thesis summary	127

6.2	Future work	130
6.2.1	Size evolution as a function of galaxy age and of galaxy ellipticity	130
6.2.2	Environment of compact ellipticals	131
6.2.3	Velocity dispersions and chemical composition of compact ellipticals at high redshifts	131
6.2.4	Spatially resolved chemical and dynamical properties of the most compact ellipticals in the local Universe	132
6.2.5	The development of the Adaptive Optics Deep Field	133

Bibliography		134
---------------------	--	------------

List of Tables

3.1	Properties of ten galaxies in GDDS sample	33
3.2	Properties of nine massive galaxies in MUNICS sample ^a . .	34
3.3	Morphological parameters of galaxies in the GDDS sample	41
3.4	Morphological parameters of galaxies in the MUNICS sample	41
4.1	Summary of the compilation of samples used to construct the size evolution diagram	69
4.2	Complete list of objects used to construct the size evolution diagram	80
4.2	Complete list of objects used to construct the size evolution diagram	81
4.2	Complete list of objects used to construct the size evolution diagram	82
4.2	Complete list of objects used to construct the size evolution diagram	83
4.2	Complete list of objects used to construct the size evolution diagram	84
4.2	Complete list of objects used to construct the size evolution diagram	85

4.2	Complete list of objects used to construct the size evolution diagram	86
4.2	Complete list of objects used to construct the size evolution diagram	87
4.2	Complete list of objects used to construct the size evolution diagram	88
5.1	Properties of the 67 55' × 55' fields optimized for AO surveys	125
5.1	Properties of the 67 55' × 55' fields optimized for AO surveys	126

List of Figures

1.1	Kormendy relation for the sample of early-type galaxies drawn from the SDSS	5
1.2	Locations of equal-mass merger remnants in the plane corresponding to the edge-on projection of the virial plane . .	11
1.3	Evolution of physical or observationally inferred surface stellar mass density profiles according to different models . . .	17
2.1	Labelled finding charts for the four GDDS fields	22
2.2	Spectra of evolved GDDS galaxies with $z > 1.3$	23
3.1	NIC3 images and the results of our 2D fitting with Galfit of 10 GDDS galaxies	36
3.2	NIC2 images and the results of our 2D fitting with Galfit of six MUNICS galaxies	37
3.3	Major axis surface brightness profiles in the F160W band for 10 GDDS galaxies	39
3.4	Kormendy relation for high- z (GDDS and MUNICS) objects and for the sample of local galaxies drawn from the SDSS .	45

3.5	Effective radius R_e as a function of stellar mass for five samples of early-type galaxies in the redshift range $1.1 < z < 2$	49
3.6	“Stellar mass Kormendy relation” for five samples of early-type galaxies in the redshift range $1.1 < z < 2$	51
3.7	The mass loss fraction $\frac{\Delta m}{m}$ as a function of population age in Gyr, for the size growth mechanism based on stellar winds	54
3.8	As in Figure 3.5, with data at $0 < z < 1$ included	56
3.9	As in Figure 3.6, with data at $0 < z < 1$ included	57
3.10	Redshift dependence of the stellar mass density within the effective radius R_e	58
4.1	Effective radius R_e as a function of stellar mass for a sample of 465 passively evolving galaxies at $0.2 < z < 2.7$	66
4.2	As in Figure 4.1, with color coding based on survey selection criteria	67
4.3	Size evolution of massive quiescent galaxies as a function of redshift	72
4.4	Size evolution of massive quiescent galaxies as a function of lookback time	75
4.5	Central stellar mass density of massive quiescent galaxies as a function of redshift	77
5.1	The galactocentric coordinates of existing deep fields and the locations of the fields better suited for AO observations overplotted on the dust emission map	90

5.2	Cosmic variance as a function of redshift for four fields covering different areas on the sky	94
5.3	All sky maps of Galactic extinction $E(B - V)$, star counts surface density Σ_{sc} , and of the $E(B - V)/\Sigma_{\text{sc}}$ ratio	100
5.4	Extinction $E(B - V)$ as a function of the star counts surface density Σ_{sc} for 442 $55' \times 55'$ fields with $\Sigma_{\text{sc}} > 0.5 \text{ arcmin}^{-2}$ and $E(B - V) \leq 0.1$	101
5.5	The three higher-order moments of the extinction and star count surface density distributions as functions of the mean star count surface density for chosen fields	102
5.6	Extinction and star surface density maps centered on the position of the ‘Adaptive Optics Deep Field’	104
5.7	CFHT MegaCam g' and z' band mosaic of the ‘Adaptive Optics Deep Field’ and its galaxy number per 0.5 mag and per $1^\circ \times 1^\circ$ as a function of g' magnitude	105
5.8	Stellar surface density, average extinction $E(B - V)$, and the standard deviation of $E(B - V)$ as functions of Galactic latitude for existing and proposed deep fields	108
5.9	Cumulative distribution and distribution of our Strehl-related figure of merit for $55' \times 55'$ AODF, COMBO 17 Field 2, and the CFHTLS W2 subfield	113
5.10	Strehl ratio as a function of its RMS variance for pointings accessible to AO in AODF, COMBO 17 Field 2, and CFHTLS W2 subfield	114

5.11	Extinction and star surface density maps of the $6'.871 \times 6'.871$ cells within the $55' \times 55'$ field with the highest mean star counts surface density	119
5.12	Extinction and star surface density maps of the $6'.871 \times 6'.871$ cells within the $55' \times 55'$ field with the lowest reddening coefficient	119
5.13	Extinction and star surface density maps of the $6'.871 \times 6'.871$ cells within the $55' \times 55'$ field with the lowest standard deviation of $E(B - V)$	120
5.14	Cumulative distribution of our Strehl-related figure of merit for $55' \times 55'$ AODF, COMBO 17 field, and the $1^\circ \times 1^\circ$ subfield of CFHT W2	122
5.15	Distribution of our Strehl-related figure of merit for $55' \times 55'$ AODF, COMBO 17 field, and the $1^\circ \times 1^\circ$ subfield of CFHT W2123	

Chapter 1

Introduction

Galaxies are the building blocks of the Universe. Nearby luminous galaxies are generally classified using Hubble’s “tuning fork” system (Hubble, 1926), which has been refined and expanded over the decades to capture both additional classes of objects (such as S0 galaxies and irregulars; Hubble, 1936) and additional features (such as rings and ovals; de Vaucouleurs et al., 1976). About 95% of nearby luminous galaxies find a home in this extended Hubble sequence (van den Bergh, 1999), although it is worth emphasizing that underluminous dwarf galaxies and ultra-luminous cD galaxies (Morgan, 1971) are not incorporated into the system.

If we neglect the Hubble system’s bifurcation into barred vs. unbarred galaxies (an arguably inessential component of the system), galaxies can be grouped into four broad categories: ellipticals, lenticular (S0) galaxies, spirals, and irregulars. In some cases it is appropriate to consider elliptical, lenticular and strongly bulge-dominated spiral galaxies to be a single class of object, and together these are often referred to as early-type galaxies. Although this is a purely morphological classification based on visual inspection (or, in some cases, computer classification), the scheme does appear to capture some underlying physics (Roberts & Haynes, 1994), with the main physical correlation being with stellar population content. If we neglect dust absorption, in the nearby Universe early-type galaxies are very red, and they exhibit stellar absorption-line spectra with no or very weak nebular emission, indicating an absence of recent star formation. In spite of this, it is important to emphasize that morphologically-selected and color-selected (or spectrally-selected) samples do not fully overlap. In a study of local early-type galaxies drawn from the Sloan Digital Sky Survey (SDSS), Bernardi et al. (2006) have found

that 70% of morphologically-selected ellipticals also satisfy photometric red criteria (i.e., they have red colors), and 81% of them show spectra with predominantly old stellar populations (i.e., they also satisfy spectroscopic criteria that can be used to select early-types). This correlation between morphology, color, and spectroscopic features continues at higher redshifts as well (e.g, Bell et al., 2004a; Weiner et al., 2005; Abraham et al., 2007; Cassata et al., 2008; Kriek et al., 2009; Szomoru et al., 2011).

Galaxies are multi-component systems and the accuracy of any description of their observed light profile depends strongly on the inherent complexity of the light distribution. However, light profiles of many galaxies can be approximated by using only a simple analytic function, the Sérsic profile (Sersic, 1968) :

$$I(r) = I_e e^{-\kappa \left[\left(\frac{r}{R_e} \right)^{\frac{1}{n}} - 1 \right]}. \quad (1.1)$$

Here $I(r)$ is the surface brightness of a galaxy at a given *circularized* radius $r = a\sqrt{b/a}$, with a as a scale length of the profile and b/a as an axial ratio. R_e is the effective (i.e., half-light) radius of a galaxy, and I_e is the surface brightness at R_e . Power law index n and parameter κ are coupled to give half of the total flux enclosed within R_e . The asymptotic approximation for κ as a function of Sérsic index is of the form:

$$\kappa(n) \sim n - \frac{1}{3} + \frac{8}{405n} + \frac{184}{25515n^2} + O(n^{-3}) \quad (1.2)$$

(Ciotti & Bertin, 1999). The Sérsic index n is related to the concentration of the galaxy light profile: large n corresponds to a steep inner profile with extended outer wings, while a low n describes a shallow inner profile. Galaxies with pure spheroidal profiles (classical bulges) are well fitted with the $n = 4$ Sérsic function, known also as the De Vaucouleurs profile (de Vaucouleurs, 1948). On the other hand, disk dominated galaxies are reasonably well characterized by the exponential $n = 1$ Sérsic profile.

It has been estimated that early-type galaxies and spiral bulges represent $\sim 75\%$ of the total stellar mass in the Universe, while disks contribute only $\sim 25\%$ and dwarfs only a tiny fraction (Fukugita et al., 1998). The mass functions of color selected early-type galaxies and of blue, star-forming objects based on the SDSS data (Baldry et al., 2004) show that above $\sim 3 \times 10^{10} M_{\odot}$ red-sequence galaxies¹ start to increasingly out-

¹Early-type galaxies follow a tightly constrained sequence in the color-magnitude diagram called ‘the red sequence’ (e.g., Terlevich et al., 2001)

number blue objects by a factor that exceeds 10 at $\sim 3 \times 10^{11} M_{\odot}$. Since early-types contain the major fraction of stellar mass in galaxies, understanding their evolution from formation to the stage observed in the local Universe is of major importance for understanding galaxy evolution in general. Historically, a distinction has been made between two classes of galaxy formation models: a) monolithic collapse (Eggen et al., 1962) models in which elliptical galaxies form from the collapsing primordial gas clouds and b) "hierarchical merging" (e.g., Toomre & Toomre, 1972; Efstathiou, G. & Silk, J., 1983; Blumenthal et al., 1984) models in which big spheroids are formed by merging of smaller disk galaxies. In § 3.2 we describe the tests that have been (and are being) performed to try to distinguish between modern versions of these evolutionary models. Here we note that the major challenges for any model of galaxy formation are to explain the tight correlations between structural and dynamical properties of early-type galaxies and the evolution of these relations with cosmic time.

1.1 The Fundamental Plane of elliptical galaxies and its projections

Early-type galaxies obey a tight scaling relation between their dynamical properties, represented by the central velocity dispersion σ_0 , and structural parameters: effective (i.e., half-light) radius R_e , and the mean surface brightness within R_e , $\langle I \rangle_e$ (Djorgovski & Davis, 1987; Dressler et al., 1987). This two-dimensional plane populated by early-type galaxies is called the *Fundamental Plane*, and can be written in the form:

$$\log R_e = a \log \sigma_0 + b \log \langle I \rangle_e + \text{const.} \quad (1.3)$$

Jørgensen et al. (1996) found $a = 1.24$, $b = -0.82$ using a sample of local cluster early-type galaxies with structural measurements based on Gunn r band imaging of 226 elliptical and S0 objects in 10 local galaxy clusters. The slope a , related to the velocity dispersion, seems to vary with the passband used for extracting structural properties (up to $\sim 20\%$ from visible to near-infrared (NIR) wavelengths), while the slope b , that connects two structural parameters of early-type objects, stays almost constant across the same wavelength range (e.g., Pahre et al., 1998; La Barbera et al., 2010).

The origin of the Fundamental Plane is usually interpreted in terms of the virial

theorem. For a static collisionless system (with total energy E) that is not influenced by external pressure the kinetic energy K is equal to the half of the absolute value of its gravitational potential energy W :

$$\begin{aligned} E = W + K &= \frac{1}{2}W, \\ K &= -\frac{1}{2}W, \\ \langle v^2 \rangle &= \frac{GM}{\langle R \rangle} \end{aligned} \quad (1.4)$$

where M is the mass of the system, $\langle R \rangle$ is the mean (or gravitational) radius defined so that the right-hand side is the mean $|W|$ per unit mass, and $\langle v^2 \rangle$ is the mean square velocity, so that $\langle v^2 \rangle/2$ is the mean K per unit mass. The observable parameters of early-type galaxies σ_0 and R_e are related to the gravitational radius and the mean square velocity as:

$$R_e = k_R \langle R \rangle, \quad \sigma_0 = k_V \sqrt{\langle v^2 \rangle}, \quad (1.5)$$

where k_R and k_V are dimensionless quantities that depend on the density profile and orbital structure of the galaxy, respectively. Following the definition of the mean surface brightness within R_e , galaxy luminosity can be written as:

$$L = 2\pi \langle I \rangle_e R_e^2, \quad (1.6)$$

and used to obtain the relation between R_e , σ_0 , and $\langle I \rangle_e$ (i.e., the Fundamental Plane):

$$R_e = \varphi_R \sigma_0^2 \langle I \rangle_e^{-1} \left(\frac{M}{L} \right)^{-1}, \quad \varphi_R = \frac{1}{2\pi G k_R k_V^2}. \quad (1.7)$$

If elliptical galaxies form a perfectly homologous class, i.e., have self-similar density and orbital distributions, φ_R is constant. Furthermore, if all ellipticals have the same mass-to-light ratio M/L , then the virial theorem defines a Fundamental Plane with $a = 2, b = -1$. The deviation of the observed a and b from these predictions is called the ‘tilt’ of the Fundamental Plane, and it indicates that M/L and/or φ_R depends on σ_0 , $\langle I \rangle_e$, and/or R_e . The finite thickness of the observed Fundamental Plane does not allow

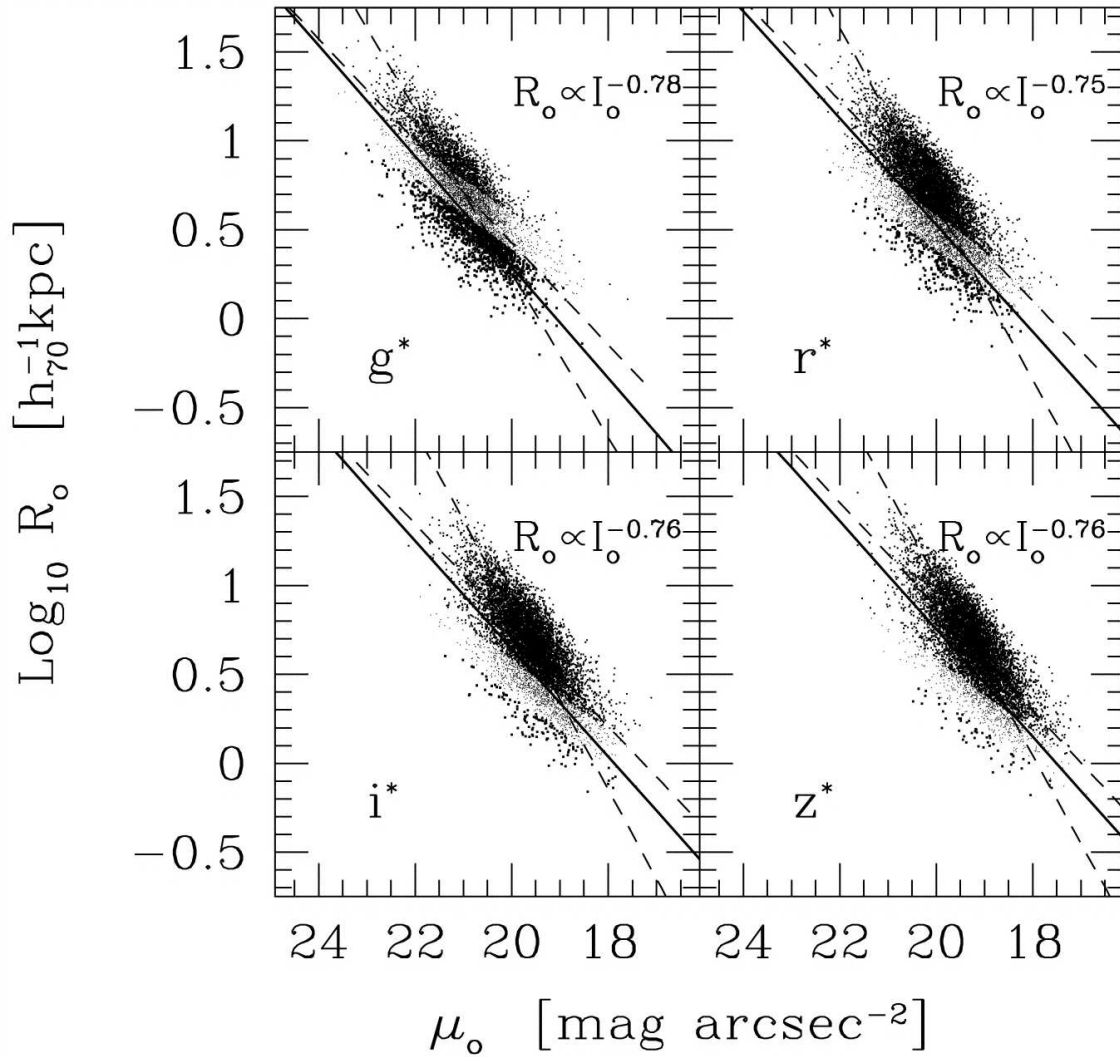


Figure 1.1 (Taken from Bernardi et al., 2003a) Relation between the effective radius and mean surface brightness within the effective radius (i.e., Kormendy relation) for the local sample of early-type galaxies drawn from the SDSS. Four panels correspond to different SDSS passbands used to measure sizes. Short dashed lines show forward and inverse fits to this relation, i.e., the effective radius at fixed mean surface brightness and the mean surface brightness at fixed effective radius, respectively. To illustrate the effect that the magnitude limit of the survey has on the zero point, a solid line shows the maximum likelihood estimate of the relation in the simulated complete parent sample for the magnitude-limited catalog.

much scatter of such a dependence, putting tight constraints on the models of elliptical galaxy formation and evolution.

There are two possible projections of the Fundamental Plane: a relation that would connect one dynamical and one structural property of early-type objects, and a relation between the two of their structural properties. The former group of scaling relations is represented by the Faber-Jackson relation of the form:

$$L \sim \sigma_0^\beta, \beta \sim 4, \quad (1.8)$$

which is an edge-on projection of the Fundamental Plane (Faber & Jackson, 1976). The projection of the Fundamental Plane along the σ_0 direction is called the Kormendy (1977) relation:

$$\langle I \rangle_e \sim R_e^\nu, \quad (1.9)$$

with $\nu = -1.3 \pm 0.1$ in the visible wavelength regime.

These two projections have been extensively explored in the local Universe using the SDSS sample (Bernardi et al., 2003a; Desroches et al., 2007; Nigoche-Netro et al., 2008; Hyde & Bernardi, 2009; Nigoche-Netro et al., 2010; La Barbera et al., 2010). These local samples define the local Kormendy relation with high precision. For example, Figure 1.1 presents the Kormendy relation in four different passbands in the visible wavelength range, as presented by Bernardi et al. (2003a). The figure shows that the slope of the best fit to the observed early-type galaxies does not vary between SDSS-*g* and SDSS-*z* bands (dashed lines), while the zero point does depend on the sample magnitude limit. The solid line in Figure 1.1 shows the relation between the effective radius and the mean surface brightness within this radius for the simulated complete catalog from which the magnitude-limited sample was drawn (details of the simulations are given in Appendix 1 of Bernardi et al., 2003a). This is an important figure in this thesis since the upper right panel, presenting the size and the mean surface brightness measured in SDSS-*r* band, has been used as a local analog to the $z \sim 1.5$ Kormendy relation in observed *H* band (presented in Figure 3.4), since at that redshift the observed $\lambda_{\text{eff}} = 1.6 \mu\text{m}$ band translates into rest-frame $\lambda_0 \sim 6400 \text{ \AA}$ or SDSS-*r* band (see § 3.4.2 for more details). It should be noted here that more recent results have show that the slope of the Kormendy

relation for nearby ($z < 0.1$) early-types does change in the NIR wavelength regime (e.g., La Barbera et al., 2010).

1.2 Scaling relations at high redshifts

The observed correlations between the structural and dynamical properties of nearby early-type galaxies are a manifestation of an underlying organization in their mass distributions. By probing the assembly of mass in such systems as a function of cosmic epoch we can determine the relative importance of different galaxy assembly processes, such as mergers and cold flows (e.g., Shankar et al., 2011, and references therein). Mapping the changing nature of the scaling relations therefore provides us with a crucible for testing models for galaxy formation.

Observations show clear evidence for evolution in the Fundamental Plane with redshift (e.g., van Dokkum et al., 1998; Treu et al., 2002; van de Ven et al., 2003; Wuyts et al., 2004; Treu et al., 2005b; Gebhardt et al., 2003; Fernández Lorenzo et al., 2011; Saglia et al., 2010). This is often interpreted as evidence for a change in the stellar mass-to-light ratio, M/L , that is in turn easily connected to star formation history by spectral synthesis modelling (e.g., Graves et al., 2009, and references therein). Stellar mass can be connected to the dynamic mass by assuming that the stellar mass is proportional to the total (i.e. dynamical) mass of a galaxy, $M_* \propto M$ (Treu et al., 2005b). Results for field galaxies out to $z \sim 1$ show $d \log(M/L_B)/dz \sim -0.7$, where M/L_B is bolometric mass-to-light ratio (e.g., Saglia et al., 2010; Treu et al., 2005b). Furthermore, observations indicate that the scatter in the Fundamental Plane increases at higher redshifts, with most evolution in the scatter occurring at the-low mass end. While the M/L ratio for the most massive galaxies evolves from $z \sim 1$ according to expectations for an aging old stellar population, a significant fraction (20 – 40%) of galaxies with stellar masses $M_* \lesssim 10^{11}$ show signatures of younger stellar populations, which suggests that these objects are coming on to the Fundamental Plane at redshifts around (or below) $z \sim 1$ (Treu et al., 2005b,a; van der Wel et al., 2005; di Serego Alighieri et al., 2005; van der Wel et al., 2004). These findings seem quite consistent with a “galaxy downsizing” scenario (Cowie et al., 1996) in which the most massive galaxies form first.

Due to the small apparent sizes of most $z > 1$ galaxies ($\lesssim 1''$), high-resolution imaging with the cameras on-board the *Hubble Space Telescope* (HST) and/or adaptive-optics

(AO) assisted ground-based imaging are critical for resolving the details of their light profiles. AO-assisted spectrographs (ideally with integral field capability) are needed to resolve dynamics on the kpc scale. However, at these redshifts it is difficult to measure the dynamical properties of passively evolving galaxies, since signal-to-noise considerations limit AO-assisted spectrographs to the investigation of strong line emitters at high-redshifts (discussed further below). As a result, most information on the (structural) evolution of these systems at $z > 1$ comes from the analysis of the Kormendy relation, which is constructed using rest-frame UV and visible wavelength HST imaging and high-resolution ground based data (Targett et al., 2011; Rettura et al., 2010; Damjanov et al., 2009; Toft et al., 2009; Ferreras et al., 2009; Saracco et al., 2009; Cimatti et al., 2008; Longhetti et al., 2007; Toft et al., 2007; Zirm et al., 2003; Moriondo et al., 2000; Fasano et al., 1998). Remarkably, the results obtained so far display a shift toward both smaller sizes and higher surface brightness values for passively-evolving high- z objects with respect to their local counterparts. The luminosity evolution that these passive systems can undergo does not seem to be sufficient to explain this offset from the Kormendy relation at $z > 1$, and the implication is that these galaxies must grow very significantly in size in order to match their local counterparts. The observed size-growth trends can be made even clearer by focusing on the relation between a galaxy’s size and its stellar mass ($R_e \propto M_*^\alpha$), and as a result analysis of this relationship has replaced analysis of the Kormendy relation in many studies (e.g., van Dokkum et al., 2010, and references therein). Most such analyses find that at a fixed stellar mass both star-forming and quiescent galaxies have smaller radii at higher redshift (e.g., Mosleh et al., 2011, and references therein). However, structural evolution seems more prominent for the passively evolving systems: at $z \sim 1 - 2$ quiescent galaxies are 2 – 5 times smaller than the local early-type galaxies of the same stellar mass (see § 4.2 for the full list of references). Furthermore, Trujillo et al. (2009) and Taylor et al. (2010) have demonstrated the paucity of similarly compact early-type systems in the local Universe (although Valentinuzzi et al. (2010a) report that a fraction of local early-type objects found in nearby clusters of galaxies are compact).

The prospect of witnessing remarkable size growth since $z \sim 1$ is exciting, but appropriate caution should be exercised when interpreting these results. In general, the various studies cited above reveal similar trends, which provides good evidence for the basic reality of the underlying phenomenon. Furthermore, information on the dynam-

ical properties of these objects, based on estimates of velocity dispersion from stellar absorption lines, has been extracted from their stacked (Cimatti et al., 2008; Cappellari et al., 2009; Javier Cenarro & Trujillo, 2009) and individual (van der Wel et al., 2008; van Dokkum et al., 2009a; Newman et al., 2010; van de Sande et al., 2011) spectra. On the whole, the estimated velocity dispersions are in agreement with the large masses inferred from stellar population modelling. However it is certainly challenging to probe mean surface brightnesses within tiny effective radii (sometimes only 2–3 pixels wide) using data which spans a range of rest-frame wavelengths, from UV to visible and NIR. It is therefore important to note the various caveats that have been raised regarding observations of apparent compactness among high-redshift quiescent galaxies. These include (van Dokkum et al., 2008): 1) the possibility of not accounting for extended low-surface brightness emission which would tend to increase inferred radii (e.g., Mancini et al., 2010); 2) biases introduced from observations which probe rest-frame UV rather than rest-frame visible wavelengths (Cimatti et al., 2008); 3) radially-dependent stellar M/L ratios increasing outwards that could cause an underestimate of the stellar mass at large radii (Tortora et al., 2011; Hopkins et al., 2010b); 4) using samples with photometric rather than spectroscopic redshifts (see § 4.5.2, but also § 4.4 for the discussion of the bias introduced by considering only spectroscopically confirmed objects at $z > 1.5$); and 5) uncertainties in the stellar population models used to estimate stellar masses (e.g., Raichoor et al., 2011, and references therein). Some of these concerns (1, 2 and 4) have been addressed using samples with spectroscopic redshifts (see Chapter 4) and deeper surface-brightness limits (Guo et al., 2011; Szomoru et al., 2010; Cassata et al., 2011; Ryan et al., 2011), in some cases in several different passbands (e.g., Cassata et al., 2011). These various caveats impact different surveys in different ways, and it is therefore quite difficult to combine results from different surveys, although the small numbers of objects in individual surveys makes analysis of a combined dataset potentially rather interesting. We will attempt a global synthesis of the existing data from various surveys in § 4.3, but will do so rather guardedly, taking care to note that the changing rest frame wavelength of observation poses a particular challenge to the interpretation of observations, since the correction for luminosity evolution strongly depends on wavelength. The disparate nature of the surveys investigated makes it quite difficult to inter-compare data from different papers in a fully satisfactory way, but we will show that some robust global trends do seem to emerge.

The small number of observations of the internal velocity dispersions of compact galaxies noted above sets the stage for future resolved spectroscopic work. At present dynamical studies of high-redshift galaxies have been limited to star-forming objects, using emission lines from ionized gas in the rest-frame visible wavelength regime, or longer wavelength emission from CO tracing molecular gas. It is clear that combining high-resolution imaging with spatially resolved dynamical maps has the potential to provide considerable insight into the nature of the galaxy assembly process at high redshift (Förster Schreiber et al., 2009; Law et al., 2009). Unfortunately, it will not be possible to obtain similar dynamical maps for passively evolving galaxies at high redshift using stellar absorption lines until 30m-class telescopes come on-line, and even then dynamical and stellar population properties on sub-kpc scale (i.e., within an effective radius) will only be available for objects close to natural guide stars. In Chapter 5 we will investigate the efficacy of such observations as a function of guide-star proximity and show how a paucity of natural guide stars will limit the effectiveness of such observations. We also propose a solution to this problem by identifying a set of preferred locations on the sky for conducting efficient AO-assisted extragalactic observations.

1.3 Driving mechanisms for the observed size evolution

The scenarios that have been proposed to explain the size evolution of early-type galaxies just described, and presented in detail in Chapters 3 and 4, can be classified into three categories: 1) equal mass mergers, 2) adiabatic expansion, and 3) minor mergers or late accretion. We outline these scenarios here in anticipation of confronting them against observations in later chapters of this thesis.

1.3.1 Dissipationless major mergers

The first mechanism to be considered for the increase of galaxy half-light radii was the merging of galaxies with similar masses (e.g., Boylan-Kolchin et al., 2005; Khochfar & Silk, 2006; Boylan-Kolchin et al., 2006). Dissipationless (‘dry’) major mergers are interactions between gas-poor objects with equal masses, occurring without additional star formation to produce massive quiescent galaxies (e.g., van Dokkum, 2005). Simulations

have shown that the slope of the size-mass relation stays preserved in this process, while its zero-point evolves towards lower values. However, the increase in size is almost directly proportional to the increase in mass, as demonstrated in Figure 1.2 which shows the results of a series of simulated dissipationless major mergers (Boylan-Kolchin et al., 2006). These authors traced the results of 1 : 1 and 0.33 : 1 mergers with various orbital properties, characterized by pericentric distance r_p and eccentricity e , and found that all stellar remnants remained on the fundamental plane defined by their progenitors, but with the positions shifted towards larger radii. We will consider the implications of this later in this thesis, but to foreshadow that discussion we note here that this is in variance with the fact that the massive quiescent galaxies at high- z and at $z = 0$ cover an equal mass range (see e.g., Figures 3.5 and 4.1). Longhetti et al. (2007) estimated that only 30% of massive passively evolving objects in their sample, the ones at the lower end of mass distribution, could grow their size (and mass) via major dry mergers at $z < 1.5$. The other challenge is the fact that the number of major ‘dry’ mergers inferred from the close pair fraction among quiescent galaxies at $0 < z < 2$ (Bundy et al., 2009; De Propris et al., 2010; Williams et al., 2011) and the number of major mergers produced in N-body Λ CDM (cold dark matter with a cosmological constant) simulations covering the full length of cosmic history (Shankar et al., 2010) are too low to produce the size growth observed in the redshift range $0 < z \lesssim 2.5$ and presented in § 4.5.

1.3.2 Adiabatic expansion and feedback

In the model for size growth proposed by Fan et al. (2008, 2010) a powerful feedback removes large amounts of cold gas from the central galaxy regions inducing a redistribution of galaxy stellar content. The type of feedback in this scenario depends on the stellar mass of a galaxy, and for masses $M_* > 3 \times 10^{10}$ it is related to quasar activity, i.e., the size growth is driven by gaseous mass loss from the central region of a galaxy due to quasar winds. For early-type galaxies with lower masses ($M_* \lesssim 2 \times 10^{10}$) (less prominent) size evolution is induced by supernovae feedback. A similar process (adiabatic expansion due to mass loss from evolved stars) has been discussed as a driving mechanism for galaxy size growth by Damjanov et al. (2009), and is presented in more detail on § 3.6. At this point it is worth noting that in any scenario involving adiabatic expansion the amount of size evolution depends on the time required for the mass ejection (e.g., Hills, 1980). If the mass loss occurs on the time scale τ_{ej} that is shorter than the dynamical timescale

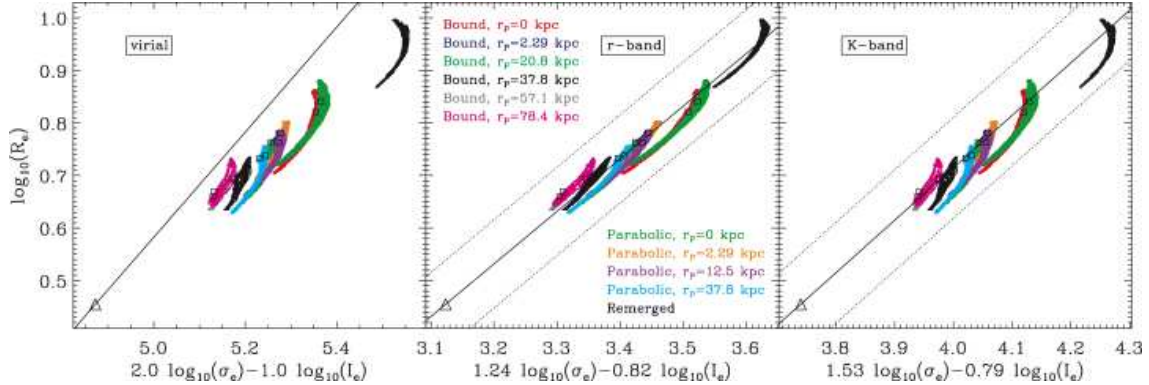


Figure 1.2 Figure taken from Boylan-Kolchin et al. (2006) showing the locations of the equal-mass merger remnants in the plane in $(\log \sigma_e, \log \langle I_e \rangle, \log R_e)$ -space that corresponds to the edge-on projection of the virial plane (left), r -band fundamental plane (middle; Jørgensen et al., 1996) and K -band fundamental plane (right; Pahre et al., 1998). The solid line in each panel indicates a slope of 1 for the edge-on view; the dotted lines in the middle and right-hand panels indicate the observed 1σ scatter in the direction of R_e . For each panel, each simulation (corresponding to a particular set of orbital parameters) is plotted with a different colour. Each point of a given colour corresponds to one of 10^4 viewing angles, while the square marks the ‘most probable’ remnant. A single remerger simulation, using the remnants of runs with parabolic orbit ($r_p = 12.5$ kpc) and bound orbit ($r_p = 78.4$ kpc) as initial galaxies and with a parabolic orbit with $r_p = 21$ kpc, is plotted in black. The initial galaxy model is a single point (large triangle). The effective radii are measured in kpc, the velocity dispersions in km s^{-1} and surface brightnesses in $10^{10} M_\odot \text{kpc}^{-2}$ for all panels.

τ_D ($\tau_D = 1/\sqrt{G\rho}$, where ρ is the density of a system), it does not perturb the velocity of stars in the system and velocity dispersion right after the mass has been lost is the same as the initial velocity dispersion. If in addition the system is in virial equilibrium before mass loss the square of the initial velocity dispersion $\langle v_0^2 \rangle$ is equal to the the mean square velocity introduced in § 1.1. Since $\tau_{ej} < \tau_D$, immediately after ejection the stellar component keeps the same initial orbit of the size R_0 . The mass loss ΔM decreases the binding energy of the system that becomes:

$$E = W + K = \left[\frac{M\langle v_0^2 \rangle}{2} - \frac{GM^2}{R_0} \right], \quad (1.10)$$

where $M = M_0 - \Delta M$ is the mass left in the system, which expands on a dynamical timescale to larger orbital size R . When this new equilibrium stage is reached, the total energy of a system is:

$$E = \frac{W}{2} = -\frac{GM^2}{2R}. \quad (1.11)$$

Combining equations 1.10 and 1.11 with the expression for $\langle v_0^2 \rangle$ (Eq. 1.4) gives the ratio between the initial and final size of the system expanding on the timescales shorter than dynamical timescale:

$$\frac{R}{R_0} = \frac{1}{1 - \frac{\Delta M}{M - \Delta M}}. \quad (1.12)$$

On the other hand, if the system experiences mass loss on much longer timescales and remains in virial equilibrium while losing mass and expanding in size, the relation between the change in orbital radius and the change in mass is:

$$\frac{R}{R_0} = \frac{1}{1 - \frac{\Delta M}{M}}. \quad (1.13)$$

Equations 1.12 and 1.13 show that the faster ejection of mass is more effective in increasing the size of a system. Fan et al. (2010) argue that the mass loss due to any type of stellar feedback proceeds on timescales much longer than τ_D , while the gas ejection time associated with quasar winds is on the order of $\tau_{ej} = (1 - 3) \times \tau_D$. In this case massive galaxy stellar content readjusts into equilibrium after a large amount of gas is ejected from the central region on the time scale $\Delta T_{\text{size}} \sim 10^8$ yr, and the size evolution

of the host galaxy follows its quasar evolution with a time delay of 0.5-1 Gyr (Fan et al., 2008). The major feature of the adiabatic expansion scenario is that its relatively short timescale is not in agreement with the the old ages measured for the compact high- z early-type galaxies (e.g., Damjanov et al., 2009; Ragone-Figueroa & Granato, 2011). We will critically examine the plausibility of this scenario in Chapter 3.

1.3.3 Minor mergers or late accretion of low density material

As discussed in 1.3.1, dry mergers between passively evolving objects of similar mass are unlikely to be the primary mechanism that propels the size evolution of massive ellipticals. In another proposed scenario the size growth of these systems is achieved through a series of mergers with low mass density galaxies, that build up an extended envelope around the high density core of massive progenitors (Hopkins et al., 2009; Naab et al., 2009). Using the virial theorem Naab et al. (2009) have estimated the change in structural properties of a simple stellar system due to addition of stellar mass. The initial parameters of the system are total energy E_i , mass M_i , gravitational radius $R_{g,i}$, and mean square velocity $\langle v_i^2 \rangle$, while the properties of accreted systems are: E_a for total accreted energy, M_a for added mass, and $\langle v_a^2 \rangle$ for mean square velocity. The fractional changes of mass and mean square velocity resulting from all accreting events are defined as:

$$\eta = \frac{M_a}{M_i}, \quad \epsilon = \frac{\langle v_a^2 \rangle}{\langle v_i^2 \rangle}, \quad (1.14)$$

respectively. If the energy is conserved during merging, the final stage of the system is characterized by the total energy E_f :

$$\begin{aligned} E_f &= E_i + E_a = -\frac{1}{2}M_i\langle v_i^2 \rangle - \frac{1}{2}M_a\langle v_a^2 \rangle = \\ &= -\frac{1}{2}M_i\langle v_i^2 \rangle(1 + \eta\epsilon) \end{aligned} \quad (1.15)$$

(see Equation 1.4). Based on Eq. 1.14, final mass of the system is given as:

$$M_f = M_i + M_a = M_i(1 + \eta). \quad (1.16)$$

The final total energy of the system can also be written as:

$$E_f = -\frac{1}{2}M_f\langle v_f^2 \rangle. \quad (1.17)$$

Equations 1.15, 1.16, and 1.17 give the ratio of the final and initial square velocity:

$$\frac{\langle v_f^2 \rangle}{\langle v_i^2 \rangle} = \frac{1 + \eta\epsilon}{1 + \eta}, \quad (1.18)$$

while based on equations 1.4, 1.16, and 1.18 the ratio of the final and initial gravitational radius is:

$$\frac{R_{g,f}}{R_{g,i}} = \frac{(1 + \eta)^2}{1 + \eta\epsilon}. \quad (1.19)$$

The increase in total mass of the system for a factor of two can be achieved either through one major merger involving two objects of similar mass and mean square velocities, or in a series of minor mergers where the accreted material comes from small systems with $\langle v_a^2 \rangle \ll \langle v_i^2 \rangle$. In the former scenario, the increase in size follows the increase in mass, i.e., the initial size of the system is doubled (Equation 1.19), while square velocity stays unchanged (Equation 1.18). The latter model of low mass accretion produces a final system with total mass two times higher, mean square velocity two times lower, and gravitational radius four times higher than the initial values. These simplified relations suggests that the main driver of massive galaxy size growth might be minor mergers (Naab et al., 2009; Bezanson et al., 2009). It is important to note that the increase in the gravitational radius in calculations presented here is assumed to follow the increase in (measured) effective radius, which is correct only if the shape of galaxy light profile does not change in the process (see Equation 1.5).

Using the virial theorem (Equation 1.4) and taking into account that the size of a quiescent galaxy is related to its mass (§ 1.2), Fan et al. (2010) have found the relation between the initial mean square velocity and initial mass of the system:

$$\langle v_i^2 \rangle = GM_i^{1-\alpha}, \quad (1.20)$$

where α is the exponent in the size-mass relation. Under the condition that α remains constant (i.e, that the size growth is independent of mass, see e.g., Damjanov et al.,

2011b), the same relation exists between accreted mean square velocity and accreted mass. Since the mass and mean square velocity ratios between the initial system and the accreted material are defined in Equations 1.14, the two ratios become related as:

$$\begin{aligned}\frac{\langle v_a^2 \rangle}{\langle v_i^2 \rangle} &= \left(\frac{M_a}{M_i} \right)^{1-\alpha}, \\ \epsilon &= \eta^{1-\alpha}.\end{aligned}\tag{1.21}$$

Equations 1.18 and 1.19 can now be rewritten as:

$$\frac{\langle v_f^2 \rangle}{\langle v_i^2 \rangle} = \frac{1 + \eta^{2-\alpha}}{1 + \eta},\tag{1.22}$$

$$\frac{R_{g,f}}{R_{g,i}} = \frac{(1 + \eta)^2}{1 + \eta^{2-\alpha}}.\tag{1.23}$$

Trujillo et al. (2011) have taken a step further in this analysis and presented the final mass of the remnant (Equation 1.16) and ratios given by Equations 1.22 and 1.23 as power-laws with exponent N representing the number of minor merger events. Furthermore, these authors have defined the final size of the remnant $R_{g,f}$ as a product of the initial size $R_{g,i}$, change in size at fixed stellar mass, and change in size due to increase in stellar mass:

$$\log R_{g,f} = \log R_{g,i} + \Delta \log R \Big|_{M_i} + \alpha \log \left(\frac{M_f}{M_i} \right).\tag{1.24}$$

As shown in § 4.5.1, the evolution in size at fixed mass is a smooth function of redshift defined by observations, and in this case given in the following form:

$$\Delta \log R \Big|_{M_i} = -\log(1 + \gamma z),\tag{1.25}$$

where the factor γ is related to the exponent β of the size-redshift relation presented in § 4.5.1 as $\gamma \sim [(1 + z)^\beta - 1]/z$. The resulting number of minor mergers N is a function of redshift and the increase in stellar mass per merger:

$$N = -\frac{\log(1 + \gamma z)}{\log \left[\frac{(1 + \eta)^{2-\alpha}}{1 + \eta^{2-\alpha}} \right]}.\tag{1.26}$$

Based on the Equation 1.26 and the uncertainties in fitting the size-redshift relation, Trujillo et al. (2011) argue that for a $\eta = 1 : 10$ mass ratio a set of $\sim 11 \pm 4$ encounters from $z = 1$ to $z = 0$ would increase the progenitor galaxy size and its mass $\sim 7 \pm 4$ and 3 ± 1 times, respectively. Furthermore, the mean square velocity would decrease by $\sim 30\%$. However, the cumulative number of minor mergers extracted from the semi-analytical models of galaxy formation constructed by Bower et al. (2006) is significantly lower than this number of encounters (even when the full range of cosmic history is taken into account, see Shankar et al., 2010). Thus the main property of this evolutionary path for massive quiescent galaxies is that it requires very fine tuning in order to enlarge the size of these systems on average 5-6 times over the redshift range $0 < z \lesssim 2$ while maintaining the slope of size-mass relation approximately constant at all redshifts (e.g., Damjanov et al., 2011a; Nipoti et al., 2009). One way to resolve this problem is to populate high density environments with compact massive galaxies and enhance their merger rate. However, recent results show that the tightly constrained properties of the local size-luminosity relation for early-type galaxies are independent of environmental density (Nair et al., 2011, 2010); one would expect larger scatter in this relation if the size evolution was driven only by highly stochastic processes such as minor mergers. On the other hand, stacked ground-based NIR surface-brightness profiles for massive galaxies of constant number density in five redshift bins over the redshift range $0 < z < 2$ show that the mass within an inner region of $r = 5$ kpc remains roughly constant, while the mass at larger radii builds up smoothly as a function of decreasing redshift (van Dokkum et al., 2010). This result suggests that the minor merger events are important for the growth of massive, elliptical galaxies, but also that the structure of elliptical galaxies is not self-similar as a function of redshift (in variance with the assumption made in calculations of the number of minor mergers presented above). It should be noted here that the recent cosmological simulations of individual massive quiescent galaxies (Oser et al., 2011) support the importance of the accretion of low mass stellar systems for galaxy growth and manage to reproduce power-law relation between effective radius and redshift similar to the one observed in the redshift range $0 < z < 2.7$ (Damjanov et al., 2011b, see § 4.7 for more details).

At this point it is worth describing the scenario proposed by Hopkins et al. (2010b) that includes all three evolutionary paths described above plus the impact of the caveats described in § 1.2. The effects that each of the three size growth scenarios: major

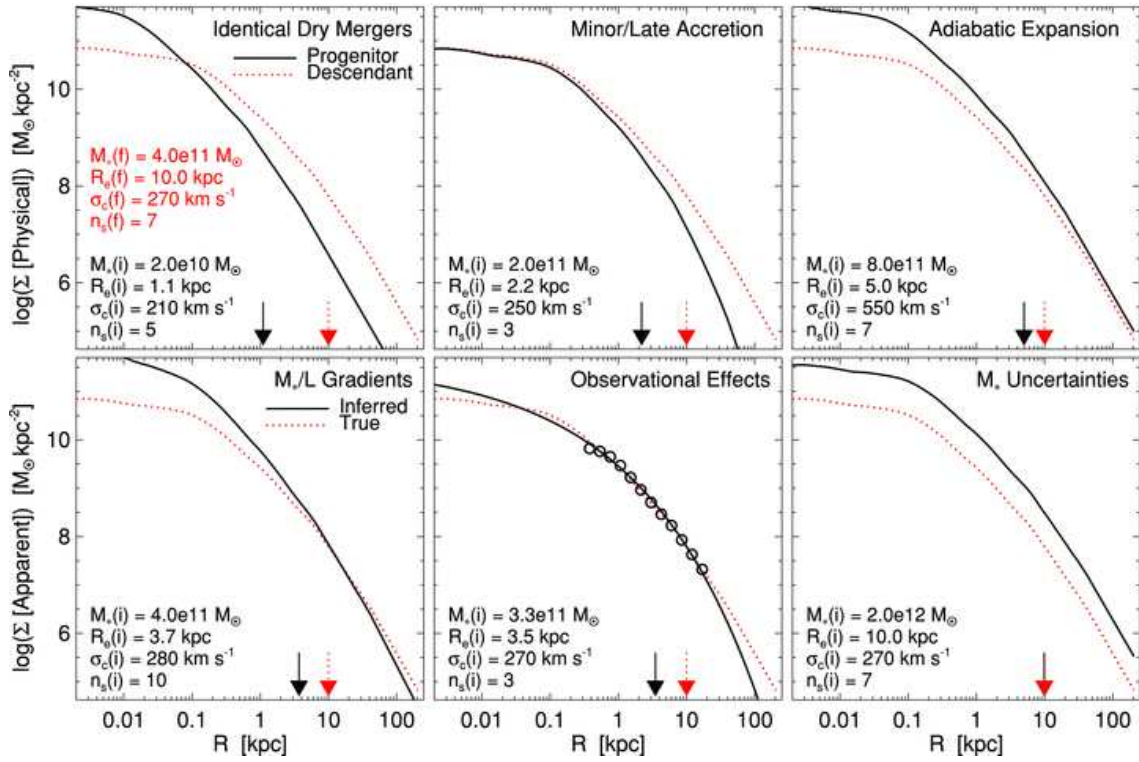


Figure 1.3 (Taken from Hopkins et al., 2010b) Evolution of physical (top) or observationally inferred (bottom) surface stellar mass density profiles, according to different models. The physical stellar mass profile can change because of identical dry mergers (top left), minor/late accretion (top center), or adiabatic expansion (top right). The inferred mass profile (fitted from observations, assuming standard stellar populations and constant stellar M/L) can change because of the presence of stellar mass-to-light ratio gradients (bottom left), seeing effects and surface brightness dimming (points show a simulated $z = 2$ profile with typical seeing and surface brightness depth, solid line is the best-fitting Sérsic profile given the observed range; bottom center), or discrepancies between the true and best-fitting stellar mass (bottom right). Each model is tuned to match the same final profile (the observed profile of a typical massive core elliptical on the local size-mass relation, NGC 4365). Properties of the initial galaxies and final remnant (same in all cases) are given; arrows show effective radii.

merger, adiabatic expansion, and a series of minor mergers have on the real stellar mass density profile of an early-type galaxy are presented in Figure 1.3 (upper panels). Three panels in the lower row show the change in observed stellar mass density profile resulting from the gradient in stellar M/L ratio, observational effects, and the uncertainties in estimated stellar mass, respectively. The authors simulate the evolution of a compact massive spheroid formed at $z \sim 3$ in a merger of two massive discs with a gas fraction of $\sim 30 - 40\%$ at the time of the merger. The compact system formed in this way is then left to evolve passively until $z = 2$, where it shows a stellar M/L gradient due to recently formed starburst populations; this effect produces an effective radius observed in the rest-frame B -band that is $\sim 20 - 30\%$ smaller than the (real) effective radius related to stellar mass. At this redshift the effect of the limited range of galaxy light profile available for Sérsic profile fitting is small, $\sim 10 - 20\%$. Finally, the uncertainties in estimating stellar mass, introduced by the use of different stellar population models, produce an additional $\sim 20\%$ difference in stellar mass and change observed effective radius accordingly. As the system evolves in time, stellar M/L ratio and uncertainties related to the stellar mass inferred from different stellar population models become negligible, and other effects, changing the physical (real) stellar mass density profile, become dominant. Firstly, stellar mass loss induces adiabatic expansion. Given the distribution of stellar population ages already in place at $z = 2$ (that depends on the stellar population models used), stars will lose $\sim 20\%$ of their mass between $z = 2$ and $z = 0$, and in turn the effective radius of the system will increase for the same percentage. This object also has a rich merger history, and experiences several mergers that can be classified either as identical ‘dry’ mergers or as minor/late mergers. At redshift $z \sim 2$ the galaxy experiences a $1 : 3$ major merger with another (less massive) spheroid formed also in a gas-rich merger at higher redshift. This encounter increases the radius of remnant by an additional $\gtrsim 30\%$ ($R_e \propto M_*$), while velocity dispersion stays almost constant. This galaxy experiences the last major merger with a $1 : 3$ mass ratio in the redshift range $0.5 < z < 1$. At $z \sim 1.5$, a series of several minor mergers, including all merger events from $1 : 3$ down to $1 : 10$ mass ratio, starts shaping the galaxy light profile. The smaller merging companions are gas-poor (with gas fraction of $10 - 20\%$), and they contribute more to galaxy’s dissipationless (stellar) content, which is of lower density than the dissipational (gaseous) component and preferentially builds up outer wings of the light profile. As the system grows in mass and radius, these mergers become progressively more minor (Hopkins et al., 2010a). The net result at $z = 0$ is a spheroid that has grown 2.5 times in mass since $z > 2$ and

has effective radius that is a factor 6 – 10 larger than at the time of formation. Thus the combination of all these effects allows for size growth that is close to an order of magnitude from $z = 3$ to $z = 0$. The most important effect here comes from minor/late mergers that contribute a factor of 3 – 4 in size growth. However, an additional factor of 2 – 3 is produced by other contributors described here. Furthermore, while the factors affecting observed stellar mass density profile play major role in the early stages of galaxy evolution, at lower redshifts ($z \lesssim 2$) the most dominant impacts are made by physical processes changing the real stellar mass density profile.

1.4 Thesis overview

This thesis encompasses a range of observational evidence for existence of a peculiar population of very compact passively evolving galaxies at high redshifts ($z \gtrsim 1$) and for continuous size evolution of quiescent objects from $z = 2.7$ to $z = 0$. In addition, it also contains a detailed description of a new idea for optimizing AO assisted observations that will enable the assembly of large statistical samples of high-redshift star-forming and passively evolving galaxies with spatially resolved kinematics and stellar population properties such as age and metallicity.

Chapter 2 gives an overview of the Gemini Deep Deep Survey (GDDS) and of a galaxy light profile fitting technique that is used in subsequent Chapters 3 and 4. Since the GDSS observations had been completed before my thesis related research started, the survey description presented in § 2.1 is extracted from other GDDS papers and is not the result of my research. The details of the method used to fit two-dimensional surface brightness profiles of quiescent GDDS galaxies with deep HST ACS and NICMOS imaging, `Galfit`, are given in § 2.2. However, some aspects of using this technique are deferred to Chapter 3.

Chapter 3 presents the results of NICMOS imaging of a sample of 19 massive passively evolving galaxies with $1.2 < z < 2$, taken from the GDDS (Abraham et al., 2004) and MUNICS (Longhetti et al., 2007) samples. This work was published in the *Astrophysical Journal* (Damjanov et al., 2009). The best fit two-dimensional models, obtained using the `Galfit` software on the NICMOS F160W (rest-frame R -band) images, show that most of these objects have compact regular morphologies which follow the classical de Vaucouleurs profile. These galaxies form a tight sequence in the size vs. surface

brightness parameter space (Kormendy relation defined in § 1.1). Surprisingly, around one-third (3/10) of the massive red objects in the GDDS sample exhibit extraordinarily compact morphologies, with effective radii under one kiloparsec. We refer to these compact galaxies as ‘red nuggets’, and introduce a new ‘stellar mass Kormendy relation’ (stellar mass density vs size) which we use to single out the effects of size evolution from those of luminosity and color evolution in stellar populations. The $1 < z < 2$ passive galaxies have mass densities that are an order of magnitude larger than early type galaxies today and are comparable to the compact distant red galaxies at $2 < z < 3$. We briefly consider mechanisms for size evolution in contemporary models focusing on equal-mass mergers and adiabatic expansion driven by stellar mass loss. As with subsequent chapters that are based on my published first-author papers, my role was to lead the investigation of pre-existing survey observations, reduce, analyze and interpret the data, and write the bulk of the papers.

The analysis of size evolution observed among early-type galaxies, presented in **Chapter 4**, is based on a synthesis of published data sets from 17 spectroscopic surveys (that include data described in Chapter 3), augmented by new measurements for the GDDS galaxies. The results of this study are presented in the paper accepted for publication in the *Astrophysical Journal Letters* (Damjanov et al., 2011b). The morphological properties of the new GDDS sample are obtained by applying the same method as in Chapter 3 to a new sample of 31 quiescent galaxies with available HST ACS F814W imaging. In total, our composite sample contains structural data for 465 galaxies (mainly early-type) in the redshift range $0.2 < z < 2.7$. We show that the size evolution of passively-evolving galaxies over this redshift range is gradual and continuous. Furthermore, the size growth appears to be independent of stellar mass, with the mass-normalized half-light radius scaling with redshift as $R_e \propto (1 + z)^{-1.62 \pm 0.34}$. Using the best fit Sérsic profile we calculate the mass density within the central kpc of these objects and find smooth and substantial evolution of central mass density by a factor of ~ 3 over our redshift range, even if only objects at constant number density (equal to number density of massive galaxies from van Dokkum et al., 2010) are taken into account. The constraints that the new evidence for smooth and continuous evolution in size and central mass density put on the contemporary models of galaxy size evolution are also discussed in this chapter.

A new approach in finding the best regions in the sky for AO assisted observations is described in **Chapter 5**. This work was published in the *Publications of the Astro-*

nomical Society of the Pacific (Damjanov et al., 2011a). We present the coordinates of $67\ 55' \times 55'$ patches of sky which have the rare combination of both high stellar surface density ($\geq 0.5\ \text{arcmin}^{-2}$ with $13 < R < 16.5\ \text{mag}$) and low extinction ($E(B - V) \leq 0.1$). These fields are found by utilizing the HEALPix software to construct all-sky stellar count surface density maps and combine them with the existing dust maps (Schlegel et al., 1998). The optimal field, centered at RA: $7^{\text{h}}24^{\text{m}}3^{\text{s}}$, Dec: $-1^{\circ}27'15''$, has an additional advantage of being accessible from both hemispheres. We propose a figure of merit for quantifying real-world AO performance, and use this to analyze the performance of multi-conjugate adaptive optics (MCAO) in these fields. We also compare our results to those that would be obtained in existing deep fields, confirming that our proposed field displays an order of magnitude better performance (i.e., order of magnitude higher number of high- z objects available for AO assisted observations).

Chapter 2

Sample and Methodology

This chapter describes the properties of the survey that plays the central role in this thesis (§ 2.1). A brief overview of the method used to obtain the morphological parameters of galaxies in our sample based on their light profiles (presented and analysed in Chapters 3 and 4) is given in § 2.2.

2.1 The Gemini Deep Deep Survey

The main sample presented in Chapter 3 and a part of the sample used in Chapter 4 have been drawn from the Gemini Deep Deep Survey (GDDS, Abraham et al., 2004). This is an ultradeep ($K < 20.6$ mag, $I < 24.5$ mag) redshift survey reaching L^* galaxies throughout the $1 < z < 2$ regime irrespective of their star formation history. The lower redshift limit of the GDDS corresponds to the epoch when the evolution of the number density of massive red galaxies ($M_* \gtrsim 2 \times 10^{10} M_\odot$) slows down considerably with respect to higher redshifts (e.g., Brammer et al., 2011). The primary goal of the GDDS was to constrain the space density and investigate the properties of high- z evolved massive galaxies.

In order to minimize the effect of cosmic variance (e.g., Szapudi & Colombi, 1996) the survey covered 4 widely separated ‘pencil beam’ fields with the total area of 121 arcmin², presented in Figure 2.1. The GDDS sample itself was drawn from the 1 deg² Las Campanas Infrared survey (McCarthy et al., 2001) that provides seven-filter ($VRIz'JHKs$) photometric galaxy catalog. Using the Gemini Multi-Object Spectrograph (GMOS) on the Gemini North telescope, spectroscopic redshifts were obtained for 309 galaxies, and

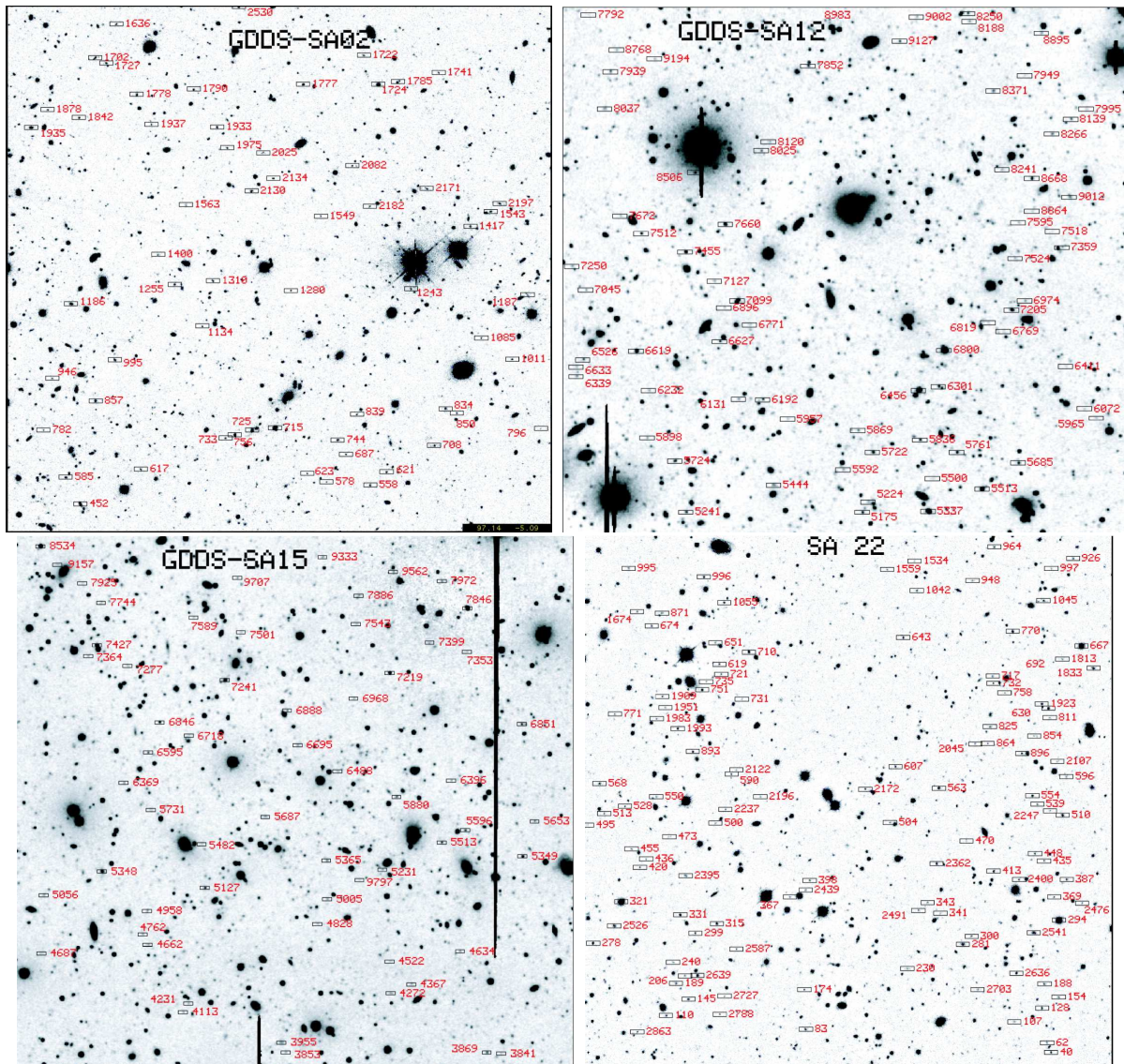


Figure 2.1 (Taken from Abraham et al., 2004) Labelled finding charts for the GDDS-SA02 (upper left, with the central coordinates $RA = 02^{\text{h}}09^{\text{m}}41.30^{\text{s}}$, $DEC = -04^{\circ}37'54.0''$), GDDS-SA12 (upper right, with the central coordinates $RA = 12^{\text{h}}05^{\text{m}}22.17^{\text{s}}$, $DEC = -07^{\circ}22'27.9''$), GDDS-SA15 (lower left, with the central coordinates $RA = 15^{\text{h}}23^{\text{m}}47.83^{\text{s}}$, $DEC = -00^{\circ}05'21.1''$), and GDDS-SA22 (lower right, with the central coordinates $RA = 22^{\text{h}}17^{\text{m}}41.00^{\text{s}}$, $DEC = +00^{\circ}15'20.0''$). The size of each field is $5'.5 \times 5'.5$. The background image is a 180 minute I -band image obtained with the KPNO 4m MOSAIC imager as part of the LCIR survey.

79% of those are of moderate to high confidence level. Glazebrook et al. (2004) show that the GDDS objects form a mass complete sample of $M_* > 5 \times 10^{10} M_\odot$ passively evolving galaxies out to redshift $z = 2$ based on the K -band magnitude limit calculated for a maximally old simple stellar population (SSP).

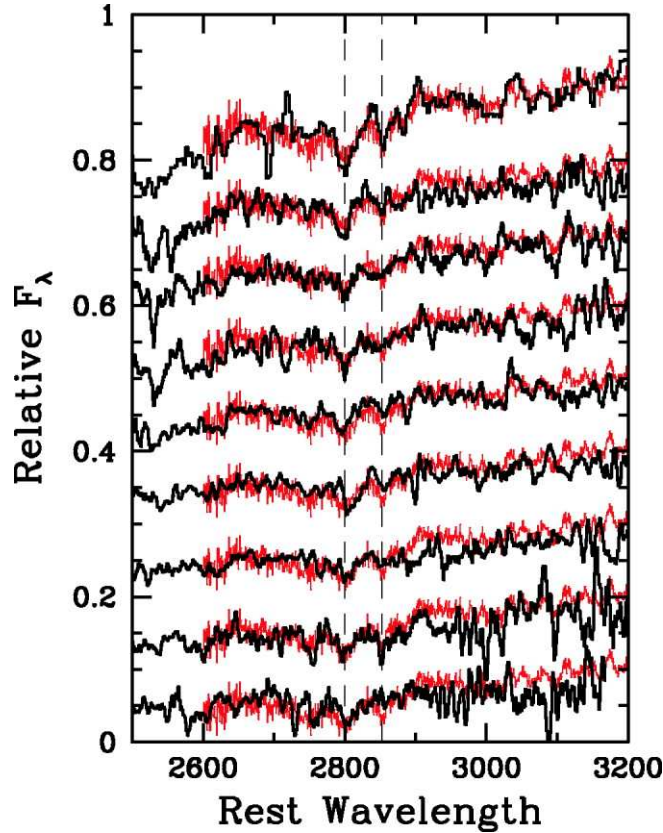


Figure 2.2 (Taken from McCarthy et al., 2004) Representative set of spectra for the GDDS evolved galaxy population at $z > 1.3$. From top to bottom, the objects shown are SA02-1255, SA22-0189, SA22-0674, SA12-5869, SA12-6072, SA12-8895, SA15-4367, SA15-7543, and SA15-5005. Out of these nine objects, SA02-1255 and SA22-0674 have been observed in high resolution with HST ACS F814W, while the remaining seven galaxies have high-resolution imaging obtain either with HST NIC3 F160W or with both NIC3 and ACS (SA12-5869 and SA15-7543). Overplotted on their spectra is the Sloan Digital Sky Survey (SDSS) luminous red galaxy template (Eisenstein et al., 2003). The offset has been applied to each spectrum, in steps of $10^{-18} \text{ erg s}^{-1} \text{ cm}^{-2} \text{ \AA}^{-1}$. The location of the stellar Mg II $\lambda 2800$ and Mg I $\lambda 2852$ lines are indicated by the dashed lines.

The red galaxy population in the GDDS is a mix of evolved and dusty star forming

systems. The GDDS and the K20 (Cimatti et al., 2002) were the first surveys to identify evolved galaxies spectroscopically at $z > 1.3$ in significant numbers. That was achieved by combining photometric data with the spectroscopic features of these objects in the rest-frame ultraviolet (UV) regime such as UV continuum and absorption lines Mg II $\lambda 2800$ and Mg I $\lambda 2852$ (McCarthy et al., 2004). As a result, $\sim 75\%$ of the GDDS red sample (i.e., with $I - K > 4$) at $z > 1.3$ are galaxies showing prominent contribution from old stellar populations in their spectra (Figure 2.2). The complete sample of 10 GDDS objects with available HST NIC3 F160W imaging, presented in Chapter 3, is taken from the subset of 20 quiescent GDDS galaxies found at $z > 1.3$, and the rest-frame UV spectra with prominent Mg absorption lines for seven of these objects are presented in Figure 2.2. Note that at these redshifts F160W filter gives galaxy surface brightness profiles in the rest-frame visible range of wavelengths.

An additional set of 31 GDDS passively evolving galaxies with known structural properties is presented in Chapter 4 of this thesis. These objects are selected from the HST ACS F814W observing campaign covering 63% of the GDDS spectroscopic sample and described in detail in Abraham et al. (2007). It is important to stress here that the methodology of the HST ACS observations provided reliable morphology for galaxies down to $I_{814W} = 24$ mag. At high redshifts the cosmological surface brightness dimming factor of $(1+z)^4$ can lower the surface brightness of disk components below the observable limit and thus enhance the contribution of a compact spheroidal component of a galaxy's light profile. That in turn would lower the estimated value of galaxy's effective (i.e., half-light) radius, as noted by e.g., Mancini et al. (2010). In their Figure 2 Abraham et al. (2007) showed that the long integration times of their ACS observations provided high enough signal-to-noise ratio per pixel to reliably probe the projected stellar mass density profile corresponding to that of the Milky Way at the solar radius redshifted out to $z = 1.7$. Furthermore, four GDDS objects - SA12-5592, SA12-5869, SA15-7543, and SA22-0189 - were observed in both F814W and F160W filters showing a small ($\lesssim 25\%$) difference in sizes measured in two bands, as one would expect based on the latest results of the HST WFC3 deep imaging (see Cassata et al., 2010, 2011). In addition to the simulations presented in Chapter 3, this concordance indirectly confirms the reliability of the structural information recovered from the F160W imaging. In conclusion, all 41 massive passively evolving GDDS galaxies described in Chapters 3 and 4 have the HST imaging that is deep enough for reliable measurements of structural parameters in the

rest-frame UV and visible spectral range.

2.2 2D Modeling of galaxy surface brightness profiles

The method used in Chapters 3 and 4 to extract structural/morphological parameters of the GDDS galaxies from their HST images is parametric fitting. This technique, implemented in the `Galfit` software package (Peng et al., 2002), employs digital imaging to model galaxy surface brightness profiles with a set of analytic functions. `Galfit` takes four input images in FITS file format: the CCD image of a galaxy, a noise array, a Point Spread Function (PSF), and an optional bad pixel mask to look for the two-dimensional (2D) galaxy light profile model that fits the data best, i.e., the model that gives the minimum of reduced χ^2 (χ_ν^2), defined as:

$$\chi_\nu^2 = \frac{1}{N_{\text{dof}}} \sum_{x=1}^{nx} \sum_{y=1}^{ny} \frac{(\text{flux}_{x,y} - \text{model}_{x,y})^2}{\sigma_{x,y}^2}, \quad (2.1)$$

where

$$\text{model}_{x,y} = \sum_{\nu=1}^{nf} f_{\nu,x,y}(\alpha_1 \dots \alpha_n). \quad (2.2)$$

N_{dof} is the number of degrees of freedom in the fit; nx and ny are image dimensions; $\text{flux}_{x,y}$ is the image flux at a given pixel; $\text{model}_{x,y}$ is the sum of nf functions $f_{\nu,x,y}(\alpha_1 \dots \alpha_n)$ with 2D model parameters given as $(\alpha_1 \dots \alpha_n)$; $\sigma_{x,y}$ is the Poisson error in each pixel, usually provided as an input image. The simple shape of early-type galaxy light profiles allows for structural properties to be estimated by using only one type of analytic function, the Sérsic profile (see Chapter 1).

`Galfit` takes several steps in order to find the best fit to a given galaxy light profile. These steps include: 1) preparing the PSF for convolution, 2) cutting out a section of the input image centered on the object to be modeled, 3) creating a model image based on the initial input parameters, 4) convolving the model with the PSF using a fast Fourier transform (FFT) technique, and 5) comparison between the data image and the model with χ_ν^2 minimization done using the Levenberg-Marquardt downhill-gradient method

(Press et al. 1997). The last three steps are iterated until convergence. The details of the procedure (e.g, the choice of the PSF to use with the HST images) are deferred for subsequent discussion Chapter 4.

Although other software for 2D galaxy fitting is also available (e.g., GIM2D, Simard et al., 2002), the analysis performed in Chapters 3 and 4 utilizes `Galfit` because our experiments show that `Galfit` converges to the best fit model (i.e., minimum χ^2_ν) faster than other 2D galaxy modeling algorithms . This property makes `Galfit` very useful when performing a high number of Monte Carlo simulations in order to estimate the errors of the best fit parameters (the method employed in Chapters 3 and 4 for the GDDS galaxy sample). Although the set of output parameters includes uncertainties based on formal statistics, those values correspond only to random uncertainties assuming normal distributions, and neglect the systematic errors which often dominate the error budget. For that reason, in order to compute realistic uncertainties of the light profile modeling it is important to use Monte Carlo methods.

Another important source of error in any procedure used to model the surface brightness profiles is the uncertainty of the estimated background sky level. In the fitting performed to obtain the results presented in Chapters 3 and 4 sky level was kept fixed to the value obtained by measuring photometry in an annulus far away from the visible galaxy outskirts. In the subsequent iterations sky level would be left as a free parameter for `Galfit` to fit, and the the two sets of results were then compared. In a few cases where the fixed sky levels did not match the ones obtained by `Galfit`, the parameters corresponding to lower background surface brightness were adopted for final results since the underestimated sky levels produce larger galaxy radii and thus give more conservative results.

Chapter 3

Red Nuggets at $z \sim 1.5$: Compact Passive Galaxies and the Formation of the Kormendy Relation

This chapter contains the article published in The Astrophysical Journal, Volume 695, Issue 1, pp. 101-115 (2009) and authored by:

Ivana Damjanov, Patrick J. McCarthy, Roberto G. Abraham, Karl Glazebrook, Haojing Yan, Erin Mentuch, Damien Le Borgne, Sandra Savaglio, David Crampton, Richard Murowinski, Stéphanie Juneau, R. G. Carlberg, Inger Jørgensen, Kathy Roth, Hsiao-Wen Chen, and Ronald O. Marzke

Reproduced by permission of the American Astronomical Society.

3.1 Abstract

We present the results of NICMOS imaging of a sample of 19 high mass passively evolving galaxies with $1.2 < z < 2$, taken primarily from the Gemini Deep Deep Survey (GDDS). Around 80% of galaxies in our GDDS sample have spectra dominated by stars with ages $\gtrsim 1$ Gyr. Our rest-frame R -band images show that most of these objects have compact regular morphologies which follow the classical $R^{1/4}$ law. These galaxies scatter along a tight sequence in the size vs. surface brightness parameter space which defines the Kormendy relation. Around one-third (3/10) of the massive red objects in the GDDS

sample are extraordinarily compact, with effective radii under one kiloparsec. Our NICMOS observations allow the detection of such systems more robustly than is possible with optical (rest-frame UV) data, and while similar systems have been seen at $z > 2$, this is the first time such systems have been detected in a rest-frame optical survey at $1.2 < z < 2$. We refer to these compact galaxies as ‘red nuggets’, and note that similarly compact massive galaxies are completely absent in the nearby Universe. We introduce a new ‘stellar mass Kormendy relation’ (stellar mass density vs size) which we use to single out the effects of size evolution from those of luminosity and color evolution in stellar populations. The $1 < z < 2$ passive galaxies have mass densities that are an order of magnitude larger than early type galaxies today and are comparable to the compact distant red galaxies at $2 < z < 3$. We briefly consider mechanisms for size evolution in contemporary models focusing on equal-mass mergers and adiabatic expansion driven by stellar mass loss. Neither of these mechanisms appears able to transform the high-redshift Kormendy relation into its local counterpart, leaving the origin and fate of these compact ‘red nuggets’ unresolved.

3.2 Introduction

The formation mechanism of elliptical galaxies has long been controversial and remains a key test of more general galaxy formation models. The original ‘nature’ (Eggen et al. (1962) monolithic collapse) vs. ‘nurture’ (formation through mergers, (e.g., Schweizer, 1986; Searle & Zinn, 1978; Toomre & Toomre, 1972) debate is still with us, but is now set in a Λ CDM cosmological context which attempts to connect the stellar component of galaxies to an underlying evolutionary picture for the clustering of dark matter halos. Testing this model requires studying the evolution of galaxies over a large redshift range.

A wide range of selection techniques have been effective in selecting galaxies in various redshift ranges on the basis of their current star formation rates (e.g. Lyman break galaxies, sub-mm sources etc), or from the spectral signatures of passively evolving old stellar populations (e.g., extremely red objects (EROs) and other color selections). The most massive local elliptical galaxies have the oldest stellar populations (Gallagher III et al., 1984), so identifying the progenitors of local early-type galaxies within the high-redshift galaxy population is of particular interest. There is a consensus that the mass density in the red sequence is evolving strongly in the $1 < z < 2$ range (GDDS Paper VIII, Abra-

ham et al., 2007; GDDS Paper III, Glazebrook et al., 2004; Fontana et al., 2004; Rudnick et al., 2003), a process that continues at redshifts below unity as well (Faber et al., 2007; Bell et al., 2004b), although the magnitude of the evolution is uncertain (Brown et al., 2007; Chen et al., 2003). Massive morphologically-confirmed elliptical galaxies have been found up to $z = 2$ (GDDS Paper IV, McCarthy et al., 2004; Cimatti et al., 2004) with spectra consistent with formation epochs up to $z > 5$. These observations were in direct contradiction with early Λ CDM models where stellar mass assembly traced the build up of cold dark matter haloes, although additional feedback mechanisms on the baryons have more recently been able to better account for this (e.g., Kang et al., 2006). A complication recently added to this picture is the observation that the space density of ellipticals is found to evolve strongly over $1 < z < 2$ (Paper VIII) even while their stellar populations evolve weakly, suggesting that one must be careful to decouple morphological evolution from evolution of the underlying stellar populations. This is seen at higher redshifts also, where the paucity of passively evolving galaxies at $z > 2$ in deep $J - K$ and $3.5 \mu\text{m}$ selected samples (Kriek et al., 2006; Labbé et al., 2005; Cimatti et al., 2002) shows that the *assembly* epoch for the red sequence may be decoupled from the epoch of the earliest star formation. Studies of star formation history and morphology can only go so far in unraveling the puzzle of galaxy formation; dynamical and chemical probes are needed to connect progenitors to descendants. Clustering signatures offer one dynamical approach to connecting progenitors to descendants and the strong clustering of the passive red galaxies (Daddi et al., 2005a, 2004; Brown et al., 2003; McCarthy et al., 2001) strongly suggest that they are linked to today’s massive elliptical galaxies.

Theoretical attempts to explain these observations have resulted in greatly improved Λ CDM models which decouple mass assembly from this stellar population downsizing. An example is the semi-analytic model of De Lucia & Blaizot (2007). Here the small ellipticals and their stars form early by disc mergers. Massive ellipticals can then grow bigger and more numerous at late times through dissipationless or dry merging. This may even have been observed (Bell et al., 2006b) though there is some disagreement as to whether the Λ CDM merger rate is high enough (Bundy et al., 2007). At this stage it is perhaps fair to say that dry merging simulations show that it does not disrupt elliptical scaling relations (Boylan-Kolchin et al., 2006, 2005; González-García & Van Albada, 2003) as one might naively expect. However only a limited number of simulations of this process have been done and they have not yet been incorporated into cosmological mod-

els in a detailed way such that they can be compared with data (e.g., numbers, sizes and masses of galaxies). Further it is not clear that a dry merging hierarchy consistent with cosmological downsizing can also be made consistent with the evolving mass-metallicity relation (Pipino & Matteucci, 2008). A contrasting picture is painted by Naab et al. (2007) using a SPH model of individual systems. They argue for a formation mode dominated by something very close to early monolithic collapse, but in a Λ CDM cosmological context, with mergers (along with accretion) playing only a minor role in stellar mass growth at late times.

High spatial resolution studies of the morphologies and structures of passive galaxies offer one approach to gauging the importance of recent major merger events. A number of studies with the *Hubble Space Telescope* (HST) have shown that half or more of red galaxies in color-selected samples have simple early type morphologies. Most of these studies are confined to redshifts of ~ 1.5 and less, and the early-type fraction varies from $\sim 50\%$ to 70% (Moustakas et al., 2004; Yan & Thompson, 2003). At higher redshifts a significant fraction of the red galaxies appear to be discs (e.g., Paper VIII, Fontana et al., 2004). Understanding the connection between these two classes of objects naturally focuses on the importance of mergers, since nearly equal-mass mergers are thought to transform discs into spheroids. Mergers, both gas-rich and dissipationless, are also thought to be important in the growth of the red sequence and evidence, both direct and indirect, supports that this is occurring at intermediate and low redshifts (e.g., Bell et al., 2006a, and the references therein). It appears that much of the high-redshift merging activity may be of the dissipationless variety where the main effect of merging is to reorganize existing stellar population *without* triggering new star formation. It is difficult to envision how this might operate unless the merging systems are themselves gas-poor, which is not generally expected (van Dokkum, 2005). In any case, the signatures of such ‘dry’ mergers are difficult to detect at high redshifts.

Recently, several imaging studies have shown that red galaxies at $z > 1$ appear smaller than their likely present-day descendants with the same stellar mass (Trujillo et al., 2007; Longhetti et al., 2007; Cimatti et al., 2008). The implications of these observations are seen most clearly in the structural and dynamical scaling relations, the Fundamental Plane and its projections (the Faber-Jackson (1976) and Kormendy (1977) relations). In the present paper we explore the nature of the Kormendy relation, (mean surface brightness within the effective radius, $\langle \mu \rangle_e$, versus effective radius, R_e). This is

the most observationally accessible projection of the fundamental plane at high-redshift. Our analysis spans the redshift range $1.2 < z < 2$ using HST NICMOS observations of a sample of quiescent high-redshift galaxies taken mainly from the Gemini Deep Deep Survey (GDDS Paper I, Abraham et al., 2004). We present NICMOS F160W images for ten of the twenty $z > 1.3$ passive red galaxies from Paper IV. These systems all have spectra dominated by old stellar populations. This extends to higher redshifts ($z > 1.7$) than the earlier NICMOS work of Longhetti et al. (2007) from the Munich Near-IR Cluster Survey (MUNICS, Drory et al., 2001). We also independently analyze the archival NICMOS data of Longhetti et al. (2007) in the redshift range $1.2 < z < 1.7$ to supplement our sample and confirm their findings. At the higher redshifts previous findings of compact galaxies were based on optical data obtained with the Advanced Camera for Surveys (ACS) onboard HST (Cimatti et al., 2008). Our use of NICMOS allows us to more robustly show that the old components in the galaxies are truly compact. Finally, we are able to unify the optical and infrared work by introducing a new ‘stellar mass Kormendy relation’ which we use to better quantify evolution in the sizes of early-type galaxies as a function of stellar mass over the redshift range $1 < z < 2$. We briefly examine the likelihood that dry mergers explain such size evolution, and examine whether an alternative process, adiabatic expansion, might be more important. We describe the observations in section 3.3, our analysis in section 3.4, and present our results in section 3.5. In section 3.6 we discuss the implications of our observations for simple models for galaxy size growth. Throughout we use standard cosmological parameters; $H_0 = 70 \text{ km s}^{-1} \text{ Mpc}^{-1}$, $\Omega_m = 0.3$, $\Omega_\Lambda = 0.7$. Unless stated otherwise, all magnitudes are based on the AB system.

3.3 Description of the observations

3.3.1 Sample definition

Our sample of galaxies was taken mainly from the GDDS, crafted to sample the galaxy population in the critical $1 < z < 2$ interval with an emphasis on red galaxies (Paper I). While modest in area (120 square arcminutes), the survey is spread over four independent and representative sightlines. Redshifts for ~ 300 galaxies brighter than $I(\text{Vega}) = 24.5$ were obtained from 30-hour long integrations using the GMOS spectrometer on Gemini

North. This magnitude limit corresponds to the stellar mass of $2.5 \times 10^{10} M_{\odot}$ for a galaxy with the redshift of formation $z_f = 10$ and maximally old stellar population observed at redshift $z = 1.5$ (Paper III). We classified the galaxies on the basis of their spectra, depending on whether they were dominated by active star formation, stars older than ~ 1 Gyr, intermediate age (0.3 – 1 Gyr) populations, or a mix of these types. Of the 302 galaxies with redshifts, 47 have spectra dominated by old stars, and twenty of these lie at redshifts beyond 1.3. Spectra of these twenty galaxies and estimates of their ages and formation redshifts are presented in Paper IV. Deep I -band images of the GDDS galaxies at $z < 1.7$ with the ACS on HST reveal that the correlation between spectral type, and hence stellar content, and morphological class seen at present is strong at these redshifts. Nearly all of the GDDS galaxies with passive spectral classes have compact morphologies consistent with early Hubble types, while the actively star forming galaxies have morphologies that range from simple disks to complex structures indicative of ongoing mergers. The GDDS galaxies discussed in this paper are a subset of the GDDS galaxies having spectra dominated by old stars (class “001” from Paper I) and $z > 1.3$. The key properties of this sample are given in Table 3.1.

Our primary sample of ten galaxies is drawn from the GDDS and determined by the number of available orbits and the desired depth of NICMOS imaging. The targets were selected randomly, with the exception of the two (12-5869 and 12-5592) that could be covered in a single pointing. We also analyzed archival data from the MUNICS survey for nine additional galaxies with properties similar to those of our GDDS sample. Longhetti et al. (2005) analyzed spectrophotometric data set for these galaxies from the near-infrared spectroscopic follow-up of a complete sample of bright ($K < 18.5$) EROs ($R - K > 5.3$) selected from the MUNICS survey¹. Low resolution spectroscopic and photometric data revealed stellar masses greater than $10^{11} M_{\odot}$ and dominant old stellar population for all objects in the sample (see Table 3.2). As will be described below, this additional data provided us with a useful check of our methodology by allowing us to compare results from our analysis pipeline against those published in Longhetti et al. (2007).

¹This is actually a blank field survey, the intention was to *find* high- z clusters from deep wide-field near-IR imaging.

Table 3.1. Properties of ten galaxies in GDDS sample

ID	z	Mass ^a [$10^{11} M_{\odot}$]	Age ^b [Gyr]
12-5592	1.623	1.16 ± 0.27	$1.1^{+0.3}_{-0.4}$
12-5869	1.51	3.14 ± 0.43	$1.2^{+0.6}_{-0.2}$
12-6072	1.576	0.59 ± 0.27	$1.6^{+2.1}_{-1.3}$
12-8025	1.397	1.25 ± 0.39	$0.8^{+0.6}_{-0.1}$
12-8895	1.646	3.18 ± 0.44	$2.5^{+0.3}_{-0.3}$
15-4367	1.725	0.56 ± 0.15	$2.1^{+0.4}_{-0.9}$
15-5005	1.845	0.67 ± 0.24	$0.5^{+0.7}_{-0.1}$
15-7543	1.801	1.06 ± 0.30	$0.9^{+0.5}_{-0.2}$
22-0189	1.49	2.85 ± 0.98	$3.0^{+0.7}_{-0.2}$
22-1983	1.488	1.34 ± 0.53	$1.1^{+3.1}_{-0.5}$

^a GDDS mass estimates are based on the Baldry & Glazebrook (2003) IMF, and taken from Paper III

^b Minimum galaxy ages from Paper IV

Table 3.2. Properties of nine massive galaxies in MUNICS sample^a

ID	z	Mass ^b [$10^{11} M_{\odot}$]	Age [Gyr]
S2F5_109	1.22	5.94 ± 0.95	1.7 ± 0.3
S7F5_254	1.22	4.68 ± 0.16	5.0 ± 0.1
S2F1_357	1.34	4.65 ± 0.40	4.0 ± 0.1
S2F1_389	1.40	2.15 ± 0.86	3.0 ± 0.5
S2F1_511	1.40	2.07 ± 0.89	1.3 ± 0.3
S2F1_142	1.43	4.06 ± 0.94	2.2 ± 0.2
S7F5_045	1.45	3.58 ± 1.10	1.7 ± 0.3
S2F1_633	1.45	3.52 ± 0.51	4.0 ± 0.5
S2F1_443	1.70	3.58 ± 1.48	3.5 ± 0.3

^a from Longhetti et al. (2007)

^b MUNICS mass estimates are taken from Longhetti et al. (2005, Salpeter IMF), and transformed to Baldry & Glazebrook (2003) IMF following the relation given in Paper III

3.3.2 NICMOS observations

The ten GDDS galaxies were observed with Camera 3 on NICMOS using the F160W filter. Each individual exposure was 896 seconds in duration with multiple samples using the STEP64 read pattern. A single orbit contained three exposures and we observed each target over four HST orbits for a total integration time of 10740 seconds. Two of the fields overlapped and the images for targets 12-5869 and 12-5592 have twice the exposure time of the others. These objects are discussed in detail in McCarthy et al. (2007). We dithered in non-integer pixel steps between each exposure. The individual frames were dark corrected, sky subtracted and combined using the DRIZZLE algorithm (Fruchter & Hook, 2002) with a final pixel size of $0''.12$. Residual sky levels in the final mosaics were derived from Gaussian fits to a histogram of sky values and were subtracted.

As noted above, we also re-analysed nine galaxies from the MUNICS sample of red galaxies described in Longhetti et al. (2007). The MUNICS data set was obtained using Camera 2 on NICMOS, and is thus more finely sampled, and somewhat shallower, than our NIC3 images. As described below, analyzing this NIC2 data allowed us to explore, and ultimately rule out, the possibility that the coarser sampling of our NIC3 data might lead to poor model fits and spurious sizes. We retrieved the pipeline-processed individual NIC2 images from the HST archive. We then corrected each image for residual pedestal effects and combined them into mosaics using the DRIZZLE algorithm with a final pixel size of $0''.05$. The properties of the nine galaxies in this sample are summarized in Table 3.2.

3.4 Analysis

3.4.1 Surface brightness profiles

Using the `Galfit` software package (Peng et al., 2002), we derived two-dimensional (2D) surface brightness profiles by fitting synthetic galaxy images to our data using a range of surface brightness profiles, ellipticities and orientations. A series of models were constructed using exponential surface brightness profiles, de Vaucouleurs $R^{1/4}$ profiles and the more general $R^{1/n}$ Sérsic profiles. We did not consider more general fitting laws due to the relatively small range of radii ($0''.12 - 2''$, or $1 - 17$ kpc at $z = 1.5$) covered by our observations. Models with a range of scale lengths and eccentricities were convolved with

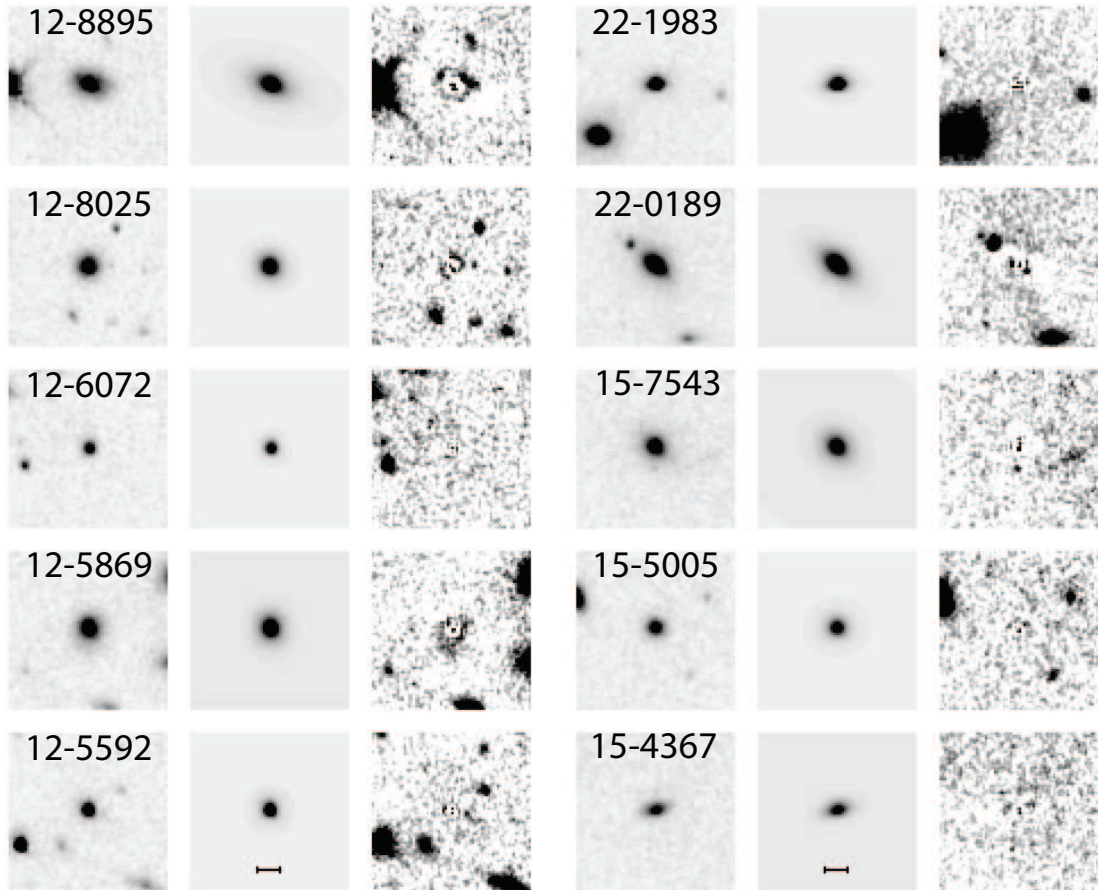


Figure 3.1 NIC3 images and the results of our 2D fitting with `Galfit` for our sample of 10 GDDS galaxies with $1.3 < z < 2$ and spectra dominated by old stars. The three columns present the drizzled F160W image, the best fitting $R^{1/4}$ model, and the residuals. The residual images have been scaled by a factor of 10 compared to the data and models to bring out faint features. The bars at the bottom are one arcsecond in length.

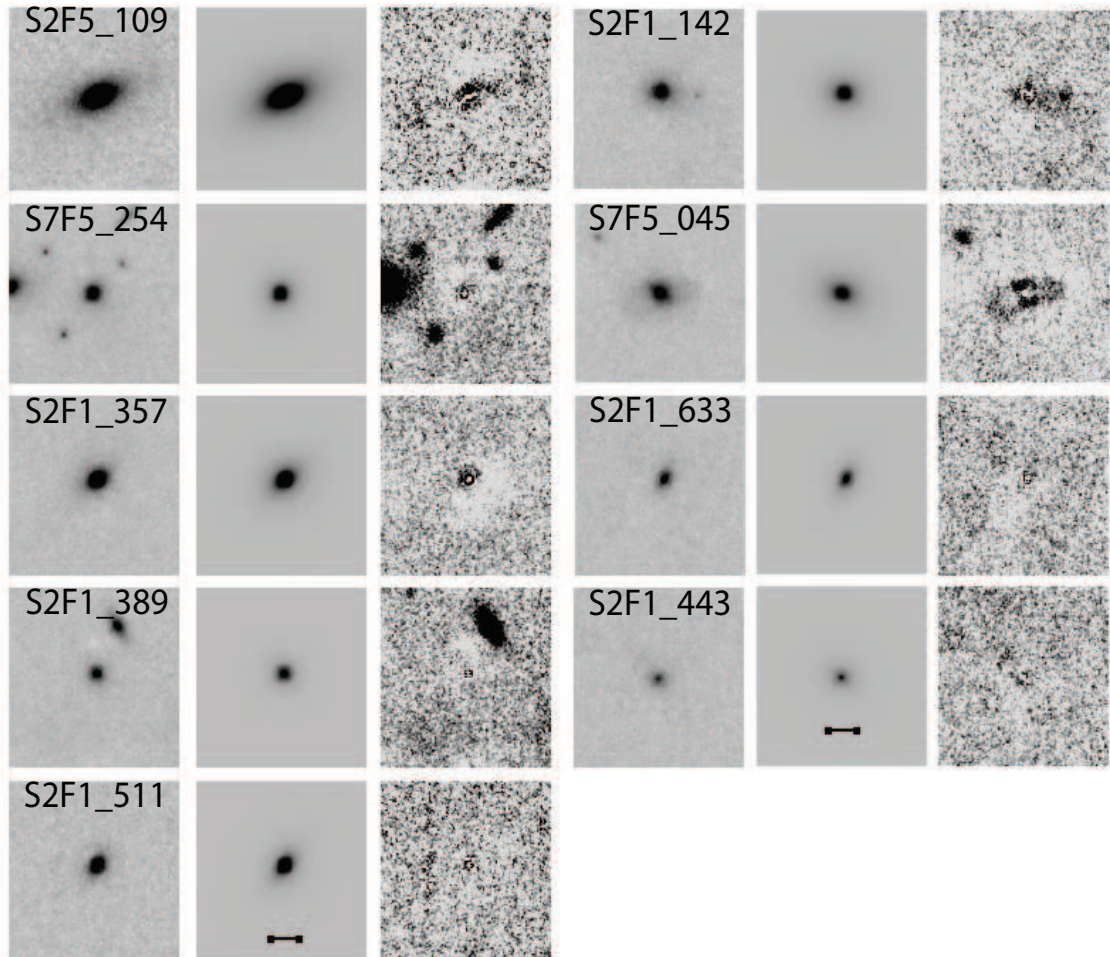


Figure 3.2 NIC2 images and the results of our 2D fitting with `Galfit` of the six galaxies from Longhetti et al. (2007). The three columns present the galaxy, the best fitting $R^{1/4}$ model, and the residuals. The residual images have been scaled by a factor of 10 compared to the data and models to bring out faint features. The bars at the bottom are one arcsecond in length.

the Point Spread Function (PSF) of the observations and subtracted from the NICMOS images. We used PSFs derived from well-detected unsaturated stars in each NIC3 field rather than the TinyTim simulations as we found the former produced better fits. The residuals were computed and the model parameters were iterated to minimize the square of the residuals within the box of $8''.4 \times 8''.4$ centered on each galaxy. The initial guess for the centroid was the position of the highest intensity pixel within the fitting box, and the total magnitude was estimated according to the total intensity confined in this box. Both initial guesses were made after masking out of the neighbouring sources. The root mean square (RMS) image was used to give relative weights to the background pixels during the fitting. By using different stars the width of the NIC3 PSF was allowed to vary to include the effects of spatial and temporal variations in the NIC3 PSF. Changing the PSF had very little impact on the derived effective radii in all cases. The best-fit models for all galaxies in the sample are presented in Figure 3.1 (middle column) along with the residual images (last column). Parameters of the best-fit $R^{1/4}$ and $R^{1/n}$ profiles for each galaxy are given in Table 3.3. The listed minima of reduced χ^2 are well below unity, suggesting that the flux uncertainties introduced by the RMS images are overestimated. We performed the same morphological analysis on the MUNICS galaxies (Longhetti et al., 2007). The NIC2 PSF used for modeling 2D profiles of these objects was derived from the TinyTim simulations. The resulting best-fit $R^{1/4}$ profiles are graphically illustrated in Figure 3.2. The parameters obtained are listed in Table 3.4, along with the results from Longhetti et al. (2007) for comparison. The reduced χ^2 are again below unity, but the values obtained for our best fit are very similar to the ones obtained for Longhetti et al. (2007) parameters, except for the total F160W magnitudes where the difference is greater than 1σ . The reasons for this discrepancy may be the simulated PSF we used for 2D fitting and the different methods applied for background subtraction. Also, resulting $R^{1/4}$ fit effective radius R_e and surface brightness $\langle\mu\rangle_e$ for objects S2F1_142, S7F5_45, S2F1_633, and S2F1_443 differ for more than 1σ from the previously reported ones. When fitted with $R^{1/n}$ profiles, the best fits for the three of these objects - S2F1_142, S2F1_633, and S7F5_45 - have lower indices n than listed in Longhetti et al. (2007) - 2 instead of 3.5, 2.5 instead of 4.1, and 1.5 instead of 2, respectively. On the other hand, the best fit $R^{1/n}$ profile for S2F1_443 has index $n = 2.8$, higher than $n = 1.9$ reported by Longhetti et al. (2007). For the rest of the MUNICS sample the difference in the goodness of fit for $R^{1/4}$ profile between our and Longhetti et al. (2007) analysis is $\Delta(\chi^2) \lesssim 0.2$.

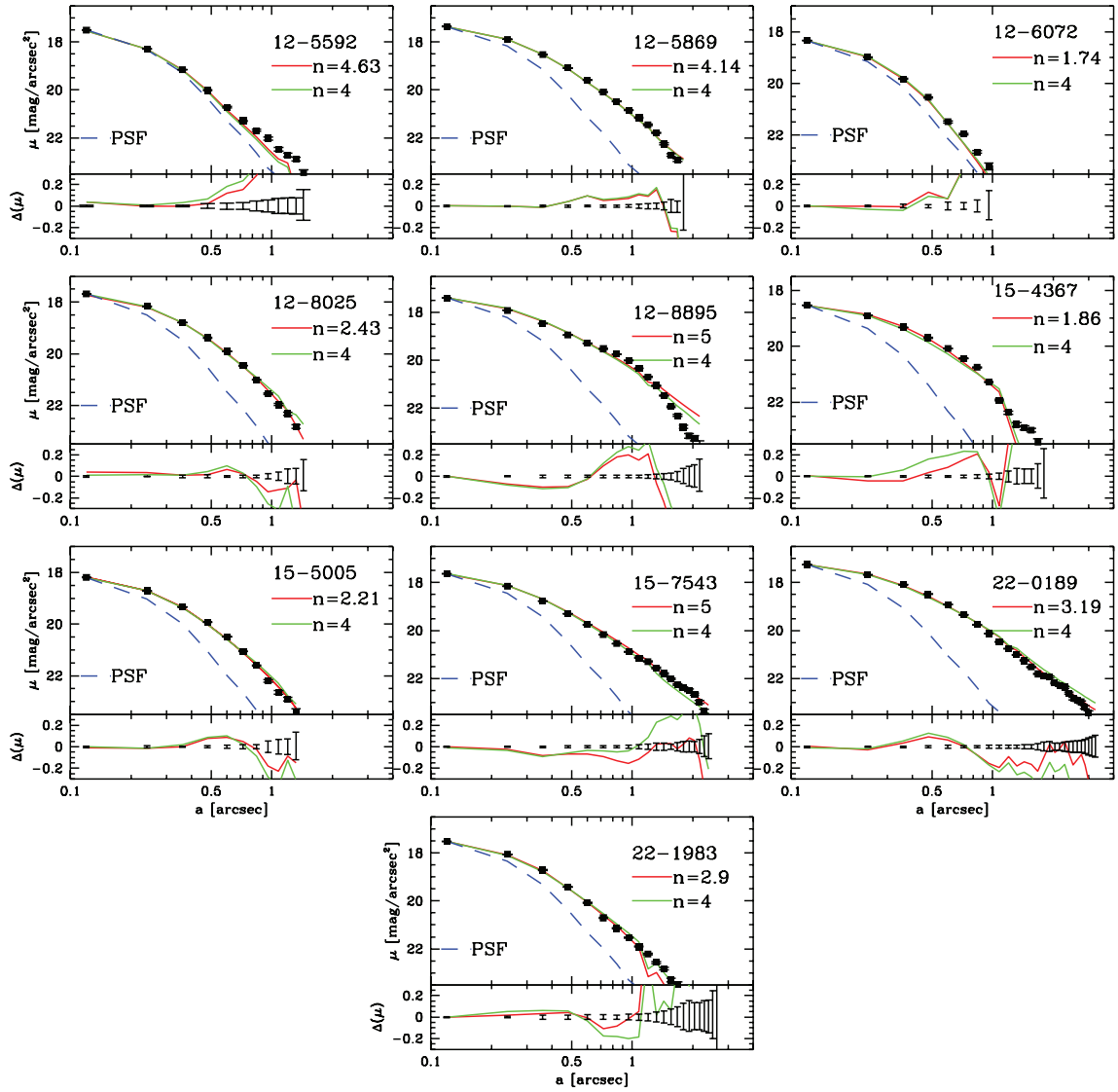


Figure 3.3 Upper panels: major axis surface brightness profiles in the F160W band for each galaxy (squares), with $R^{1/4}$ (green line) best-fit profile, $R^{1/n}$ (red line) best-fit profile, and a PSF profile (blue dashed line) overplotted. The step used to present isophotal surface brightness corresponds to the pixel scale of our drizzled NIC3 images ($0''.12$). The limiting surface brightness in each panel presents (roughly) 5σ limit for our observations. The lower part of each panel shows the residual differences between the data points and the model fits, with the 1σ errors on the data shown for comparison.

As a consistency check, we also determined one-dimensional (1D) azimuthally averaged radial surface brightness profiles for each galaxy and for the corresponding models resulting from its 2D profile fits. These 1D radial profiles were extracted using the approach developed by Jedrzejewski (1987) as implemented in IRAF (Tody, 1993). Integrated magnitudes were determined within a series of elliptical isophotes, the spacing of which grows with radius. We masked objects closer than $10''$ before determining the surface brightness profiles of the galaxies. In most cases we are able to determine the profile over roughly six magnitudes of surface brightness and to radii of $1''.5$, or ~ 13 kpc at $z = 1.5$. The 5σ limiting surface brightness for most of our observations is $\mu_{F160} \approx 23$ mag arcsec $^{-2}$; the data for 12-5869 and 12-5592 reach approximately 0.3 magnitudes deeper. This surface brightness limit corresponds to $\mu_r \approx 20$ mag arcsec $^{-2}$ ($\mu_r \approx 20.3$ mag arcsec $^{-2}$ for 12-5869 and 12-5592) for a galaxy at redshift $z = 1.5$ that is formed at $z_f = 6$ with exponentially declining SFR and e -folding time $\tau = 0.1$ Gyr. Surface brightness profiles were determined in a similar fashion for each star that served as a local measure of the PSF. Azimuthally averaged surface brightness profiles for all of our GDDS objects are presented in Figure 3.3, with the profiles of best-fitting 2D models and a PSF profile shown as solid lines and a dashed line, respectively. Figure 3.3 confirms that all galaxies in our GDDS sample are well resolved, except for the target 12-6072 that seems only marginally resolved when compared to the PSF 1D profile. The profiles are smooth in nearly all cases, the exception being object 15-4367 which shows a step at $a = 1''.5$. Careful examination of this object's NIC3 image revealed that it was not perfectly symmetric and harboured a weak disk. The best $R^{1/n}$ profile index of ~ 2 confirms these findings. In addition, 15-4367 has a very faint neighbouring object that had to be masked out before fitting. These two effects produced the step in its 1D profile seen in Fig. 3.3.

In order to estimate the errors on parameters obtained by our 2D and 1D fitting procedures, we undertook a series of Monte Carlo (MC) simulations which incorporated all the sources of systematic and random errors we were able to identify. We constructed a set of galaxy images from our best-fit model for each galaxy and convolved these with a range of PSFs (i.e., PSFs obtained from different stars) and added these to the background images. We dithered the position image about the central value to explore the importance of binning, and used RMS images to construct 2D arrays of random numbers to capture poisson noise and structure in the sky background. Each image constructed

Table 3.3. Morphological parameters of galaxies in the GDDS sample

ID	F160W [mag]	n	r_e [arcsec]	R_e [kpc]	$\langle \mu \rangle_e^{160W}$ [mag/arcsec ²]	$\langle \mu \rangle_e^{corr}$ [mag/arcsec ²]	b/a	χ^2
12-5592	21.60 ± 0.04	4	0.05 ± 0.03	0.4 ^{+0.2} _{-0.3}	17 ± 1	14 ± 1	0.9 ^{+0.08} _{-0.4}	0.205
	21.58 ± 0.07	5 ± 2	0.05 ± 0.05	0.4 ± 0.4	17 ± 2	14 ± 2	0.9 ^{+0.1} _{-0.3}	0.200
12-5869	20.79 ± 0.09	4	0.25 ± 0.06	2.1 ± 0.5	19.8 ± 0.5	16.6 ± 0.5	0.82 ± 0.07	0.495
	20.78 ± 0.06	4.1 ± 0.9	0.25 ± 0.04	2.1 ± 0.3	19.8 ± 0.3	16.7 ± 0.3	0.82 ± 0.07	0.495
12-6072	22.30 ± 0.08	4	0.04 ± 0.04	0.3 ± 0.3	17 ± 3	14 ± 3	0.97 ^{+0.03} _{-0.3}	0.174
	22.31 ± 0.07	1.7 ± 1.2	0.09 ± 0.04	0.8 ± 0.3	19.1 ± 0.9	15.9 ± 0.9	0.96 ^{+0.04} _{-0.2}	0.172
12-8025	21.05 ± 0.05	4	0.25 ± 0.05	2.1 ± 0.4	20.1 ± 0.4	17.2 ± 0.4	0.79 ± 0.06	0.258
	21.13 ± 0.03	2.4 ± 0.6	0.24 ± 0.03	2.0 ± 0.2	20.0 ± 0.3	17.1 ± 0.3	0.89 ± 0.06	0.240
12-8895	20.6 ± 0.2	4	0.3 ± 0.1	2.9 ± 0.7	20.2 ± 0.6	16.8 ± 0.6	0.42 ± 0.06	0.418
	20.44 ± 0.04	5.0 ± 0.6	0.50 ± 0.05	4.2 ± 0.4	20.9 ± 0.2	17.5 ± 0.2	0.52 ± 0.04	0.407
15-4367	21.81 ± 0.06	4	0.19 ± 0.04	1.6 ± 0.3	20.2 ± 0.4	16.7 ± 0.4	0.22 ± 0.05	0.248
	21.91 ± 0.03	1.9 ± 0.3	0.22 ± 0.03	1.9 ± 0.2	20.6 ± 0.3	17.1 ± 0.3	0.32 ± 0.06	0.231
15-5005	21.69 ± 0.05	4	0.17 ± 0.05	1.4 ± 0.4	19.8 ± 0.6	16.1 ± 0.6	0.74 ± 0.08	0.247
	21.73 ± 0.03	2.2 ± 0.6	0.21 ± 0.03	1.8 ± 0.2	20.4 ± 0.2	16.6 ± 0.2	0.86 ± 0.08	0.240
15-7543	20.86 ± 0.06	4	0.40 ± 0.06	3.0 ± 0.5	20.6 ± 0.4	17.0 ± 0.4	0.79 ± 0.04	0.275
	20.71 ± 0.08	5.0 ± 0.7	0.48 ± 0.08	4.0 ± 0.7	21.1 ± 0.4	17.4 ± 0.4	0.78 ± 0.04	0.267
22-0189	20.32 ± 0.06	4	0.42 ± 0.06	3.6 ± 0.5	20.4 ± 0.3	17.3 ± 0.3	0.49 ± 0.04	0.454
	20.40 ± 0.04	3.2 ± 0.7	0.37 ± 0.03	3.1 ± 0.3	20.2 ± 0.2	17.1 ± 0.2	0.50 ± 0.04	0.431
22-1983	21.33 ± 0.04	4	0.09 ± 0.04	0.7 ± 0.4	18 ± 1	15 ± 1	0.2 ± 0.2	0.259
	21.35 ± 0.02	2.9 ± 0.8	0.09 ± 0.04	0.7 ± 0.4	18 ± 1	15 ± 1	0.2 ± 0.2	0.242

Table 3.4. Morphological parameters of galaxies in the MUNICS sample

ID	F160W [mag]	n	r_e [arcsec]	R_e [kpc]	$\langle \mu \rangle_e^{160W}$ [mag/arcsec ²]	$\langle \mu \rangle_e^{corr}$ [mag/arcsec ²]	b/a	χ^2
S2F5_109 ^a	18.57 ± 0.03	4	0.66 ± 0.03	5.5 ± 0.2	19.65 ± 0.08	17.14 ± 0.08	0.48 ± 0.02	0.320
S2F5_109 ^b	18.64 ± 0.03	4	0.67 ± 0.01	5.57 ± 0.09	19.77 ± 0.04	17.25 ± 0.04 ^c	0.49 ± 0.01	0.532 ^d
S7F5_254 ^a	20.42 ± 0.02	4	0.36 ± 0.01	3.00 ± 0.08	20.20 ± 0.07	17.68 ± 0.07	0.90 ± 0.01	0.265
S7F5_254 ^b	20.56 ± 0.03	4	0.34 ± 0.01	2.80 ± 0.11	20.20 ± 0.09	18.86 ± 0.09 ^c	0.83 ± 0.02	0.402 ^d
S2F1_357 ^a	19.80 ± 0.03	4	0.41 ± 0.02	3.4 ± 0.1	19.9 ± 0.08	17.08 ± 0.08	0.67 ± 0.01	0.312
S2F1_357 ^b	19.89 ± 0.03	4	0.39 ± 0.01	3.28 ± 0.07	19.84 ± 0.06	17.07 ± 0.06 ^c	0.66 ± 0.01	0.440 ^d
S2F1_389 ^a	20.99 ± 0.05	4	0.23 ± 0.02	1.9 ± 0.2	19.8 ± 0.2	16.9 ± 0.2	0.93 ± 0.07	0.312
S2F1_389 ^b	21.21 ± 0.03	4	0.18 ± 0.02	1.54 ± 0.15	19.52 ± 0.24	16.58 ± 0.24 ^c	0.86 ± 0.03	0.340 ^d
S2F1_511 ^a	20.35 ± 0.05	4	0.22 ± 0.02	1.9 ± 0.2	19.1 ± 0.2	16.2 ± 0.2	0.59 ± 0.05	0.269
S2F1_511 ^b	20.43 ± 0.03	4	0.23 ± 0.01	1.91 ± 0.07	19.21 ± 0.09	16.33 ± 0.09 ^c	0.59 ± 0.01	0.343 ^d
S2F1_142 ^a	20.06 ± 0.03	4	0.62 ± 0.03	5.2 ± 0.2	21.02 ± 0.09	18.05 ± 0.09	0.79 ± 0.02	0.309
S2F1_142 ^b	19.95 ± 0.03	4	0.35 ± 0.01	2.95 ± 0.7	19.67 ± 0.06	16.70 ± 0.06 ^c	0.73 ± 0.01	0.915 ^d
S7F5_045 ^a	19.73 ± 0.02	4	1.00 ± 0.02	8.5 ± 0.2	21.73 ± 0.05	18.72 ± 0.05	0.70 ± 0.02	0.389
S7F5_045 ^b	19.61 ± 0.03	4	1.13 ± 0.04	9.53 ± 0.33	21.87 ± 0.09	18.10 ± 0.09 ^c	0.69 ± 0.01	0.394 ^d
S2F1_633 ^a	20.98 ± 0.03	4	0.31 ± 0.02	2.6 ± 0.1	20.4 ± 0.1	17.4 ± 0.1	0.56 ± 0.02	0.301
S2F1_633 ^b	20.36 ± 0.03	4	0.26 ± 0.01	2.23 ± 0.07	19.46 ± 0.08	16.42 ± 0.08 ^c	0.53 ± 0.01	1.258 ^d
S2F1_443 ^a	20.96 ± 0.08	4	0.81 ± 0.06	6.9 ± 0.5	22.5 ± 0.2	19.0 ± 0.2	0.81 ± 0.05	0.252
S2F1_443 ^b	20.30 ± 0.03	4	0.72 ± 0.03	6.13 ± 0.24	21.6 ± 0.1	18.1 ± 0.1 ^c	0.76 ± 0.02	0.676 ^d

^a our best fit parameters for MUNICS sample^b best-fit model from Longhetti et al. (2007)^c mean effective surface brightness correction includes K correction and $(1+z)^4$ dimming factor^d χ^2 of our fit with the parameters from Longhetti et al. (2007)

in this way went through the same fitting procedure as the real galaxy image from our sample. The standard deviations of resulting parameters are shown as the error estimates reported in Table 3.3. The reduced χ^2 values for the best fits to the MC simulations are of the order of unity and larger than reduced χ^2 of the best fits to the data, which makes our error estimates very conservative.

3.4.2 K-corrections and cosmological dimming

Our analysis requires comparison between the properties of our $1.2 < z < 2$ samples observed at $1.6 \mu\text{m}$ (H -band) to those of present-day galaxies observed at visible wavelengths. In order to make a proper comparison, we need to transform the various data sets to a common bandpass and apply a K-correction. We computed appropriate spectral energy distributions (SEDs) using PEGASE-HR spectral synthesis models (Le Borgne et al., 2004). The model that we used is based on the Baldry & Glazebrook (2003) initial mass function (IMF), solar metallicity, and an exponentially declining star formation rate with a time scale of $\tau = 0.1$ Gyr, very similar to a single burst. The typical ages of GDDS and MUNICS passive galaxies at $1.2 < z < 2$ are 3 – 4 Gyr (Paper IV, Longhetti et al., 2005) and we used a 4 Gyr model to approximate their SED. It is important to emphasize that the correction needed to reduce our H -band data to rest-frame SDSS- r is remarkably insensitive to SED shape since redshifted H -band closely matches rest-frame SDSS- r at $z \sim 1.5$. The photometry for the two samples is listed in Tables 3.3 and 3.4. Cosmological surface brightness dimming will reduce the observed surface brightness and these must be corrected by $(1+z)^4$ to transform them to the rest-frame.

3.5 Results

3.5.1 Morphologies of passive galaxies at $z > 1.3$

All of the objects in our NICMOS F160W sample (shown in Figures 3.1 and 3.2) have compact morphologies and none show obvious evidence of interactions, such as double nuclei or disturbed isophotes at bright levels. The star-forming massive galaxies drawn from the GDDS sample, by contrast, exhibit a wide range of disturbed morphologies as shown in Paper VIII. The intermediate age and composite population systems primarily

have disk morphologies, while the passive galaxies at $z < 1.3$ discussed in Paper VIII exhibit a preponderance for compact and regular morphologies. Six of the 10 GDDS galaxies in the present sample appear to be early types with $R^{1/n}$ profile index $n > 2.5$ (Table 3.3), while the four potential disk systems in our $z > 1.3$ passive sample appear to have prominent bulges. Thus 60% of our GDDS sample defined by spectral properties have pure early type morphologies, and this fraction rises to 90% when the prominent bulges with very weak disks are also taken into account as early type object. To a first approximation, our NICMOS Camera 3 images extend the correlation between spectra indicative of old stellar populations and compact early-type morphologies from $z \sim 1.3$ to $z \sim 2$. This is not surprising given previous indications in this direction from smaller samples (e.g., Cimatti et al., 2004).

The correlation between color and morphological type is not as strong for the red galaxies, as a number of studies have shown. At redshifts near unity, red $R - K$ or $I - K$ selected samples contain roughly as many disk as early-type galaxies (e.g., Moustakas et al., 2004; Yan & Thompson, 2003, etc.). At higher redshifts red selected samples also show a mix of morphologies, as shown for the $z \sim 1.5$ range in Paper VIII and at $z > 2$ by Labbé et al. (2005), Stockton et al. (2004), and others.

3.5.2 Surface brightness profiles & sizes

Azimuthally averaged surface brightness profiles presented in Figure 3.3 confirm that six of our 10 GDDS galaxies are well-fit by $R^{1/4}$ profiles. The effective radii for these six objects range from as small as $0''.05$ to as large as $0''.42$, or from 0.4 to 3.6 kpc. The median effective radius is $0''.26$ or 2.2 kpc. As Figure 3.1 shows, for the most part the 2-D models fit the data well and the residuals are not significantly greater than the sky noise. In 12-8895 and 12-5869 there appear to be some non-axisymmetric structures within the central one arcsecond, while in 12-6072 the model is too peaked. Four of our 10 GDDS galaxies are clearly better fit by $R^{1/n}$ profiles with indices near 2, rather than the $R^{1/4}$ law. These are: 12-6072, 12-8025, 15-4367 and 15-5005. As can be seen in Figure 3.3 the significance with which the $R^{1/4}$ law fit is rejected in these objects is low except in the case of 12-8025 where the outer isophotes depart strongly from the $R^{1/4}$ law profile.

The effective radii of the GDDS galaxies are smaller than those of present-day cluster

ellipticals and early-type field galaxies. The median effective radius for low redshift cluster ellipticals is ~ 4 kpc (Jørgensen et al., 1995; Schombert, 1986), and the field early type galaxies at $z \sim 0.5$ from the CFRS (Schade et al., 1999) have a fairly similar median size. The hosts of luminous radio galaxies at $z \sim 0.8 - 1$ studied by Zirm et al. (2007) probably represent the most massive end of the field & group early type populations at these redshifts. Their sizes are also similar to the lower redshift samples and larger than the GDDS elliptical galaxies that have median effective radius of 2.2 kpc. In contrast, the distant red galaxies (DRGs), defined by their $J - K$ colors, at $2 < z < 3$ have a median effective radius of 1.4 kpc (Toft et al., 2007), somewhat smaller than the passive GDDS galaxies in our sample at $z \sim 1.7$.

The sizes of the GDDS passive galaxies appear to support a fairly strong evolution in scale length among the early type galaxies in the $1 < z < 3$ interval. A mundane potential explanation for this result is that the under-sampling of the NIC3 PSF data has led to unreliable fits. We can rule out this hypothesis on the basis of three tests. Firstly, we have re-fitted the six galaxies with more finely sampled NIC2 data from the Longhetti et al. (2007) sample, and we recover very similar fits (see Table 3.4). These fits are shown in Figure 3.4 using dashed lines to join the values of points obtained by Longhetti et al. (2007) to those obtained by us. Secondly, we have undertaken detailed MC simulations (used to set our error bars in Figure 3.4) based on generating idealized over-sampled images which are randomly displaced by sub-pixel shifts before being binned to NIC3 resolution and re-fitted. Lastly, four of our objects - 12-5592, 12-5869, 15-7543, and 22-1983 - were observed in the F814W band with ACS on HST. The sizes that we measure for these galaxies, albeit at shorter rest-frame wavelengths, are in good agreement with the sizes derived from our NIC3 data. Thus we are confident that our size determinations are robust.

The strong correlation between mass and size, as measured by the effective radius, makes comparisons between the average or median properties of different samples imprecise measures of evolution. The lower redshift samples ($z < 1$ Jørgensen et al., 1995; Schombert, 1986; Schade et al., 1999) cover a broad range of the parent luminosity functions while the higher redshift objects ($1 < z < 3$), including the DRGs, the GDDS and MUNICS samples (Toft et al., 2007, Paper III, Longhetti et al., 2005), sample the high mass end of the galaxy population and thus are biased to large values in their median sizes. This further strengthens the conclusion that there is strong evolution in the

characteristic sizes of early type galaxies above $z \sim 1$. The evolution in galaxy sizes can be further quantified by examining the size-mass correlation and its evolution, as is discussed in section 3.5.4.

3.5.3 The Kormendy relation to $z = 2$

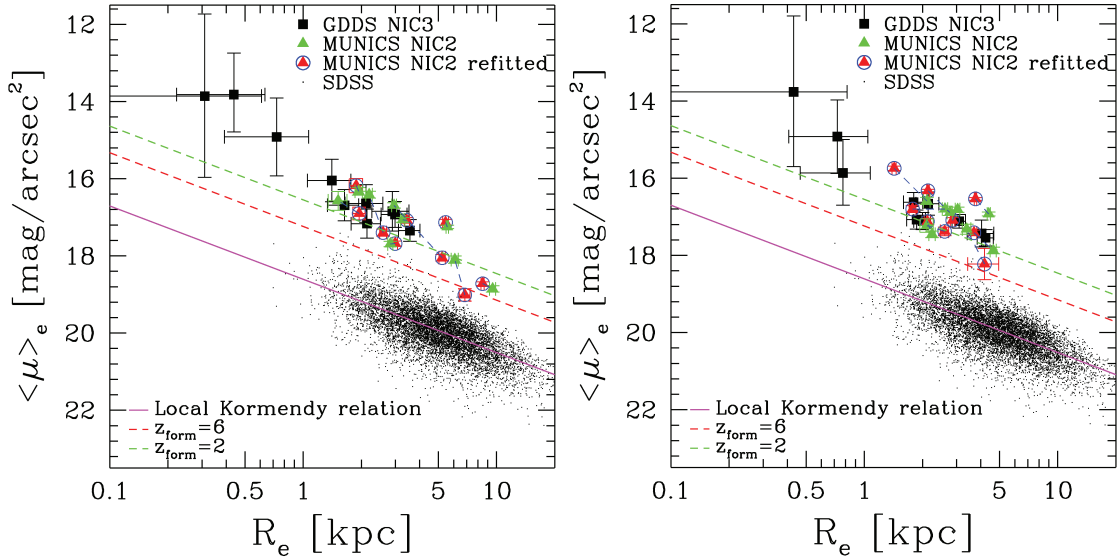


Figure 3.4 Mean rest frame Gunn- r surface brightness within effective radius R_e as a function of R_e (Kormendy relation) for objects at redshifts $1.2 < z < 1.9$ (GDDS and MUNICS samples) and for the sample of local galaxies (SDSS, Bernardi et al., 2003b). The solid line is the best-fit relation to the SDSS objects. The dashed lines represent the expected luminosity evolution of the local (SDSS, solid line) relation at $z = 1.5$ for galaxies formed at $z_{form} = 6, 2$ with exponentially declining SFR and e -folding time $\tau = 0.1$ Gyr. Different symbols correspond to different samples, and circled triangles denote re-fitted MUNICS sample. Left panel shows $R^{1/4}$ profile parameters for the galaxies from the GDDS and MUNICS samples, while the right one shows their best-fit $R^{1/n}$ profile parameters.

In Figure 3.4 we present the rest-frame r -band Kormendy relation, $\langle \mu \rangle_e$ vs. R_e , for the GDDS and MUNICS samples. As noted earlier, our construction of this diagram is particularly robust because our observed H -band observations match rest-frame r -band at $z = 1.5$ and hence there is negligible residual K-correction uncertainty. We have not

applied any evolutionary corrections to the observed surface brightness values. Figure 3.4 includes the corresponding distribution for present-day early-type galaxies from the SDSS (Bernardi et al., 2003b).

Figure 3.4 shows that the tightness and slope of the Kormendy relation in the GDDS + MUNICS sample is similar to that defined by the local relation. There is a hint that the high-redshift slope may be slightly steeper than the local value, but the difference is not significant. While the high-redshift ellipticals fall along a tight Kormendy relation, the relationship itself is offset to higher surface brightness from the low-redshift reference sample. The simplest explanation for this is that we are seeing galaxies nearer to their epoch of formation, when they are brighter, and thus the Kormendy relation is shifted upwards. This evolutionary effect cannot fully explain the evolution in the Kormendy relation. The offset in surface brightness compared to the $z \sim 0$ sample is too large (~ 2.5 mag) to be explained by pure luminosity evolution of stellar populations unless the redshift of formation is very recent ($z_{\text{form}} \lesssim 2$), which is inconsistent with both their colors and spectra (see Paper IV) which argue that these are old systems with $z_{\text{form}} \gtrsim 4$. In the latter case, the maximum dimming allowed is 1 to 1.5 mag, depending on the selected IMF and the star formation history. In addition, we also see from this figure that, in spite of their large masses, typical high- z ellipticals are substantially smaller than their local counterparts. In contrast to the median effective radius for the GDDS sample of 2.2 kpc, early-type galaxies in the SDSS sample presented in Fig. 3.4 span the range of effective radii with the median value of 4.9 kpc. Finally, we see that three out of ten galaxies in the GDDS sample are ‘ultra-compact’ ($R_e < 1$ kpc), and thus are of much higher stellar density. Cimatti et al. (2008) found a similar fraction from ACS imaging and estimate that the number density of comparably dense objects at $z = 0$ is up to 10^4 times lower than at $z = 1.5$. In contrast, in the MUNICS sample of elliptical galaxies ($1.2 < z < 1.7$) no ‘ultra-compact’ objects are found. As we will discuss in the following section, our findings lead us to also conclude that strong size evolution (a factor of 2 or more) is the additional ingredient needed to explain the shift in the Kormendy relation.

3.5.4 The mass-size relation and the stellar mass Kormendy relation

As the previous section illustrates, a proper comparison between galaxy samples at high and low redshifts nearly always entails corrections for luminosity evolution. We can, however, improve on the standard procedure of using simple models of luminosity evolution by using multi-color SED data to fit stellar population models and derive stellar masses for the galaxies in question (this was done and described in Paper III for the GDDS sample). We then recast the data into a new ‘stellar mass Kormendy relation’ which allows a more fundamental comparison. By doing this we are using the complete set of information (the colors) to measure and remove the luminosity evolution. A further advantage to the use of stellar mass is that it allows us to compare optical and near-IR samples and plot them on the same diagram. A possible disadvantage is that we rely heavily on the mapping from light to stellar mass given by our spectral synthesis modeling, which, in turn, depends on the correctness of our assumptions. So for example derived masses would be in error if the assumed IMF is evolving rather than static.

We consider two projections of the structural evolution that minimize the impact of luminosity and spectral evolution. The first is the size-mass relation, while the second is the relation between stellar mass density and size, which we will refer to as the stellar mass Kormendy relation. In deriving the stellar mass *density* we assume that the F160W light traces the stellar mass.

In Figure 3.5 we plot the size-mass relation for our sample. To enhance the usefulness of this figure, we augmented our GDDS and MUNICS data using published measurements obtained for passive galaxies in the redshift range $1.1 < z < 2.0$ taken from two surveys in the HUDF (Daddi et al., 2005b; Maraston et al., 2006), a survey of six galaxies with dominant old stellar population in the fields of radio-loud quasars (McGrath et al., 2007, 2008), and GMASS (Cimatti et al., 2008). While McGrath et al. (2007) use NIC3 F160W observations for their morphological analysis, GMASS (Cimatti et al., 2008) and HUDF (Daddi et al., 2005b) effective radii were measured by fitting ACS F850LP (z band) galaxy images. We corrected all of the stellar mass determinations to a common IMF, using Baldry & Glazebrook (2003) IMF, according to the relations given in Cimatti et al. (2008) and Paper III. Finally, to place our data in a broader context, Figure 3.5 also shows the size-mass relationship for local early-type galaxies in the SDSS (Bernardi

et al., 2003b). We recomputed the stellar masses for the Bernardi et al. (2003b) SDSS sample using the same prescription applied to the GDDS sample (Baldry et al., 2008; Paper III). The derived masses are in good agreement with those of Kauffmann et al. (2003). The size-mass relationship for early-type galaxies shown in Figure 3.5 shows a number of interesting features, the most striking of which is that the high-redshift and low-redshift populations show relatively little overlap. In fact, they seem to describe nearly independent loci in size-mass parameter space, with similar slopes, but with galaxies at $z = 1 - 2$ systematically smaller, at a fixed mass, than galaxies at $z = 0$. The error bars on individual data points are rather large, but taken as a whole, only $\sim 25\%$ of high redshift early-type galaxies lie in the region of size-mass space occupied by low-redshift systems.

The size-mass relationship of elliptical galaxies at $z \sim 0$ is well described by a power law with the same exponent (~ 0.5) as for the early-types at $z \sim 1.5$. Galaxies with stellar masses of $8 \times 10^{10} M_{\odot}$, comparable to M^* today, are approximately three times smaller at $z \sim 1.5$ than their apparent counterparts today. The number density of compact galaxies with $R_e < 1$ kpc (‘red nuggets’) in the redshift range $1.1 < z < 2$ is $2 \times 10^{-5} \text{ Mpc}^{-3}$. In contrast, number density of these objects in the SDSS sample (Bernardi et al., 2003b) is $3 \times 10^{-8} \text{ Mpc}^{-3}$, three orders of magnitude lower than that for the higher redshift objects. The ‘red nuggets’ in two samples are different with respect to mass, too - the median of GDDS compact galaxies mass is $10^{11} M_{\odot}$, while the objects of the same compactness in the local Universe have masses with ten times lower median (i.e., $10^{10} M_{\odot}$). The passive galaxy population at $1.1 < z < 2$ span a similar range in stellar mass as galaxies today ($2 \times 10^{10} - 6 \times 10^{11} M_{\odot}$) so, at least at the high mass end, the bulk of the evolution from $z \sim 2$ to $z \sim 0$ appears to be in size rather than mass.

In Figure 3.6 we plot the projected stellar mass density within a radius equal to R_e (i.e., $\rho_e = 3M_*(R < R_e)/(4\pi R_e^3)$) versus R_e - the stellar mass Kormendy relation. This projection shows the evolution in the structural properties of the passive early-type galaxies very clearly. The $z > 1.1$ galaxies are offset to smaller radii and dramatically higher projected surface mass densities compared to massive early-type galaxies today. Compact objects in the local SDSS sample appear less dense since they are less massive than high redshift objects with the same size. In the density space populated by red nuggets at higher redshifts ($\rho_e > 10^{10} M_{\odot} \text{ kpc}^{-3}$), there are no galaxies in the SDSS sample, implying that number density of these objects at $z = 0$ is $\lesssim 4 \times 10^{-9} \text{ Mpc}^{-3}$.

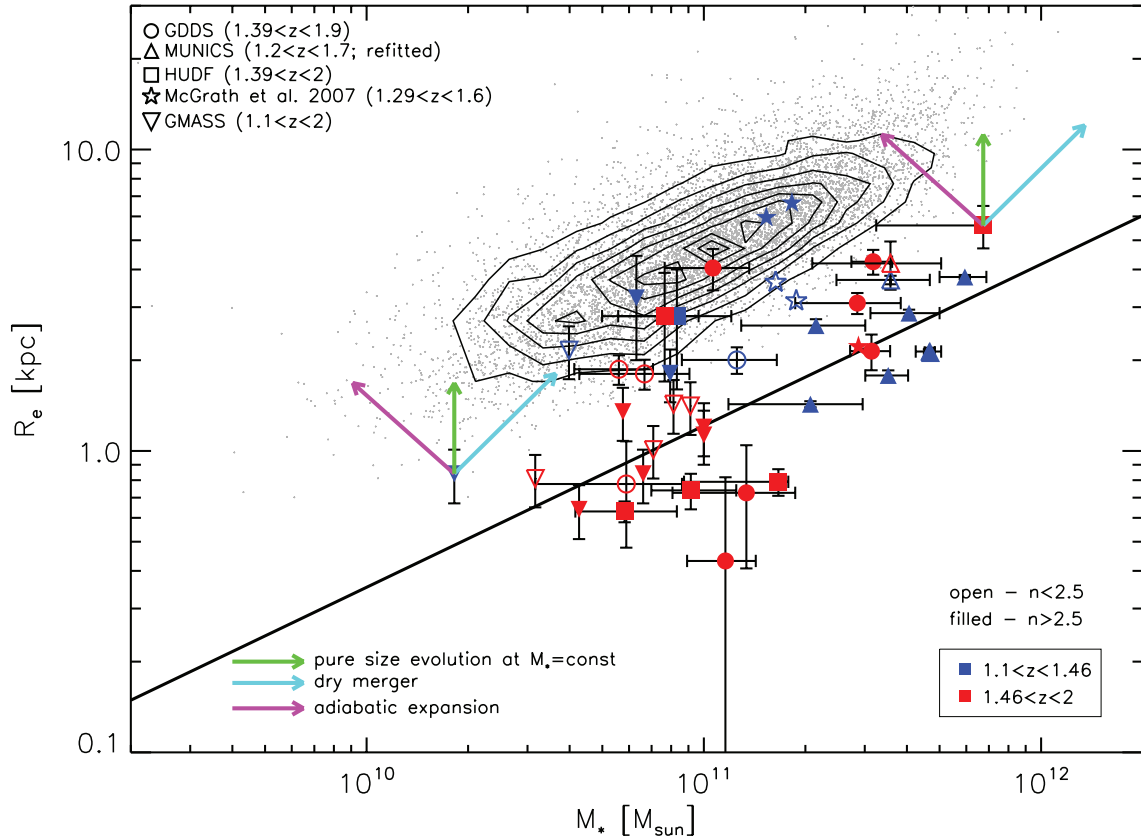


Figure 3.5 Effective radius R_e as a function of stellar mass for five samples of early-type galaxies in the redshift range $1.1 < z < 2$. Points are color-coded by two redshift ranges (red = $z > 1.46$, blue = $z < 1.46$). Different symbols correspond to different surveys, with triangles denoting re-fitted object from the MUNICS sample (as in Fig. 3.4). The size-mass relation for local early-type galaxies in the SDSS is presented with sizes taken from Bernardi et al. (2003b), and matched with masses calculated following Baldry et al. (2008) (black points). Contours represent linearly spaced regions of constant density of galaxies in size-mass parameter space. The solid line is the best-fit relation to the data points at redshifts $1.1 < z < 2$. Three arrows denote the effects that 1:1 dry merger (Boylan-Kolchin et al., 2006), adiabatic expansion with 50% mass loss, and pure size evolution at constant stellar mass would have on the positions of both the least and the most massive galaxy. See text for details.

In both figures 3.5 and 3.6 we have color coded the symbols according to redshift into two sub-samples: $1.1 < z < 1.46$ and $1.46 < z < 2$. This splits the sample into two equal time intervals of duration 1.1 Gyr and nearly equal sample sizes. There is a significant difference in the size distributions in the two sub-samples. In the lower redshift sub-sample 6/18 galaxies, or $\sim 33\%$ of the sample, fall within the range of the local sample, while in the high redshift sample, only 4/25, or $\sim 17\%$ of the galaxies fall within the locus of the local systems. Thus it appears that the strongest evolution in size is occurring in the $1 < z < 1.5$ interval, although as we will describe in the next section, the heterogeneous nature of the data does not allow us to conclude this with much confidence. A number of other studies (e.g., Treu et al., 2005b) show that $z \sim 1$ early type galaxies have normal sizes and mass densities.

3.6 Discussion

The key result of this paper are that the sizes and projected mass densities of early-type passively evolving galaxies have changed very significantly since $z \sim 2$. A number of other studies, noted above, have reached similar conclusions in samples with higher and overlapping redshift intervals. Our analysis has removed much of the uncertainty associated with evolutionary corrections in luminosity and spectral shape by dealing with the mass density rather than surface brightness.

There are a number of potential explanations for the dramatic evolution in the sizes and densities of the passive galaxies. If the compact massive galaxies at $z \sim 2$ are to evolve into massive elliptical galaxies at $z \sim 0$ they must grow by a factor of 2 – 3 in size. The two most plausible paths to this evolution are injection of energy into, or the loss of mass from, the central regions. One possibility is that mergers input energy into the stellar systems and increase their equilibrium sizes. The quiescent spectra of galaxies in the same stellar mass range at $1 < z < 1.5$ suggest that any such merger be “dry” and produce little star formation and related activity. Dry mergers have been identified as a likely evolutionary path for the compact massive galaxies at $z > 2$ discussed recently by van Dokkum et al. (2008). The large stellar masses of the compact passive galaxies at $z < 2$ suggest that equal mass mergers cannot be ubiquitous at later epochs. In Figures 3.5 and 3.6 we show vectors that approximate the impact of an equal mass merger, based on the simulations performed by Boylan-Kolchin et al. (2006). Galaxies become both larger and

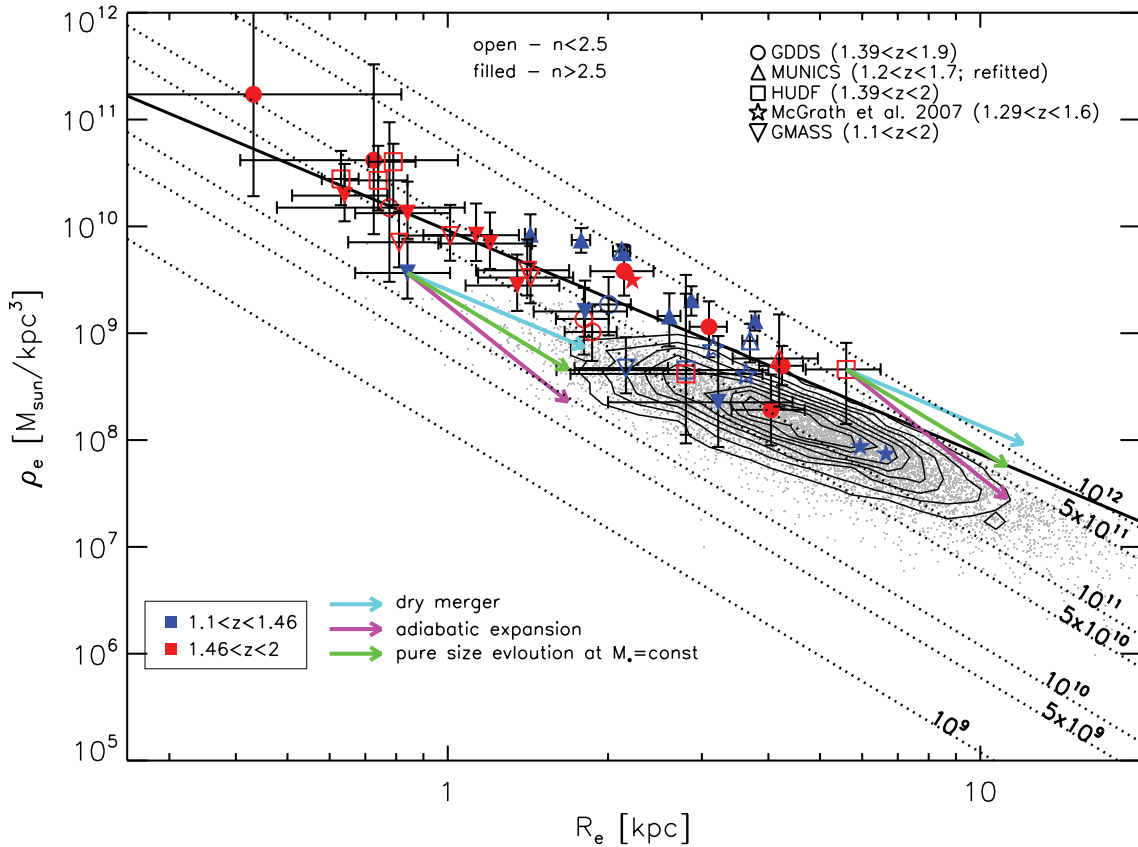


Figure 3.6 Stellar mass density within the effective radius R_e as a function of R_e (the "stellar mass Kormendy relation") for five samples of early-type galaxies in the redshift range $1.1 < z < 2$. Symbols are as in Fig. 3.5. The local sample of SDSS galaxies is presented with both points and overlaid contours that denote linearly spaced regions of constant density of galaxies in this parameter space. Dotted lines present the loci of constant total stellar mass, noted on each line in units of M_\odot . The solid line is the best-fit relation to the data points at redshifts $1.1 < z < 2$. Three arrows denote the effects that 1:1 dry merger (Boylan-Kolchin et al., 2006), adiabatic expansion with 50% mass loss, and pure size evolution at constant stellar mass. See text for details.

more massive and move primarily along the mass-radius and mass-Kormendy relations rather than normal to them. This problem makes this explanation for size evolution unsatisfactory. While there is good evidence for an increase of roughly a factor of two in the total stellar mass density in red sequence galaxies since $z \sim 1.3$, this appears to be in the form of new galaxies appearing on the red sequence rather than mass growth in previously passive systems (e.g., Faber et al., 2007; Bell et al., 2004b). One could perhaps appeal to many minor mergers to puff up a galaxy’s size, but they would have to all be dry to keep a galaxy on the red sequence and numerous enough to have a significant effect, which seems somewhat contrived.

It has been pointed out to us (N. Murray, private communication) that adiabatic expansion is an interesting alternative to dry merging for increasing the size of galaxies. This process has long been familiar to stellar dynamicists (Hills, 1980) and been verified by numerical simulation (e.g., Baumgardt & Kroupa, 2007). The process has also been used to model the influence of strong stellar winds in conditioning the Galactic globular cluster distribution (Zhao, 2002). In the present context, the potential for adiabatic expansion to explain the existence of massive small ellipticals at high redshift is developed in a paper by Murray et al. (2010, hereafter MQT). To motivate the present discussion, a basic version of the some of the key theoretical ideas in the latter paper, kindly communicated to us in advance of publication by the authors, will be applied to the GDDS sample here.

Adiabatic expansion will occur in any relaxed system that is losing mass. As mass is lost the potential becomes shallower, so the system expands in order to relax into a new stable equilibrium. The amount that a system expands depends on both the extent and speed of the mass loss (see Zhao, 2002, for details). In general, if a fraction $\frac{\Delta m}{m} = (m_{\text{initial}} - m_{\text{final}})/m_{\text{initial}}$ of the total mass is lost on a dynamical timescale (or longer), the size of the system increases by a factor of approximately $\frac{1}{1 - \frac{\Delta m}{m}}$. If the mass is lost more quickly than the dynamical timescale, then the expansion of the system will be larger than this estimate. It is trivial to show that as the system loses mass the dynamical timescale increases in proportion to $\frac{1}{(1 - \frac{\Delta m}{m})^2}$ while the escape velocity decreases as $1 - \frac{\Delta m}{m}$, so there are at least two sources of positive feedback leading to further increase the size as the system evolves. Of course, in the extreme case where a significant fraction of the total mass is lost on a short timescale, the system may become unbound.

What processes might lead to mass loss in elliptical galaxies? The obvious candidate is stellar winds from sites of active star formation. However, the early-type galaxies being studied here are relatively red and spectroscopically passive, so winds from young stellar populations are unlikely candidates for mass loss. An interesting alternative is mass loss from evolved A and F-type stars, and we have explored this idea using the following toy model. We model a galaxy as an instantaneous burst with a solar-metallicity stellar population whose main sequence lifetime (as a function of mass) is that given in Table 5.2 of Binney & Merrifield (1998). We assume that after leaving the main sequence all stars more massive than 8 solar masses wind up as stellar remnants of 1.5 solar mass, and that all stars less than 8 solar masses wind up as remnants with 0.6 solar mass. We also assume that mass loss from stars is never recycled into future star formation and it outflows far out into the galaxy's potential well, or is lost completely.

In this case, $\frac{\Delta m}{m}$ as a function of time takes on the form shown in Figure 3.7 for three initial mass functions (Salpeter IMF, Scalo IMF, and the Baldry & Glazebrook (2003) IMF). Our toy model suggests that $\frac{\Delta m}{m}$ rises sharply with time until ages of around 2 Gyr, at which point $\frac{\Delta m(t)}{m(t)}$ flattens out, peaking at around 30% for the Salpeter IMF, and at 50% for the top-heavy Baldry & Glazebrook (2003) IMF. Thus the degree of mass loss from a very top-heavy IMF could explain the size growth. This is shown by the arrows in Figures 3.5 and 3.6, which show the effects that 1:1 dry merger (Boylan-Kolchin et al., 2006, cyan arrow), adiabatic expansion with 50% mass loss (magenta arrow), and pure size evolution at constant stellar mass (green arrow) have on the positions of both the least and the most massive galaxies in our sample. However, the timescale over which this occurs poses a huge challenge for explaining the size growth entirely by adiabatic expansion. In this paper we study the size distribution of the population at a time when their stellar populations are already rather old (see Tables 3.1 and 3.2 and discussion in Paper IV) so over the redshift range being probed the galaxies are old enough that the mass loss curves in Figure 3.7 are already nearly flat. Another constraint on the importance of adiabatic expansion is that it does not explain the steady factor of (at least) three growth in the stellar mass density locked up in massive galaxies over the redshift range $1 < z < 2$ reported in Paper IV and in other surveys, (e.g., Dickinson et al., 2003b; Rudnick et al., 2006), especially on the red sequence (Paper VIII). As the typical mass does not appear to evolve (Fig. 3.5) this primarily seems to be an evolution in number.

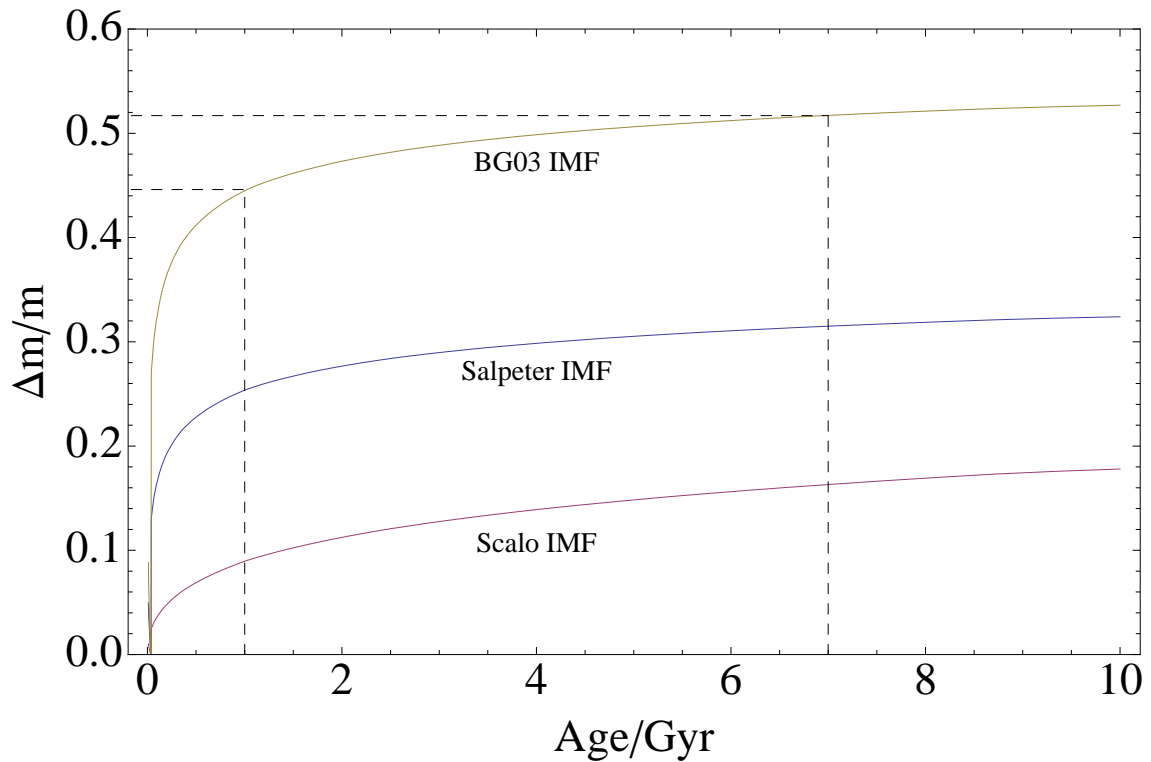


Figure 3.7 The mass loss fraction $\frac{\Delta m}{m}$ as a function of population age in Gyr, for the simple model described in the text. We assume an instantaneous burst of star formation and show $\frac{\Delta m}{m}$ as a function of time with three initial mass functions. As expected, the total mass loss is a strong function of the fraction of stars at the high mass end of the IMF. The relative mass loss is small in the age range 1 – 7 Gyr (dashed lines). See text for details.

In spite of the problems noted above, adiabatic expansion does appear attractive because it moves the high-redshift distribution shown in Figure 3.5 in the right direction to match the low-redshift distribution shown in the figure. This is not the case with equal-mass dry mergers, which, as shown by the cyan arrows in the figure, and as noted by previous authors (Boylan-Kolchin et al., 2006), drive evolution along the Kormendy relation rather than displacing the relation itself. While a top-heavy IMF loses enough mass to grow the galaxies by the required factor of two over their complete lifetime, the main problem with the adiabatic expansion model is that to explain our observations that mass loss would have to occur over the age range of 1 – 7 Gyr, over which Fig. 3.7 shows only a 5 – 10 % effect. Ages of the GDDS galaxies are taken from Paper IV, and it is worthwhile to consider whether we might have significantly over-estimated the ages of the galaxies in that paper. We think this unlikely for two reasons. Firstly, because broadband color-based ages for these galaxies seem consistent with ages inferred from spectra of these systems, which often exhibit photospheric features from old stars. Secondly, because changing to a more top-heavy IMF than the Salpeter IMF used in Paper IV would not result in systematically younger ages. In fact the reverse is true, since a more top-heavy IMF would tend to produce synthetic spectra which are bluer for a given star formation history at a given age. So to match the observed colors, any fitting routine would compensate by deriving *older* ages for the best fit. Quantitatively, we checked the size of this effect by generating models with an exponentially declining star-formation history (e-folding timescale $\tau = 1$ Gyr) with various stellar metallicities, using both Salpeter and BG03 IMFs (without extinction). We determined that ages using the (top-heavy) BG03 IMF are $\sim 40 - 50\%$ larger for galaxies which are found to be ~ 1 Gyr old using a Salpeter IMF. (Note that derived metallicities using the BG03 IMF are larger too).

Some constraints on the duty cycle for the size change can be inferred from our observations, by noting that the redshift range spanned by our sample is $1.1 < z < 2.0$, corresponding to a spread in time of ~ 2.2 Gyr. The division of the sample in half at $z = 1.46$ using different symbols in Figures 3.5 and 3.6 subdivides this redshift interval into two equal time bins, each of which is ~ 1.1 Gyr wide. The sample shown in Figures 3.5 and 3.6 contains data from a number of different surveys, and it is certainly unwise to attempt to compare the high-redshift and low-redshift subsets at a detailed level. But it is perhaps worth noting the following very general qualitative trends. Figure 3.5

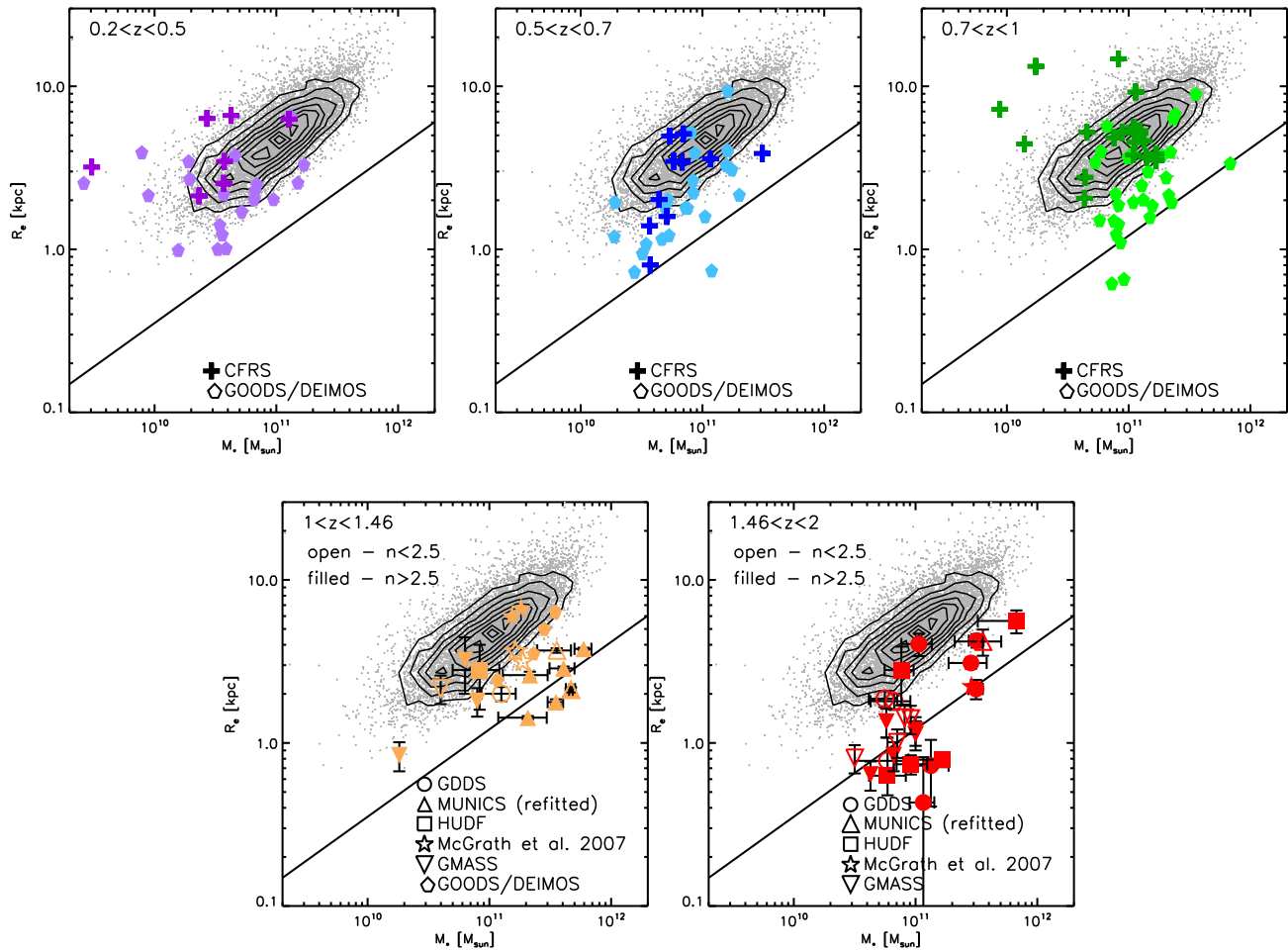


Figure 3.8 As in Figure 3.5, with data from the GOODS/DEIMOS and CFRS redshift surveys included. Points corresponding to different redshift bins are presented in separate panels. The solid line is the best-fit relation from Figure 3.5.

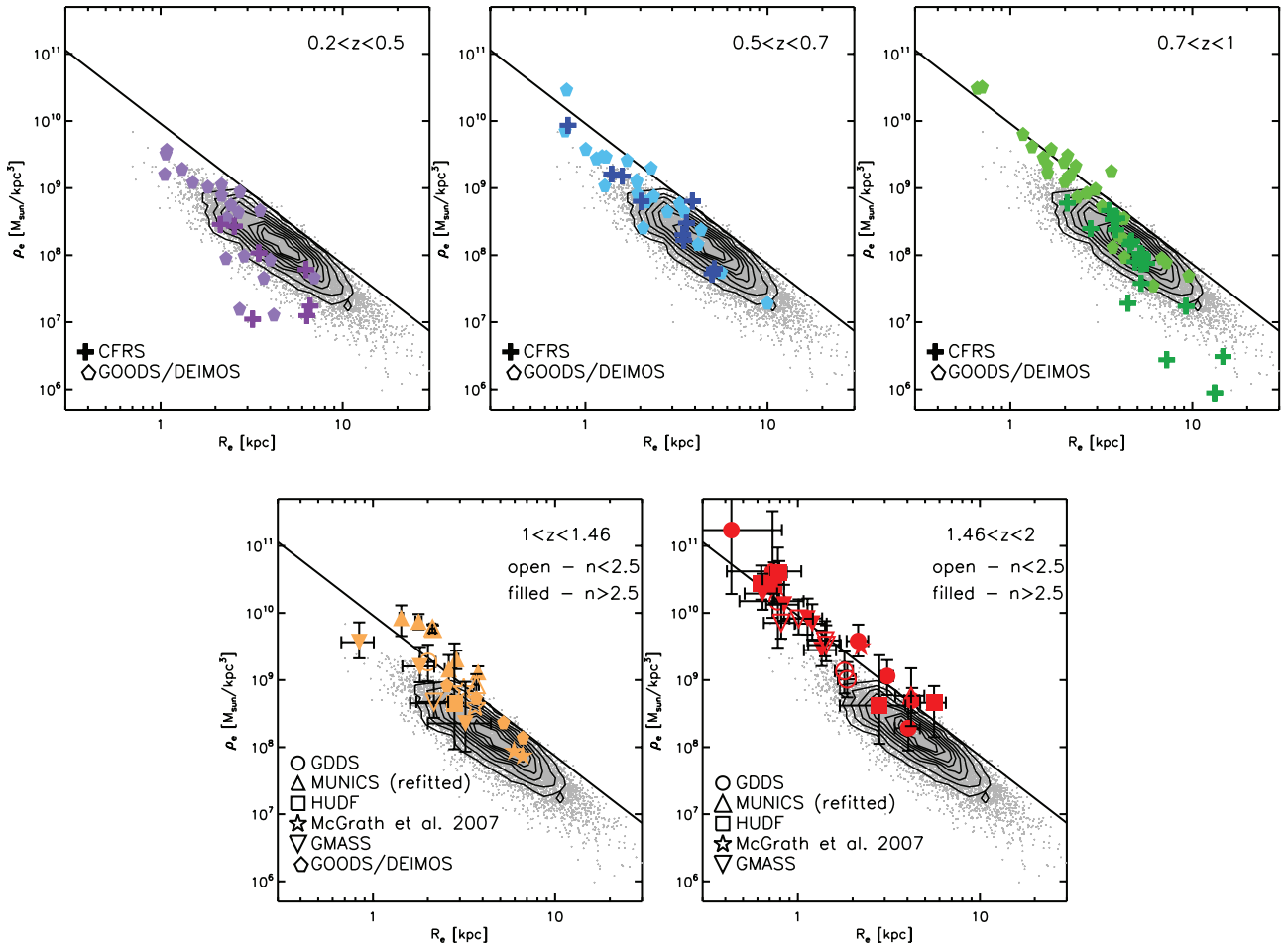


Figure 3.9 As in Figure 3.6, with data from the GOODS/DEIMOS and CFRS redshift surveys included. Points corresponding to different redshift bins are presented in separate panels. The solid line is the best-fit relation from Figure 3.6.

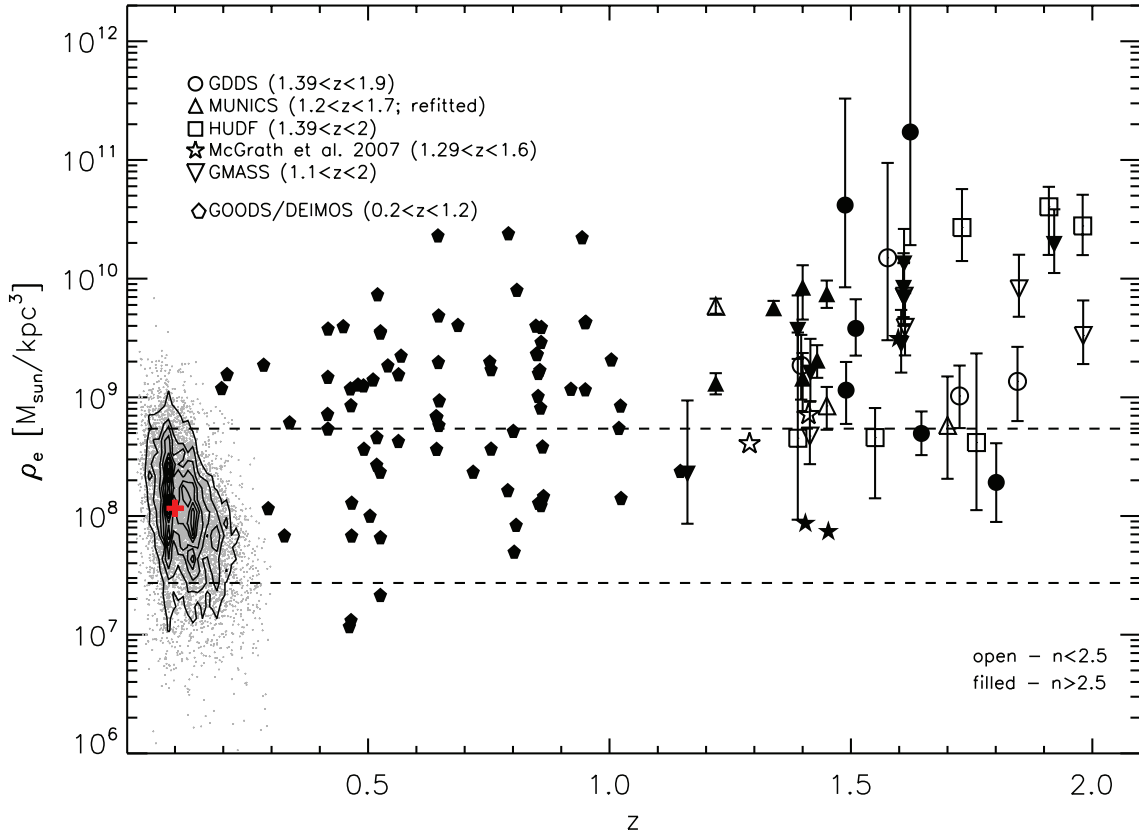


Figure 3.10 Redshift dependence of the stellar mass density within the effective radius R_e . Symbols are as in Figures 3.8 and 3.9. The local sample of SDSS galaxies is presented with both points and overlaid contours that denote linearly spaced regions of constant density of galaxies in this parameter space. Red cross represents the median stellar mass density and the median redshift of the local sample. Limiting stellar mass densities for the 90th percentiles for the SDSS objects with stellar mass densities above and below the median value are given with upper and lower dashed lines, respectively. Following the discussion on the quality of CFRS imaging in Section 3.6 corresponding points are excluded from this figure.

appears to show that the character of the size-mass distribution is rather different in the $1.1 < z < 1.46$ and $1.46 < z < 2.0$ intervals, with neither distribution resembling the local data distribution closely. This suggests some degree of evolution between the bins, but with the caveat that these two redshift bins primarily consist of data from different surveys so the strength of the evolution cannot be confidently inferred. On a more speculative note, it can be argued that nothing in Figure 3.5 rules out the possibility that the high-redshift distribution is evolving into the low-redshift distribution differentially, with different physics operating at the low mass and high mass ends. In fact, some evidence for this is also hinted at in the figure, which appears to show that the smallest and least massive galaxies lie at $z > 1.5$. It is possible that dry mergers may well be growing the smallest and least massive galaxies along the fundamental plane early in a galaxy's life cycle, before some other process takes over and grows them further in some other way.

It is interesting to contrast the data presented in Figures 3.5 and 3.6 with data which spans the redshift range in between the SDSS data and our high-redshift observations. Figures 3.8 and 3.9 augment the data in Figures 3.5 and 3.6 with intermediate-redshift data taken from the CFRS (Schade et al., 1999; Lilly et al., 1995) and GOODS/DEIMOS (Bundy et al., 2007; Treu et al., 2005b) surveys. Effective radii for the CFRS objects are obtained from the WFPC2 814W images. Estimates based on the images in three ACS filters (606W, 814W, and 850W) are available for the GOODS/DEIMOS sample. All objects shown in the upper three panels of figures 3.8 and 3.9 have sizes based on the WFPC2 or ACS 814W imaging that translates approximately into the rest-frame V -band for the median redshifts in the $0.2 < z < 0.5$ and $0.5 < z < 0.7$ panels, and into the rest-frame B -band for the median redshift in the $0.7 < z < 1$. panel. GOODS/DEIMOS objects in the $1 < z < 1.46$ panel are presented with the effective radii in ACS 850W filter (approximately B -band rest frame). The CFRS masses are obtained following Baldry et al. (2008) and using imaging data of relatively low quality. We note that the difference in the rest-frame wavelengths that are probed at different redshifts makes it impossible to draw any quantitative conclusions about galaxy size evolution. However, figures 3.8 and 3.9 show qualitative trends consistent with smooth evolution over the $0.2 < z < 2$ range. The dispersion on the size-mass plot in the $0.2 < z < 1$ regime is large (upper panels in Figures 3.8 and 3.9), but there seems to be some evidence for a systematic offset relative to the local trends with the increasing redshift. The GOODS/DEIMOS

data in Figures 3.8 and 3.9 spans *both* the low-redshift and high-redshift loci identified in each panel of Figures 3.8 and 3.9 by contours and the line of the best fit, respectively. However, the majority of the low-redshift ($0.2 < z < 0.5$) GOODS/DEIMOS data lie closer to the local relation, in contrast to the $0.7 < z < 1$ panel where the most of the GOODS/DEIMOS points are close to the $z \sim 1.5$ objects locus. The CFRS data in the $0.7 < z < 1$ panel of Figure 3.8 does not seem to follow this trend, and we suggest that it may be due to the shallow imaging of these objects (Lilly et al., 1995). In the lower redshift panels of Figure 3.8 ($z < 0.7$) the positions of the CFRS objects are consistent with the GOODS/DEIMOS dataset. In order to compare the number of high mass objects at different redshifts, we use a subsample of 68 GOODS/DEIMOS objects with masses above the GDDS detection limit (see section 3.3.1). It is interesting to note that relatively few (14/68, $\sim 21\%$) points from the GOODS/DEIMOS subsample have masses greater than $1.5 \times 10^{11} M_{\odot}$ (M^* at $1 < z < 2$, Fontana et al., 2006). In contrast, the high-redshift data set presented in Figures 3.5 and 3.6 includes large fraction of objects with $M_{\star} > M^* - 18/43$ ($\sim 42\%$). While this could perhaps be consistent with adiabatic mass loss, the arguments presented in our discussion of Figure 3.7 are compounded by the data presented in Figures 3.8 and 3.9 which indicates that size growth is still occurring in galaxies even older than those in our GDDS sample. We think it is likely that the absence of very high mass objects in the GOODS/DEIMOS data is simply due subtle differences in various groups' methodologies for computing stellar masses from photometric data. To further address the question of structural evolution of galaxies presented in Figures 3.8 and 3.9 we plot the redshift dependence of the projected stellar mass density (defined in section 3.5.4) in Figure 3.10. Dashed lines encompass the range of mass density which contains 90% of the local (SDSS) data points. The median stellar mass density of the SDSS galaxies is $\rho_e = 1.1 \times 10^8 M_{\odot} \text{ kpc}^{-3}$ and this value is denoted by a red cross plotted at $z = 0.1$ in Figure 3.10. Large fraction (88%) of the GOODS/DEIMOS objects have mass densities above the local median value, and 65% of these galaxies have mass densities above the upper dashed line in the figure. For the $1.1 < z < 2$ sample the corresponding numbers are 90% and 77%, respectively. On this basis we can conclude that the stellar mass density increases over an extended redshift range, though the dispersion of the plot is large, and more points in both intermediate and high redshift regime are needed to properly constrain this redshift dependence. We intend to revisit the topic in a future paper.

On balance, we conclude that at present neither adiabatic expansion nor equal-mass dry mergers seem able to explain the size growth in early-type galaxies. A successful model will have to simultaneously explain the size change in the galaxies, the duty cycle for this size change, and the epoch in a galaxy's life history at which the change occurs. And, as noted above, mass density growth over the redshift interval being probed suggests that the size growth being witnessed is operating within a broader context for galaxy formation. Over the redshift interval where early-type galaxies are growing in size, the volume-averaged stellar mass density in massive galaxies is increasing, and the morphological mix is changing.

3.7 Conclusions

The size-mass relationship for early-type galaxies evolves significantly from $z = 2$ to $z = 1$. Over the whole of this redshift range early type galaxies tend to be a factor of 2 – 3 smaller than local counterparts of similar mass. Similarly compact galaxies are seen at $z > 2$ (van Dokkum et al., 2008), and we speculate that the very compact galaxies studied in the present paper are simply the evolved counterparts of these higher-redshift objects, caught at a time before subsequent size growth. By comparing the size distribution of our sample with that of lower redshift surveys, we conclude that significant size growth is probably occurring over the redshift range explored in the present paper. The physics of this growth remains mysterious. By comparing the size-mass relation at $z \sim 1.5$ with its local counterpart we conclude that equal mass dry mergers play only a limited role in growing early-type galaxies, at least once they are older than a few Gyr. Other processes may be as important as dry merging in growing early-type galaxies. Adiabatic expansion is one such process that we have examined, and while it may be important in growing young early-type galaxies, it is hard to see how this mechanism can be invoked to obtain a factor of two growth in the sizes of galaxies as old as those in the present survey.

Acknowledgements

Acknowledgments

We thank Norm Murray for generously sharing his ideas and papers in advance of publication. We also thank Kevin Bundy for useful discussions.

This paper is based on observations obtained at the Gemini Observatory, which is operated by the Association of Universities for Research in Astronomy, Inc., under a cooperative agreement with the NSF on behalf of the Gemini partnership: the National Science Foundation (United States), the Particle Physics and Astronomy Research Council (United Kingdom), the National Research Council (Canada), CONICYT (Chile), the Australian Research Council (Australia), CNPq (Brazil) and CONICET (Argentina).

Based on observations made with the NASA/ESA Hubble Space Telescope, obtained at the Space Telescope Science Institute, which is operated by the Association of Universities for Research in Astronomy, Inc., under NASA contract NAS 5-26555. These observations are associated with program #9760. Support for program #9760 was provided by NASA through a grant from the Space Telescope Science Institute, which is operated by the Association of Universities for Research in Astronomy, Inc., under NASA contract NAS 5-26555.

RGA thanks NSERC, the Government of Ontario, and the Canada Foundation for Innovation for funding provided by an E. W. R. Steacie Memorial Fellowship.

Chapter 4

Red Nuggets at High Redshift: Structural Evolution of Quiescent Galaxies Over 10 Gyr of Cosmic History

This chapter contains the article that has been accepted for publication in The Astrophysical Journal Letters in July 2011, and is authored by:

Ivana Damjanov, Roberto G. Abraham, Karl Glazebrook, Patrick J. McCarthy, Evelyn Caris, Raymond G. Carlberg, Hsiao-Wen Chen, David Crampton, Andrew W. Green, Inger Jørgensen, Stéphanie Juneau, Damien Le Borgne, Ronald O. Marzke, Erin Mentuch, Richard Murowinski, Kathy Roth, Sandra Savaglio, Haojing Yan

The results presented in the accepted article are here augmented by analyses (described in Sections 4.5.3 and 4.6) that had to be omitted from the article due to the space constraints.

Reproduced by permission of the American Astronomical Society.

4.1 Abstract

We present an analysis of the size growth seen in early-type galaxies over 10 Gyr of cosmic time. Our analysis is based on a homogeneous synthesis of published data from

16 spectroscopic surveys observed at similar spatial resolution, augmented by new measurements for galaxies in the Gemini Deep Deep Survey. In total, our sample contains structural data for 465 galaxies (mainly early-type) in the redshift range $0.2 < z < 2.7$. The size evolution of passively-evolving galaxies over this redshift range is gradual and continuous, with no evidence for an end or change to the process around $z \sim 1$, as has been hinted at by some surveys which analyze subsets of the data in isolation. The size growth appears to be independent of stellar mass, with the mass-normalized half-light radius scaling with redshift as $R_e \propto (1+z)^{-1.62 \pm 0.34}$. Surprisingly, this power law seems to be in good agreement with the recently reported continuous size evolution of UV-bright galaxies in the redshift range $z \sim 0.5 - 3.5$. It is also in accordance with the predictions from recent theoretical models which suggest minor mergers as dominant channel for the size growth of massive early type galaxies. However, we also find smooth and substantial evolution of central density within the central kpc – by a factor of 3 over our redshift range – suggesting that size growth is not just driven by accretion onto the outskirts of galaxies.

4.2 Introduction

The discovery of a puzzling new population of compact ($R_e \lesssim 1$ kpc) massive elliptical galaxies existing at epoch when the Universe was not more than one-third of its current age has posed profound challenges for both monolithic and hierarchical model of galaxy formation and evolution. A handful of these objects were first reported by Cimatti et al. (2004), and later work by several groups has grown the number of similar galaxies at redshifts $z \gtrsim 1.5$ by more than a factor of 30 (e.g, Daddi et al., 2005b; Trujillo et al., 2006, 2007; Longhetti et al., 2007; Toft et al., 2007; Zirm et al., 2007; Buitrago et al., 2008; Cimatti et al., 2008; van Dokkum et al., 2008; Damjanov et al., 2009; Cassata et al., 2010; Newman et al., 2010; Ryan et al., 2011; Saracco et al., 2011). Although some concerns have been noted regarding the uncertainties in size measurements based on the *Hubble Space Telescope* (*HST*) imaging (Mancini et al., 2010), recent results based on the ultra-deep *HST* WFC3 data (Cassata et al., 2010; Ryan et al., 2011; Szomoru et al., 2010) have confirmed that the typical sizes of quiescent galaxies at high redshifts are several times smaller than the sizes of their local massive counterparts. Furthermore, visible and near-infrared (*NIR*) spectroscopy of individual high- z ‘red and dead’ galaxies

have revealed high velocity dispersions and central stellar densities (van der Wel et al., 2008; van Dokkum et al., 2009a; Newman et al., 2010; van de Sande et al., 2011) which are consistent with those expected from compact galaxies.

In the present Letter we synthesize the results from these published surveys, which together span a redshift range from the nearby universe ($z \sim 0.2$) all the way out to redshifts $z \sim 2.7$. This redshift range spans ~ 10 Gyr of cosmic time. By combining published data with new measurements for galaxies in the Gemini Deep Deep Survey (GDDS), we are able to compile a sample of 465 galaxies with spectroscopic redshifts over the full redshift range. Our main aim is to use these galaxies to determine whether galactic size growth is a continuous process that occurs over this full redshift range, or a process that is mainly associated with a particular epoch. Our result will place additional constraints on two mechanisms that have been proposed to explain the observed size growth: (1) minor dry mergers or late accretion (e.g., Oser et al., 2011) and (2) adiabatic expansion due to extreme mass loss (caused by stellar winds or quasar activity, Damjanov et al., 2009; Fan et al., 2010).

4.3 Sample and data reduction

Table 4.1 presents a summary of the structural parameters based on high resolution *HST* and adaptive optics ground-based imaging for 434 galaxies obtained from the literature for 16 spectroscopic surveys, augmented with additional analysis of imaging data for 31 objects from our own survey (GDDS; Abraham et al., 2004). The available data include redshifts, stellar masses, and the Sérsic surface brightness profile parameters - circularized half-light radii R_e and Sérsic profile indices n - in the rest frame. All data were harmonized to a common cosmology ($H_0 = 70 \text{ km s}^{-1} \text{ Mpc}^{-1}$, $\Omega_m = 0.3$, and $\Omega_\Lambda = 0.7$). Likewise, stellar masses were harmonized to a common initial mass function (IMF, Baldry & Glazebrook, 2003). In six surveys indices n were not available for individual objects : EDisCS, CFRS, GN/DEIMOS, MS1054/CDFS, CL1252/CDFS, and EGS/SSA22/GN. Four of these surveys reported R_e corresponding to the best fitting de Vaucoulers ($R^{1/4}$) profile for all objects. The median Sérsic index of the EDisCS sample is $\langle n \rangle = 3.7$, and 19 objects in Figure 4 of Saglia et al. (2010) are best described with $n \lesssim 2.5$ profiles. The CL1252/CDFS survey presented in Rettura et al. (2010) provided Sérsic profiles of quiescent galaxies along with their half-light radii, but

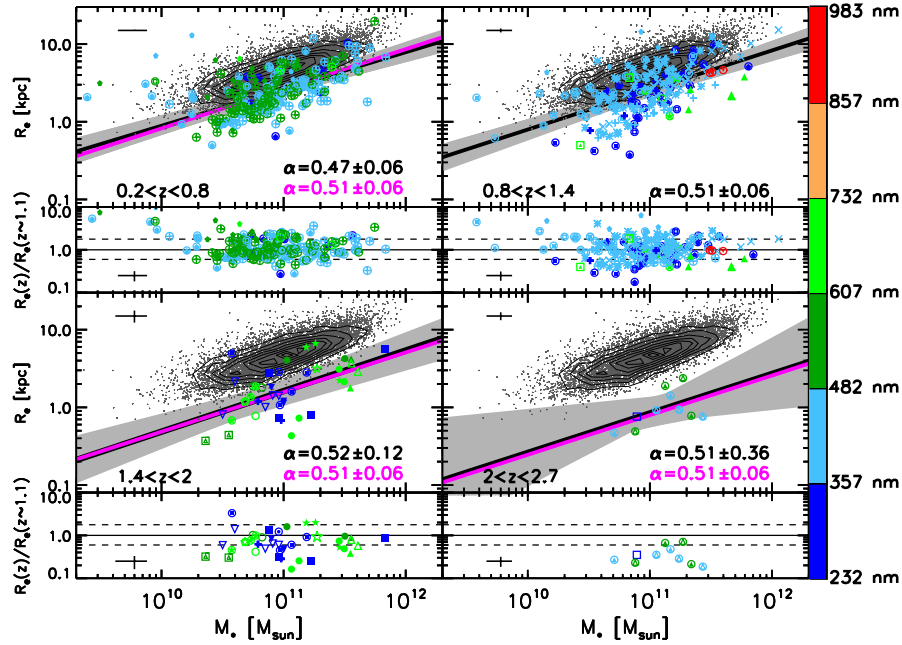


Figure 4.1 Effective radius R_e as a function of stellar mass for a sample of 465 passively evolving galaxies in the redshift range $0.2 < z < 2.7$. Different symbols correspond to different surveys (listed in the legend of Figure 4.3) and are color coded based on the *rest-frame* central wavelength of the size measurements with the key shown as a color bar at right. Data points are compared to the local sample drawn from the SDSS (gray points) in separate redshift panels. Contours represent linearly spaced regions of constant density of local SDSS galaxies in size-mass parameter space. The solid black line and gray area represent the best-fit relation to the data points in each redshift bin and its $\pm 1\sigma$ errors, respectively. In each upper sub-panel the slope α of the magenta line is the best fit to the data in a given redshift range with the slope fixed to the slope of the $0.8 < z < 1.4$ relation. (Note that the linear fits exclude objects with masses $< 10^{10} M_\odot$ to avoid being skewed by very low-mass outliers.). Average error bars for objects in different redshift bins are given in the left top corner of each panel. Note that we do not have information on the size measurement errors for $> 95\%$ of objects at $z < 1$ (Table 4.2). Lower sub-panels show the ratio between the measured size and the size at $0.8 < z < 1.4$ based on the size-mass relation plotted in the upper panels, as a function of mass. The solid line corresponds to the same sizes in a given redshift bin and at $0.8 < z < 1.4$ ($R_e(z)/R_e(z \sim 1.1) = 1$), and the dotted lines encompass the $\pm 1\sigma$ spread of the $z \sim 1.1$ data.

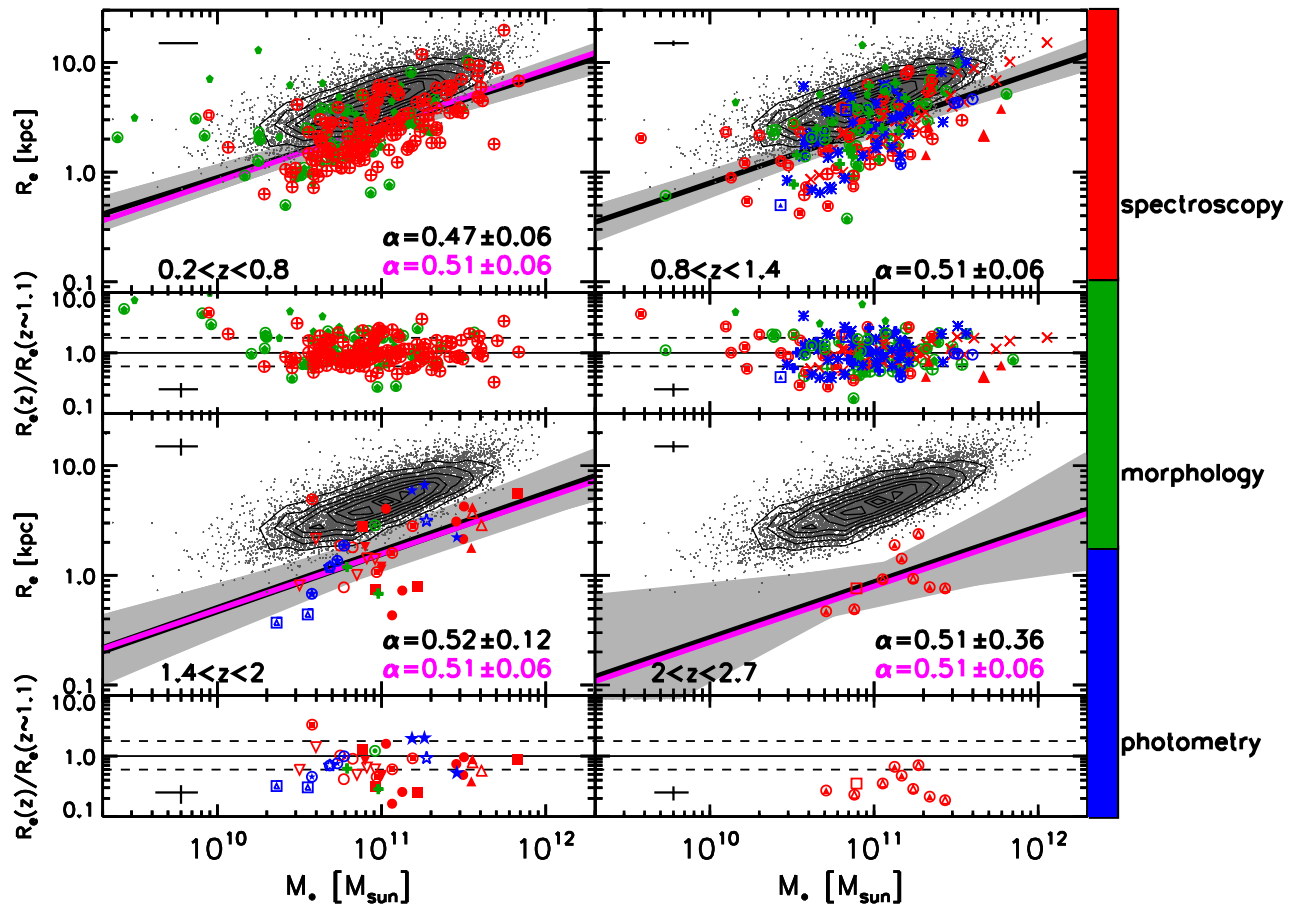


Figure 4.2 Effective radius R_e as a function of stellar mass for a sample of 465 passively evolving galaxies in the redshift range $0.2 < z < 2.7$. The notation is the same as in Figure 4.1 except that the color coding is now based on the sample selection criteria given in Table 4.1.

without corresponding Sérsic indices. In 8 out of 11 remaining surveys, for which the shape of galaxy’s surface brightness profiles can be classified as disk-like or spheroid-like based on the Sérsic index, the majority of quiescent galaxies and compact objects are spheroids with $n \geq 2.5$. The three spectroscopic surveys in our compilation with more than 50% of disk-dominated compact objects are the MUSYC survey (van Dokkum et al., 2008), the survey presented in Cassata et al. (2010), and the GMASS (Cimatti et al., 2008). While the MUSYC focuses on galaxies at $z > 2$, all disk-like objects with compact morphologies from Cassata et al. (2010) and Cimatti et al. (2008) are found at $z > 1.6$. We note that van der Wel et al. (2011) claim that the majority of massive compact galaxies at $z > 1.6$ are disk-dominated.

In compiling the data summarized in Table 4.1 we augmented our published NICMOS sizes for quiescent galaxies in the GDDS fields (Damjanov et al., 2009) with additional measurements obtained from imaging with the Advanced Camera for Surveys (ACS). The observational strategy for this ACS imaging was laid out in Abraham et al. (2007), and the images were processed using the techniques described in Damjanov et al. (2009). Out of the 40 quiescent GDDS galaxies imaged with ACS, four objects were also imaged with *HST* NICMOS Camera 3 in *H* band in Damjanov et al. (2009). Sizes obtained with ACS agreed to within $\lesssim 25\%$ with those obtained from NICMOS. In cases with duplicate measurements we chose to retain the NICMOS sizes because they probe longer rest frame wavelengths, which are less affected by dust extinction and are better tracers of total stellar emission. Residual images for another three galaxies show asymmetric features and their two-dimensional profiles cannot be reliably modelled with one-component or two-component Sérsic profiles. Finally, two objects appear in the ACS images as mergers (one merging pair is spectroscopically confirmed) and modelling of their two-dimensional profiles depends critically on details of how the companion galaxy is masked, so we omitted these galaxies from our sample. After making these cuts, an additional 31 GDDS quiescent massive galaxies were added to our total sample.

The complete list of objects in our compilation with all their properties we used to construct relations presented in this Letter is given in Table 4.2. We note that there are overlaps between a few $z > 1$ samples drawn from the south field of the Great Observatories Origin Deep Survey (GOODS): MS1054/CDFS, CL1252/CDFS, GS/WFC3, GS/ACS, HUDF/WFC3, GMASS, and HUDF. In order to exclude all duplicate entries for the objects with unpublished positions we flagged all galaxies in Table 4.2 having the

Table 4.1. Summary of the compilation of samples used to construct the size evolution diagram

Sample ^a	z_{spec}	$\lambda_{\text{rest}} (R_e)$	M_*^b	N	$n \geq 2.5$	Quiescent	$n \geq 2.5$ quiescent	Compact	$n \geq 2.5$ compact	Ref
(1)	(2)	(nm)	($10^{11} M_\odot$)	(5)	(%)	(%)	(%)	(%)	(%)	(11)
(3)	(4)	(5)	(6)	(7)	(8)	(9)	(10)	(11)	(11)	
EDisCS.....	0.24-0.96	415- 656	0.12- 6.85	154	87.66	100.00	87.66	23.37	≥ 47.22	1
CFRS	0.29-0.99	409- 631	0.04- 3.09	36	100.00	72.50	100.00	5.55	100.00	2
GN/DEIMOS ...	0.18-1.14	283- 514	0.03- 7.04	76	100.00	75.00	100.00	26.32	100.00	3,4
MS1054/CDFS....	0.84-1.14	353- 464	0.42-11.33 ^c	32	100.00	100.00	100.00	9.37	100.00	5
<i>CL1252/CDFS</i>	1.09-1.35	362- 407	0.29- 3.64	44	N/A	100.00	N/A	25.00	N/A	6
EGS/SSA22/GN	1.05-1.59	328- 397	0.33- 1.55	17	100.00	100.00	100.00	35.29	100.00	7
<i>Radio-loud QSOs</i> ...	1.29-1.59	618- 699	1.54- 2.87	5	60.00	100.00	60.00	0.00	0.00	8,9
MUNICS.....	1.23-1.71	590- 717	2.06- 5.95	9	66.66	100.00	66.66	11.12	100.00	10
<i>GS/WFC3</i>	1.33-1.62	611- 687	0.37- 1.45	6	66.66	100.00	66.66	66.66	75.00	11
GDDS/ACS.....	0.62-1.74	297- 502	0.04- 2.25	31	54.84	100.00	54.84	41.94	53.85	12
<i>EGS</i>	1.24-1.36	932- 982	3.09- 3.98	3	66.66	N/A	N/A	0.00	0.00	13
GDDS/NICMOS..	1.39-1.85	561- 669	0.55- 3.17	10	60.00	90.00	55.55	30.00	66.66	14
GS/ACS	0.95-1.92	291- 436	0.05- 2.08	15	100.00	100.00	100.00	13.34	100.00	15,16
<i>HUDF/WFC3</i>	1.32-1.98	537- 690	0.23- 0.67	4	50.00	100.00	50.00	75.00	33.34	17
GMAS.....	1.42-1.98	285- 351	0.32- 0.99	8	37.51	100.00	37.51	75.00	33.34	18
HUDF.....	1.39-2.67	232- 356	0.76- 6.74	6	83.34	100.00	83.34	50.00	66.66	19
MUSYC.....	2.03-2.55	451- 528	0.52- 2.71	9	44.45	100.00	44.45	77.77	42.85	20
TOTAL.....	0.2 – 2.67	232 – 982	0.03 – 11.33	465	≥ 78.07	≥ 92.90	≥ 76.09	25.80	≥ 59.17	

Note. — Column 1: survey from which the sample is drawn; Column 2: redshift range; Columns 3: the range of rest-frame central wavelengths of the R_e measurements; Column 4: mass range; Column 5: number of objects in the sample; Column 6: fraction of passively evolving objects; Column 7: fraction of spheroids; Column 8: fraction of passively evolving galaxies with spheroid-like profiles; Column 9: fraction of (compact) objects with $R_e \lesssim 1$ kpc; Column 10: fraction of compact objects with spheroid-like profiles ; Column 11: references: 1. Saglia et al. (2010); 2. Schade et al. (1999); 3. Treu et al. (2005b); 4. Bundy et al. (2007); 5. van der Wel et al. (2008); 6. Rettura et al. (2010); 7. Newman et al. (2010); 8. McGrath et al. (2007); 9. McGrath et al. (2008); 10. Longhetti et al. (2007); 11. Ryan et al. (2011); 12. data presented here; 13. Carrasco et al. (2010); 14. Damjanov et al. (2009); 15. Gargiulo et al. (2011); 16. Saracco et al. (2011); 17. Cassata et al. (2010); 18. Cimatti et al. (2008); 19. Daddi et al. (2005b); 20. van Dokkum et al. (2008)

^aSelection criteria for each sample are denoted by the font style: roman denotes spectroscopically selected objects with old stellar population, boldface is used for morphologically selected early-type galaxies, and italics font corresponds to the quiescent galaxies selected by colour.

^bStellar mass estimates have been converted to the Baldry & Glazebrook (2003) IMF.

^cBased on dynamical masses M_{dyn} and the $M_{\text{dyn}} \sim 1.4 \times M_*$ relation (van der Wel et al., 2008).

same redshifts and similar mass and size estimates and kept the results based on deeper imaging (e.g., WFC3) whenever possible. Our approach ensures that all 465 entries in Table 4.2 are unique.

4.4 The size-mass relation

Figure 4.1 presents the size-mass relation obtained from nearly 500 massive galaxies with known structural parameters spanning the (spectroscopically confirmed) redshift range from $z_{\text{spec}} \sim 0.2$ to $z_{\text{spec}} \sim 2.7$. The figure shows the data in four different redshift bins

and in each panel the high-redshift sample is shown relative to the local distribution of galaxies on the size-mass plane. These local data are from the Sloan Digital Sky Survey (SDSS), with sizes taken from Bernardi et al. (2003b) and matched with masses calculated following Baldry et al. (2008). The linear relation shown in each panel is the best-fit line obtained by fitting to the data in the $0.8 < z < 1.4$ panel (corresponding to roughly the half-way point in our redshift range). At the bottom of each panel the residual obtained by removing this $0.8 < z < 1.4$ linear relation is shown. The residuals are flat in all panels except possibly in the lowest redshift bin, where we do not have complete mass coverage. This suggests that for galaxies with masses greater than $10^{10} M_{\odot}$ the slope of the size-mass relationship remains constant at all redshifts, although its normalization does not. This is in good agreement with the findings of Damjanov et al. (2009), who reported that the slope of the relation between size R_e and stellar mass M_* of massive quiescent galaxies stays constant, while its zero point smoothly evolves towards lower half-light radii with increasing redshift.

It is important to consider whether different survey strategies used to obtain the data in Figure 4.1 play an important role in our interpretation of the observations. The galaxy sizes presented in Figures 4.1 and 4.2 and listed in Table 4.2 are measured over a wide range of rest-frame wavelengths ($\lambda_{\text{rest}} = 232 - 982 \text{ nm}$). However, available data suggest that this is not an important source of error. For example, all but three objects from the EGS subsample (Carrasco et al., 2010) have reported sizes based on the imaging that spans the range of $\lambda_{\text{rest}} = 300 - 700 \text{ nm}$, where half-light radii show weak dependence on wavelength (Cassata et al., 2010). Furthermore, the GDDS objects with available NICMOS F160W and ACS F814W images have very similar sizes in both bands, as noted in § 4.3. To further investigate possible biases, different selection criteria used to construct the compiled samples are shown in Table 4.1 coded by font style. Figure 4.2 presents the same data shown in Figure 4.1, but with symbols colors keyed to the selection criteria used to define the various surveys. In most of the listed surveys quiescent galaxies have been selected based either on their ultraviolet (UV) absorption spectral features (red points in Figure 4.2) or on their passive colors (blue points in Figure 4.2). Four out of 17 subsamples (containing 32% of all objects) are based on the morphological selection of spheroid-like systems (green points in Figure 4.2). No trends with selection strategy are seen.

Perhaps the strongest bias in our sample originates in the spectroscopic selection of

passive galaxies at $z > 1.5$, since these objects need to be bright enough to be detected in the rest frame UV. Our sample contains 38 objects (less than 10%) in that redshift range and for the high- z surveys in the sample with known spectroscopic completeness level it varies from $\sim 50\%$ (GMASS) to 80 – 90% (GDDS, GS/ACS). Although this may affect the slopes of the size-mass relation in the last two panels of Figures 4.1 and 4.2, our main conclusion presented in § 4.5 will not be altered since it is heavily based on the lower redshift bins where our selection of galaxies with known z_{spec} is far less biased.

4.5 The size growth of quiescent galaxies

4.5.1 The size-redshift relation

An even clearer picture of the size evolution of massive quiescent galaxies can be obtained by normalizing out the trends with stellar mass. Figure 4.3 shows a plot of size versus redshift in which we have used the slope $\alpha = 0.51$ of the $R_e \propto M_*^\alpha$ relation to normalize the sizes in order to remove the trend with stellar mass. The full distribution of data is shown in the left-hand panel, while the right-hand panel shows the corresponding ‘box and whisker’ plot¹. A legend mapping data points to individual surveys is provided in the bottom section of Figure 4.3.

It is interesting to consider whether a smooth function fits the data shown in Figure 4.3, but a straightforward fit to all the data points would be quite biased. The major portion of the $z > 0$ objects (63%) presented in this Letter lies in the redshift range $0.2 < z < 1$. On the other hand the local data outnumbers the high-redshift data by orders of magnitude and a straightforward unweighted fit to all the data points clearly places unfair emphasis on fitting the $z = 0$ galaxies. Furthermore, the size measurements of the brightest and most massive galaxies in the SDSS sample are affected by the uncertainties in the estimated background sky level producing a steeper slope of the size-mass relation observed locally (Guo et al., 2009). Therefore, as a first (fairly robust) step toward understanding the trends with redshift, we have instead chosen to calculate the best fit obtained by fitting the median values in the six redshift bins,

¹The top and bottom of the box show the 25th and 75th percentile of the distribution. The horizontal line bisecting the box is the 50th percentile (the median). The top and bottom of the error bars correspond to the 9th and 91st percentile. Circles are outliers.

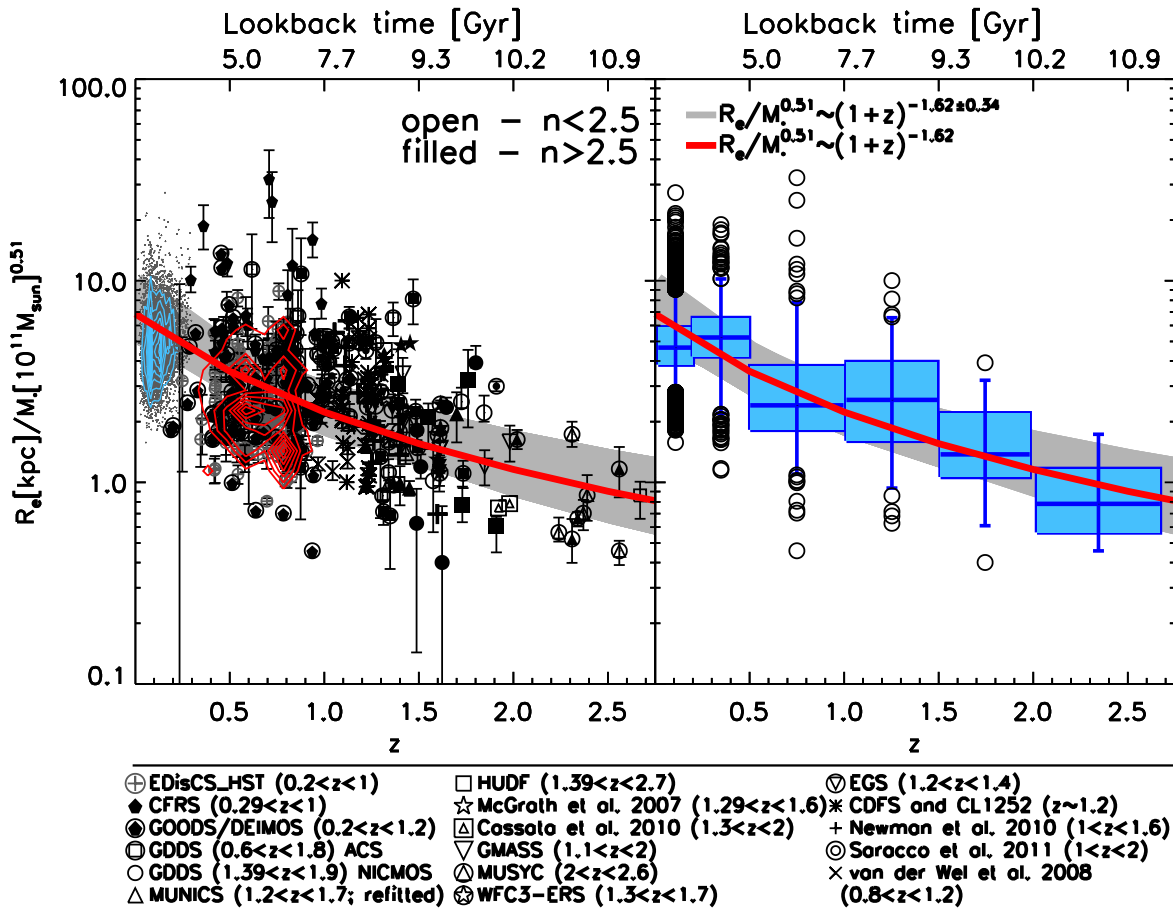


Figure 4.3 Size evolution of massive quiescent galaxies as a function of redshift. The y-axis represents the effective radius divided by M_*^α , where M_* is the stellar mass of a galaxy and $\alpha = 0.51$ is the slope of the size-mass relation shown in Figure 4.1. *Left:* Each symbol type corresponds to a different survey, while blue (red) contours denote the regions of constant density of $z \sim 0$ ($0.2 < z \lesssim 0.9$) galaxies in size-redshift parameter space. *Right:* The box-and-whisker diagram for $R_e/M_*^{0.51}$ divided into six redshifts bins. The red line and the gray shaded area in both panels show the best fit to the median redshift points and the $\pm 1\sigma$ errors of the best relation, respectively. *Bottom:* The list of spectroscopic surveys included in the presented sample. See text for details.

i.e. giving each redshift range equal weight. This results in $R_e/M_*^{0.51} \propto (1+z)^\beta$, where $\beta = -1.62 \pm 0.34$ (with the range of 1σ errors obtained by using the bootstrap resampling method). This fit is shown in red in Figure 4.3, with the corresponding uncertainty shown as a gray band. We emphasize that none of the main conclusions of this Letter depend on the specific parametric form represented by this fit.

4.5.2 Continuous size evolution with redshift

The overall conclusion from our analysis is that the median size of massive early-type galaxies is continuously growing from $z \sim 2.5$ to $z \sim 0$. This seems to be in disagreement with some previously reported results showing that a) the size evolution occurs rapidly at $z \gtrsim 1$ and becomes negligible at $z < 1$ (Fan et al., 2010; Valentinuzzi et al., 2010b; Maier et al., 2009) or b) there is no strong evidence for size growth from $z = 2$ to $z = 0$ (Saracco et al., 2010). This apparent discrepancy might be the result of earlier studies being based on samples spanning a limited redshift range, or which combine spectroscopic and photometric redshift samples, or which group passively evolving and star-forming objects together, or which contain small number of objects (four things we have tried to avoid doing in the present Letter). On the other hand, perhaps it will eventually prove interesting to group *some* star-forming objects with quiescent galaxies at a range of redshifts, since the form of *continuous* size evolution we obtain for our spectroscopic sample of massive quiescent galaxies is in good agreement with the somewhat shallower size-redshift relation found for UV-bright and submillimetre galaxies in GOODS-North field with secure spectroscopic redshifts over the $z = 0.6 - 3.5$ range ($R_e \sim (1+z)^{1.11 \pm 0.13}$, Mosleh et al., 2011). This unexpected concordance hints at a possible evolutionary connection between extreme star-forming and passively evolving galaxies.

Figure 4.3 highlights the main point of our analysis: size growth is both continuous and gradual, at least for the large sample of quiescent objects with spectroscopic redshifts as a whole. It is interesting to compare our results with the ones based on large photometric surveys. Recently, Williams et al. (2010) have performed structural analysis of $\sim 3 \times 10^4$ star-forming and passively evolving galaxies in the redshift range $z = 0.5 - 2$ from the UKIDSS Ultra-Deep Survey. In addition to the uncertainties introduced by photometric redshifts, the individual size measurements are largely affected by the use of ground based imaging in this survey. Nevertheless, their simulations and empirical tests show that the data provides robust estimates of the *average* sizes of a large galaxy

sample down to ~ 1 kpc radii. These authors also find a smooth evolution of half-light radii with time for both quiescent and star-forming galaxies described by power laws $(1+z)^\beta$ with similar exponents that depend on the stellar mass of galaxies and range from $\beta = -0.75 \pm 0.10$ for stellar masses $M_* = 10^6 - 10^8 M_\odot$ to $\beta = -1.30 \pm 0.10$ for $M_* > 10^{11} M_\odot$. A similar trend with mass, i.e., the more prominent size evolution of the most massive quiescent galaxies, has also been found using a small spectroscopic sample of 17 objects in the redshift range $z = 1.1 - 1.6$ (Newman et al., 2010) and at $1 \lesssim z \lesssim 2.5$ based on a predominantly photometric samples (Ryan et al., 2011). On the other hand, in a spectroscopic sample of 62 quiescent galaxies at $z = 1 - 2$ with $M_* = 10^{11} - 10^{12} M_\odot$ the fraction of compact objects does not depend on their mass (Saracco et al., 2010). All above listed spectroscopic samples are included in our analysis.

4.5.3 Size evolution with lookback time

Our analysis has focused on the size evolution of massive passively evolving galaxies as a function of redshift. However it is not obvious why the physical mechanism(s) driving size growth should be directly coupled to redshift (i.e. to the scale size of the Universe), as opposed to some process internal to an individual galaxy. By this logic the most interesting variable against which to explore size growth might be the time elapsed from the epoch of formation. Unfortunately there is insufficient published data to allow us to probe this directly, and the best we are able to do at present is probe lookback time from the present epoch, which is shown in Figure 4.4.

The size-lookback time relation shown in Figure 4.4 is best described by an exponential $R_e/M_*^{0.51} \propto t^\gamma$, where t is the lookback time and the exponent has a value of $\gamma = -0.71 \pm 0.46$. (Once again, fits were obtained by fitting to median values in six bins, with 1σ errors obtained by bootstrap resampling). While the logarithmic spread of the data seems fairly uniform in the six redshift bins (at least if the last $z > 2$ bin with the least data points is not taken into account), the first two lookback time bins have somewhat more centrally concentrated distributions than the following three bins. Also the number of outliers appears to be much larger if the galaxy sizes are represented in lookback time bins. Finally, the root mean square error of the median values with respect to the best fit for the size-lookback time relation is a factor of two higher than

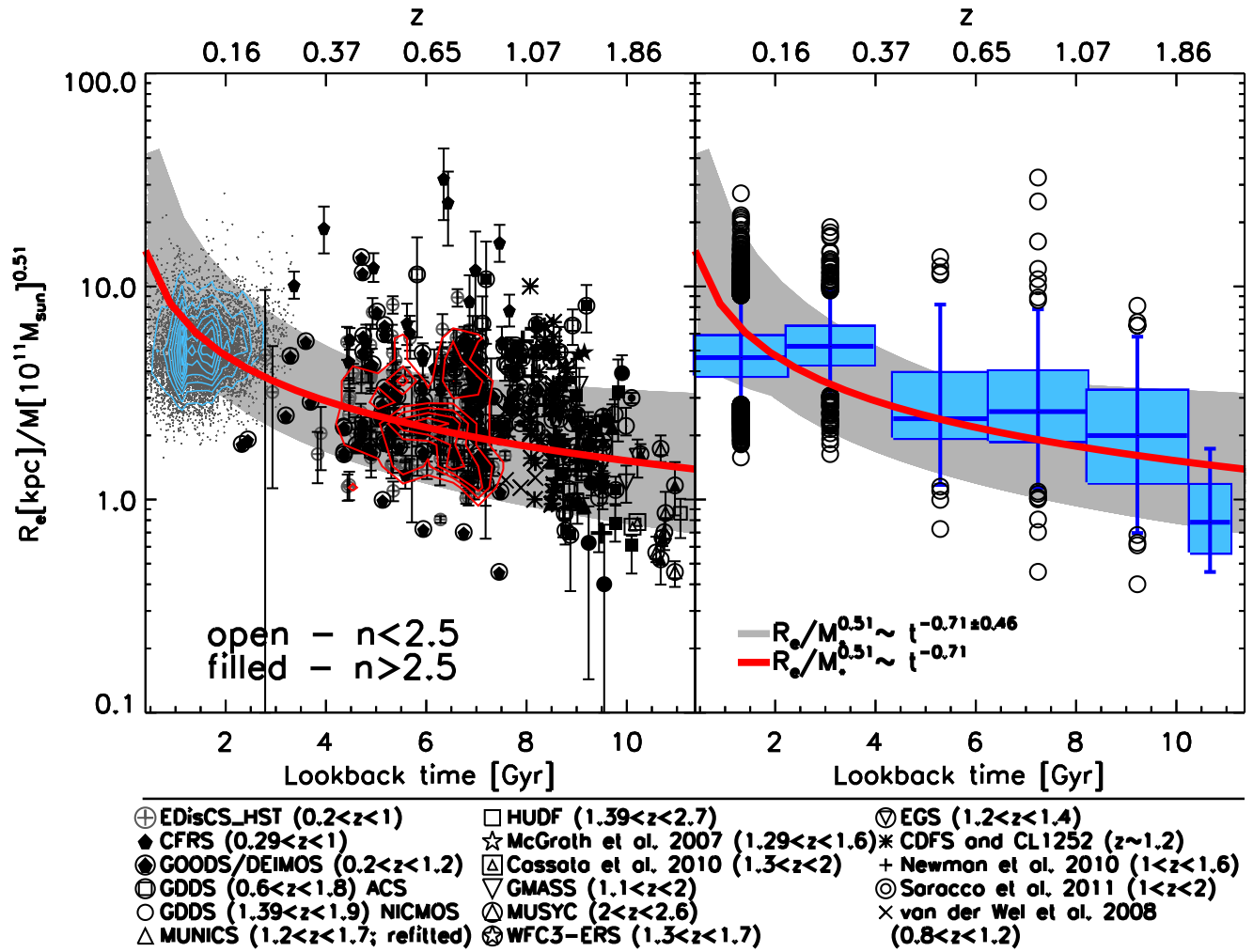


Figure 4.4 Size evolution of massive quiescent galaxies as a function of lookback time. Notation is the same as in Figure 4.2.

for the size-redshift relation². Our overall impression is that the trend with lookback time is less convincing than the trend with redshift, and this impression is reinforced by comparing the width of the gray band (the uncertainty) to the dynamic range spanned by the data in Figures 4.3 and 4.4.

As noted earlier, one really wishes it were possible to focus on the systematics of size versus the time from the epoch of major mass building, as opposed to size versus lookback time. Some work has already been done in this direction, and while some results obtained at redshifts $z < 1$ show that all quiescent objects lie further away from the local size-mass relation with increasing redshift irrespective of their age (Trujillo et al., 2011, but see also van der Wel et al., 2009; Valentinuzzi et al., 2010a), at $z \sim 1.5$ larger spheroids are on average younger and occupy a narrower age range than compact spheroids of the same mass (Saracco et al., 2011). This discrepancy may suggest that at higher redshifts the dominant mechanism for size growth could be adiabatic expansion followed by a series of minor mergers at later times, but a larger and more homogeneous galaxy sample is really needed to test this hypothesis.

Although Figure 4.4 has limited interpretive power, it does highlight the main point made earlier, which is that size growth is both continuous and gradual, at least for the sample as a whole. This has implications for some mechanisms proposed to explain the size evolution, such as feedback from active galactic nucleus, supernovae, or evolved stellar populations (e.g., Damjanov et al., 2009; Fan et al., 2010), and for models in which a sequence of minor mergers drives the growth (e.g., Naab et al., 2009; Hopkins et al., 2010b). The long timescales over which activity is occurring could be seen as an argument against stellar feedback as the only driver of galaxy size growth, because mass loss from evolved stars can trigger adiabatic expansion and produce observed changes in galaxy sizes, but this effect is likely relevant on relatively short timescales (< 2 Gyr, see Damjanov et al., 2009). Invoking quasar activity to explain the size evolution of the most massive objects offers an even shorter epoch for large increases in size due to the gas outflows (of the order of 0.1 Gyr, see Fan et al., 2010). These authors propose supernovae feedback as driving mechanism for the size growth of less massive objects ($M_* \lesssim 2 \times 10^{10} M_\odot$), and that operates over a longer timescale, albeit with a much

²There is also a clear drop in the number of objects at lookback times around $t \sim 3$ Gyr, corresponding to the redshift bin $0.2 < z < 0.5$ from Figure 4.1. We caution against drawing any conclusions from this, as it appears to be driven by a small number of large objects with stellar masses $M_* < 10^{10} M_\odot$. As noted earlier, surveys are very incomplete at these low masses.

weaker effect on galaxy sizes.

4.6 Central mass density evolution

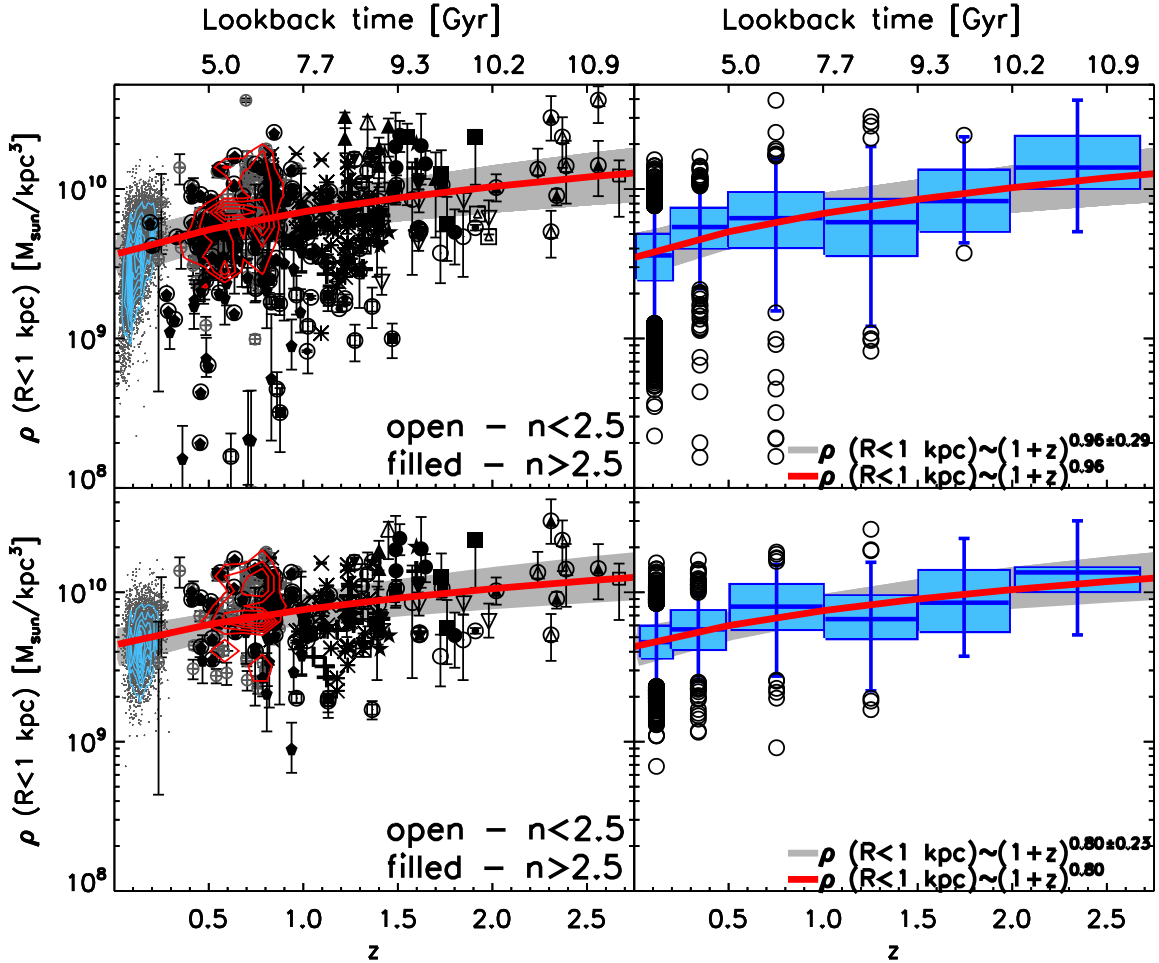


Figure 4.5 Central stellar mass density (within 1 kpc) of massive quiescent galaxies as a function of redshift. Upper panels show the complete sample presented in Figures 4.3 and 4.4, while the lower panels present the objects at constant number density (based on the analysis given in van Dokkum et al., 2010). Notation is the same as in Figures 4.3 and 4.4

One of the consequences of the continuous size growth in massive quiescent galaxies is a corresponding continuous decrease in their central stellar mass density, which is conveniently described by the mass density within the central kiloparsec, $\rho(R_e < 1 \text{ kpc})$.

We calculate this central mass density by assuming that the total stellar mass is following the light profile and that systems in our sample have spherical symmetry. The resulting values are in excellent agreement with the results of a previous analysis where a slightly different method was used for deprojecting galaxy light profile (MYSIC subsample, Bezanson et al., 2009). Upper panels of Figure 4.5 show the steady evolution in the central mass density as a function of redshift for our sample with high resolution imaging that provides spatial sampling of ~ 1 kpc at $z \sim 2$ (e.g., Carrasco et al., 2010; van Dokkum et al., 2008; Longhetti et al., 2007). Within our uncertainties, this growth of central stellar mass density with redshift can be parameterized rather simply as almost linear growth with redshift: $\rho \propto (1+z)^{0.96 \pm 0.29}$ (once again based on the median values over six redshift bins). In the model based on cosmological simulations and presented by Hopkins et al. (2010b), the central mass density (within the central few kpc) of a quiescent galaxy undergoing minor mergers should stay roughly constant. Therefore the decrease in ρ by a factor of ~ 3.5 since $z \sim 2.5$ may prove challenging to explain in a scenario in which the size growth is driven by a succession of minor mergers. Taking dynamical friction into account, a factor of 1.5 change in the mass density within the central 1 kpc is expected over our redshift range (Naab et al., 2009), which seems insufficient to explain the rather dramatic changes in size and, consequently, central density observed in our sample.

The resulting steady evolution of the central mass density is based on the assumption that the mass of passive galaxies does not change in the redshift range we are probing. However, it has been shown that the number density of massive quiescent galaxies evolves with redshift (e.g., Brammer et al., 2011). In order to take into account the change of mass in the merger scenario, we selected a subsample of quiescent galaxies that follow the change in mass with redshift at constant number density by employing equation 1 and the range of errors presented in Figure 2 from van Dokkum et al. (2010). The change in the central mass density of these objects can be presented by a power law that is very similar to the one obtained using the complete sample (lower panels of Figure 4.5), confirming that even at the constant number density central mass density of quiescent galaxies decreases by a factor of $\gtrsim 2.7$ from $z = 2.5$ to $z = 0$. This result implies that it might be difficult to explain the observed size growth by invoking minor mergers, unless they involve some star formation, in which case merger remnant would not be in our current sample.

4.7 Summary and conclusions

We have analyzed the size growth of 465 early-type galaxies taken from 17 spectroscopic surveys spanning the redshift range $0.2 < z < 2.7$. The size evolution of passively evolving galaxies is continuous and gradual over this redshift range. Size growth appears to be independent of stellar mass. Galactic half-light radius scales with redshift as $R_e/M_*^{0.51} \propto (1+z)^{-1.62 \pm 0.34}$, while the mean value of the central stellar mass density appears to be increasing approximately linearly with redshift. Although surveys at higher z are less sensitive to lower surface brightness galaxies and thus tend to reduce the slopes of the size-redshift relation, based on the lower z distribution this is not expected to be a large effect. Our resulting power law quantifying smooth size evolution is comparable to the $R_e \sim (1+z)^\beta$ relation for massive ($M_* > 6.3 \times 10^{10} M_\odot$) quiescent galaxies with the exponent $\beta = -1.44$ determined by frequent minor mergers at $z = 0 - 2$ in recent cosmological simulations (Oser et al., 2011). However, these simplified simulations neither include strong supernova-driven winds nor active galactic nucleus feedback. Any mechanism proposed to explain size evolution will have to take into account the fact that size growth is a continuous process that has been occurring more-or-less smoothly and gradually over the last 10 Gyr.

We thank the referee for a positive feedback. ID and RGA acknowledge the financial support provided by the NSERC.

Table 4.2. Complete list of objects used to construct the size evolution diagram

Object ID	<i>R.A.</i> J2000 (deg)	<i>Dec.</i> J2000 (deg)	z_{spec}	Selection	M_* ($10^{11} M_{\odot}$)	ΔM_* ($10^{11} M_{\odot}$)	Observing filter	R_e (kpc)	ΔR_e (kpc)	n	Δn
(1)	(2)	(3)	(4)	(5)	(6)	(7)	(8)	(9)	(10)	(11)	(12)
EDCSNJ1040403-1156042	160.167917	-11.934500	0.7020	spectroscopy	2.663	0.368	F814W	6.153	3.700
EDCSNJ1040407-1156015	160.169583	-11.933750	0.7030	spectroscopy	1.463	0.168	F814W	1.698	3.700
EDCSNJ1040346-1157566	160.144167	-11.965722	0.7024	spectroscopy	1.366	0.252	F814W	3.348	3.700
EDCSNJ1040396-1155183	160.165000	-11.921750	0.7046	spectroscopy	0.945	0.196	F814W	2.244	3.700
EDCSNJ1040356-1156026	160.148333	-11.934056	0.7081	spectroscopy	1.719	0.475	F814W	2.345	3.700
EDCSNJ1054244-1146194	163.601667	-11.772056	0.6965	spectroscopy	4.031	0.464	F814W	5.945	3.700
EDCSNJ1054250-1146238	163.604167	-11.773278	0.6968	spectroscopy	2.602	0.360	F814W	3.465	3.700
EDCSNJ1054309-1147095	163.628750	-11.785972	0.6998	spectroscopy	0.842	0.155	F814W	3.840	3.700
EDCSNJ1054263-1148407	163.609583	-11.811306	0.7014	spectroscopy	0.945	0.174	F814W	4.523	3.700
EDCSNJ1054338-1149299	163.640833	-11.824972	0.6945	spectroscopy	1.929	0.267	F814W	2.965	3.700
EDCSNJ1054280-1149598	163.616667	-11.833278	0.6964	spectroscopy	4.846	0.335	F814W	1.802	3.700
EDCSNJ1054296-1147123	163.623333	-11.786750	0.6981	spectroscopy	2.165	0.249	F814W	2.547	3.700
EDCSNJ1054278-1149580	163.615833	-11.832778	0.6949	spectroscopy	1.929	1.955	F814W	3.372	3.700
EDCSNJ1054305-1146536	163.627083	-11.781556	0.6986	spectroscopy	3.939	1.360	F814W	9.346	3.700
EDCSNJ1054303-1149132	163.626250	-11.820333	0.6964	spectroscopy	3.849	0.532	F814W	4.856	3.700
EDCSNJ1054237-1146107	163.598750	-11.769639	0.6962	spectroscopy	0.385	0.071	F814W	0.956	3.700
EDCSNJ1054246-1146124	163.602500	-11.770111	0.7034	spectroscopy	0.967	0.334	F814W	6.194	3.700
EDCSNJ1054467-1245035	163.694583	-12.750972	0.7304	spectroscopy	0.882	0.203	F814W	1.883	3.700
EDCSNJ1054435-1245519	163.681250	-12.764417	0.7503	spectroscopy	3.431	0.316	F814W	9.555	3.700
EDCSNJ1054451-1247336	163.687917	-12.792667	0.7305	spectroscopy	0.786	0.072	F814W	1.516	3.700
EDCSNJ1054436-1244202	163.681667	-12.738944	0.7463	spectroscopy	0.786	0.090	F814W	1.297	3.700
EDCSNJ1054438-1245409	163.682500	-12.761361	0.7568	spectroscopy	1.430	0.132	F814W	1.606	3.700
EDCSNJ1054445-1246173	163.685417	-12.771472	0.7498	spectroscopy	0.639	0.059	F814W	1.373	3.700
EDCSNJ1054440-1246390	163.683333	-12.777500	0.7496	spectroscopy	0.639	0.074	F814W	1.692	3.700
EDCSNJ1054442-1245331	163.684167	-12.759194	0.7446	spectroscopy	0.116	0.019	F814W	1.684	3.700
EDCSNJ1054439-1245556	163.682917	-12.765444	0.7531	spectroscopy	0.733	0.084	F814W	2.806	3.700
EDCSNJ1054398-1246055	163.665833	-12.768194	0.7482	spectroscopy	2.165	0.349	F814W	5.880	3.700
EDCSNJ1054396-1248241	163.665000	-12.806694	0.7478	spectroscopy	0.882	0.122	F814W	2.259	3.700
EDCSNJ1054431-1246205	163.679583	-12.772361	0.7553	spectroscopy	0.768	0.141	F814W	5.025	3.700
EDCSNJ1216470-1159267	184.195833	-11.990750	0.7971	spectroscopy	0.624	0.086	F814W	2.120	3.700
EDCSNJ1216454-1200017	184.189167	-12.000472	0.7996	spectroscopy	1.012	0.163	F814W	2.494	3.700
EDCSNJ1216490-1200091	184.204167	-12.002528	0.7863	spectroscopy	0.902	0.145	F814W	4.425	3.700
EDCSNJ1216453-1201176	184.188750	-12.021556	0.7955	spectroscopy	5.074	0.584	F814W	8.920	3.700
EDCSNJ1216420-1201509	184.175000	-12.030806	0.7941	spectroscopy	2.988	0.482	F814W	3.867	3.700
EDCSNJ1216468-1202226	184.195000	-12.039611	0.7987	spectroscopy	1.162	0.134	F814W	6.409	3.700
EDCSNJ1216401-1202352	184.167083	-12.043111	0.8022	spectroscopy	1.304	0.210	F814W	1.410	3.700
EDCSNJ1216462-1200073	184.192500	-12.002028	0.7847	spectroscopy	0.403	0.056	F814W	1.052	3.700
EDCSNJ1216418-1200449	184.174167	-12.012472	0.7967	spectroscopy	1.085	0.150	F814W	2.802	3.700
EDCSNJ1216438-1200536	184.182500	-12.014889	0.7945	spectroscopy	2.267	0.209	F814W	1.855	3.700
EDCSNJ1216461-1201143	184.192083	-12.020639	0.7997	spectroscopy	3.939	0.453	F814W	4.748	3.700
EDCSNJ1216456-1201080	184.190000	-12.018889	0.8058	spectroscopy	1.568	0.144	F814W	7.863	3.700
EDCSNJ1216453-1201209	184.188750	-12.022472	0.8054	spectroscopy	2.165	0.299	F814W	5.509	3.700
EDCSNJ1216443-1201429	184.184583	-12.028583	0.7918	spectroscopy	2.020	0.233	F814W	1.846	3.700
EDCSNJ1216438-1202155	184.182500	-12.037639	0.8028	spectroscopy	0.376	0.061	F814W	0.621	3.700
EDCSNJ1216417-1203054	184.173750	-12.051500	0.8012	spectroscopy	0.519	0.072	F814W	0.962	3.700
EDCSNJ1216359-1200294	184.149583	-12.008167	0.7930	spectroscopy	0.862	0.099	F814W	0.940	3.700
EDCSNJ1216446-1201089	184.185833	-12.019139	0.8001	spectroscopy	0.786	0.109	F814W	1.600	3.700
EDCSNJ1216449-1201203	184.187083	-12.022306	0.8035	spectroscopy	3.431	0.395	F814W	2.972	3.700
EDCSNJ1216403-1202029	184.167917	-12.034139	0.7976	spectroscopy	0.432	0.080	F814W	1.948	3.700
EDCSNJ1216522-1200595	184.217500	-12.016528	0.7882	spectroscopy	0.485	0.078	F814W	1.641	3.700
EDCSNJ1216382-1202517	184.159167	-12.047694	0.7900	spectroscopy	1.463	0.236	F814W	3.456	3.700
EDCSNJ1216387-1201503	184.161250	-12.030639	0.8008	spectroscopy	1.085	0.100	F814W	1.297	3.700
EDCSNJ1232318-1249049	188.132500	-12.818028	0.5408	spectroscopy	0.412	0.095	F814W	2.125	3.700
EDCSNJ1232280-1249353	188.116667	-12.826472	0.5449	spectroscopy	1.800	0.373	F814W	4.062	3.700
EDCSNJ1232303-1250364	188.126250	-12.843444	0.5419	spectroscopy	5.564	1.025	F814W	19.730	3.700
EDCSNJ1232250-1251551	188.104167	-12.865306	0.5399	spectroscopy	0.463	0.171	F814W	2.304	3.700
EDCSNJ1232287-1252369	188.119583	-12.876917	0.5432	spectroscopy	1.304	0.240	F814W	2.445	3.700

Table 4.2 (cont'd)

Object ID	<i>R.A.</i>	<i>Dec.</i>	z_{spec}	Selection	M_*	ΔM_*	Observing filter	R_e	ΔR_e	n	Δn
(1)	J2000 (deg)	J2000 (deg)	(4)	(5)	($10^{11} M_\odot$)	($10^{11} M_\odot$)	(8)	(kpc)	(kpc)	(11)	(12)
EDCSNJ1232271-1253013	188.112917	-12.883694	0.5445	spectroscopy	0.842	0.233	F814W	2.554	3.700
EDCSNJ1232343-1249265	188.142917	-12.824028	0.5395	spectroscopy	0.654	0.181	F814W	1.420	3.700
EDCSNJ1232350-1250103	188.145833	-12.836194	0.5397	spectroscopy	0.945	0.239	F814W	5.685	3.700
EDCSNJ1232313-1250327	188.130417	-12.842417	0.5496	spectroscopy	0.507	0.140	F814W	1.440	3.700
EDCSNJ1232317-1249275	188.132083	-12.824306	0.5420	spectroscopy	1.246	0.287	F814W	5.449	3.700
EDCSNJ1232309-1249408	188.128750	-12.828000	0.5485	spectroscopy	2.854	0.329	F814W	3.620	3.700
EDCSNJ1232303-1251092	188.126250	-12.852556	0.5428	spectroscopy	0.299	0.076	F814W	1.087	3.700
EDCSNJ1232303-1251441	188.126250	-12.862250	0.5500	spectroscopy	0.485	0.123	F814W	2.704	3.700
EDCSNJ1232370-1248239	188.154167	-12.806639	0.5401	spectroscopy	0.804	0.222	F814W	1.831	3.700
EDCSNJ1232372-1249258	188.155000	-12.823833	0.5377	spectroscopy	0.193	0.053	F814W	0.631	3.700
EDCSNJ1232296-1250119	188.123333	-12.836639	0.5509	spectroscopy	1.275	0.323	F814W	5.102	3.700
EDCSNJ1232301-1250362	188.125417	-12.843389	0.5424	spectroscopy	0.569	0.105	F814W	1.105	3.700
EDCSNJ1232288-1250490	188.120000	-12.846944	0.5470	spectroscopy	1.162	0.294	F814W	2.169	3.700
EDCSNJ1232299-1251034	188.124583	-12.850944	0.5493	spectroscopy	0.412	0.085	F814W	1.526	3.700
EDCSNJ1232207-1252016	188.086250	-12.867111	0.5416	spectroscopy	3.058	0.563	F814W	7.029	3.700
EDCSNJ1232204-1249547	188.085000	-12.831861	0.5460	spectroscopy	1.642	0.340	F814W	4.347	3.700
EDCSNJ1037527-1243456	159.469583	-12.729333	0.5807	spectroscopy	0.733	0.118	F814W	1.268	3.700
EDCSNJ1037548-1245113	159.478333	-12.753139	0.5789	spectroscopy	1.532	0.212	F814W	1.740	3.700
EDCSNJ1037447-1246050	159.436250	-12.768056	0.4222	spectroscopy	0.359	0.058	F814W	1.483	3.700
EDCSNJ1037552-1246368	159.480000	-12.776889	0.4245	spectroscopy	0.422	0.087	F814W	1.942	3.700
EDCSNJ1037535-1241538	159.472917	-12.698278	0.5789	spectroscopy	0.902	0.145	F814W	3.661	3.700
EDCSNJ1037525-1243541	159.468750	-12.731694	0.5772	spectroscopy	0.842	0.116	F814W	1.731	3.700
EDCSNJ1037428-1245573	159.428333	-12.765917	0.4225	spectroscopy	0.882	0.122	F814W	3.259	3.700
EDCSNJ1037527-1244485	159.469583	-12.746806	0.4223	spectroscopy	0.733	0.152	F814W	2.494	3.700
EDCSNJ1037473-1246245	159.447083	-12.773472	0.4229	spectroscopy	0.385	0.115	F814W	0.720	3.700
EDCSNJ1103365-1244223	165.902083	-12.739528	0.7031	spectroscopy	6.845	1.261	F814W	6.787	3.700
EDCSNJ1103372-1245215	165.905000	-12.755972	0.6251	spectroscopy	0.733	0.169	F814W	2.682	3.700
EDCSNJ1103363-1246220	165.901250	-12.772778	0.6288	spectroscopy	1.136	0.340	F814W	2.645	3.700
EDCSNJ1103444-1245153	165.935000	-12.754250	0.9640	spectroscopy	2.067	0.190	F814W	2.327	3.700
EDCSNJ1103349-1246462	165.895417	-12.779500	0.6257	spectroscopy	2.663	0.429	F814W	5.823	3.700
EDCSNJ1103413-1244379	165.922083	-12.743861	0.7038	spectroscopy	1.246	0.229	F814W	2.637	3.700
EDCSNJ1103357-1246398	165.898750	-12.777722	0.6278	spectroscopy	0.669	0.123	F814W	1.741	3.700
EDCSNJ1138068-1132285	174.528333	-11.541250	0.4787	spectroscopy	0.544	0.263	F814W	3.893	3.700
EDCSNJ1138102-1133379	174.542500	-11.560528	0.4801	spectroscopy	2.485	0.630	F814W	6.071	3.700
EDCSNJ1138069-1134314	174.528750	-11.575389	0.4819	spectroscopy	0.610	0.140	F814W	1.692	3.700
EDCSNJ1138074-1137138	174.530833	-11.620500	0.4528	spectroscopy	1.246	0.229	F814W	2.877	3.700
EDCSNJ1138104-1133319	174.543333	-11.558861	0.4844	spectroscopy	0.306	0.099	F814W	4.137	3.700
EDCSNJ1138107-1133431	174.544583	-11.561972	0.4764	spectroscopy	0.768	0.212	F814W	1.604	3.700
EDCSNJ1138127-1134211	174.552917	-11.572528	0.4804	spectroscopy	0.279	0.148	F814W	0.906	3.700
EDCSNJ1138116-1134448	174.548333	-11.579111	0.4571	spectroscopy	0.544	0.150	F814W	1.442	3.700
EDCSNJ1138069-1132044	174.528750	-11.534556	0.4798	spectroscopy	0.531	0.135	F814W	1.138	3.700
EDCSNJ1138130-1132345	174.554167	-11.542917	0.4791	spectroscopy	0.583	0.174	F814W	2.817	3.700
EDCSNJ1138110-1133411	174.545833	-11.561417	0.4825	spectroscopy	0.463	0.202	F814W	2.813	3.700
EDCSNJ1138022-1135459	174.509167	-11.596083	0.4541	spectroscopy	0.882	0.244	F814W	3.447	3.700
EDCSNJ1138065-1136018	174.527083	-11.600500	0.4561	spectroscopy	0.422	0.204	F814W	3.032	3.700
EDCSNJ1138031-1134278	174.512917	-11.574389	0.4549	spectroscopy	0.376	0.104	F814W	1.293	3.700
EDCSNJ1354098-1231098	208.540833	-12.519389	0.7568	spectroscopy	0.412	0.038	F814W	0.914	3.700
EDCSNJ1354098-1231015	208.540833	-12.517083	0.7562	spectroscopy	3.849	0.532	F814W	7.568	3.700
EDCSNJ1354097-1230579	208.540417	-12.516083	0.7565	spectroscopy	1.605	0.185	F814W	1.926	3.700
EDCSNJ1354026-1230127	208.510833	-12.503528	0.5942	spectroscopy	0.403	0.074	F814W	1.385	3.700
EDCSNJ1354114-1230452	208.547500	-12.512556	0.5947	spectroscopy	0.989	0.387	F814W	5.690	3.700
EDCSNJ1354159-1232272	208.566250	-12.540889	0.5929	spectroscopy	0.285	0.066	F814W	0.732	3.700
EDCSNJ1354102-1230527	208.542500	-12.514639	0.7593	spectroscopy	1.759	0.324	F814W	11.840	3.700
EDCSNJ1354101-1231041	208.542083	-12.517806	0.7612	spectroscopy	1.110	0.153	F814W	1.595	3.700
EDCSNJ1354204-1234286	208.585000	-12.574611	0.6006	spectroscopy	1.719	2.217	F814W	3.009	3.700
EDCSNJ1354106-1230499	208.544167	-12.513861	0.7634	spectroscopy	0.967	0.111	F814W	2.117	3.700
EDCSNJ1040391-1155167	160.162917	-11.921306	0.7660	spectroscopy	0.463	0.075	F814W	1.025	3.700

Table 4.2 (cont'd)

Object ID	<i>R.A.</i>	<i>Dec.</i>	z_{spec}	Selection	M_*	ΔM_*	Observing filter	R_e	ΔR_e	n	Δn
(1)	J2000 (deg)	J2000 (deg)	(4)	(5)	($10^{11} M_\odot$)	($10^{11} M_\odot$)	(8)	(kpc)	(kpc)	(11)	(12)
EDCSNJ1040343-1155414	160.142917	-11.928167	0.7807	spectroscopy	2.920	0.336	F814W	3.543	3.700
EDCSNJ1040476-1158184	160.198333	-11.971778	0.6171	spectroscopy	0.751	0.138	F814W	2.091	3.700
EDCSNJ1054253-1148349	163.605417	-11.809694	0.8657	spectroscopy	0.989	0.159	F814W	1.526	3.700
EDCSNJ1054289-1146428	163.620417	-11.778556	0.2491	spectroscopy	2.485	3.148	F814W	5.073	3.700
EDCSNJ1054353-1246528	163.599583	-11.756556	0.7408	spectroscopy	1.800	0.290	F814W	2.635	3.700
EDCSNJ1054339-1147352	163.641250	-11.793111	0.8608	spectroscopy	1.036	0.215	F814W	1.916	3.700
EDCSNJ1054240-1147364	163.600000	-11.793444	0.6124	spectroscopy	4.125	0.380	F814W	4.464	3.700
EDCSNJ1054525-1244189	163.718750	-12.738583	0.7283	spectroscopy	1.842	0.170	F814W	4.663	3.700
EDCSNJ1054353-1246528	163.647083	-12.781333	0.6932	spectroscopy	3.129	0.432	F814W	3.469	3.700
EDCSNJ1054487-1245052	163.702917	-12.751444	0.6189	spectroscopy	0.700	0.129	F814W	1.629	3.700
EDCSNJ1216402-1201593	184.167500	-12.033139	0.3463	spectroscopy	2.165	1.146	F814W	2.423	3.700
EDCSNJ1216508-1157576	184.211667	-11.966000	0.6501	spectroscopy	0.639	0.118	F814W	1.096	3.700
EDCSNJ1216476-1202280	184.198333	-12.041111	0.5434	spectroscopy	1.246	0.258	F814W	1.228	3.700
EDCSNJ1216545-1203359	184.185417	-12.059972	0.2344	spectroscopy	0.945	1.893	F814W	4.625	3.700
EDCSNJ1216364-1200087	184.151667	-12.002417	0.7868	spectroscopy	0.717	0.099	F814W	1.345	3.700
EDCSNJ1216449-1202139	184.187083	-12.037194	0.6691	spectroscopy	0.967	0.156	F814W	2.355	3.700
EDCSNJ1216527-1202553	184.219583	-12.048694	0.8263	spectroscopy	0.751	0.086	F814W	0.919	3.700
EDCSNJ1216548-1157451	184.228333	-11.962528	0.8746	spectroscopy	1.430	2.272	F814W	4.144	3.700
EDCSNJ1232326-1249355	188.135833	-12.826528	0.4186	spectroscopy	0.945	0.261	F814W	1.116	3.700
EDCSNJ1232285-1252553	188.118750	-12.882028	0.8457	spectroscopy	1.110	0.179	F814W	3.761	3.700
EDCSNJ1232315-1251578	188.131250	-12.866056	0.4171	spectroscopy	1.036	0.358	F814W	5.594	3.700
EDCSNJ1037540-1241435	159.475000	-12.695417	0.4329	spectroscopy	0.359	0.074	F814W	2.322	3.700
EDCSNJ1037448-1245026	159.436667	-12.750722	0.4456	spectroscopy	0.285	0.072	F814W	0.997	3.700
EDCSNJ1037534-1246259	159.472500	-12.773861	0.4948	spectroscopy	0.733	0.101	F814W	1.655	3.700
EDCSNJ1037595-1245095	159.497917	-12.752639	0.8736	spectroscopy	1.719	0.158	F814W	2.377	3.700
EDCSNJ1037529-1246428	159.470417	-12.778556	0.6452	spectroscopy	0.474	0.087	F814W	1.555	3.700
EDCSNJ1103531-1243328	165.971250	-12.725778	0.7221	spectroscopy	1.304	0.300	F814W	3.073	3.700
EDCSNJ1103418-1244344	165.924167	-12.742889	0.3539	spectroscopy	0.394	0.254	F814W	1.272	3.700
EDCSNJ1103430-1245370	165.929167	-12.760278	0.6584	spectroscopy	1.217	0.196	F814W	2.203	3.700
EDCSNJ1138100-1136361	174.541667	-11.610028	0.4389	spectroscopy	0.463	0.171	F814W	1.381	3.700
EDCSNJ1138126-1131500	174.552500	-11.530556	0.9079	spectroscopy	1.335	0.246	F814W	1.649	3.700
EDCSNJ1138078-1134468	174.532500	-11.579667	0.5282	spectroscopy	0.700	0.177	F814W	1.974	3.700
EDCSNJ1354144-1228536	208.560000	-12.481556	0.8245	spectroscopy	2.267	0.418	F814W	2.011	3.700
EDCSNJ1354107-1231236	208.544583	-12.523222	0.6183	spectroscopy	0.569	0.118	F814W	1.085	3.700
EDCSNJ1354016-1231578	208.506667	-12.532722	0.4783	spectroscopy	0.463	0.085	F814W	1.583	3.700
EDCSNJ1354055-1234136	208.522917	-12.570444	0.5142	spectroscopy	0.768	0.159	F814W	2.393	3.700
EDCSNJ1354139-1229474	208.557917	-12.496500	0.6865	spectroscopy	0.583	0.188	F814W	1.504	3.700
EDCSNJ1354161-1234210	208.567083	-12.572500	0.5391	spectroscopy	0.260	0.030	F814W	1.061	3.700
EDCSNJ1354164-1229192	208.568333	-12.488667	0.6846	spectroscopy	2.165	0.299	F814W	3.845	3.700
EDCSNJ1354130-1230263	208.554167	-12.507306	0.8223	spectroscopy	0.945	0.109	F814W	1.183	3.700
CFRS-03.0337	45.618333	0.103889	0.3610	morphology	0.030	0.015	F814W	3.199	4.000
CFRS-03.0560	45.650000	0.206389	0.6970	morphology	1.164	0.598	F814W	3.589	4.000
CFRS-03.1031	45.661250	0.099722	0.4220	morphology	0.232	0.088	F814W	2.128	4.000
CFRS-03.1032	45.661250	0.103056	0.6180	morphology	0.509	0.204	F814W	1.592	4.000
CFRS-03.1077	45.635833	0.100000	0.9380	morphology	0.824	0.319	F814W	14.723	4.000
CFRS-03.1381	45.732917	0.118611	0.6360	morphology	0.581	0.207	F814W	3.467	4.000
CFRS-03.1384	45.730833	0.116111	0.7850	morphology	0.759	0.238	F814W	4.842	4.000
CFRS-03.1395	45.720417	0.117778	0.7080	morphology	0.173	0.125	F814W	13.243	4.000
CFRS-03.1413	45.707917	0.121111	0.4870	morphology	0.269	0.081	F814W	6.353	4.000
CFRS-10.0794	150.131250	25.238333	0.5800	morphology	0.372	0.111	F814W	0.802	4.000
CFRS-10.1189	150.213333	25.238889	0.9490	morphology	0.885	0.289	F814W	5.212	4.000
CFRS-10.1207	150.195417	25.235833	0.7060	morphology	0.439	0.117	F814W	2.761	4.000
CFRS-10.1209	150.165417	25.235833	0.8410	morphology	1.400	0.451	F814W	3.664	4.000
CFRS-10.1231	150.198750	25.231944	0.4730	morphology	0.370	0.118	F814W	2.541	4.000
CFRS-10.1243	150.166250	25.231389	0.5850	morphology	0.537	0.231	F814W	4.955	4.000
CFRS-10.1255	150.182500	25.229167	0.4670	morphology	1.268	0.470	F814W	6.281	4.000
CFRS-10.1262	150.203333	25.226667	0.5770	morphology	0.367	0.151	F814W	1.393	4.000

Table 4.2 (cont'd)

Object ID	<i>R.A.</i>	<i>Dec.</i>	z_{spec}	Selection	M_*	ΔM_*	Observing filter	R_e	ΔR_e	n	Δn
(1)	J2000 (deg)	J2000 (deg)	(4)	(5)	($10^{11} M_\odot$)	($10^{11} M_\odot$)	(8)	(kpc)	(kpc)	(11)	(12)
CFRS-10.1423	150.203333	25.209722	0.7240	morphology	0.087	0.065	F814W	7.228	4.000
CFRS-14.0207	214.566250	52.510278	0.5460	morphology	3.097	0.121	F814W	3.873	4.000
CFRS-14.0746	214.481667	52.531111	0.6750	morphology	0.681	0.287	F814W	3.428	4.000
CFRS-14.0807	214.473750	52.489722	0.9850	morphology	0.454	0.152	F814W	5.224	4.000
CFRS-14.0854	214.466667	52.491667	0.9920	morphology	1.167	0.395	F814W	5.176	4.000
CFRS-14.0854	214.466667	52.491667	0.9920	morphology	1.167	0.395	F814W	5.321	4.000
CFRS-14.1028	214.441667	52.509167	0.9880	morphology	1.675	0.883	F814W	3.516	4.000
CFRS-14.1028	214.441667	52.509167	0.9880	morphology	1.675	0.883	F814W	3.846	4.000
CFRS-14.1277	214.405417	52.447222	0.8100	morphology	1.340	1.027	F814W	4.624	4.000
CFRS-14.1311	214.399167	52.446111	0.8070	morphology	1.140	0.688	F814W	9.226	4.000
CFRS-14.1356	214.390000	52.446944	0.8310	morphology	0.139	0.136	F814W	4.426	4.000
CFRS-14.1415	0.7450	morphology	1.122	1.018	F814W	4.539	4.000
CFRS-14.1496	214.365000	52.446111	0.8990	morphology	0.435	0.392	F814W	2.056	4.000
CFRS-22.0501	334.492500	0.303056	0.4240	morphology	0.374	0.085	F814W	3.459	4.000
CFRS-22.0758	334.460833	0.283333	0.2940	morphology	0.425	0.121	F814W	6.622	4.000
CFRS-22.0890	334.445833	0.284444	0.8200	morphology	1.102	0.794	F814W	5.585	4.000
CFRS-22.1037	334.431667	0.293333	0.5500	morphology	0.440	0.198	F814W	2.023	4.000
CFRS-22.1279	334.404167	0.300556	0.5940	morphology	0.697	0.255	F814W	5.105	4.000
CFRS-22.1507	334.380417	0.306944	0.8200	morphology	1.094	0.458	F814W	3.793	4.000
GN/DEIMOS-17	189.469180	62.246950	0.5111	morphology	1.615	F606W	3.120	4.000
GN/DEIMOS-18	189.472170	62.248280	0.5107	morphology	1.649	F606W	3.475	4.000
GN/DEIMOS-27	189.484160	62.253710	0.1895	morphology	0.595	F606W	1.334	4.000
GN/DEIMOS-38	189.477450	62.257440	0.4563	morphology	0.535	F606W	1.413	4.000
GN/DEIMOS-43	189.488750	62.263250	0.4574	morphology	1.548	F606W	2.762	4.000
GN/DEIMOS-47	189.481870	62.261800	0.4588	morphology	1.354	F606W	5.519	4.000
GN/DEIMOS-63	189.506580	62.274180	0.4834	morphology	0.354	F606W	0.935	4.000
GN/DEIMOS-83	189.482540	62.282330	0.4415	morphology	0.341	F606W	0.997	4.000
GN/DEIMOS-951	189.159260	62.268050	0.8542	morphology	1.931	F606W	3.936	4.000
GN/DEIMOS-957	189.193160	62.274830	0.5033	morphology	0.748	F606W	1.971	4.000
GN/DEIMOS-959	189.179960	62.273640	0.8511	morphology	2.489	F606W	8.356	4.000
GN/DEIMOS-982	189.167370	62.282120	0.9422	morphology	0.814	F606W	0.935	4.000
GN/DEIMOS-996	189.254330	62.291560	0.7105	morphology	1.098	F606W	2.402	4.000
GN/DEIMOS-1020	189.248630	62.304060	0.4969	morphology	0.092	F606W	2.151	4.000
GN/DEIMOS-1021	189.277250	62.305100	0.8563	morphology	0.612	F606W	2.944	4.000
GN/DEIMOS-1032	189.282240	62.314280	0.2009	morphology	0.371	F606W	1.101	4.000
GN/DEIMOS-1046	189.189740	62.327510	0.2766	morphology	0.161	F606W	0.933	4.000
GN/DEIMOS-1061	189.212830	62.340850	0.7449	morphology	2.201	F606W	2.386	4.000
GN/DEIMOS-1062	189.296710	62.340170	0.6338	morphology	1.797	F606W	2.714	4.000
GN/DEIMOS-1066	189.305050	62.336100	0.6348	morphology	0.197	F606W	2.030	4.000
GN/DEIMOS-1076	189.251710	62.344420	0.8011	morphology	0.884	F606W	1.121	4.000
GN/DEIMOS-1084	189.254620	62.352550	0.7995	morphology	3.673	F606W	10.370	4.000
GN/DEIMOS-1088	189.289220	62.352760	0.9439	morphology	1.612	F606W	2.734	4.000
GN/DEIMOS-1089	189.260910	62.352520	0.7955	morphology	0.682	F606W	3.690	4.000
GN/DEIMOS-1107	189.274550	62.364060	0.3303	morphology	0.690	F606W	2.269	4.000
GN/DEIMOS-1215	189.103910	62.123790	0.9967	morphology	0.806	F606W	2.332	4.000
GN/DEIMOS-1236	189.134720	62.137370	0.8503	morphology	1.489	F606W	4.017	4.000
GN/DEIMOS-1261	189.084590	62.145680	1.0168	morphology	3.696	F606W	9.834	4.000
GN/DEIMOS-1267	189.033600	62.147470	0.4096	morphology	0.975	F606W	1.536	4.000
GN/DEIMOS-1278	189.151580	62.148510	0.5125	morphology	0.285	F606W	0.501	4.000
GN/DEIMOS-1285	189.086290	62.151870	1.0124	morphology	2.461	F606W	5.846	4.000
GN/DEIMOS-1286	189.137130	62.152680	0.8461	morphology	2.395	F606W	6.811	4.000
GN/DEIMOS-1287	189.132480	62.151820	0.8457	morphology	7.031	F606W	5.163	4.000
GN/DEIMOS-1292	189.120210	62.156510	0.5184	morphology	0.547	F606W	1.287	4.000
GN/DEIMOS-1297	189.128010	62.158120	1.0157	morphology	1.243	F606W	3.358	4.000
GN/DEIMOS-1303	189.094680	62.162850	0.7476	morphology	1.017	F606W	4.388	4.000
GN/DEIMOS-1308	189.073090	62.162780	0.8434	morphology	0.778	F606W	1.784	4.000
GN/DEIMOS-1323	189.024020	62.167500	0.9362	morphology	0.750	F606W	0.377	4.000

Table 4.2 (cont'd)

Object ID	<i>R.A.</i> J2000 (deg)	<i>Dec.</i> J2000 (deg)	z_{spec}	Selection	M_* ($10^{11} M_{\odot}$)	ΔM_* ($10^{11} M_{\odot}$)	Observing filter	R_e (kpc)	ΔR_e (kpc)	n	Δn
(1)	(2)	(3)	(4)	(5)	(6)	(7)	(8)	(9)	(10)	(11)	(12)
GN/DEIMOS-1328	189.071210	62.169840	0.8450	morphology	0.852	F606W	1.195	4.000
GN/DEIMOS-1329	189.035890	62.170060	0.6354	morphology	0.508	F606W	2.260	4.000
GN/DEIMOS-1336	189.083180	62.172340	0.4541	morphology	0.027	F606W	2.076	4.000
GN/DEIMOS-1342	189.030720	62.175410	0.6397	morphology	0.536	F606W	1.859	4.000
GN/DEIMOS-1346	189.033870	62.176640	0.6790	morphology	1.081	F606W	1.769	4.000
GN/DEIMOS-1353	189.017760	62.180530	0.8512	morphology	0.853	F606W	1.737	4.000
GN/DEIMOS-1354	189.135300	62.184810	0.5183	morphology	1.657	F606W	8.142	4.000
GN/DEIMOS-1362	189.013670	62.186430	0.6376	morphology	1.224	F606W	0.769	4.000
GN/DEIMOS-1364	189.146960	62.186080	0.4100	morphology	0.398	F606W	0.999	4.000
GN/DEIMOS-1373	189.056170	62.188500	1.1396	morphology	3.003	F606W	5.506	4.000
GN/DEIMOS-1385	189.025670	62.192240	0.7476	morphology	0.594	F606W	1.708	4.000
GN/DEIMOS-1399	189.153120	62.198900	0.5560	morphology	0.194	F606W	1.264	4.000
GN/DEIMOS-1403	189.040040	62.199660	0.7836	morphology	0.942	F606W	0.651	4.000
GN/DEIMOS-1417	189.063750	62.206030	0.3197	morphology	0.196	F606W	2.302	4.000
GN/DEIMOS-1430	189.115780	62.211320	0.5185	morphology	0.477	F606W	1.245	4.000
GN/DEIMOS-1436	189.155670	62.214550	0.4843	morphology	0.381	F606W	2.516	4.000
GN/DEIMOS-1440	189.104460	62.216910	0.5185	morphology	0.830	F606W	5.173	4.000
GN/DEIMOS-1441	189.095050	62.216630	0.4720	morphology	0.677	F606W	1.384	4.000
GN/DEIMOS-1454	189.073670	62.228970	0.5338	morphology	0.776	F606W	1.805	4.000
GN/DEIMOS-1463	189.082050	62.231450	0.2861	morphology	0.200	F606W	1.981	4.000
GN/DEIMOS-1464	189.069430	62.230880	0.6390	morphology	0.330	F606W	0.907	4.000
GN/DEIMOS-1485	189.142550	62.242540	0.5180	morphology	0.891	F606W	3.019	4.000
GN/DEIMOS-1491	189.103760	62.244110	0.6404	morphology	0.864	F606W	2.579	4.000
GN/DEIMOS-1503	189.112670	62.252650	0.7937	morphology	2.285	F606W	4.615	4.000
GN/DEIMOS-1506	189.080960	62.251550	0.7822	morphology	0.549	F606W	3.809	4.000
GN/DEIMOS-1543	189.122090	62.270440	0.8487	morphology	1.124	F606W	2.039	4.000
GN/DEIMOS-1558	189.155090	62.279420	0.8518	morphology	1.541	F606W	1.806	4.000
GN/DEIMOS-1559	189.155670	62.279930	0.9428	morphology	1.321	F606W	2.168	4.000
GN/DEIMOS-1577	189.158290	62.291390	0.5557	morphology	0.861	F606W	2.055	4.000
GN/DEIMOS-1633	189.011460	62.158810	0.8405	morphology	2.328	F606W	2.932	4.000
GN/DEIMOS-1685	188.980870	62.180890	0.4090	morphology	1.738	F606W	2.785	4.000
GN/DEIMOS-1706	189.007680	62.190730	0.9130	morphology	2.094	F606W	4.229	4.000
GN/DEIMOS-1709	188.952650	62.192180	0.8417	morphology	1.357	F606W	1.783	4.000
GN/DEIMOS-1718	189.002290	62.198840	0.5612	morphology	2.067	F606W	2.441	4.000
GN/DEIMOS-1740	188.984240	62.208260	0.6385	morphology	0.355	F606W	0.948	4.000
GN/DEIMOS-1741	189.002590	62.208780	0.4576	morphology	0.081	F606W	3.078	4.000
GN/DEIMOS-1743	188.956740	62.210550	0.4590	morphology	0.471	F606W	3.815	4.000
GN/DEIMOS-1764	188.992250	62.232410	0.4097	morphology	0.710	F606W	1.744	4.000
MS-10541649	164.263792	-3.587528	0.8310	spectroscopy	2.084 ^a	0.480	F775W	4.910	4.000
MS-10542409	164.272917	-3.633611	0.8310	spectroscopy	1.954 ^a	0.449	F775W	3.300	4.000
MS-10543058	164.264167	-3.629722	0.8310	spectroscopy	6.732 ^a	1.466	F775W	10.200	4.000
MS-10543768	164.260417	-3.627222	0.8310	spectroscopy	1.162 ^a	0.251	F775W	3.280	4.000
MS-10543910	164.258333	-3.630278	0.8310	spectroscopy	1.126 ^a	0.321	F775W	1.800	4.000
MS-10544345	164.255417	-3.630556	0.8310	spectroscopy	3.530 ^a	0.714	F775W	4.350	4.000
MS-10544520	164.249583	-3.627028	0.8310	spectroscopy	11.330 ^a	2.111	F775W	15.200	4.000
MS-10544705	164.251250	-3.624722	0.8310	spectroscopy	4.068 ^a	1.158	F775W	8.840	4.000
MS-10544926	164.248333	-3.628056	0.8310	spectroscopy	1.409 ^a	0.346	F775W	2.040	4.000
MS-10545280	164.243750	-3.621111	0.8310	spectroscopy	1.775 ^a	0.425	F775W	3.680	4.000
MS-10545298	164.243333	-3.621667	0.8310	spectroscopy	2.053 ^a	0.564	F775W	3.540	4.000
MS-10545347	164.240000	-3.611389	0.8310	spectroscopy	1.364 ^a	0.258	F775W	2.940	4.000
MS-10545450	164.236667	-3.628056	0.8310	spectroscopy	3.212 ^a	0.714	F775W	8.160	4.000
MS-10545529	164.239167	-3.618333	0.8310	spectroscopy	0.772 ^a	0.195	F775W	3.240	4.000
MS-10545577	164.237500	-3.613611	0.8310	spectroscopy	1.786 ^a	0.468	F775W	2.670	4.000
MS-10545666	164.233333	-3.650278	0.8310	spectroscopy	2.934 ^a	0.472	F775W	4.990	4.000
MS-10545756	164.232917	-3.599722	0.8310	spectroscopy	1.540 ^a	0.358	F775W	3.980	4.000
MS-10546036	164.232083	-3.635000	0.8310	spectroscopy	1.359 ^a	0.235	F775W	2.930	4.000
MS-10546301	164.230000	-3.620000	0.8310	spectroscopy	1.582 ^a	0.305	F775W	3.550	4.000

Table 4.2 (cont'd)

Object ID	<i>R.A.</i>	<i>Dec.</i>	z_{spec}	Selection	M_*	ΔM_*	Observing filter	R_e	ΔR_e	n	Δn
(1)	J2000 (deg)	J2000 (deg)	(4)	(5)	($10^{11} M_\odot$)	($10^{11} M_\odot$)	(8)	(kpc)	(kpc)	(11)	(12)
MS-10546688	164.224167	-3.638611	0.8310	spectroscopy	1.581 ^a	0.427	F775W	2.930	4.000
vdW-CDFS1	53.104832	-27.913926	1.0890	spectroscopy	1.086 ^a	0.150	F850W	2.830	4.000
vdW-CDFS2	53.095527	-27.909540	0.9640	spectroscopy	0.661 ^a	0.066	F850W	2.300	4.000
vdW-CDFS3	53.109558	-27.901400	1.0440	spectroscopy	0.647 ^a	0.138	F850W	1.000	4.000
vdW-CDFS4	53.080367	-27.901707	0.9640	spectroscopy	5.551 ^a	0.628	F850W	6.840	4.000
vdW-CDFS7	53.130708	-27.888653	1.1350	spectroscopy	2.233 ^a	0.385	F850W	5.770	4.000
vdW-CDFS12	53.188120	-27.827765	1.1230	spectroscopy	0.464 ^a	0.074	F850W	0.940	4.000
vdW-CDFS13	53.164995	-27.819334	0.9800	spectroscopy	0.965 ^a	0.086	F850W	2.200	4.000
vdW-CDFS14	53.225958	-27.817715	0.9840	spectroscopy	0.781 ^a	0.182	F850W	2.800	4.000
vdW-CDFS18	53.154977	-27.768907	1.0960	spectroscopy	2.996 ^a	0.666	F850W	3.970	4.000
vdW-CDFS20	53.041828	-27.725868	1.0220	spectroscopy	0.638 ^a	0.103	F850W	2.240	4.000
vdW-CDFS25	53.115417	-27.678802	0.9670	spectroscopy	0.412 ^a	0.061	F850W	0.860	4.000
vdW-CDFS29	53.125810	-27.658400	1.1280	spectroscopy	0.558 ^a	0.091	F850W	1.590	4.000
Rettura-CDFS-1	1.1282	photometry	2.573	F850LP	8.190
Rettura-CDFS-2	1.1460	photometry	0.934	F850LP	3.820
Rettura-CDFS-3	1.2150	photometry	0.852	F850LP	1.410
Rettura-CDFS-4	1.3270	photometry	1.447	F850LP	4.780
Rettura-CDFS-5	1.2970	photometry	1.048	F850LP	1.820
Rettura-CDFS-6	1.0970	photometry	1.290	F850LP	3.100
Rettura-CDFS-7	1.1005	photometry	1.149	F850LP	2.250
Rettura-CDFS-8	1.0954	photometry	1.447	F850LP	2.450
Rettura-CDFS-10	1.1188	photometry	0.538	F850LP	0.730
Rettura-CDFS-11	1.1580	photometry	0.525	F850LP	1.360
Rettura-CDFS-12	1.0939	photometry	0.372	F850LP	6.050
Rettura-CDFS-13	1.0999	photometry	0.295	F850LP	0.840
Rettura-CDFS-14	1.2150	photometry	0.381	F850LP	1.980
Rettura-CDFS-15	1.2220	photometry	0.538	F850LP	3.560
Rettura-CDFS-16	1.2220	photometry	0.550	F850LP	0.700
Rettura-CDFS-17	1.2210	photometry	0.458	F850LP	1.880
Rettura-CDFS-18	1.0974	photometry	0.372	F850LP	1.400
Rettura-CDFS-19	1.1860	photometry	0.513	F850LP	3.660
Rettura-CDFS-20	1.2220	photometry	1.447	F850LP	3.230
Rettura-CDFS-21	1.3460	photometry	1.024	F850LP	1.650
Rettura-CDFS-22	1.2210	photometry	1.320	F850LP	5.770
Rettura-CDFS-23	1.1790	photometry	0.725	F850LP	4.780
Rettura-CDFS-24	1.2980	photometry	0.408	F850LP	2.170
Rettura-CDFS-25	1.3142	photometry	1.024	F850LP	4.230
Rettura-CDFS-26	1.1230	photometry	1.290	F850LP	1.690
Rettura-CDFS-27	1.1780	photometry	0.661	F850LP	5.310
CL1252-1	193.250000	-29.436056	1.2354	photometry	1.447	F850LP	1.420
CL1252-2	193.227167	-29.444389	1.2306	photometry	0.381	F850LP	1.800
CL1252-3	193.244458	-29.452889	1.2297	photometry	0.661	F850LP	0.880
CL1252-4	193.203083	-29.462583	1.2353	photometry	0.661	F850LP	0.880
CL1252-5	193.240208	-29.468750	1.2475	photometry	0.490	F850LP	2.250
CL1252-6	193.226750	-29.456583	1.2472	photometry	1.024	F850LP	2.600
CL1252-7	193.225083	-29.455139	1.2384	photometry	1.624	F850LP	2.230
CL1252-8	193.224708	-29.452750	1.2312	photometry	0.742	F850LP	2.830
CL1252-9	193.213125	-29.458722	1.2351	photometry	2.633	F850LP	2.860
CL1252-10	193.216583	-29.462833	1.2318	photometry	0.427	F850LP	2.270
CL1252-11	193.238625	-29.450639	1.2295	photometry	0.468	F850LP	0.650
CL1252-12	193.227250	-29.454750	1.2378	photometry	3.635	F850LP	9.960
CL1252-13	193.226708	-29.454917	1.2343	photometry	3.240	F850LP	12.390
CL1252-14	193.217958	-29.455306	1.2455	photometry	1.447	F850LP	3.270
CL1252-15	193.218292	-29.455000	1.2342	photometry	1.149	F850LP	6.240
CL1252-16	193.276708	-29.450667	1.2373	photometry	0.417	F850LP	0.690
CL1252-17	193.230083	-29.454639	1.2455	photometry	1.624	F850LP	3.900
CL1252-18	193.206875	-29.467694	1.2382	photometry	0.603	F850LP	1.510

Table 4.2 (cont'd)

Object ID	<i>R.A.</i>	<i>Dec.</i>	z_{spec}	Selection	M_*	ΔM_*	Observing filter	R_e	ΔR_e	n	Δn
(1)	J2000 (deg)	J2000 (deg)	(4)	(5)	($10^{11} M_\odot$)	($10^{11} M_\odot$)	(8)	(kpc)	(kpc)	(11)	(12)
Newman-E1	214.985300	52.951300	1.0540	morphology	1.349	F814W	6.440	4.000
Newman-S1	334.352900	0.273400	1.1100	morphology	1.549	F814W	4.740	4.000
Newman-E2	214.970200	52.991100	1.1130	morphology	0.741	F814W	4.020	4.000
Newman-E3	215.006100	52.975500	1.1240	morphology	0.933	F814W	6.110	4.000
Newman-E4	214.984700	52.961400	1.1790	morphology	0.912	F814W	2.650	4.000
Newman-E5	214.981500	52.950100	1.2250	morphology	0.339	F814W	1.430	4.000
Newman-E6	215.035100	52.983000	1.2430	morphology	1.413	F814W	2.380	4.000
Newman-GN1	189.268100	62.226400	1.2530	morphology	1.072	F850W	1.290	4.000
Newman-E7	215.131900	53.016300	1.2620	morphology	0.724	F814W	1.570	4.000
Newman-E8	215.137100	53.017300	1.2620	morphology	0.741	F814W	1.380	4.000
Newman-GN2	189.063400	62.162300	1.2660	morphology	0.692	F850W	1.580	4.000
Newman-GN3	188.934500	62.206800	1.3150	morphology	0.933	F850W	3.440	4.000
Newman-S2	334.350200	0.303200	1.3150	morphology	0.447	F814W	2.470	4.000
Newman-S3	334.423300	0.225600	1.3940	morphology	1.122	F814W	2.500	4.000
Newman-GN4	189.113200	62.132500	1.3950	morphology	0.324	F850W	0.770	4.000
Newman-E9	215.121900	52.957600	1.4060	morphology	0.617	F814W	1.190	4.000
Newman-GN5	188.962500	62.228600	1.5980	morphology	0.955	F850W	0.680	4.000
TXS-0145+386-ER1	27.103333	38.905278	1.4533	photometry	1.824	F160W	6.650	4.300
B2-1018+34-ER2	155.322917	34.622778	1.4057	photometry	1.532	F160W	5.950	3.600
4C+15.55-ER2	246.305000	15.755833	1.4120	photometry	1.879	F160W	3.150	1.500
TXS-1211+334-ER1	183.517083	33.162778	1.5980	photometry	2.873	F160W	2.220	3.900
TXS-1812+412-ER2*	273.594583	41.218333	1.2900	photometry	1.632	F160W	3.630	1.500
MUNICS-S2F5-109	46.587917	-0.299444	1.2200	spectroscopy	5.941	0.941	F160W	3.777	0.059	2.780	0.040
MUNICS-S7F5-254	203.748333	16.819722	1.2200	spectroscopy	4.677	0.161	F160W	2.121	0.079	2.730	0.070
MUNICS-S2F1-357	46.717500	-0.002778	1.3400	spectroscopy	4.651	0.403	F160W	2.138	0.036	2.200	0.040
MUNICS-S2F1-389	46.616667	0.008889	1.4000	spectroscopy	2.151	0.860	F160W	2.606	0.129	5.000	0.200
MUNICS-S2F1-511	46.641667	0.041944	1.4000	spectroscopy	2.070	0.887	F160W	1.429	0.033	2.660	0.080
MUNICS-S2F1-142	46.652083	-0.050278	1.4300	spectroscopy	4.059	0.941	F160W	2.866	0.077	1.980	0.060
MUNICS-S7F5-45	203.604167	16.763611	1.4500	spectroscopy	3.575	1.102	F160W	3.693	0.119	1.530	0.040
MUNICS-S2F1-633	46.646250	0.078889	1.4500	spectroscopy	3.522	0.511	F160W	1.780	0.071	2.480	0.080
MUNICS-S2F1-443	46.632083	0.020278	1.7000	spectroscopy	3.575	1.478	F160W	4.190	0.764	2.800	0.300
GS-WFC3-3152	53.108542	-27.710083	1.3670	photometry	1.452	0.054	F160W	1.178	4.660	0.120
GS-WFC3-3237	53.149625	-27.711361	1.6150	photometry	0.591	0.054	F160W	1.864	7.540	0.300
GS-WFC3-3471	53.116417	-27.712694	1.6100	photometry	0.376	0.000	F160W	0.678	4.400	0.160
GS-WFC3-3812	53.152750	-27.716250	1.6140	photometry	0.538	0.000	F160W	1.356	3.120	0.070
GS-WFC3-4534	53.124958	-27.722972	1.6040	photometry	0.484	0.000	F160W	1.186	2.210	0.070
GS-WFC3-7202	53.026667	-27.765194	1.3290	photometry	0.914	0.000	F160W	2.519	2.290	0.040
SA02-1011	32.381625	-4.648322	1.1330	spectroscopy	0.300	0.088	F160W	1.150	0.017	2.120	0.105
SA02-1186	32.457958	-4.638733	1.0500	spectroscopy	2.254	0.415	F160W	6.960	0.261	3.690	0.076
SA02-1255	32.440000	-4.635331	1.3400	spectroscopy	1.663	0.536	F160W	1.450	0.023	1.190	0.063
SA02-1543	32.385292	-4.622736	1.1310	spectroscopy	0.637	0.223	F160W	3.890	0.101	2.090	0.061
SA02-1842	32.456583	-4.606497	1.3420	spectroscopy	0.899	0.213	F160W	1.500	0.104	1.470	0.270
SA02-1937	32.444042	-4.607644	1.3640	spectroscopy	1.629	0.458	F160W	8.410	1.044	2.090	0.174
SA02-2197	32.383750	-4.621353	1.1320	spectroscopy	0.912	0.193	F160W	6.310	0.348	2.950	0.105
SA12-5836	181.329542	-7.404200	1.3480	spectroscopy	0.524	0.467	F160W	0.490	0.005	4.140	0.138
SA12-6131	181.359542	-7.397550	1.3080	spectroscopy	0.748	0.098	F160W	0.740	0.006	2.100	0.056
SA12-6771	181.357708	-7.385306	1.2730	spectroscopy	0.200	0.121	F160W	2.170	0.020	1.290	0.036
SA12-7045	181.384708	-7.379644	1.2970	spectroscopy	0.168	0.166	F160W	0.540	0.005	2.720	0.097
SA12-7455	181.368333	-7.373400	0.8300	spectroscopy	0.135	0.025	F160W	0.890	0.005	2.060	0.033
SA15-5348	230.978667	-0.101358	0.9640	spectroscopy	1.138	0.170	F160W	4.620	0.682	1.450	0.587
SA15-6595	230.971083	-0.081708	1.7340	spectroscopy	0.933	0.282	F160W	1.070	0.018	3.370	0.111
SA15-6846	230.969167	-0.076708	0.9620	spectroscopy	0.527	0.121	F160W	1.600	0.014	2.600	0.045
SA15-7241	230.958375	-0.069739	0.7490	spectroscopy	0.501	0.162	F160W	2.860	0.078	2.100	0.083
SA22-0083	334.426125	0.216517	0.8610	spectroscopy	0.125	0.083	F160W	2.320	0.010	0.860	0.010
SA22-0128	334.385792	0.220278	1.0240	spectroscopy	0.355	0.225	F160W	2.330	0.403	0.740	1.934
SA22-0174	334.426375	0.223222	0.8270	spectroscopy	0.271	0.061	F160W	1.260	0.018	2.400	0.076
SA22-0315	334.441333	0.234364	0.9090	spectroscopy	0.491	0.113	F160W	1.540	0.023	3.610	0.072

Table 4.2 (cont'd)

Object ID	<i>R.A.</i>	<i>Dec.</i>	z_{spec}	Selection	M_*	ΔM_*	Observing filter	R_e	ΔR_e	n	Δn
(1)	J2000 (deg)	J2000 (deg)	(4)	(5)	($10^{11} M_\odot$)	($10^{11} M_\odot$)	(8)	(kpc)	(kpc)	(11)	(12)
SA22-0435	334.385500	0.245303	0.8770	spectroscopy	0.038	0.037	F160W	2.040	0.120	6.630	0.319
SA22-0455	334.455917	0.246961	1.3130	spectroscopy	0.352	0.096	F160W	0.420	0.011	4.560	0.285
SA22-0470	334.398750	0.248606	1.4700	spectroscopy	0.378	0.183	F160W	4.940	0.206	2.680	0.102
SA22-0510	334.382333	0.253017	0.8200	spectroscopy	0.324	0.098	F160W	2.730	0.194	8.170	0.355
SA22-0554	334.387542	0.256306	0.8750	spectroscopy	0.163	0.058	F160W	1.210	0.012	3.040	0.059
SA22-0674	334.452625	0.284897	1.4930	spectroscopy	1.161	0.350	F160W	1.600	0.078	4.720	0.248
SA22-0710	334.436000	0.280550	0.8790	spectroscopy	0.589	0.174	F160W	1.080	0.009	3.530	0.060
SA22-0721	334.440708	0.276750	1.4830	spectroscopy	1.545	0.409	F160W	2.810	0.128	4.860	0.174
SA22-0893	334.445500	0.263556	0.8750	spectroscopy	0.385	0.161	F160W	0.730	0.006	3.300	0.077
SA22-0948	334.397833	0.292828	1.3960	spectroscopy	0.705	0.273	F160W	2.090	0.221	4.530	0.261
SA22-2541	334.387250	0.233033	0.6170	spectroscopy	0.089	0.086	F160W	3.310	0.006	0.740	0.005
EGS-12008481	214.291901	52.477417	1.2300	photometry	3.236	K220	4.320	0.650	1.470	0.290
EGS-22022016	252.747849	34.891380	1.2700	photometry	3.090	K220	4.260	0.640	6.050	3.030
EGS-22035487	252.908646	34.986378	1.3600	photometry	3.981	K220	4.630	0.690	4.610	2.300
SA12-5592	181.342208	-7.409067	1.6230	spectroscopy	1.159	0.267	F160W	0.432	0.391	5.000	2.000
SA12-5869	181.339792	-7.402622	1.5100	spectroscopy	3.141	0.427	F160W	2.143	0.291	4.100	0.900
SA12-6072	181.302417	-7.399017	1.5760	spectroscopy	0.589	0.273	F160W	0.777	0.299	1.700	1.200
SA12-8025	181.355833	-7.356794	1.3970	spectroscopy	1.253	0.392	F160W	2.004	0.203	2.400	0.600
SA12-8895	181.309708	-7.337369	1.6460	spectroscopy	3.177	0.439	F160W	4.244	0.401	5.000	0.600
SA15-4367	230.927625	-0.119925	1.7250	spectroscopy	0.560	0.147	F160W	1.867	0.209	1.900	0.300
SA15-5005	230.941500	-0.105911	1.8450	spectroscopy	0.667	0.240	F160W	1.802	0.206	2.200	0.600
SA15-7543	230.936792	-0.060436	1.8010	spectroscopy	1.064	0.299	F160W	4.045	0.635	5.000	0.700
SA22-0189	334.448292	0.224208	1.4900	spectroscopy	2.851	0.985	F160W	3.094	0.248	3.200	0.700
SA22-1983	334.451708	0.269114	1.4880	spectroscopy	1.337	0.529	F160W	0.726	0.319	2.900	0.800
Saracco-GS-12965	1.0200	morphology	0.054	F850LP	0.610	0.020	3.800	0.200
Saracco-GS-11888	1.0400	morphology	0.501	F850LP	2.370	0.050	4.780	0.060
Saracco-GS-11539	1.1000	morphology	2.089	F850LP	4.200	0.400	4.000	0.100
Saracco-GS-9066	1.1900	morphology	0.251	F850LP	2.430	0.160	3.500	0.200
Saracco-GS-12789	1.2200	morphology	0.245	F850LP	2.200	0.200	5.000	0.300
Saracco-GS-12000	1.2200	morphology	0.240	F850LP	2.400	0.070	5.000	0.000
Saracco-GS-9369	1.3000	morphology	0.501	F850LP	1.980	0.150	4.700	0.200
Saracco-GS-11804	1.9100	morphology	0.912	F850LP	2.860	0.160	4.500	0.000
Saracco-GS-2	0.9600	morphology	1.175	F850LP	5.690	0.130	5.710	0.060
Saracco-GS-13	0.9800	morphology	0.794	F850LP	3.710	0.040	5.460	0.030
Saracco-GS-20	1.0200	morphology	0.912	F850LP	3.850	0.090	5.380	0.060
Saracco-GS-23	1.0400	morphology	0.324	F850LP	2.800	0.080	3.900	0.070
Saracco-GS-3	1.0400	morphology	0.380	F850LP	1.390	0.020	4.870	0.060
Saracco-GS-11	1.0900	morphology	0.832	F850LP	2.400	0.200	5.000	0.020
Saracco-GS-8	1.1200	morphology	0.417	F850LP	2.070	0.040	5.000	0.000
Cassata-HUDF-22704	53.153799	-27.774587	1.3840	photometry	0.269	F160W	0.500	2.650
Cassata-HUDF-23555	53.158810	-27.797155	1.9210	photometry	0.355	F160W	0.440	1.970
Cassata-HUDF-24279	53.163005	-27.797655	1.9800	photometry	0.229	F160W	0.370	1.630
Cassata-HUDF-24626	53.165159	-27.785869	1.3170	photometry	0.677	F160W	3.690	7.420
GMASS-1498	53.174644	-27.753372	1.8480	spectroscopy	0.708	F850LP	1.010	0.200	1.500	0.200
GMASS-2148	53.151238	-27.713738	1.6090	spectroscopy	1.000	F850LP	1.200	0.240	3.700	0.300
GMASS-2239	53.130482	-27.721159	1.4150	spectroscopy	0.398	F850LP	2.160	0.430	2.200	0.200
GMASS-2355	53.059647	-27.725803	1.6100	spectroscopy	0.316	F850LP	0.810	0.160	2.200	0.200
GMASS-2361	53.108555	-27.710157	1.6090	spectroscopy	1.000	F850LP	1.130	0.230	4.100	0.400
GMASS-2470	53.142155	-27.711268	1.4160	spectroscopy	0.794	F850LP	1.810	0.360	4.200	0.300
GMASS-2543	53.149647	-27.711384	1.6120	spectroscopy	0.912	F850LP	1.410	0.280	2.200	0.300
GMASS-2599	53.176407	-27.701158	1.9810	spectroscopy	0.813	F850LP	1.430	0.290	1.000	0.500
HUDF-8238	53.153750	-27.774583	1.3900	photometry	0.832	0.374	F850LP	2.800	1.200	8.200	1.500
HUDF-4950	53.125000	-27.790778	1.5500	photometry	6.737	3.493	F850LP	5.600	0.900	4.300	0.400
HUDF-1025	53.179167	-27.812528	1.7300	photometry	0.915	0.333	F850LP	0.740	0.100	4.200	0.500
HUDF-3523	53.140417	-27.797528	1.7600	photometry	0.765	0.208	F850LP	2.800	1.100	9.000	1.600
HUDF-3650	53.158750	-27.797167	1.9100	photometry	1.664	0.790	F850LP	0.790	0.080	4.700	0.600
HUDF-1446	53.163333	-27.809000	2.6700	photometry	0.782	0.266	F850LP	0.760	0.120	0.800	0.200

Table 4.2 (cont'd)

Object ID	<i>R.A.</i>	<i>Dec.</i>	z_{spec}	Selection	M_*	ΔM_*	Observing filter	R_e	ΔR_e	n	Δn
(1)	J2000 (deg)	J2000 (deg)	(4)	(5)	($10^{11} M_\odot$)	($10^{11} M_\odot$)	(8)	(kpc)	(kpc)	(11)	(12)
1030-1813	157.712917	5.426667	2.5600	spectroscopy	2.710	0.672	F160W	0.760	0.060	1.900	0.500
1030-2559	157.667083	5.442778	2.3900	spectroscopy	1.129	0.366	F160W	0.920	0.180	2.300	0.600
1256-0	193.748333	1.191667	2.3100	spectroscopy	2.183	0.575	F160W	0.780	0.170	3.200	0.900
1256-1967	193.857083	1.056944	2.0200	spectroscopy	1.333	0.215	F160W	1.890	0.150	3.400	0.100
1256-142	193.761250	1.125556	2.3700	spectroscopy	1.731	0.581	F160W	0.930	0.040	0.900	0.300
ECDFS-5856	53.055417	-27.873889	2.5600	spectroscopy	1.473	0.414	F160W	1.420	0.350	4.500	0.400
ECDFS-11490	53.187500	-27.719167	2.3400	spectroscopy	0.511	0.059	F160W	0.470	0.030	2.800	0.800
HDFS1-1849	338.408333	-60.554167	2.3100	spectroscopy	1.866	0.538	F160W	2.380	0.110	0.500	0.200
HDFS2-2046	337.845417	-60.542778	2.2400	spectroscopy	0.758	0.269	F160W	0.490	0.020	2.300	0.800

^aBased on dynamical masses M_{dyn} and the $M_{\text{dyn}} \sim 1.4 \times M_*$ relation (van der Wel et al., 2008).

Chapter 5

Extragalactic Fields Optimized for Adaptive Optics

This chapter contains the article published in The Publications of the Astronomical Society of the Pacific, Volume 123, issue 901, pp. 348-365 (2011) and authored by:

Ivana Damjanov, Roberto G. Abraham, Karl Glazebrook, Peter McGregor, Francois Rigaut, Patrick J. McCarthy, Jarle Brinchmann, Jean-Charles Cuillandre, Yannick Mellier, Henry Joy McCracken, Patrick Hudelot, David Monet

Reproduced by the permission of the Astronomical Society of the Pacific.

5.1 Abstract

In this paper we present the coordinates of 67 $55' \times 55'$ patches of sky which have the rare combination of both high stellar surface density ($\geq 0.5 \text{ arcmin}^{-2}$ with $13 < R < 16.5 \text{ mag}$) and low extinction ($E(B - V) \leq 0.1$). These fields are ideal for adaptive-optics based follow-up of extragalactic targets. One region of sky, situated near Baade's Window, contains most of the patches we have identified. Our optimal field, centered at $R.A. : 7^{\text{h}}24^{\text{m}}3^{\text{s}}$, $Dec. : -1^{\circ}27'15''$, has an additional advantage of being accessible from both hemispheres. We propose a figure of merit for quantifying real-world adaptive optics performance, and use this to analyze the performance of multi-conjugate adaptive optics in these fields. We also compare our results to those that would be obtained in existing deep fields. In some cases adaptive optics observations undertaken in the fields given

in this paper would be orders of magnitude more efficient than equivalent observations undertaken in existing deep fields.

5.2 Introduction

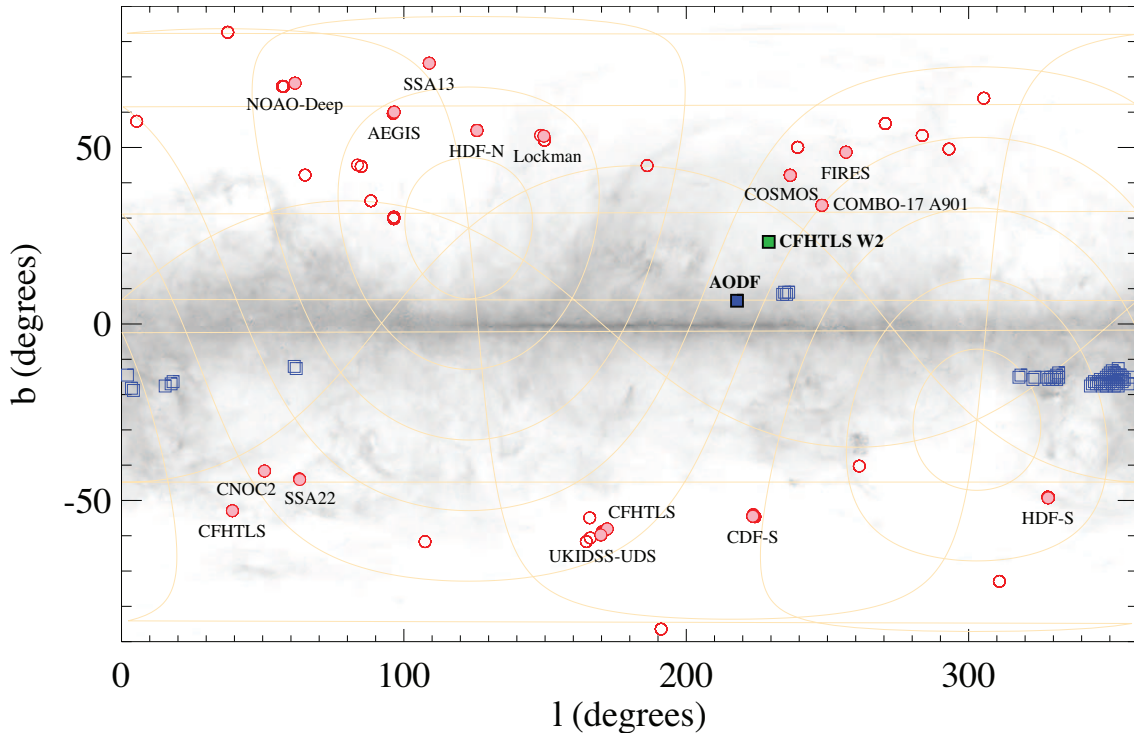


Figure 5.1 The galactocentric coordinates of existing deep fields (red circles) and the locations of the fields better suited for AO observations presented in Table 5.1 of this paper (blue squares, see § 5.4 for details). The location of the fields has been overplotted on the dust emission map from the Schlegel, Finkbeiner & Davis (1998) study. Labeled existing deep fields are indicated with filled circles. The green square denotes a 1 square degree region within the CFHTLS W2 field (§ 5.6.2). The field labeled ‘AODF’ is our suggested optimal field whose properties are studied in detail in Sections 5.5 and 5.6.

Our understanding of the high redshift universe has been revolutionized by deep fields, several of which have been extensively surveyed at all accessible wavelengths. Figure 5.1 shows an up-to-date summary of the locations of all existing deep fields (red circles). These fields have been primarily used to study galaxy formation and evolution out to very high redshifts (Cowie et al., 1995; Yee et al., 2000; Labbé et al., 2003; Bell et al.,

2004b; Egami et al., 2004; van Dokkum et al., 2004; Arnouts et al., 2007; Davis et al., 2007; Scoville et al., 2007; Bouwens et al., 2010; Ono et al., 2010). Because galaxies at such high redshifts are typically < 1 arcsec in size, kinematical investigations of galaxies in these fields require adaptive optics (AO) spectroscopy (Law et al., 2009; Förster Schreiber et al., 2009). The promise of such observations has been held out as an exciting next step for over a decade (e.g., Ellis, 1997). Unfortunately, it is now clear that only very limited AO observations are going to be undertaken in any existing deep fields.

Coupling integral-field spectroscopy to AO is crucial for understanding the formation of massive galaxies, particularly disks, since at high redshift it has proven difficult for slit spectroscopy to reliably identify kinematic disks as kinematic and morphological axes are not necessarily correlated (Erb et al., 2006). Even at intermediate redshift ($z \sim 0.6$), it has been demonstrated that galaxies are already kinematically complex and that 3D integral field spectroscopy (IFS) is essential to physical understanding and kinematic modeling (Rix et al., 1997; Flores et al., 2006). At the highest redshifts AO IFS observations by some groups have given different results compared to non-AO observations of other groups. For example Laser Guide Star (LGS) AO observations with kpc resolution (Law et al., 2009) show that $z = 2 - 3$ Lyman-break selected galaxies have high intrinsic velocity dispersions and no significant rotational gradients about a preferred kinematic axis. Förster Schreiber et al. (2009) found similarly high velocity dispersions but a much greater incidence of disk rotation in a predominantly non-AO dataset of predominantly near-IR selected galaxies. It remains inconclusive whether such differences arise from a difference in sample (massive vs low mass galaxies) or the fact that the non-AO data has seven times poorer resolution on average in natural seeing. This is an important question: physical differences in kinematics at high redshift may diagnose the prevalence of fast gas accretion along cold flows in the early Universe (e.g., Bournaud et al., 2007), but they may also arise from sample selection effects or observational limitations (for example Green et al. (2010) suggest it is simply the high-star-formation rates which drive the large velocity dispersions). Most IFS observations at high redshift are still done without AO due to the technical difficulties of AO and also to the practical difficulties of finding enough targets near sufficiently bright stars in existing deep field samples.

The next stage in the development of this field is to complement kinematical studies by probing chemical abundance gradients at a sub-kpc scale in star-forming galaxies, and to extend existing kinematical investigations to encompass more representative galaxies.

This requires AO systems to be operating more efficiently (i.e. without performance limitation imposed by natural guide star availability) and, ultimately, to multiplex if truly large samples are to be obtained. A step in this direction is already being taken with the MASSIV survey on the VLT, which targets star-forming galaxies in the redshift range $1 < z < 2$ with SINFONI (Epinat et al., 2009; Queyrel et al., 2009). The targets are more representative than those being probed by SINS, with median stellar masses of $\sim 10^{10} M_{\odot}$ and median star formation rates of $\sim 10 M_{\odot} \text{ yr}^{-1}$ (the corresponding values for SINS are $\sim 10^{10.5} M_{\odot}$ and $\sim 30 M_{\odot} \text{ yr}^{-1}$, respectively). However, most of the SINFONI data acquired during the MASSIV survey are seeing-limited leading to a final median spatial resolution of $\sim 0.6 - 0.7''$ with only 25% of the MASSIV sample presently being observed with adaptive optics. Of these AO targets only a few are being acquired with the smallest pixel size ($0.05''$). The main reasons are (i) the limitations in the availability of natural guide stars which precludes usefully observing at finer available pixel scale, and (ii) the difficulty to reach the depth required to probe the low-surface brightness component of galaxies in a reasonable exposure time with the smallest pixel size. This latter point leads to expectations of considerable progress in this subject with the advent of 30m-class Extremely Large Telescopes (ELTs).

A basic problem with undertaking AO in existing deep fields, even with laser guide stars, is that one still needs at least one reasonably proximate natural guide star to supply the information needed for tip-tilt correction (Rigaut & Gendron, 1992). In contrast, two of the main selection criteria when identifying deep fields have been that they contain as few bright stars as possible to avoid light scattering contamination and saturation in long exposures, and that they lie in regions of low Galactic extinction (e.g., Alcal et al., 2004). Thus all existing deep fields are near the Galactic poles, where the density of suitable natural guide stars is near a minimum. For example, Davies et al. (2008) report that only 1% of the Lyman break galaxy sample of Mannucci (2007) are accessible to the VLT laser guide star system (Bonaccini et al., 1999): the loss of 75% of the targets is due to the absence of suitably close natural guide stars, while additional 25% are lost after suitable color cuts and elimination of systems at redshifts obscured by strong OH features. The situation is similar with Gemini, whose AO system has similar sky coverage (Ellerbroek & Tyler, 1998). Even with the upcoming Gemini Multi-Conjugate AO system (MCAO), the H -band sky coverage at the galactic poles will only be around 15% (Rigaut et al., 2000), and large benefits for MCAO emerge from having more than

the minimum number of natural guide stars. This is because the geometry of the guide stars on the sky impacts the uniformity of Strehl ratio (Flicker & Rigaut, 2002).

The issue of guide star rarity in deep fields becomes prominent in cases where target source density is low. This is often the case for extragalactic programs which focus on unusual objects. For example, many of the key projects described in the *James Webb Space Telescope* (JWST) Design Reference Mission (Gardner et al., 2006) rely on either extreme depth or serendipitous lines-of-sight. If such JWST observations are to be synergistic with ground-based AO follow-up, in particular with next generation telescopes like TMT or E-ELT, they cannot be undertaken efficiently in any existing deep field. It would be disappointing indeed if only 1%–10% of rare targets imaged with JWST in a deep field could be followed-up with a ground-based integral field units (IFU). It is becoming clear that existing and planned AO systems are set to enable transformative high redshift science, but they will do so only in the regions of the sky in which they are effective. It is arguable that no existing deep field is suitable for efficient extragalactic AO work (though of course the cost of obtaining ancillary data equivalent to that already obtained in existing deep fields may overwhelm the gains obtained from high-efficiency adaptive optics).

In this paper we report on the results we have obtained in searching for those fields on the sky most suitable for high-efficiency extragalactic adaptive optics observations. In § 5.3 we describe the important characteristics of deep fields in the context of adaptive optics observations, such as the acceptable level of dust extinction, field size, and magnitude range of natural guide stars. In § 5.4 we describe our attempts to identify the most suitable areas on the sky for undertaking extragalactic AO work, which is based on the strategy of combining information from all-sky stellar density and extinction maps. Our preferred ‘AO-friendly’ field and its first imaging results are described in § 5.5. In the following § 5.6 we define a figure of merit for adaptive optics and use this to compare the efficiency of AO observing in the proposed fields relative to the efficiency in representative deep fields. Our conclusions are summarized in § 5.7. All magnitudes in this paper are based on the Vega system.

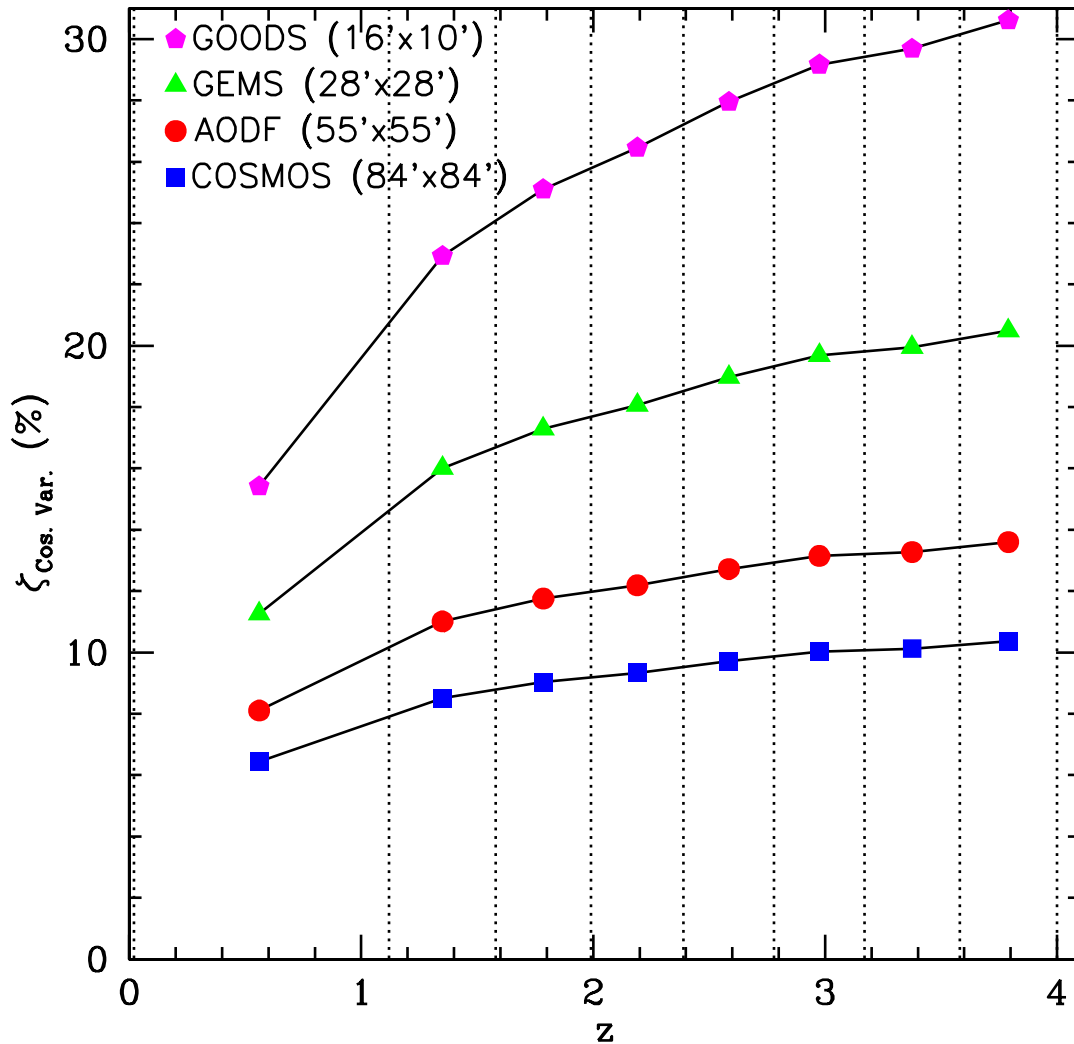


Figure 5.2 Cosmic variance, quantified using Eq. 5.1, as a function of redshift for four fields covering different areas on the sky. Redshifts of presented points correspond to median values for redshift ranges indicated with dotted lines. The effect of small-scale inhomogeneity on the field size we propose (~ 1 square degree, denoted as AODF) is comparable to the COSMOS field cosmic variance, and much less prominent than in the other two (smaller) fields, GEMS and GOODS.

5.3 Desirable characteristics of extragalactic fields optimized for adaptive optics

In this section we consider the desirable characteristics of extragalactic fields optimized for adaptive optics. The relevant considerations include the maximum acceptable level of extinction from the intergalactic medium, the minimum useful area on the sky, and number density and magnitude range of available natural guide stars. We will consider each of these factors in turn, and discuss the importance of each of these factors using very general principles, in order to look for considerations that will remain relevant for future AO systems.

5.3.1 Extinction

Although most adaptive optics is undertaken in the near-infrared (NIR) where extinction is lower than at visible wavelengths, it is clear that for any number of reasons, including reliability of photometric redshifts and ‘future-proofing’ the fields so as to make them useful when AO work moves to shorter wavelengths, that the ideal fields will lie in regions of low Galactic extinction. As any glance at the night sky will attest, patchy extinction can be rather high in regions with high star counts. It is therefore important to define an upper limit to the acceptable extinction in order to exclude unsuitable fields. A value of $E(B-V) \sim 0.15$ mag is a good starting point, because Fukugita et al. (2004) and Yasuda et al. (2007) show that galactic extinction estimates become fairly unreliable in regions with $E(B-V) \gtrsim 0.15$ mag. To err on the conservative side, in this paper we will use an upper limit of $E(B-V) = 0.1$ mag on the mean extinction as a constraint when exploring star count surface density maps for suitable fields. We note that $E(B-V) = 0.1$ mag corresponds to $A_V = R_V \times E(B-V) \sim 0.3$ mag at visible wavelengths, and that this is a factor of three to ten times higher than the corresponding extinction in NIR passbands used by current AO systems.

5.3.2 Field size

The next factor to consider is the required size of the field. For extragalactic fields, the area of the field is driven by a desire to minimize the impact of cosmic variance, because

scale-dependent inhomogeneity is often the dominant source of error in measurements derived from galaxy populations within a survey volume. The survey volume naturally depends on the area on the sky and the chosen redshift range, but for concreteness we will assume that most extragalactic work will explore a range of redshifts from $z = 0$ to $z = 4$, which encompasses most of the star-formation history of the Universe. For such surveys, areas on the order of a square degree are needed in order to maintain fractional errors on number counts near the 10% level, and to probe a wide range of cosmic structures. This is fairly easy to demonstrate using on-line tools such as the Cosmic Variance Calculator¹ described in Trenti & Stiavelli (2008), but an even simpler way to show this is to use the analytic expressions provided by Driver & Robotham (2010) to estimate and compare cosmic variance for different field sizes. These authors employed counts of galaxies near the characteristic break in the luminosity function (M^*) in the Sloan Digital Sky Survey Data Release 7 (SDSS DR7, Abazajian et al., 2009) to derive an empirical expression connecting cosmic variance and survey volume. Assuming a single sight-line and a rectangular geometry, the fractional error in the counts of M^* galaxies is given by:

$$\begin{aligned} \zeta = & (1 - 0.03(\sqrt{(A/B)} - 1)) \\ & \times (219.7 - 52.4(\log_{10} [A \cdot B \cdot 291.0])) \\ & + 3.21(\log_{10} [A \cdot B \cdot 291.0]^2)) \\ & \sqrt{C/291.0}. \end{aligned} \quad (5.1)$$

where A , B , and C are the median redshift transverse lengths and the radial depth of the survey, respectively, expressed in units of $h_{0.7}^{-1}$ Mpc. (Note that the derived cosmic variance is for $M^* \pm 1$ mag population only and will take higher values for more massive halos, see e.g., Moustakas & Somerville, 2002). Results computed using this equation are presented in Figure 5.2, which shows the calculated cosmic variance for a number of surveys, and compares these with our proposed field size of around one square degree (actually $55' \times 55'$, for technical reasons described below).

Figure 5.2 shows that the calculated cosmic variance for our proposed field size results in fractional counting errors of around 10 – 15% (per unit redshift interval) for counts of

¹ <http://casa.colorado.edu/~trenti/CosmicVariance.html>

M^* galaxies at redshifts between $z = 1$ and $z = 4$. This is only slightly higher than for the COSMOS field (Scoville et al., 2007), but quite significantly better than for smaller volume survey fields, such as GEMS (Rix et al., 2004) and GOODS (Dickinson et al., 2003a). On this basis alone we would argue that something around square degree is probably the right minimum size for a contiguous area survey field intended to allow a broad range of investigations using adaptive optics, although another important factor is that a survey of this size will contain many thousands of strong line emitting objects, which are obvious targets for present-generation AO systems.

We have computed the surface density of strong H_α line emitters (which we define to be $F_{H_\alpha} > 10^{-16}$ erg cm² s⁻¹, corresponding to the flux density of bright line emitters in Förster Schreiber et al., 2009; Law et al., 2009) on the basis of direct measurement (Villar et al., 2008; Shim et al., 2009) as well as using indirect estimates scaled from UV flux (Bouwens et al., 2009) and measurements of [OII] (Cooper et al., 2007). By incorporating all the available information we estimate this value to be 2–5 H_α line emitters with flux $> 10^{-16}$ erg cm² s⁻¹ Å⁻¹ per square arcmin at $1 < z < 1.5$, declining to 1–2 per square arcmin in the redshift interval $2 < z < 2.5$. The deep fields proposed in this paper will thus have around 10,000 suitable targets for AO-based follow-up. A significant fraction of these will be lost for various reasons (e.g., if H_α lies on an airglow emission line, Davies et al. 2008), and a small number of remaining objects will still lack suitable guide stars (see § 5.6). However, thousands of AO-accessible targets will remain, presenting a multiple order-of-magnitude change from the current situation.

5.3.3 Guide star limitations

We now explore the brightness of natural guide stars needed for effective use of adaptive optics. Our focus will be on the the following three classes of AO systems:

- Case 1: Laser-assisted adaptive optics systems on 8m-class telescopes, for which natural guide stars are needed to supply tip-tilt corrections. Such systems will define the state of the art for the next few years.
- Case 2: Ground-layer adaptive optics systems for 4m-class telescopes. Such systems are now being proposed as a means of revitalizing 4m-class facilities (e.g CFHT IMAKA, Lai et al., 2008). These facilities will also require natural guide stars for tip-tilt correction.

- Case 3: AO systems on 30m-class telescopes, some designs for which rely on AO for routine operation. In this case we mainly seek fields with an abundance of natural guide stars bright enough to feed laser-*unassisted* AO systems. Laser beacons may not be available at all times, and the existence of extragalactic fields in which they are not essential may be extremely attractive for telescopes that heavily emphasize AO.

We will begin by first outlining the general problem before focusing on the parameter space appropriate to the specific cases above. As will be shown below, in practise it is Cases 2 and 3 that drive our chosen magnitude limits.

In order to function an AO system needs to capture photons from a star, compute a correction, and apply this correction to an optical surface. The frequency over which an AO system must operate is set by the velocity of the atmosphere and the atmospheric coherence length. The coherence length is the length scale over which the index of refraction of the atmosphere is effectively constant, and is typically around 10 cm at a good site. Wind speeds in the upper atmosphere are around 20 m/s, so it typically takes around 0.005s for a patch of atmosphere to move a coherence length (Roggemann & Welsh, 1996). The minimum frequency of an AO system is therefore around 200 Hz, although in reality one would want to both Nyquist sample the signal and allow time for actuator lag in applying a correction, so a realistic minimum is around 1 kHz.

How many photons from a natural guide star are needed in this time depends on the specific type of correction, but we can bracket our analysis by considering two extremes: (i) tip-tilt correction, for which relatively faint stars suffice, and (ii) full correction to obtain diffraction-limited performance, for which bright stars are needed.

A zeroth magnitude star has a R -band flux of 3080 Jy at the top of the atmosphere², corresponding to 2.02×10^{11} photon/m²/s (Bessell, 1979). Thus an 8m telescope captures ~ 600 R -band photons from an 18th magnitude star in one millisecond. In the foreseeable future no AO system will have a quantum efficiency approaching unity, but even with an end-to-end efficiency of 20% over 100 photons will remain, which is ample for obtaining a reasonable centroid. Thus, at least in principle, an AO system on an 8m telescope can use $R = 18$ mag stars for tip-tilt corrections. Since the number of photons from a star imaged with a 30m telescope is about fourteen times greater than for an 8m telescope, a 30m

²For concreteness we consider the brightness of guide stars at visible wavelengths, though the argument can be generalized to stars at arbitrary wavelength.

telescope can do tip-tilt corrections on guide stars down to around $R = 21$ mag. On the other hand, a 4m telescope needs stars of about $R = 16.5$ mag for tip-tilt corrections. We emphasize that these numbers are all for rather idealized AO systems. For example, in the real-world situation of the Gemini Altair AO system, tip-tilt reference stars of around $R \sim 16.5$ mag (over a magnitude brighter than the somewhat ideal case discussed above) are found to be highly desirable for high-performance AO operation.

Much brighter natural guide stars are needed for use with natural guide AO star systems that attempt to achieve diffraction-limited performance. In this case the size of relevance is not the full aperture of the telescope, but rather the sub-aperture defined by the coherence length of the atmosphere which in turn drives the number of needed actuators. An $R = 13$ mag star supplies ~ 10 photons in 1 ms to a 10 cm diameter sub-aperture. The number of photons per bin needed to reliably compute a wavefront depends critically on factors such as the read noise of the detector, but ten photons per coherence-length sized patch on the pupil is a reasonable lower limit. Note that in the case of diffraction-limited AO (and unlike the case with tip-tilt correction), having a larger telescope does not gain one a fainter magnitude limit for natural guide stars, and in fact AO becomes harder because the system requires more actuators. We also note that the presence of bright stars ($R \lesssim 14$ mag) in the field *with* AO correction can potentially cause problem for infrared (IR) detectors by leaving long-lasting (up to an hour) residual flux. Although this would affect imaging in case when AO correction is applied across a wide field of view, the main motives for developing an AO-friendly deep field (see Sections 5.2 and 5.6) are high resolution IFU or multi-object spectroscopic surveys, that would not be influenced.

On the basis of the considerations just given, our search for locations on the sky suitable for extragalactic adaptive optics focuses on stars in the magnitude range $13 < R < 16.5$ mag. The bright end is set by the apparent magnitude of stars needed to supply guide stars for natural guide star AO systems (independent of telescope aperture), which is essentially Case 3 above. The faint end is set by the apparent magnitude of stars needed to supply tip-tilt reference stars for real-world operation of existing AO systems on 8m-class telescopes (Case 1) and for ideal-case laser-based ground-layer AO with 4m-class telescopes (Case 2 above).

5.4 Identification of the suitable fields for Adaptive Optics

In order to find the regions on the sky with the properties we have just described, we rely on full sky reprocessed composites of the COBE/DIRBE and IRAC/ISSA dust maps (Schlegel et al., 1998) and the UCAC2 astrometric catalog of $\sim 5 \times 10^7$ stars with declination in the $[-90 \text{ deg}, +(40 - 52) \text{ deg}]$ range (Zacharias et al., 2004). We constructed a full sky map of star count surface density for UCAC2 stars in the range 13 – 16.5 mag using the HEALPIX data analysis package (Gorski et al., 2005) that performs pixelization of the sphere with equal area pixels. Two maps have been produced: one with the resolution of 6'871 to match the resolution of the available HEALPIX map of Galactic reddening $E(B - V)$ and the other (see Figure 5.3) with the coarser sampling of 55' (the HEALPIX resolution that is closest to the $1^\circ \times 1^\circ$ field size, see § 5.3.2). The resolution of the existing $E(B - V)$ map was degraded to match the 55' resolution of the star counts surface density map by taking the average extinction value for each cell. The coarse resolution extinction and star count maps are both shown as panels at the top-left and top-right of Fig. 5.3. Note that the UCAC2 catalog has a gap in coverage at high declination (shown in gray in the figure), but any AO-optimized fields which might exist at these very high declinations would be generally unsuitable anyway. Any such fields would be inaccessible from Chile and be at quite high airmass most of the time for major northern hemisphere observatories (including those on Mauna Kea).

Before proceeding with a detailed analysis, it is instructive to note that many positions in the sky likely to be suitable for our purposes can be identified easily by simply looking for maxima in a map obtained by multiplying the stellar density map by the inverse of the extinction map. This is shown as the large bottom panel in Figure 5.3. Local maxima in this map do not necessarily define regions suitable for AO, because some local maxima correspond to regions with low star counts but extremely low extinction. However, this figure acts as a natural starting point for the next step in our analysis.

Having identified candidate fields using the analysis just described, we then looked at all the candidate fields individually to try to better understand their characteristics. To be explicit, we first identified all HEALPIX cells whose 13 < R < 16.5 mag stellar density Σ_{sc} was $\Sigma_{\text{sc}} > 0.5 \text{ arcmin}^{-2}$ and whose extinction was $E(B - V) \leq 0.1$. We found 442 one square degree cells that met these criteria, and these were then examined

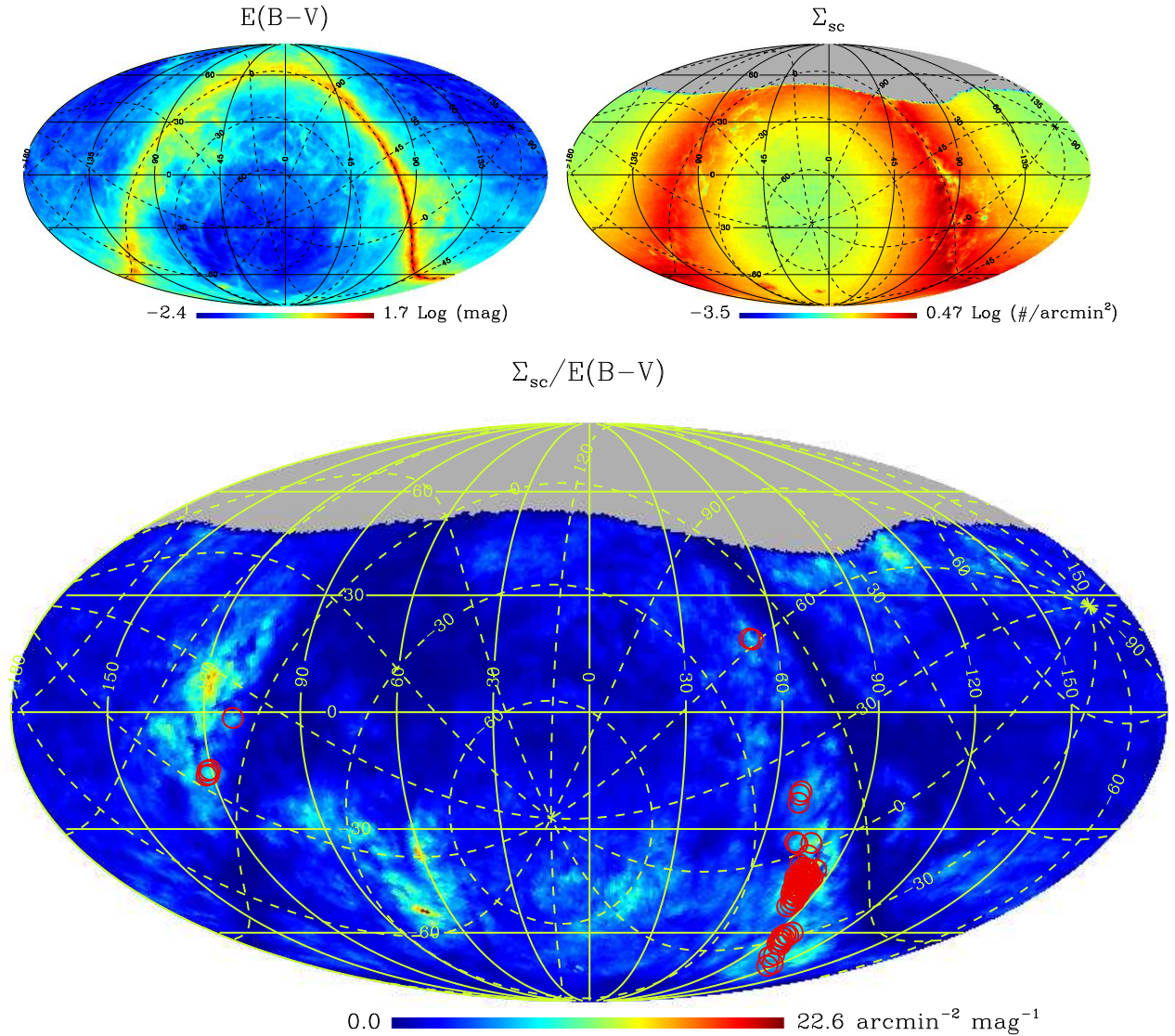


Figure 5.3 (*Top left:*) An all sky map of extinction, scaled logarithmically. The solid line grid corresponds to the celestial coordinate system with RA in degrees increasing to the left. Zero degrees lies at the center of the figure. A Galactic coordinate system is over-plotted with dashed lines. (*Top right:*) The corresponding map of star count surface density for stars in the 13 – 16.5 magnitude range. The region shown in gray corresponds to a high declination gap in coverage in the UCAC2 stellar catalog. As noted in the text, any AO-friendly fields which might exist at very high declination would be unsuitable for other reasons. (*Bottom:*) A map constructed by multiplying the map at the top left by the inverse of the map at the top right. Maxima in this figure correspond to potentially interesting locations for undertaking extragalactic adaptive optics observations. Red circles present the positions of 67 fields well-suited to extragalactic AO.

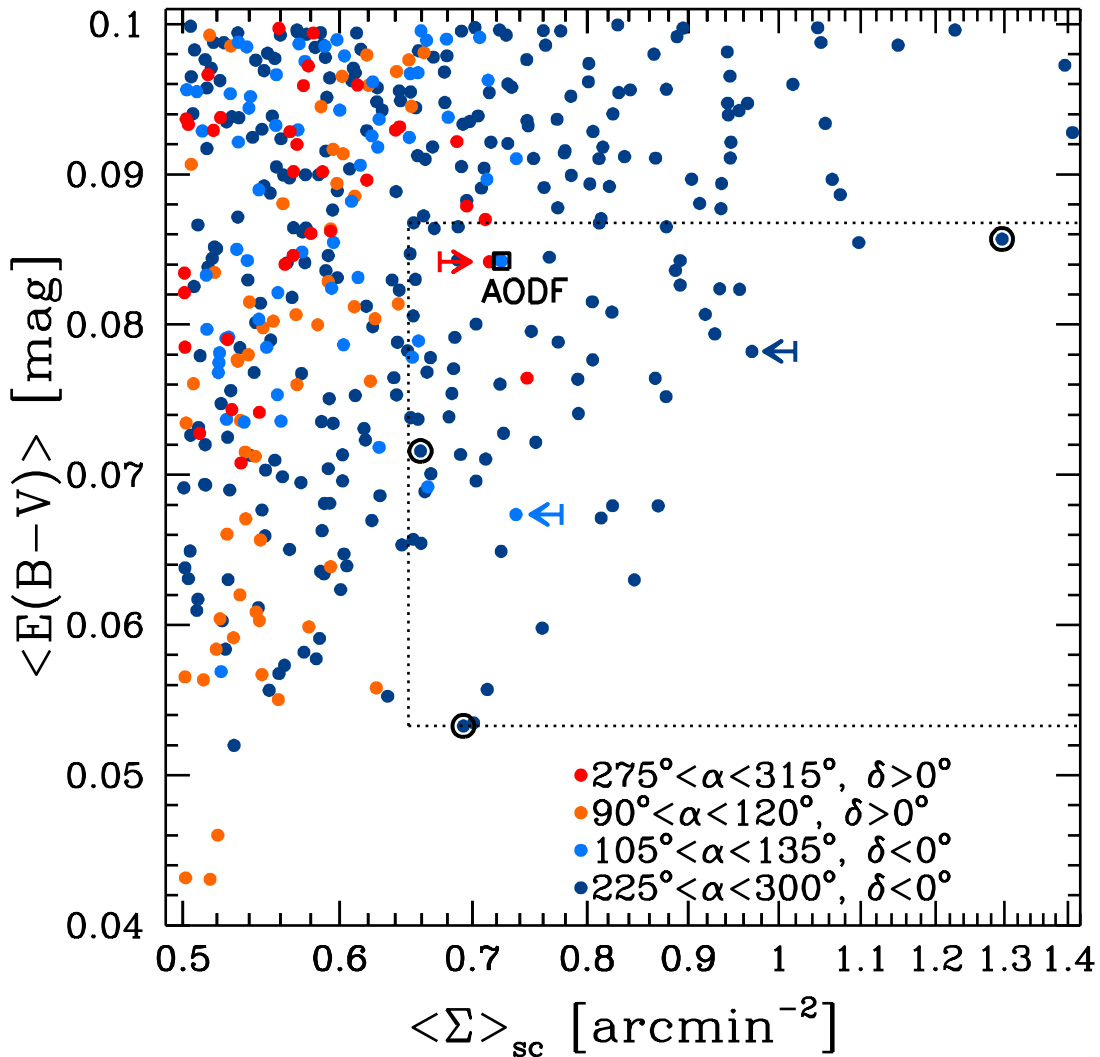


Figure 5.4 Extinction $E(B - V)$ as a function of the star counts surface density Σ_{sc} for 442 $55' \times 55'$ fields with $\Sigma_{sc} > 0.5 \text{ arcmin}^{-2}$ and $E(B - V) \leq 0.1$. The fields are color-coded based on their equatorial coordinates. The dashed line encloses 67 fields with $\Sigma_{sc} \geq 0.65 \text{ arcmin}^{-2}$ and $0.05 \lesssim E(B - V)[\text{mag}] \lesssim 0.087$. The fields flagged with open circles have the highest star counts surface density or the lowest mean extinction or its standard deviation. Colored arrows point at the representative fields for each of the three sightlines (see Appendix 5.8.1 for details). The proposed ‘optimal’ field described in § 5.5 is labeled ‘AODF’ and flagged with an open box.

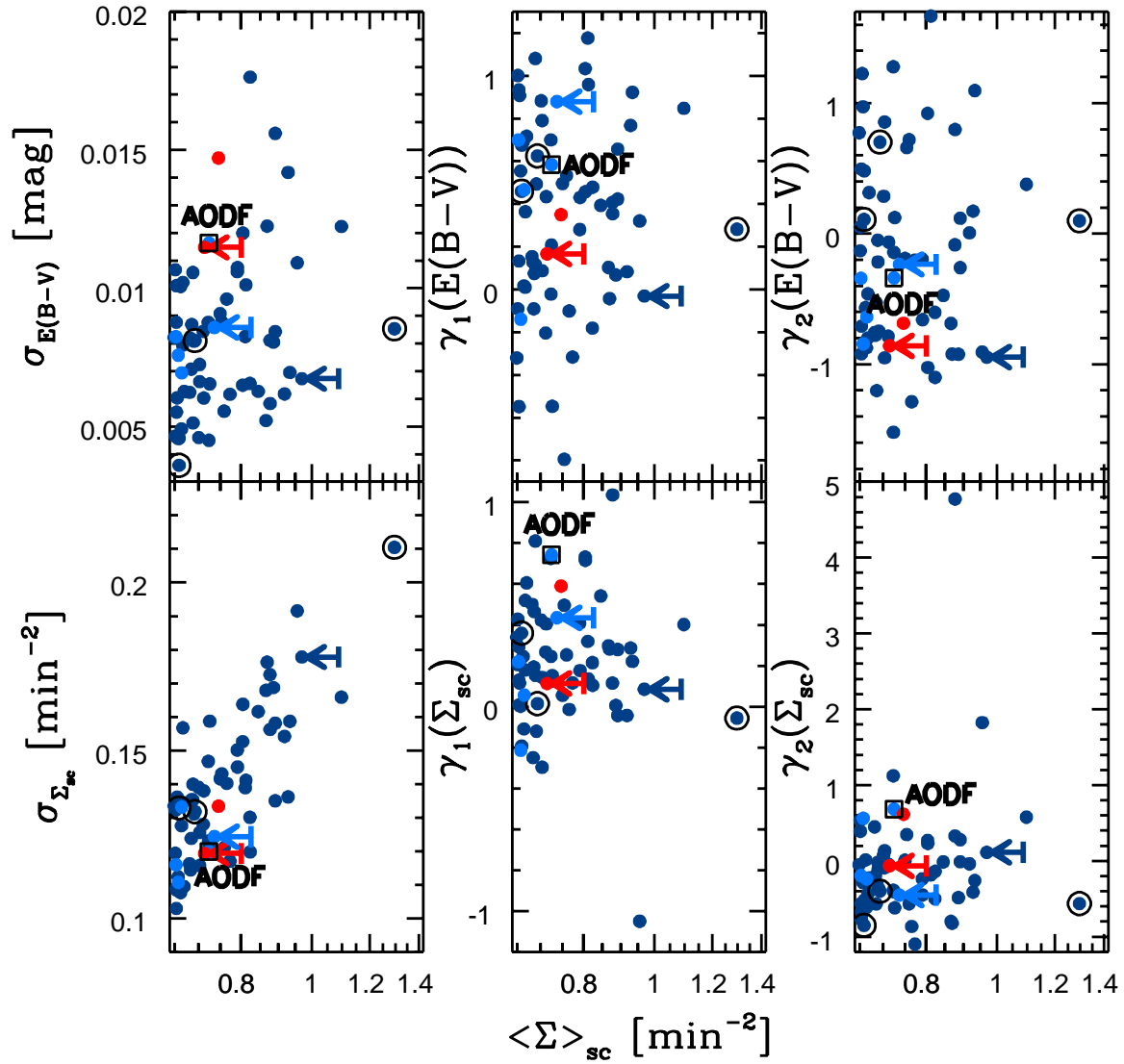


Figure 5.5 The three higher-order moments of the extinction and star count surface density distributions as functions of the mean star count surface density for 67 fields from Table 5.1. The fields are color-coded based on their equatorial coordinates, as given in Figure 5.4. The fields flagged with open circles or with colored arrows correspond to the flagged fields in Figure 5.4. Our optimal AO-friendly field is labeled as in Figure 5.4.

further. The distribution of stellar density and extinction for these cells is shown in Fig. 5.4, color-coded by right ascension. In order to cull these fields down to a more manageable number, we then restricted the sample further to include only those fields whose extinction is lower than the average extinction, and whose stellar density is higher than the average density. This translates into selecting fields with a stellar density greater than 0.65 arcmin^{-2} and reddening less than $\sim 0.087 \text{ mag}$. This final cut corresponds to selecting fields inside the dashed region shown in Fig. 5.4, and brings the total number of fields down to 67 from 442. The positions of these fields are shown as open red circles in Figure 5.3 and open blue squares in Figure 5.1.

The locations and properties of the 67 fields are given in Table 5.1. Variances and higher-order moments of stellar counts and extinction within each field are also tabulated. These moments are based on computations within sub-cells with widths of $6'.871$. The fields flagged with open circles in Fig. 5.4 have the highest star count surface density or the lowest average value or standard deviation of the reddening coefficient, and rows corresponding to these fields are italicized in the table. Colored arrows point at some more representative fields for the three sightlines (see Appendix 5.8.1 for details). A graphical summary of all higher-order statistics is presented in Figure 5.5, from which it can be seen that there is a substantial variation in the distribution of both star count and extinction throughout the fields we have identified. While all the tabulated fields should be quite good for extragalactic adaptive optics work, the best field for a given purpose will depend upon the specific application (e.g. upon whether it is more important to maximize uniformity of star counts, or to minimize absolute extinction, or to minimize variation in extinction). The various trade-offs that need to be balanced in order to choose the best field for a given set of requirements are explored in Appendix 5.8.1.

5.5 CFHT imaging results for a proposed ‘optimal’ field

All fields labeled in Figure 5.1 and in the lower panel of Figure 5.3 have exceptional characteristics in terms of stellar surface density and/or extinction³. However, a practical

³It is interesting to speculate on why these fields exist. While many of them lie in the vicinity of Badde’s window, characterized by very low dust content, a smaller group of fields is found near the Galactic anti-center. One possibility, suggested to us by Sidney van den Bergh, is that these fields have

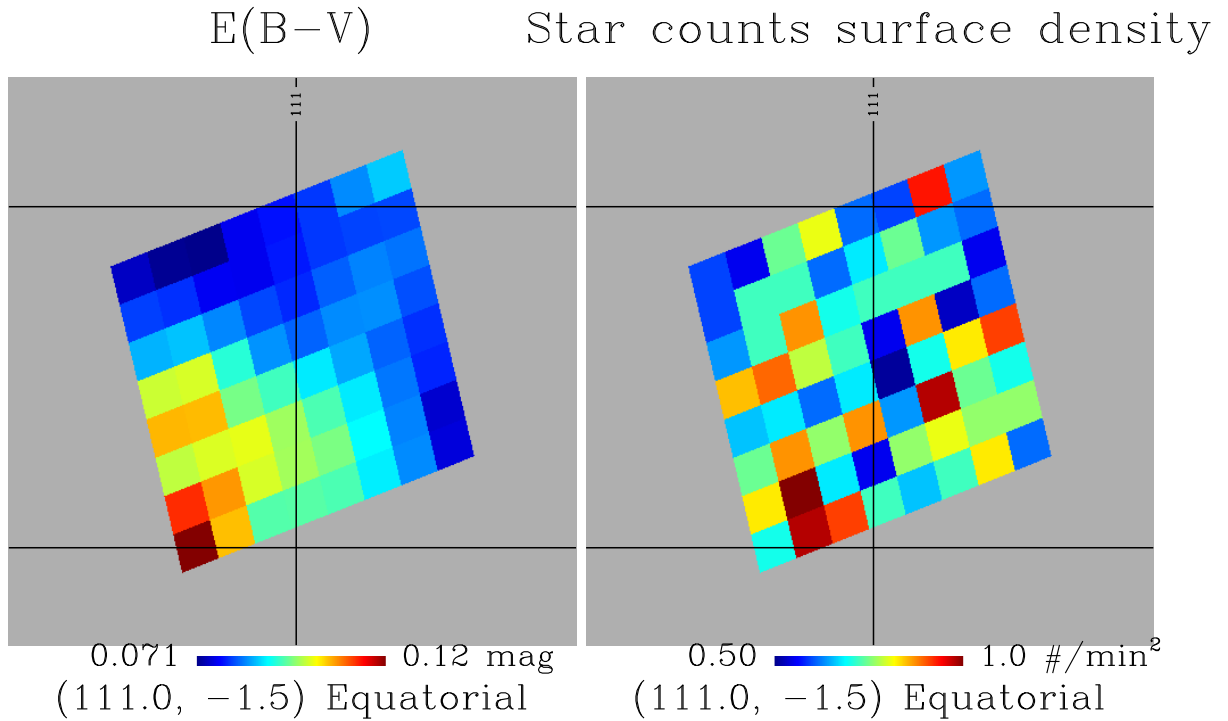


Figure 5.6 Extinction and star surface density maps centered on the position of our chosen field. Each pixel is $6'.871 \times 6'.871$. There are $\gtrsim 2200$ 13 – 16.5 mag stars suitable for AO guide in the field corresponding to ~ 3300 star-forming galaxy candidates with the number surface density of 3 arcmin^{-2} . The field is centered at $R.A. = 7^{\text{h}}24^{\text{m}}2.67^{\text{s}}$, $Dec. = -1^{\circ}27'14.44''$. Solid line grid corresponds to the celestial coordinate system.

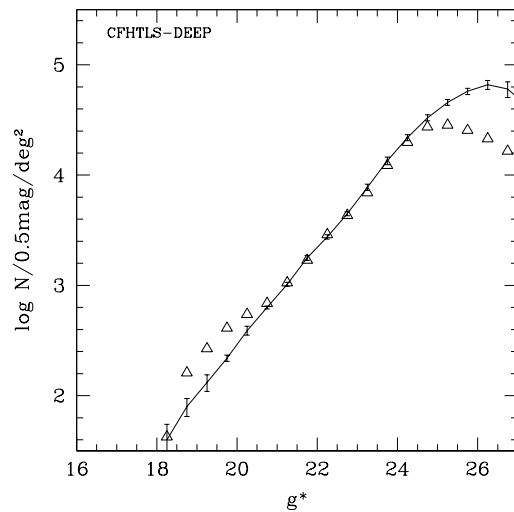
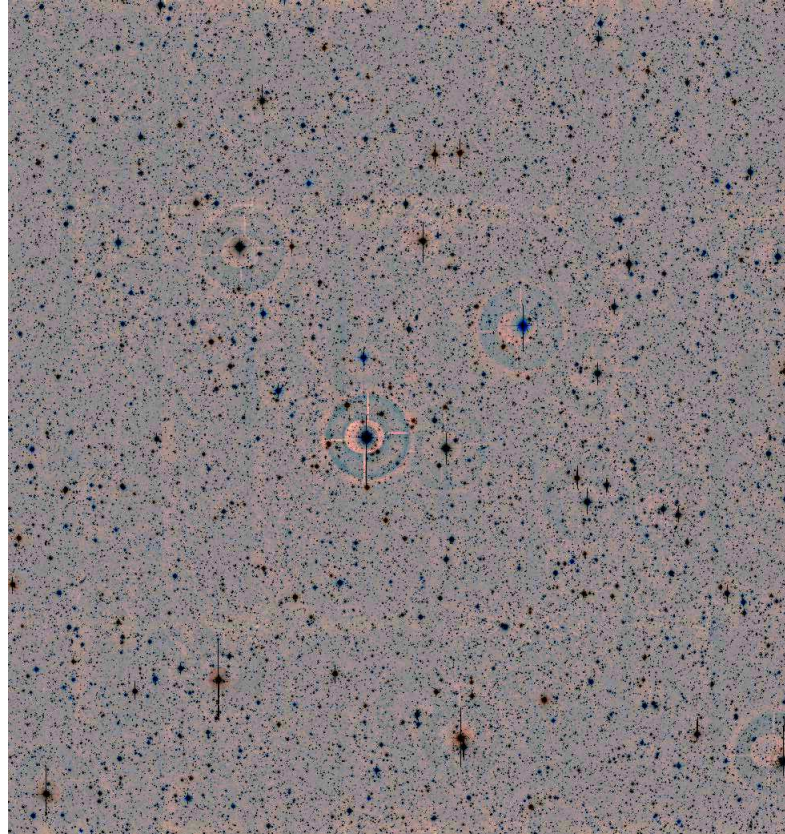


Figure 5.7 *Upper panel:* CFHT MegaCam g' and z' band mosaic of the $1^\circ \times 1^\circ$ field centered on $R.A. = 7^{\text{h}}24^{\text{m}}$, $Dec. = -1^\circ27'15''$. Note that there are only a few bright stars in this field, with the brightest one (in the middle of the field) at $V=9.9$ mag. *Lower panel:* Galaxy number per 0.5 mag and per $1^\circ \times 1^\circ$ as a function of g' magnitude. Solid line represents the expected values based on CFHTLS Deep data set and triangles correspond to the recovered galaxy number counts.

factor that has not yet been considered is the position of the field for accessibility with a broad range of telescopes. An ideal field lies near zero degrees declination in order to be reachable from both hemispheres. With this consideration in mind, the most interesting region for further analysis proves to be the rather large $30^\circ \times 60^\circ$ region centered at $R.A. = 8^h$, $Dec. = 0^\circ$ (see the bottom map in Figure 5.3). To identify the best one square degree patch within this region, we tessellated the region into $55' \times 55'$ cells and explored the distribution of star counts and $E(B - V)$ on a cell-by-cell basis. After identifying a handful of promising cells, we then looked for both low absolute extinction and uniformity in extinction within individual cells. (Uniformity in extinction is desirable for accurate photometric redshifts). Figure 5.6 shows the intra-cell stellar surface density and the extinction map for the best $55' \times 55'$ cell, which we refer to as the ‘Adaptive Optics Deep Field’ (AODF). The field lies at $R.A. : 7^h 24^m 3^s$, $Dec. : -1^\circ 27' 15''$ and is labeled with ID 8328 in Table 5.1. It has a stellar surface density of more than two stars per $2' \times 2'$ region over $> 99\%$ of its area. In addition, for $> 85\%$ of the field presented in Figure 5.6 extinction is $E(B - V) \leq 0.1$ ($A_V < 0.3$; NIR extinction at AO wavelengths will be far lower, see § 5.3). Another important practical consideration is that the number of very bright stars (which scatter and raise the sky background) in this ~ 1 square degree field is low: there are only a handful of stars brighter than 11th magnitude in the field.

Since this ‘AODF’ field seems highly interesting for future follow-up, Director’s Discretionary time on the Canada-France-Hawaii Telescope was used to explore its properties further (and to act as a sanity check on the analysis presented in this paper). A 10 min snapshot in g' and z' bands was acquired using CFHT’s MegaCam in March 2010 in order to evaluate the distribution and color of the brightest stars in the AODF (see Bertin et al., 2002 for the description of the TERAPIX software modules designed for processing MegaCam data). The upper panel of Figure 5.7 presents the $\sim 1^\circ \times 1^\circ$ field of view (made out of 5 dithered exposures), and it is apparent here that bright stars are indeed sparse, with the most prominent one ($V=9.9$ mag) in the center of the field. The main drawback of such a star is not the vertical blooming which affects a small fraction of the imaging area but the halos due to internal reflections in the MegaPrime optics: such a halo increases locally the sky background and limit detectivity. The upper panel of

high counts but low extinction because metallicity decreases with increasing Galactocentric distance. As a result the Galactic anti-center has a low dust to gas ratio.

Figure 5.7 shows that there are four stars that cause a potential problem. Each halo covers a disk of $3'$ in radius, leading to ~ 120 square arcmin for the whole field. When compared to the MegaCam field of view of ~ 1 square degree, those four halos produce a negligible loss of less than 4%. (We note that brighter galaxies can still be extracted from these areas).

We also compared AODF galaxy counts in g' and z' bands with the expected number based on the CFHT Legacy Survey (CFHTLS) Deep data (details on galaxy/star separation method used by the TERAPIX pipeline are given in Coupon et al., 2009). The resulting depth found in both g' and z' bands follow the expectations (within the range of error), and the recovered galaxy number surface density closely tracks the distribution of CFHTLS Deep objects, as shown in the lower panel of Figure 5.7. The slight excess at the bright end is the combined effect of shot noise and cosmic variance (see § 5.3.2), and the turnover at $g = 24.5$ mag is due to the (much) shorter exposure time compared to the CFHTLS Deep.

We conclude from analysis of the CFHT data that all the characteristics discussed in this section (namely a position that allows observations from different sites, a large number of suitable tip-tilt stars for laser AO, a generally low and fairly uniform Galactic extinction, coupled with the small number of very bright stars) make this particular field an excellent choice for future deep extragalactic AO observations.

5.6 Benefits of undertaking observations in AO-optimized fields

How do the properties of the fields identified in the previous sections compare with those of existing extragalactic deep fields? Figure 5.8 presents a comparison of the average stellar density, average extinction, and standard deviation of the extinction coefficient for the set of $67\ 55' \times 55'$ fields from Table 5.1 to those in 55 existing deep fields⁴. Quantities are shown as functions of Galactic latitude, with our candidate fields shown in red, and existing deep fields in blue. Our preferred field is labelled ‘F’ in each panel. The figure illustrates that our proposed fields typically have over ten times the stellar

⁴From the list compiled by J. Brinchmann, see <http://www.strw.leidenuniv.nl/~jarle/Surveys/DeepFields/index.html>

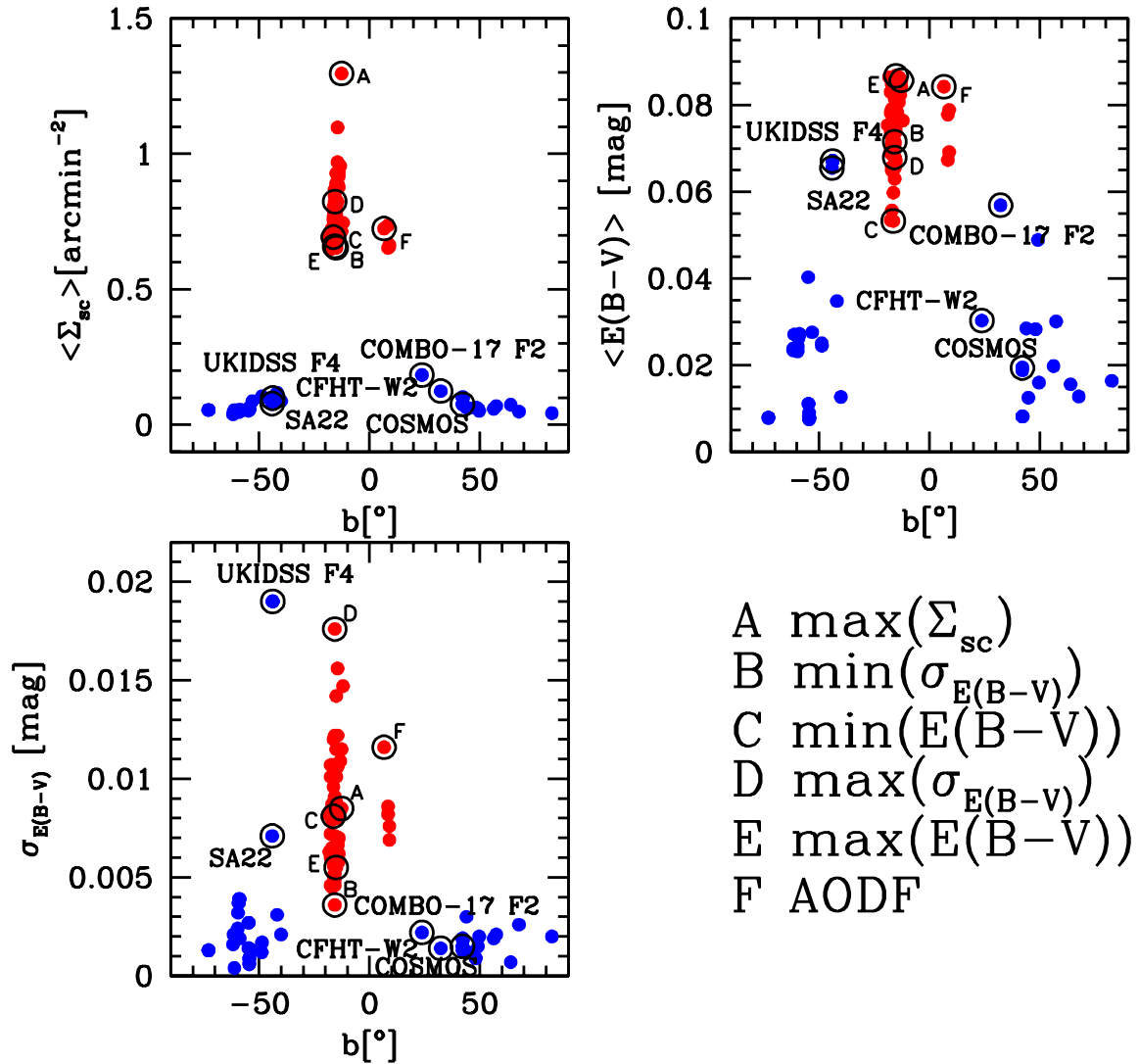


Figure 5.8 *Top left*: Stellar surface density as a function of Galactic latitude for two sets of deep fields: 55 existing deep fields plus 1 square degree region within the CFHTLS W2 field (blue filled circles) and 67 low latitude pointings we have explored in detail (red filled circles, detailed properties listed in Table 5.1). *Top right*: Average $E(B - V)$ as a function of Galactic latitude for the same two sets of fields. *Bottom right*: Standard deviation of $E(B - V)$ for the data in the other panels (this panel quantifies the patchiness of the extinction). Our chosen field (AODF) and five other fields from Table 5.1 with extreme properties are labelled.

density of existing deep fields coupled with extinction values and extinction variations across the field at the high end of those in existing deep fields⁵. How does this translate into practical performance benefits for undertaking AO observations? Are the existing fields already good enough? In order to investigate these questions, we will define a fairly generic figure of merit for AO observations in § 5.6.1, and compare the distribution of this figure of merit in our proposed fields to the corresponding distribution in a typical existing deep field (§ 5.6.2).

For the sake of concreteness, much of the following analysis will be undertaken in the context of the predicted performance of the soon-to-be-commissioned Gemini Multi-Conjugate Adaptive Optics System (GeMS, Ellerbroek, 2003). GeMS is intended to feed NIR instruments with a high Strehl ratio beam at relatively short wavelengths (Strehl ratios up to $\sim 50\%$ in J -band), and in particular to feed the FLAMINGOS-2 NIR MOS spectrograph (Eikenberry, 2004) and the GSAOI imaging camera (McGregor, 2004). The benefits of undertaking observations in the AODF are fairly obvious for science programs which use imaging cameras or resolved integral field spectrographs, but the AODF will also be of considerable interest for programs of NIR MOS spectroscopy. Some spatially resolved kinematical and chemical composition information can be recovered with narrow slits if these span individual objects that are not obliterated by seeing. Furthermore, AO-assisted MOS spectrographs will be able to effectively use narrow slits, which minimize background contamination.

We have chosen to focus our analysis on GeMS because it is the most advanced AO system likely to be available on 8m-class telescopes for the foreseeable future, and because Multi-Conjugate Adaptive Optics (MCAO) is virtually certain to be an important operational mode for future 30m-class Extremely Large Telescopes. We will not describe the fundamentals of MCAO here, and refer the reader to Rigaut et al. (2000) for an explanation of the general principles. For our purposes it suffices to note that MCAO's purpose is to deliver high image quality over a wider area than conventional adaptive optics systems, and it does so by using a constellation of laser guide stars beacons and several natural guide stars to determine the shape of the wavefront, which is then corrected by multiple deformable mirrors. (The natural guide stars are essential, because

⁵Note that in Figure 5.8 we have also included a region within the Canada-France Hawaii Survey Legacy Survey Wide-2 Field (CFHTLS W2). This is not technically a 'deep field', but CFHTLS W2 is worthy of inclusion because it is the most commonly-observed extragalactic field that lies in the general vicinity of our preferred field (for detailed descriptions and comparisons with this field, see § 5.6.2).

they are needed in order to establish tip-tilt corrections). In the case of the GeMS MCAO system, five artificial guide star beacons and three natural guide stars are used. Another important point that should be emphasized here is that the precision of the tip-tilt corrections depends on distance from the guide stars, so the geometric arrangement of the natural guide stars plays an important role in establishing AO performance (Flicker & Rigaut, 2002). We assume nominal performance of GeMS, and emphasize that both the areal coverage and PSF stability expected from MCAO are substantially larger than in the case with conventional (single-laser, single wavefront sensor) AO.

5.6.1 Figure of merit

Any number of figures of merit can be devised for inter-comparing the performance of various AO systems, but in this paper we propose to use a figure of merit that captures the basic idea that real-world AO performance generally depends not only on image quality, but also on the variation of that image quality over the field of view. We therefore adopt the following figure of merit:

$$F = \frac{1}{\sigma_S^{0.25} \times (1 - \langle S \rangle)^{1.5}} \quad (5.2)$$

where $\langle S \rangle$ is the average Strehl ratio achieved in the field of view, and σ_S is the RMS variation in Strehl over the field of view. In the present paper our purpose is to understand the impact of tip-tilt stars, so we will be calculating Strehl ratios using simulation software that computes the distortion in the wavefront due to anisokineticism and assumes perfect correction for other aberrations in the wavefront. Our procedure for doing this will be described in the next section.

The distribution of F across the sky characterizes the performance of an AO system. The specific values of the exponents in our definition of F are chosen to weight the peak Strehl at the expense of some uniformity in the value of the Strehl ratio over the field of view. However, uniformity in Strehl is not completely de-emphasized, and a guide star configuration resulting in a generally high but strongly variable Strehl across the field of view will have a significantly lower value of F . None of main conclusions of this paper are strongly dependent on the specific values of the exponents used in Equation 5.2, as shown in Appendix 5.8.2.

5.6.2 MCAO observations in existing and proposed fields

To investigate limitations in MCAO performance in various fields as a function of natural guide star magnitudes and configurations, we used the Gemini MCAO simulator (F. Rigaut, private communication) to compute the distribution of the figure of merit F for ~ 1000 uniformly distributed pointings within several fields. As noted earlier, we wish to study the errors introduced into the corrected wavefront by a paucity of tip-tilt stars, so the Strehl ratio used in our analysis isolates the RMS contribution to the distorted wavefront introduced by anisoplanatism. In other words, the simulation assumes that all other contributions to the wavefront degradation are negligible, so if the tip-tilt correction were perfect, the Strehl ratio would be unity. In practise of course errors other than anisoplanatism will contribute to the wavefront⁶. However, the point is that our analysis allows us to study *the best performance possible from the AO system*, limited only by the number of natural tip-tilt guide stars.

Each simulated pointing was $80'' \times 80''$ in size (appropriate to Gemini's GeMS). We analyzed performance in the AODF, and for comparison with performance in un-optimized deep fields, we also examined ~ 1000 uniformly distributed positions in the COMBO 17 Field 2 deep field and in the 1 square degree region of the CFHTLS wide field (W2). COMBO 17 Field 2 (labeled as A 901 in Wolf et al., 2003) was chosen because it is the existing deep field with the highest star counts. We chose to include (a part of) the CFHTLS W2 field in this comparison because (a) it is located fairly close to the AODF, and (b) its star counts surface density is high. However, large portions of this $7^\circ \times 7^\circ$ field are 'contaminated' with very bright stars⁷. In order to avoid those regions we performed our analysis in the $1^\circ \times 1^\circ$ subfield within CFHTLS W2 centered on $R.A. = 8^{\text{h}}42^{\text{m}}$, $Dec. = -1^\circ 15'$, which has few very bright stars but an abundance of stars in the range suitable for tip-tilt correction.

To determine the optimal set of guide stars in each pointing, we looked for the best set of three stars with magnitudes in the range $13 < R < 16.5$ mag with distances between $40''$ and $60''$ from the field center (these distances are set by the patrol fields of pick-off mirrors in GeMS). As noted by Flicker & Rigaut (2002), the ideal geometry for these stars is an equilateral triangle, so we searched for three stars lying in the

⁶The interested reader is directed to Table 2 of this web page for a census of other contributions to the MCAO wavefront: <http://www.gemini.edu/sciops/instruments/mcao?q=node/10749>

⁷See <http://legacy.astro.utoronto.ca/Fields/images/w2.html>

40'' – 60'' annulus whose interior angles were within $60^\circ \pm 20^\circ$ from each other. If we failed to find suitable stars we then relaxed our criterion that the guide stars approximate equilateral triangles and simply searched for three stars defining a triangle with any set of side lengths. Where multiple triangles existed we retained the one that gave the best value of F . When three stars in any geometry could not be found we calculated MCAO performance with available stars, either single or in pairs. In cases where no stars in the suitable magnitude range were found in the vicinity of our pointing, the value of F was set to zero.

The results from our investigation are shown in Figure 5.9, which compares the distribution and cumulative distribution functions of F for the AODF, shown in blue, with the corresponding distributions for the COMBO 17 Field 2 and a 1 square degree region of the CFHTLS W2 field, shown in red and green, respectively. The two panels of Figure 5.9 correspond to a limiting natural guide star magnitude of 16.5 mag in R-band (corresponding to the anticipated limit for GeMS bright time observing). Although the limiting guide-star magnitude will vary with lunation, the only difference in the case where the faintest natural guide stars is $R = 18.5$ mag (the ideal dark sky performance of GeMS) will be a higher number of pointings with low F .

The enormous benefits that emerge from observing in an AO-optimized field are obvious from even a cursory inspection of Figure 5.9, but it is worth discussing the figure in some detail. In analyzing this figure, we noted that even in our adaptive-optics optimized deep field (ID 8328, see Table 5.1), for bright time observing only about $\sim 1\%$ of the pointings in the field fall within triangles of guide stars that are approximately equilateral (as defined above). However, if we allow any configuration of three suitably bright guide stars, sky coverage in the AODF is 55%. The $0 \leq F < 20$ range in this case covers the MCAO performance when less than three natural guide stars are available. If we assume dark time observing, the sky coverage is $\sim 92\%$ but the highest figure of merit still corresponds to the configurations of brighter ($R \leq 16.5$) stars. In contrast to this, *none* of ~ 1000 uniformly distributed pointings in the COMBO 17 Field 2 and only *one* pointing in the CFHTLS W2 subfield falls within equilateral triangles of natural guide for our simulated bright time conditions, and this fraction rises to only 0.2% (COMBO 17 Field 2) and 1.2% (CFHTLS W2) at dark time. If the MCAO requirement is relaxed to allow any configuration of three NGS, COMBO 17 Field 2 coverage is 0.4% and 3.8% for bright and dark time observing conditions, respectively. Three AO-suitable stars with

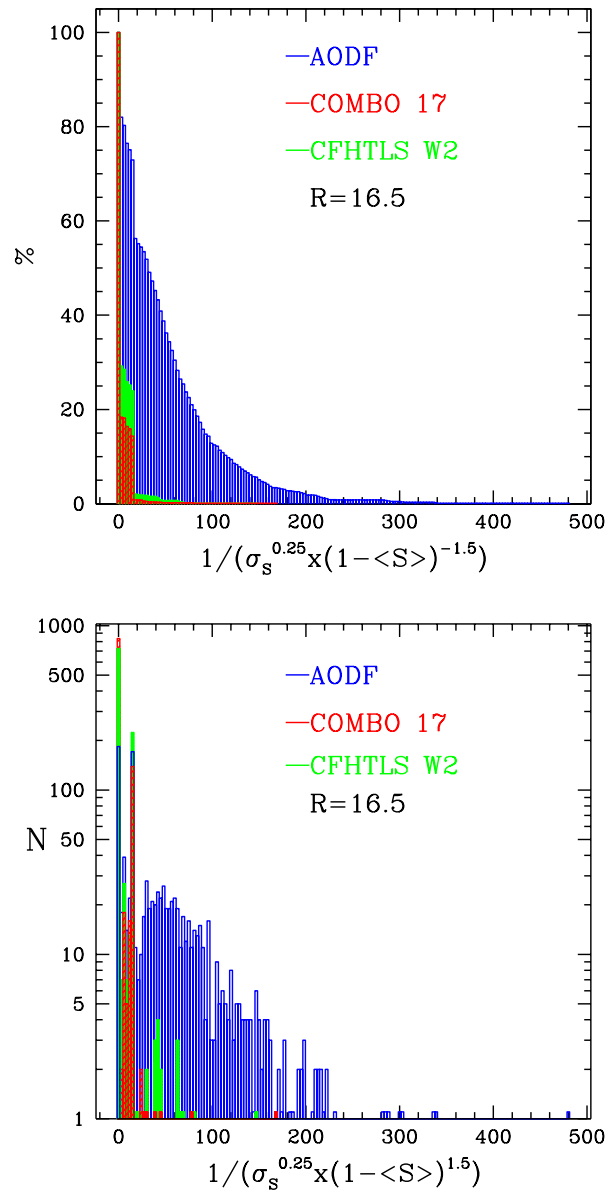


Figure 5.9 Cumulative distribution (*top*) and distribution (*bottom*) of our Strehl-related figure of merit for $55' \times 55'$ AODF (blue), COMBO 17 Field 2 (red), and the CFHTLS W2 subfield (green). Data points are binned according to their figure of merit value in 3 unit wide bins. The left-side vertical axis gives the percentage of field area with the figure of merit value equal or higher than the corresponding bin's lower limit. In the right-side panel ordinate represents the number of pointings contained in each bin. Both panels correspond to a guide star magnitude limit of 16.5 mag in R -band (foreseen bright time limit for the Gemini GeMS MCAO system). See text for details.

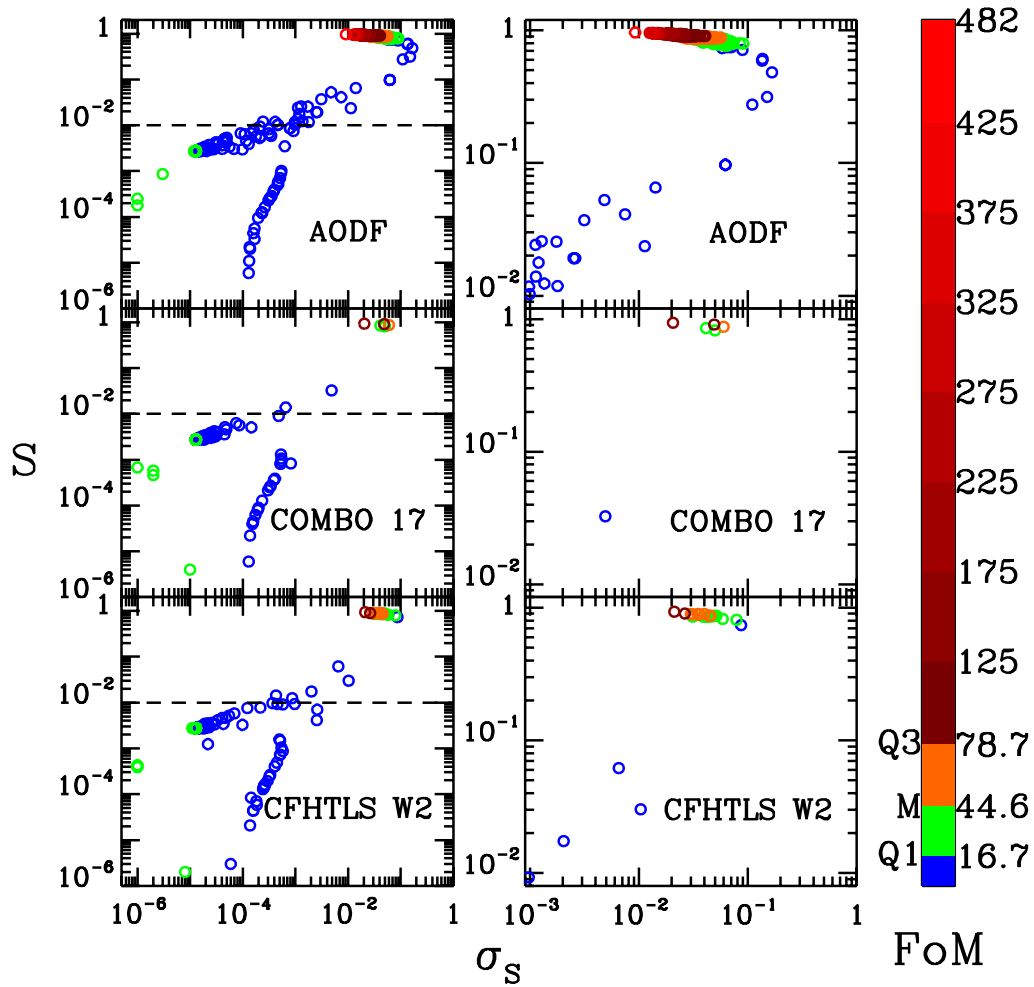


Figure 5.10 Strehl ratio as a function of its RMS variance for pointings accessible to AO in AODF, COMBO 17 Field 2, and CFHTLS W2 1 square degree subfield. Left-side panels display full range of values for Strehl ratio and its variance. The dashed line corresponds to MCAO ‘failure’ for pointings where only one or two guide stars are available. The right-side panels show the range of Strehl ratios and related variances for pointings where MCAO is efficient (i.e., where at least one set of three AO-friendly stars forming a triangle is available). In each panel points are color-coded according to figure of merit value (equation 2). Color bar labels Q1, M, and Q3 represent the first quartile, median, and the third quartile of the figure of merit distribution across the AODF. All panels correspond to a guide star magnitude limit of 16.5 mag in R -band (the expected bright time magnitude limit for the Gemini GeMS MCAO system).

$R \leq 16.5$ forming a triangle were found around 1.8% of the CFHTLS W2 pointings. If the magnitude limit is lowered to $R \leq 18.5$, CFHTLS W2 coverage for sets of three stars arranged in any type of triangle reaches 21%. For both COMBO 17 and CFHTLS W2, the most common figure of merit values that emerge ($0 \lesssim F \lesssim 20$) correspond to MCAO performance with only one or two natural tip-tilt stars. Thus the low sky coverage in the COMBO 17 Field 2 and CFHTLS W2 subfield results in the large spike in the first bin in Figure 5.9, with only a few (out of 1000) positions with high F producing a steep decline at $F \approx 20$. In contrast to this, the median value of F in the AO-optimized field is a factor of three higher than in COMBO 17 Field 2 and CFHTLS W2, and a significant tail of F extends out to $F \sim 500$ (a factor of three better than the best F obtained in COMBO 17 Field 2 and CFHTLS W2 subfield).

Figure 5.9 shows the superiority of the AODF over both COMBO 17 Field 2 and CFHTLS W2 in terms of the figure of merit. The relation between the figure of merit values and the quantities that enter Equation 5.2 (the average Strehl ratio and its RMS variation over the field of view) is explored in Figure 5.10, where points are color-coded according to their figure of merit values. (The reader is once again reminded that the Strehl ratios in our calculations take into account only the tip-tilt correction). Dashed line in the left-hand panels denotes threshold value of the average Strehl ratio at which MCAO fails, i.e., when there are only one or two natural guide stars available. While $\sim 70\%$ of the AODF pointings with available natural guide stars have Strehl ratios above the MCAO threshold, for the COMBO 17 Field 2 and the CFHTLS W2 that fraction is 3.8% and 8%, respectively. The right-hand panels show the distribution of Strehl ratios and corresponding variances for MCAO performance when the required geometry of guide stars is available. Figure 5.10 confirms that the figure of merit we have defined does rather nicely map onto fields with the combination of high average Strehl ratios *and* low RMS variation in Strehl over the $80'' \times 80''$ field of view. The third and fourth quartile of the figure of merit distribution for the AODF (orange and red points in Fig. 5.10), that enclose Strehl ratios of $90\% < \langle S \rangle < 97\%$ and RMS variations of $1\% < \sigma_S < 6\%$, contains only 3% of the CFHTLS W2 pointings available for AO and 1.5% of the corresponding pointings within the COMBO 17 Field 2. This hugely better AO performance clearly illustrates the benefits of undertaking extragalactic AO observations in fields optimized for adaptive optics.

5.6.3 The AODF in the era of upcoming methods and instruments

Although the MCAO has been emphasized in the present paper, other AO methods are in development especially for use with the 30m-class telescopes. These methods include multi-object adaptive optics (MOAO) and systems with faint infrared (IR) tip-tilt sensors whose images are “sharpened” by the AO system. Future AO systems are expected to be less sensitive to the (bright) natural guide stars surface density.

MOAO (Assémat et al., 2007) is a technique that allows simultaneous AO corrections for several small IFU target fields (typically $2 - 4''$ in diameter, sufficient to map velocity fields of large spiral galaxies at $z \gtrsim 1$) within a wider field of view ($\text{FOV} \sim 5 - 10'$, driven by the surface density of line emitting galaxies at $z \gtrsim 1$). Each IFU target field is corrected by a separate deformable mirror (DM) that provides AO correction along a given line-of-sight only (in contrast with MCAO systems that provide this correction across the whole FOV). Multiple natural guide stars are used for tomographic wavefront sensing (Ragazzoni et al., 2000), i.e., to probe the 3D phase perturbations in the atmosphere above the telescope primary aperture. A real-time control system then slices multiple columns through the mapped turbulent volume in the directions of all targets and applies a correcting signal to multiple independent DMs. The critical difference between MOAO and MCAO is that the former is an open loop system where the wavefront sensors do not get any feedback from DMs. In other words, the wavefront error is measured and corrected only once, and the accurate system calibration is essential.

While an advantage of open-loop MOAO is that it does not need a guide star for each target, the limiting magnitude of the natural guide stars is set by the requirement for low system error level. Thus even MOAO designed for the 30m-class telescopes will still need guide stars brighter than $R = 17$ mag. For example, an appropriate configuration for mapping turbulent atmospheric layers using the EAGLE MOAO system that is being developed for the E-ELT involves 5 natural guide stars with $R < 17$ mag in the $7:3$ patrol FOV (Rousset et al., 2010). Based on the average star counts surface density, only one out of 55 existing deep fields mentioned earlier (COMBO 17) lies above (and very close to) this threshold. On the other hand, the number density of available natural guide stars in the AODF is six times higher than EAGLE MOAO requirements.

As was noted earlier, as the primary mirror of a telescope becomes larger, its sen-

sitivity allows fainter stars to be used for wavefront sensing. AO systems on 30m-class telescope will give satisfying performance with a natural guide stars magnitude limit of $R \approx 21$ mag (though the limiting magnitude will be lower in MOAO mode, as noted above). We performed the same analysis as in previous section on the COMBO-17 field using GeMS MCAO simulator and looked for stars arranged into triangles within magnitude range $13 < R < 21$, based on the USNO-B catalog (with limiting magnitude of $R = 22$, Monet et al., 2003). Although the sky coverage in this case is $\sim 47\%$, only $\sim 15\%$ of these sets of three stars will provide Strehl ratio greater than 0.5. On the other hand, the sky coverage for high Strehl ratio values (i.e., guide stars arranged in equilateral or isosceles triangles) using MCAO system in the AODF is 100%.

Another advanced type of AO planned for 30m-class telescopes will utilize IR tip-tilt wavefront sensing. A major advantage of this approach is increased guide star density, since faint IR natural guide stars images are sharpened by the AO system. For example, for the TMT NFIRAOS the probability of finding at least 1 tip-tilt star brighter than $J = 21$ mag is 95% at high galactic latitude. However, at least three natural guide stars are still required to detect the effects of tilt anisoplanatism; the use of only one off-axis tip-tilt star would give blurred time-averaged images of the science objects. This condition lowers the sky coverage that NFIRAOS will achieve to 50% at high latitudes (Wang et al., 2008). Even with three guide stars one expects to get a continuum of performance. Fainter stars will force the system to run slower which in turn leaves larger tip, tilt and focus errors. Thus, although MCAO system on a 30m-class telescope will operate over much of the sky, an insufficient number of bright guide stars will impair imaging performance, as diffraction-limited cores will be blurred out by these tip/tilt/focus errors and the variation across the FOV will be increased. (IFU work will be less affected, because the ensquared energy loss in a spaxel a few times larger than the diffraction limit will be lower). This type of systems will give the best results when used on a field densely populated with bright NGS, where the AO is not pushing the boundaries of the control system. Finally, we note that AO using natural guide stars only (of magnitude ~ 12 and within $\sim 15''$ of the science object) is capable of achieving higher Strehls than MCAO, is easier to do, and removes all the complications of changing plate scales, cone effect, laser elongation, etc. A major benefit of doing AO in the proposed field is that it will allow much of the of the 30m-class telescope science to be done in natural guide stars mode. For example, if an AO system, similar to EAGLE MOAO, that uses only

bright natural guide stars were employed in the AODF, sky coverage would be $\gtrsim 75\%$.

We conclude this section by noting that fields optimized for ground-based adaptive optics with 30m-class telescopes will not be made obsolete by upcoming space missions, such as JWST and Euclid/WFIRST (both of which are 5–10 years away in any case). Euclid/WFIRST will likely only operate in slitless spectroscopy mode, while JWST will be equipped with a micro-shutter array for simultaneous spectroscopy of ~ 100 sources and with an IFU for 3D spectroscopy, spanning the wavelength range of $1\text{--}5\ \mu\text{m}$ (Gardner et al., 2006). However, the main point is that the future ground-based observations will still be undertaken at spatial resolutions a factor of 5 and 15 times higher than the angular resolution of JWST and Euclid/WFIRST, respectively.

5.7 Summary and conclusions

We have combed through stellar density and extinction maps to identify 67 low Galactic latitude fields with high star density, remarkably low extinction, relatively large area (1 square degree, to mitigate the effects of cosmic variance), and an AO-friendly stellar mix of many $R = 13 - 16.5$ mag but few < 8 mag stars. These fields allow highly efficient adaptive optics to be undertaken in low extinction extragalactic fields with minimal saturation and scattering. A comparison of these fields with existing deep fields reveals that while the number of guide stars per square arcminute is on average 15 times higher in the AO-friendly fields, the mean level of extinction is comparable to the more extinguished existing deep fields.

By augmenting our analysis with some practical considerations (such as the desire for an equatorial field accessible from both hemispheres), we identify a single one square degree field (which we designate the Adaptive Optics Deep Field, or AODF) as being particularly promising for extragalactic AO work. This field is centered at $R.A. : 7^{\text{h}}24^{\text{m}}3^{\text{s}}$, $Dec. : -1^{\circ}27'15''$. Analysis of galaxy counts in this field based on short observations of this AODF in g' and z' bands (using MegaCam on CFHT) confirm both the absence of extinction and the abundance of suitable tip-tilt stars the AODF. In fact, galaxy counts in this field closely follow the counts found in the CFHTLS Deep data set.

Simulations were undertaken to estimate the practical performance benefits of undertaking AO observations in the AODF. Our analysis shows enormous advantages emerging from undertaking AO observations in optimized fields such as the one described here. For

example, for geometries of natural guide stars which produce spatially stable high Strehl ratio PSFs, dark time sky coverage in the AODF is essentially 100% using the Gemini MCAO system, which is a factor of over 50 times higher than for most existing deep fields.

5.8 Appendices

5.8.1 Properties of selected fields

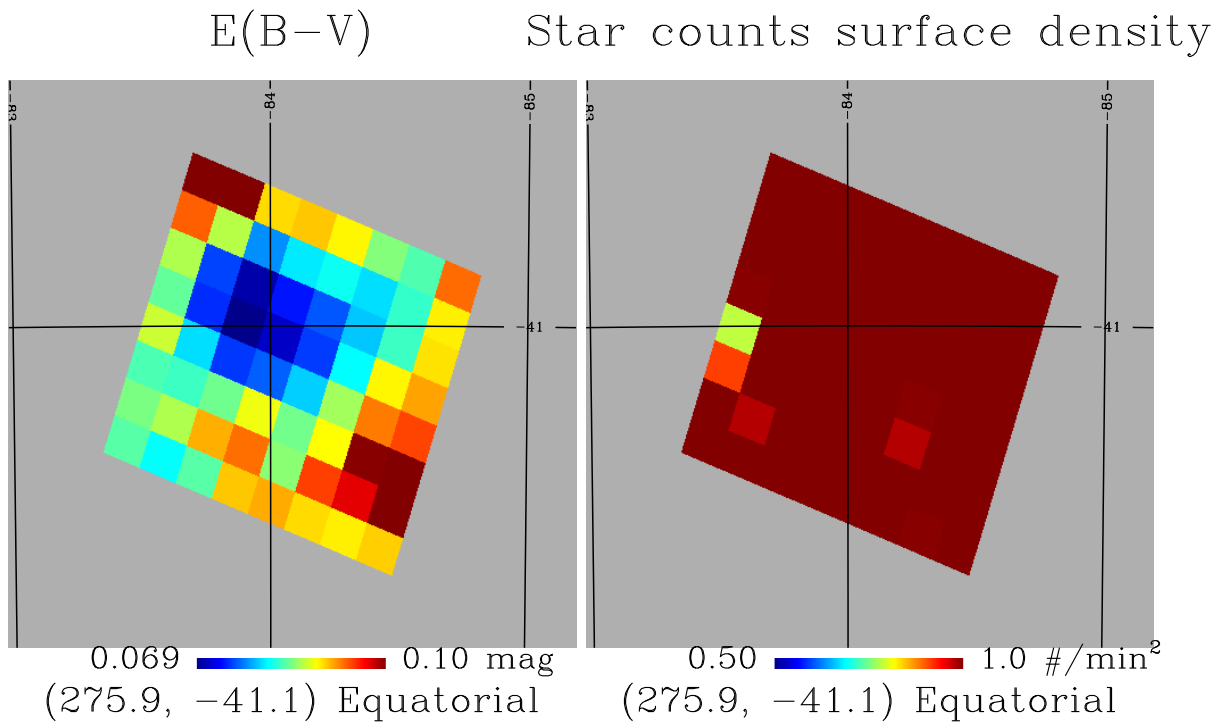


Figure 5.11 Extinction and star surface density maps of the $6'871 \times 6'871$ cells within the $55' \times 55'$ field with the highest mean star counts surface density of $\langle \Sigma_{sc} \rangle = 1.3 \text{ arcmin}^{-2}$ (i.e., with 11,000 star-forming galaxies potentially observable with AO if the average number surface density of these objects is 3 arcmin^{-2}). The field is centered at $R.A. = 18^{\text{h}}23^{\text{m}}39^{\text{s}}.53$, $Dec. = -41^{\circ}6'44''.3$. Solid line grid corresponds to the celestial coordinate system with $R.A.[^{\circ}] = 360^{\circ} + \alpha[^{\circ}]$.

Figure 5.4 demonstrates how the set of $55' \times 55'$ fields that are most suitable for AO observations were selected. Amongst this set we chose our preferred field (the ‘AODF’)

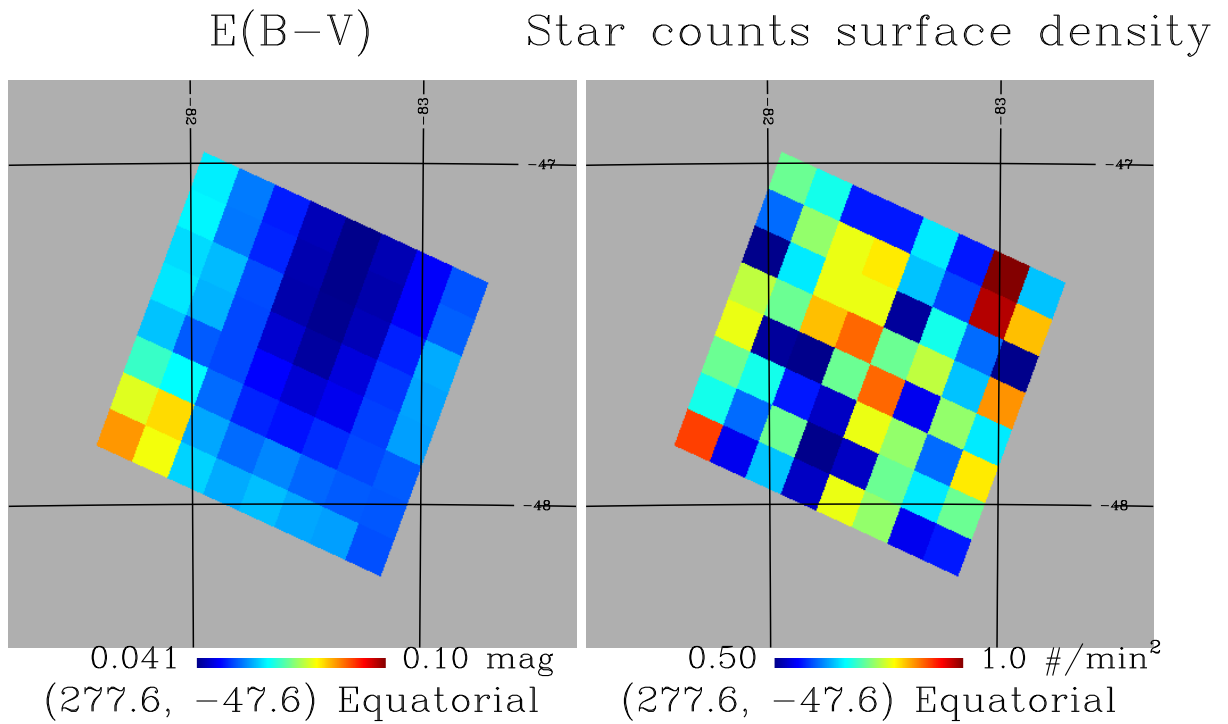


Figure 5.12 Extinction and star surface density maps of the $6'871 \times 6'871$ cells within the $55' \times 55'$ field with the lowest reddening coefficient ($\langle E(B - V) \rangle = 0.053$ mag) but still containing more than 2500 possible guide stars (~ 5900 observable star-forming galaxies with number surface density of 3 arcmin^{-2}). The field is centered at $R.A. = 18^{\text{h}}30^{\text{m}}14^{\text{s}}.96$, $Dec. = -47^{\circ}35'20''.76$. Solid line grid corresponds to the celestial coordinate system with $R.A.[^{\circ}] = 360^{\circ} + \alpha[^{\circ}]$.

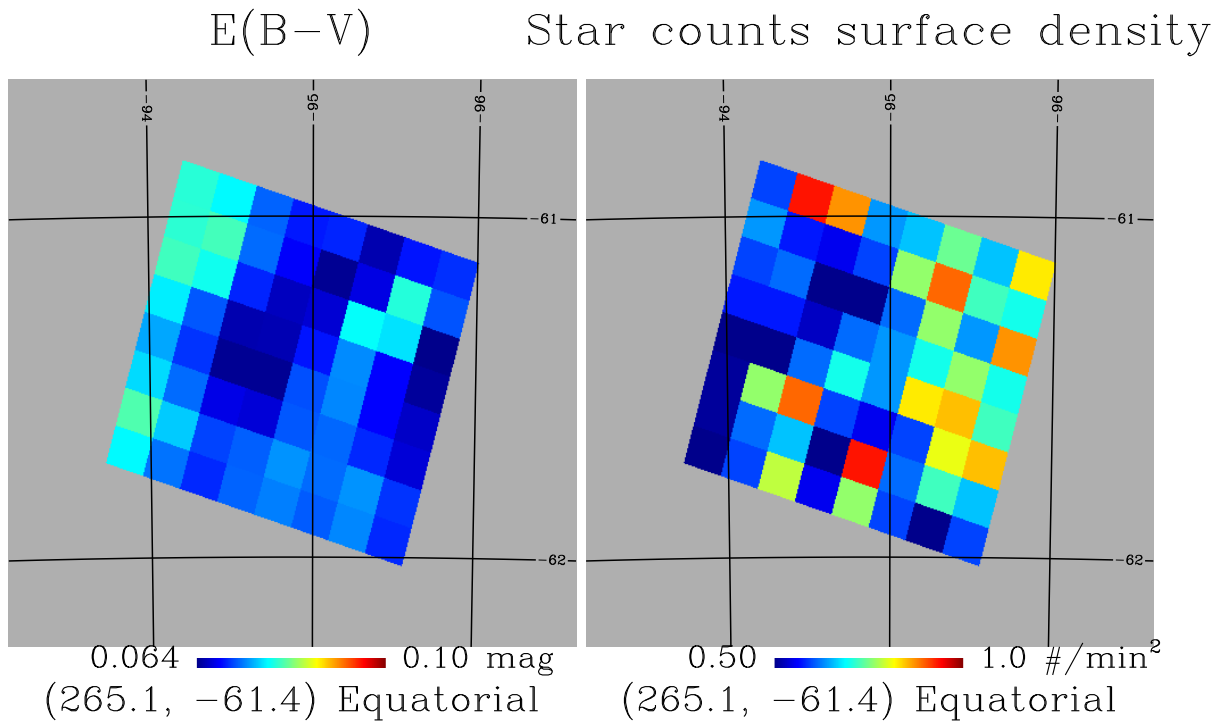


Figure 5.13 Extinction and star surface density maps of the $6'.871 \times 6'.871$ cells within the $55' \times 55'$ field with the lowest standard deviation of $E(B - V)$ that translates into the smallest variation in dust content across the field. There are $\gtrsim 2350$ $13 - 16$ mag stars suitable for AO guide in the field corresponding to ~ 5600 observable star-forming galaxies with the number surface density of 3 arcmin^{-2} . The field is centered at $R.A. = 17^{\text{h}}40^{\text{m}}30^{\text{s}}.18$, $Dec. = -61^{\circ}25'54''.54$. Solid line grid corresponds to the celestial coordinate system with $R.A.[^{\circ}] = 360^{\circ} + \alpha[^{\circ}]$.

partly on the basis of accessibility to both hemispheres. Other fields may be equally (or even more) suitable if this criterion is relaxed. A field of obvious interest is the one with the highest star count surface density. Table 5.1 shows that this field is located at $R.A. = 18^{\text{h}}21^{\text{m}}57^{\text{s}}.52$, $Dec. = -43^{\circ}14'2''.775$. It is flagged with an open circle in Figures 5.4 and 5.8 and presented in more detail in Figure 5.11, where star count surface density and extinction maps with finer sampling ($6'.871 \times 6'.871$) are used to bring out the features of individual cells within the field. The number of stars in this field is ~ 5000 , corresponding to more than one star per arcminute squared.

Another property worth optimizing for is dust extinction, so it is interesting to look for fields with extraordinarily low extinction in Table 5.1. The field with the lowest reddening coefficient $E(B - V)$ is centered at $R.A. = 18^{\text{h}}30^{\text{m}}14^{\text{s}}.96$, $Dec. = -47^{\circ}35'20''.76$ and also flagged in Figures 5.4 and 5.8. A close-up view of its stellar surface density and reddening coefficient distribution is given in Figure 5.12. Although this field features lower extinction than some of already explored deep fields, the number of its potential AO guide stars is almost an order of magnitude higher than in the existing deep fields labeled in Figure 5.8.

Finally, it is interesting to consider fields with highly homogenous extinction. The third flagged field in Figures 5.4 and 5.8 is the one with the lowest value of standard deviation for $E(B - V)$ from Table 5.1 at $R.A. = 17^{\text{h}}40^{\text{m}}30^{\text{s}}.18$, $Dec. = -61^{\circ}25'54''.54$. The properties of this field's $6'.871 \times 6'.871$ cells are given in Figure 5.13. Despite not having the highest number of AO suitable stars ($\gtrsim 2350$ vs. $\gtrsim 4600$) or the lowest dust extinction (its $\langle E(B - V) \rangle$ is $\sim 35\%$ higher than in the field with minimum extinction), this field may be interesting for certain studies in which reddening homogeneity is more important than other factors.

The higher order statistical moments of star counts within sub-fields, along with proximity to other suitable areas, may be other factors worth considering when choosing fields. Whether the the higher order moments really matter depends on the specific science objectives of the observations. The skewness, γ_3 , in the star count surface density distribution might be worthwhile to consider in cases where one wishes to optimize for having a smaller number of fields with many NGS. For example, $\gamma_3 < 0$ corresponds to the mass of distribution shifted towards higher values. For such fields there are many patches of very high star density. On the other hand, kurtosis in the $E(B - V)$ distribution, γ_4 , could be important if one wishes to optimize a field for photo-z consistency. Fields with

$\gamma_4 < 0$ have a less peaked distribution of $E(B-V)$, i.e., more uniform extinction. The area within dashed lines in Figure 5.4 contains the fields from three regions in the sky. When identifying the best AO field in each region (coloured arrows in Figures 5.4 and 5.5), we have taken into account all four moments of both star counts surface density and extinction distributions. In Figure 5.5 we present three moments - standard deviation, skewness, and kurtosis - for all 67 fields from Table 5.1 as functions of the mean star count surface density (the most important factor for identifying AO-friendly fields).

5.8.2 The form of the figure of merit

Our proposed figure of merit, given in Equation 5.2, is useful for characterizing AO system performance, but there is considerable flexibility in choosing the values of the exponents in this equation. We chose exponents which strike a balance between emphasizing the importance of peak Strehl ratio in a field and emphasizing the uniformity of the Strehl ratio throughout the field. Other, equally valid, choices of these exponents could be made that strike a different balance. In order to investigate how different combinations of exponents in Equation 5.3 might influence our general conclusions, we have defined a more generic form of the figure of merit:

$$F = \frac{1}{\sigma_S^\alpha \times (1 - \langle S \rangle)^\beta}, \quad (5.3)$$

where exponents α and β can take several values: $\alpha \in \{0.25, 0.125\}$, $\beta \in \{1, 1.5, 2\}$. The maximum image quality (i.e., average Strehl ratio) is weighted by the β exponent. Constraints on the range of values for α are set so that the high values of the figure of merit cannot coincide with extremely low values for *both* Strehl ratio and its variance.

The resulting distributions for all six possible combinations are given in Figures 5.14 and 5.15. In these figures we have examined and compared three fields: AODF, COMBO 17, and a $1^\circ \times 1^\circ$ subfield within CFHT W2. The corresponding histograms are presented in blue, red, and green, respectively. Of course the range of values that the figure of merit can take is seen to depend rather strongly on the choice of exponents, but the important thing to note is that none of the distributions show major changes in shape or relative position for different combinations of α and β . Furthermore, the highest figures of merit in all six cases (for all three fields) correspond to the pointings with the highest average Strehl ratio ($\langle S \rangle > 90\%$) and relatively low variation of Strehl across the $80'' \times 80''$ field of

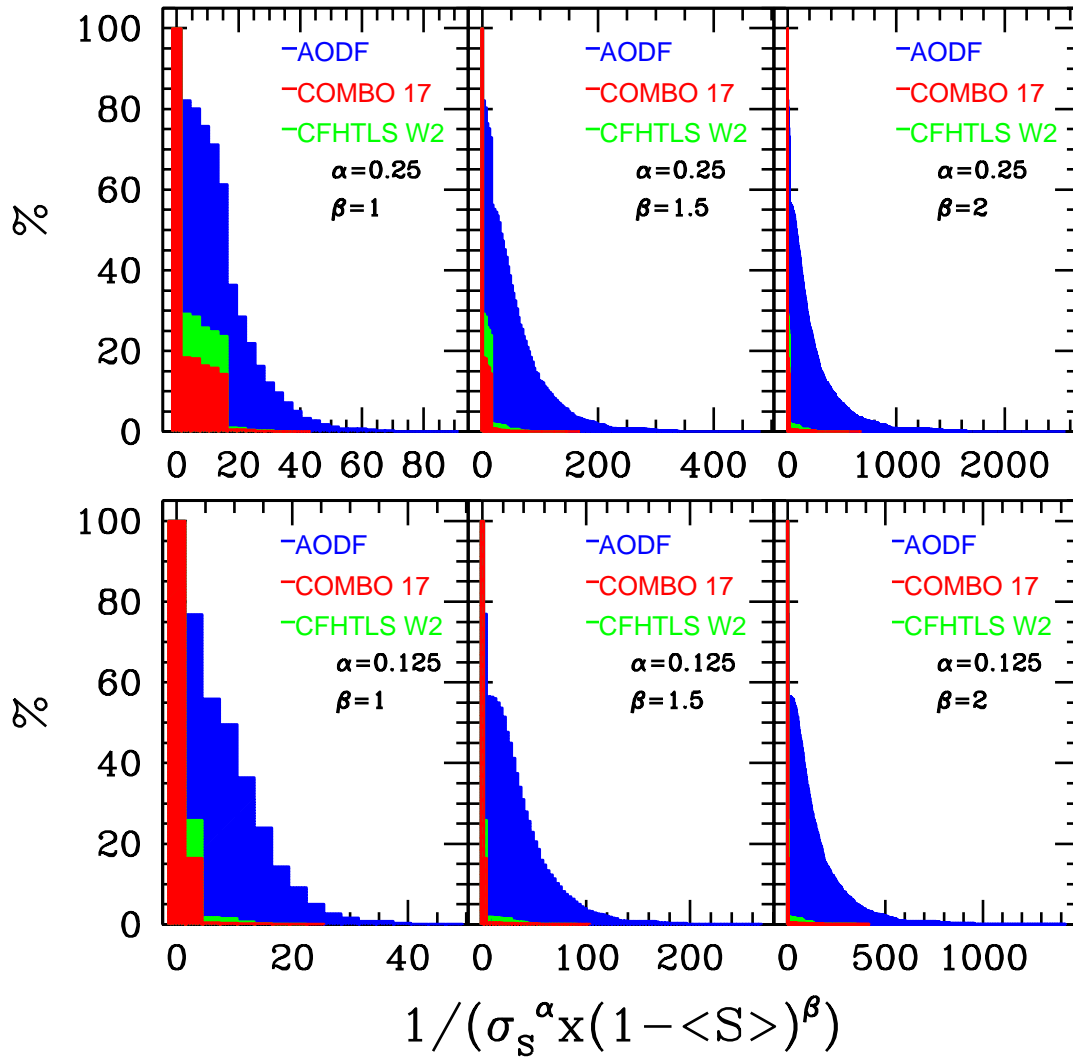


Figure 5.14 Cumulative distribution of our Strehl-related figure of merit for $55' \times 55'$ AODF (black), COMBO 17 (red) field, and the $1^\circ \times 1^\circ$ subfield of CFHT W2 (green). Data points are binned according to their figure of merit value in 3 (units) wide bins. Vertical axis gives the percentage of field area with the figure of merit value equal or higher than the corresponding bin's lower limit. In each panel the figure of merit is defined by different combination of the two exponents (Eq. 5.3). All panels correspond to a guide star magnitude limit of 16.5 mag in R -band (foreseen bright time limit for the Gemini GeMS MCAO system).

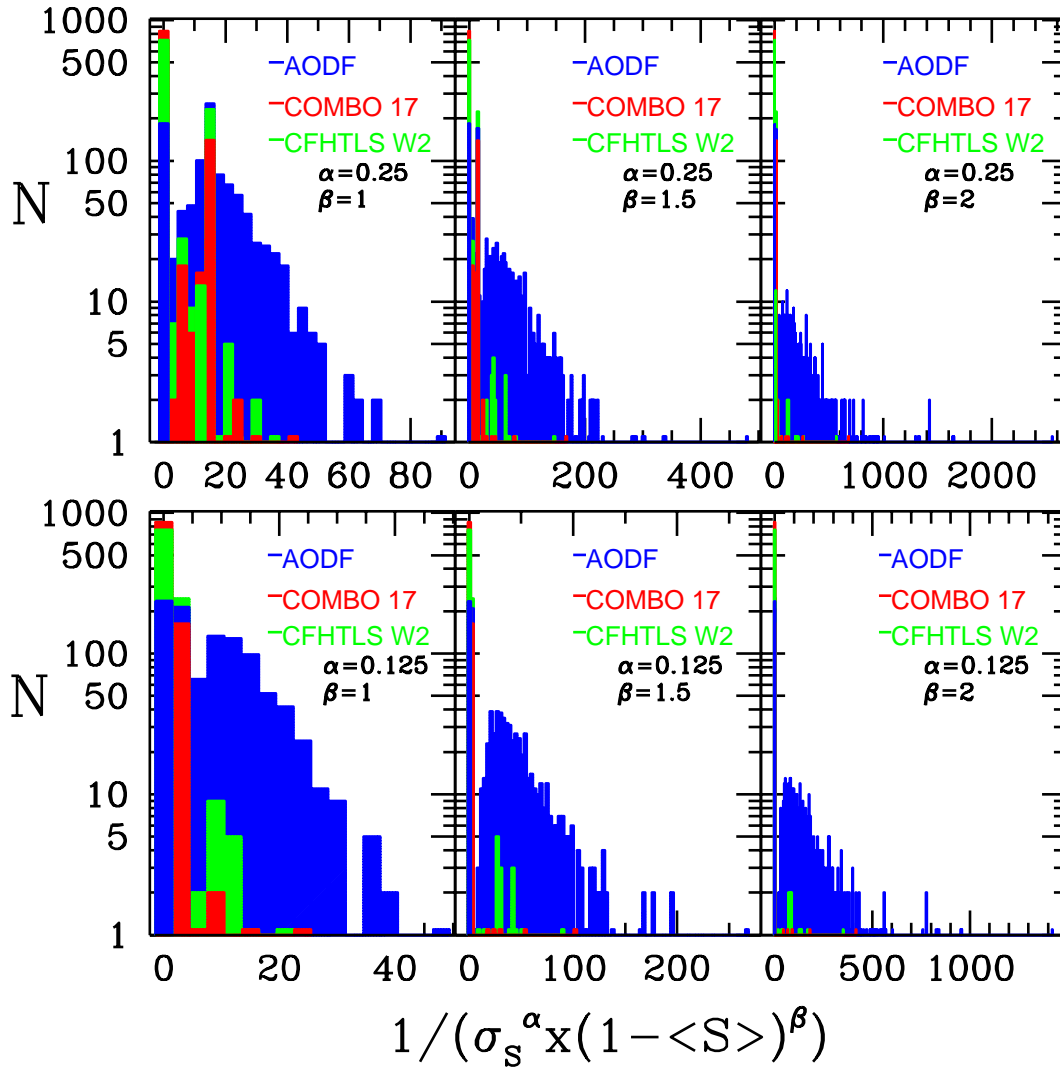


Figure 5.15 Distribution of our Strehl-related figure of merit for $55' \times 55'$ AODF (black), COMBO 17 (red) field, and the $1^\circ \times 1^\circ$ subfield of CFHT W2 (green). Data points are binned according to their figure of merit value in 3 (units) wide bins. Ordinate represents the number of pointings contained in individual bin. In each panel the figure of merit is defined by different combination of the two exponents (Eq. 5.3). All panels correspond to a guide star magnitude limit of 16.5 mag in R -band (foreseen bright time limit for the Gemini GeMS MCAO system).

view ($\sigma_S \lesssim 2\%$). Since our analysis relies only on relative comparisons between different fields, our overall conclusions seem quite robust to the specific choices of the exponents.

Acknowledgements

ID and RGA thank NSERC, the Government of Ontario, and the Canada Foundation for Innovation for funding. We thank Sidney van den Bergh, Chuck Steidel and Thierry Contini for interesting discussions. This work is based in part on data products produced at the TERAPIX data center located at IAP.

Table 5.1. Properties of the 67 $55' \times 55'$ fields optimized for AO surveys

# ^a	R.A. h m s	Dec. ° ' "	Σ_{sc} min ⁻²	$\sigma_{\Sigma_{sc}}$ min ⁻²	$\gamma_1(\Sigma_{sc})^b$	$\gamma_2(\Sigma_{sc})^c$	$E(B-V)$ mag	$\sigma_{E(B-V)}$ mag	$\gamma_1(E(B-V))^d$	$\gamma_2(E(B-V))^e$
8273	08 01 55.8886	-14 35 51.1368	0.6529	0.1159	0.2201	-0.1935	0.0778	0.0082	0.6996	-0.3415
8276	08 05 33.3355	-14 52 48.6047	0.6648	0.1331	0.0565	-0.2372	0.0692	0.0069	0.4663	-0.6372
8328	07 24 02.6662	-01 27 14.4438	0.7243	0.1199	0.7418	0.6834	0.0842	0.0116	0.5841	-0.3379
16758	19 26 57.2356	-21 00 06.8527	0.6512	0.1322	0.4283	0.5339	0.0847	0.0046	-0.0902	-0.1311
16759	19 25 39.0129	-20 08 11.7480	0.6886	0.1399	0.1533	-0.1122	0.0865	0.0051	0.1163	-0.2162
16760	19 26 03.2858	-23 06 02.0956	0.6552	0.1361	0.1152	-0.6959	0.0830	0.0060	0.9076	1.2258
16807	19 13 28.5182	-33 29 53.6142	0.6836	0.1144	-0.2496	-0.1904	0.0754	0.0082	0.1264	-0.7768
16813	19 09 30.5475	-33 53 54.2514	0.6698	0.1095	0.6056	-0.2252	0.0864	0.0063	0.7165	0.3145
17007	18 45 32.0045	-44 18 15.3369	0.6625	0.1077	0.2454	0.0127	0.0689	0.0101	0.6913	-0.5662
17013	18 51 34.5808	-39 41 51.5158	0.6859	0.1354	0.4643	-0.2977	0.0791	0.0087	0.0751	-1.2020
17016	18 48 11.6290	-43 03 10.6952	0.6493	0.1335	0.3393	-0.0503	0.0782	0.0082	-0.3202	0.7728
17018	18 43 39.3947	-43 27 05.7019	0.6668	0.1345	0.5197	-0.5390	0.0778	0.0079	0.0102	-0.8005
17019	18 41 51.8111	-42 35 40.4388	0.8053	0.1637	0.7161	0.2299	0.0776	0.0120	0.4575	-1.0243
17020	18 44 35.3906	-41 20 37.7884	0.7226	0.1468	0.7250	1.1223	0.0843	0.0088	0.6999	1.2784
17021	18 42 54.1928	-40 28 59.3417	0.8050	0.1526	0.7322	0.2712	0.0815	0.0065	1.0337	0.9215
17022	18 40 08.9584	-41 44 00.6738	0.8661	0.1679	0.2980	-0.7967	0.0764	0.0052	0.1027	-0.6874
17023	18 38 30.5484	-40 52 07.4231	0.8916	0.1350	-0.0433	0.2787	0.0826	0.0084	0.6570	-0.2598
17075	18 27 58.8002	-51 47 48.6539	0.6516	0.1194	0.2052	0.3915	0.0738	0.0107	1.0010	0.0506
17077	18 29 04.8143	-49 41 42.1637	0.6572	0.1124	0.0020	-0.2874	0.0737	0.0046	0.5543	0.9716
17078	18 25 53.1372	-50 56 23.1299	0.7260	0.1587	0.1519	-0.6180	0.0728	0.0065	-0.5469	0.1232
17079	18 23 54.2239	-50 04 40.8792	0.7656	0.1402	-0.0137	-0.8646	0.0845	0.0096	-0.1007	-1.2872
17091	18 40 01.0208	-46 48 19.8550	0.7031	0.1157	0.1433	-0.0895	0.0696	0.0072	0.7903	0.8552
17093	18 40 53.8719	-44 42 07.6520	0.6906	0.1311	-0.1203	-0.3673	0.0713	0.0081	0.4937	-0.7466
17094	18 38 04.1331	-45 57 07.0615	0.6536	0.1029	0.1297	-0.5615	0.0657	0.0101	0.1336	-0.9206
17095	18 36 12.7661	-45 05 38.2141	0.7593	0.1210	0.2531	-0.5653	0.0598	0.0056	0.5337	0.7193
17096	18 37 08.7827	-48 03 18.3032	0.7012	0.1389	0.4229	0.0800	0.0535	0.0046	0.8826	0.2867
17097	18 35 09.7115	-47 12 03.1888	0.7124	0.1380	0.4046	-0.0505	0.0557	0.0060	0.4347	-0.0656
17098	18 32 10.1262	-48 26 55.1962	0.7240	0.1214	0.1241	-0.4096	0.0649	0.0045	0.2076	-0.1427
<i>17099</i>	<i>18 30 14.9620</i>	<i>-47 35 20.7596</i>	<i>0.6929</i>	<i>0.1318</i>	<i>0.0147</i>	<i>-0.3991</i>	<i>0.0533</i>	<i>0.0081</i>	<i>0.6250</i>	<i>0.7012</i>
17100	18 33 16.4493	-46 20 31.8008	0.7921	0.1450	0.1766	-0.4501	0.0741	0.0107	0.4304	-0.6588
17101	18 31 28.6253	-45 28 45.3891	0.8453	0.1615	0.5415	-0.0136	0.0630	0.0063	0.3935	-0.4720
17102	18 28 25.4970	-46 43 31.1481	0.8691	0.1763	0.2818	-0.8206	0.0679	0.0122	-0.0426	-0.9224
17103	18 26 41.3603	-45 51 27.5153	0.7914	0.1501	0.4085	-0.2372	0.0764	0.0106	0.2804	-0.1952
17104	18 39 04.4069	-43 50 40.8234	0.7537	0.1431	0.4959	0.3473	0.0722	0.0088	-0.7946	0.6602
17105	18 37 19.8926	-42 58 59.3005	0.7498	0.1416	0.0553	0.0113	0.0795	0.0091	0.4961	-0.1894
17106	18 34 26.5970	-44 13 54.4803	0.8241	0.1198	0.1038	-0.1377	0.0679	0.0176	0.4784	-1.1006
17107	18 32 45.2756	-43 21 56.9586	0.8132	0.1411	0.1348	-0.1838	0.0671	0.0101	0.9592	1.6666
17108	18 35 40.0269	-42 07 04.1409	0.8770	0.1726	0.1150	0.3291	0.0752	0.0081	0.4070	-0.0853
17109	18 34 04.5145	-41 14 56.3333	0.8866	0.1687	0.0054	-0.4840	0.0836	0.0080	0.0681	-0.9237
17110	18 31 08.5135	-42 29 46.6791	0.8916	0.1581	0.2791	-0.0116	0.0843	0.0156	0.4232	0.1181
17112	18 29 45.8757	-44 36 45.0522	0.9283	0.1362	0.2869	-0.4116	0.0794	0.0142	0.7674	0.1725
17114	18 25 02.1950	-44 59 10.9323	0.9693	0.1778	0.0847	0.1121	0.0782	0.0067	-0.0307	-0.9453
17115	18 23 27.6851	-44 06 42.3880	0.9336	0.1587	0.2213	-0.2587	0.0824	0.0070	0.9227	1.0957
17116	18 26 34.3634	-42 52 06.7502	0.9180	0.1542	-0.0436	-0.0388	0.0807	0.0062	0.0834	0.0063
17118	18 21 57.5217	-43 14 02.7750	0.9554	0.1916	-1.0498	1.8245	0.0823	0.0109	0.3205	-0.9074
17120	18 27 07.7550	-48 50 04.1290	0.6671	0.1567	0.1793	-0.4337	0.0701	0.0102	0.3642	-0.4607
17121	18 25 16.6832	-47 58 10.7959	0.7111	0.1280	0.2671	-0.0459	0.0710	0.0084	-0.2037	-0.7853
17177	18 50 24.7353	-33 44 49.6317	1.0975	0.1658	0.4016	0.5773	0.0855	0.0122	0.8477	0.3780
17188	18 46 40.5524	-37 07 01.4218	0.8116	0.1389	0.3189	-0.1815	0.0867	0.0083	1.1766	1.7831
<i>17288</i>	<i>18 23 39.5297</i>	<i>-41 06 44.2969</i>	<i>1.2965</i>	<i>0.2105</i>	<i>-0.0562</i>	<i>-0.5628</i>	<i>0.0857</i>	<i>0.0085</i>	<i>0.2818</i>	<i>0.0993</i>
18560	17 30 04.4220	-59 55 39.3082	0.8774	0.1563	1.0359	4.7730	0.0865	0.0058	0.3543	0.7979
22659	20 34 01.8777	+18 41 40.5432	0.7140	0.1193	0.1133	-0.0646	0.0842	0.0115	0.1667	-0.8588
22665	20 30 15.9096	+18 28 26.4926	0.7461	0.1334	0.5894	0.6151	0.0764	0.0147	0.3505	-0.6854
31486	08 04 54.9932	-15 47 16.2648	0.7365	0.1243	0.4348	-0.4508	0.0674	0.0086	0.8794	-0.2353
31487	08 08 34.1773	-16 03 51.0974	0.6575	0.1107	-0.2133	0.5630	0.0789	0.0076	-0.1390	-0.8436
<i>48510</i>	<i>17 40 30.1826</i>	<i>-61 25 54.5380</i>	<i>0.6592</i>	<i>0.1329</i>	<i>0.3597</i>	<i>-0.8497</i>	<i>0.0716</i>	<i>0.0036</i>	<i>0.4596</i>	<i>0.1084</i>
48511	17 38 41.6103	-60 32 25.4590	0.7031	0.1256	-0.2966	0.1368	0.0800	0.0066	0.0875	-0.9509
48593	17 34 57.5166	-62 37 09.1809	0.6595	0.1102	-0.1926	-0.5202	0.0654	0.0046	0.6758	0.4808

Table 5.1 (cont'd)

# ^a	<i>R.A.</i> h m s	<i>Dec.</i> ° ' "	Σ_{sc} min ⁻²	$\sigma_{\Sigma_{sc}}$ min ⁻²	$\gamma_1(\Sigma_{sc})^b$	$\gamma_2(\Sigma_{sc})^c$	$E(B-V)$ mag	$\sigma_{E(B-V)}$ mag	$\gamma_1(E(B-V))^d$	$\gamma_2(E(B-V))^e$
48594	17 29 01.5184	-63 47 46.8549	0.6850	0.1238	0.1940	-0.5662	0.0771	0.0071	-0.0907	-0.5278
48595	17 27 18.9816	-62 53 54.7870	0.7736	0.1170	0.1161	-1.0970	0.0788	0.0062	-0.3162	-0.2015
48596	17 33 11.4505	-61 43 28.8547	0.7230	0.1231	0.2457	-0.3871	0.0760	0.0115	-0.0218	-1.5210
48597	17 31 34.0292	-60 49 38.5446	0.8235	0.1301	0.2149	-0.4993	0.0808	0.0066	-0.1810	-0.6031
48600	17 21 01.3747	-64 03 37.7765	0.6813	0.1162	0.5003	0.4488	0.0739	0.0062	0.1536	-0.7576
48610	17 00 14.0968	-68 21 58.8538	0.6641	0.1276	-0.1090	-0.6135	0.0768	0.0049	0.0170	-0.8740
48611	16 59 02.2874	-67 27 18.9130	0.6539	0.1090	0.0080	-0.6701	0.0868	0.0055	-0.5483	-0.7081
48915	16 19 26.1713	-71 39 37.6062	0.6536	0.1084	0.2919	-0.7719	0.0806	0.0088	0.9343	0.4950
48918	16 19 40.9547	-70 44 32.6440	0.6883	0.1352	0.8101	-0.0178	0.0843	0.0106	1.0809	-0.0507

^a pixel number based on $N_{side} = 64$ HEALPix partition of the sphere

^b the third moment of distribution (skewness) for star counts surface density

^c the fourth moment of distribution (kurtosis) for star counts surface density

^d the third moment of distribution (skewness) for extinction

^e the fourth moment of distribution (kurtosis) for extinction

Chapter 6

Conclusions and Future Prospects

The structure of early-type galaxies carries important clues about the evolutionary history of these systems. This thesis presents measurements of the changing structural properties of massive quiescent galaxies from $z \sim 2$ down to $z \sim 0$. Although it has been found that both star-forming and quiescent galaxies have smaller radii at higher redshift, this evolution in the $R_e - M_*$ relationship is especially dramatic for quiescent systems. As has been noted by many authors, $z \sim 1 - 2$ massive quiescent galaxies have effective radii that are 2 – 5 times smaller than those of their massive counterparts found locally. This implies that these high- z objects have undergone extreme structural changes without acquiring large amounts of stellar mass. The mechanisms that have been proposed to explain this include (major or minor) dry mergers and adiabatic expansion (caused by stellar winds or quasar activity). None of these mechanisms seem to work perfectly on their own, and hybrid models which combine them to explain the size growth seem to require suspiciously high amounts of fine-tuning. At this point there is no widely accepted explanation for what amounts to pure size evolution of elliptical galaxies at constant mass.

6.1 Thesis summary

This thesis has made a number of contributions to our understanding of galactic size growth. These are listed below according to the chapter in which they are presented.

- **Chapter 3**

- Deep NICMOS F610W observations of a sample of ten GDDS early-type galaxies at $z \sim 1.5$ has allowed us to detect compact systems ($R_e < 1$ kpc) more robustly than is possible with the data obtained in the visible wavelength range (rest-frame UV).
- Although similarly compact massive spheroids have been seen at $z > 2$, this is the first time such systems (three out of ten) have been detected in a rest-frame visible range (Gunn- r band) survey at $z \sim 1.5$.
- Relations such as size vs. mass and stellar mass density vs. size, used to minimize the impact of variations in luminosity and color evolution in stellar populations, show that $1 < z < 2$ passive galaxies have sizes 2 – 5 times smaller (depending on their redshift) and mass densities that are on average an order of magnitude larger than early type galaxies today.
- Since sizes and stellar mass densities of these objects are comparable to the compact distant red galaxies at $2 < z < 3$, they can be the evolved counterparts of the higher-redshift objects.
- Comparison between the size-mass relation at $z \sim 1.5$ with its local counterpart reveals that equal mass dry mergers can only play a limited role in growing early-type galaxies, at least once they are older than a few Gyr; such a process would enlarge galaxy size proportionally to the increase in mass, and the observed high- z and local early-types span the same range of masses.
- One of the alternative mechanisms that can drive galaxy size evolution, the adiabatic expansion triggered by mass loss from evolved A and F-type stars, has been examined in detail. While this process may be important in growing young early-type galaxies, it cannot produce a factor of two growth in the sizes of galaxies as old as those in our survey.

- **Chapter 4**

- Based on the analysis of the size growth of 465 early-type galaxies taken from 17 spectroscopic surveys spanning the redshift range $0.2 < z < 2.7$, the size evolution of passively evolving galaxies is continuous and gradual over this redshift range. Several recent studies of small samples in isolation have found

that only a subset of the early-type galaxies evolve, and this work is the clearest demonstration yet of regular evolution.

- This smooth process of size evolution does not seem to depend on galaxy stellar mass. The mass-normalized galactic half-light radius scales with redshift as $R_e/M_*^{0.51} \propto (1+z)^{-1.62 \pm 0.34}$.
- The mean value of the stellar mass density within one kiloparsec from galactic center, inferred from the best fit Sérsic profile, is increasing approximately linearly with redshift, even if only evolved objects at constant number density are taken into account.
- Brief comparison with the effects that a series of minor mergers and adiabatic expansion can have on the structural properties of quiescent galaxies shows that neither of the two mechanisms on its own can easily reproduce the observational fact that the size growth is a continuous process that has been occurring more-or-less smoothly and gradually over the last 10 Gyr of cosmic time.

- **Chapter 5**

- Internal velocity dispersion measurements of compact galaxies are a powerful tool in discriminating between evolutionary paths for these objects. Resolved spectroscopic observations will produce spatially resolved velocity maps and the stellar properties of these objects as functions of their galactocentric distance. However, even in the era of 30m-class telescopes, this will only be possible for objects close to natural guide stars. In order to construct statistical samples of compact galaxies with measured dynamical and stellar population properties on sub-kpc scale, future surveys will need to concentrate on the regions of the sky densely populated with natural guide stars.
- A combination of stellar count surface density and extinction maps has been used to identify 67 low Galactic latitude fields with remarkably low extinction, 1 square degree area (suitable to reduce the effect of cosmic variance), and a mix of many $R = 13 - 16.5$ mag, suitable for AO-assisted observations, but few < 8 mag stars (important for minimizing saturation and scattering).
- The number of natural guide stars per square arcminute is on average 15 times higher in this set of AO-friendly fields than in any of the existing deep fields.

Furthermore, the mean level of extinction in the fields and in the existing deep fields is comparable.

- A single one square degree equatorial field (the Adaptive Optics Deep Field [AODF] centered at RA: $7^{\text{h}}24^{\text{m}}3^{\text{s}}$, Dec: $-1^{\circ}27'15''$) seems particularly promising for extragalactic AO work.
- An analysis based on simulations designed to estimate the performance of the Gemini MCAO system (software kindly provided by F. Rigaut) quantifies the enormous benefits of undertaking AO observations in the proposed optimized fields. This analysis shows that for geometries of natural guide stars which produce spatially stable high Strehl ratio PSFs, the dark time sky coverage in the AODF is essentially 100% using the Gemini MCAO system, which is over 50 times higher than for most existing deep fields.

6.2 Future work

This section gives brief outlines of several future avenues that can (and will) be undertaken in order to extend the work in this thesis.

6.2.1 Size evolution as a function of galaxy age and of galaxy ellipticity

Since we have compiled a large sample of early-type objects with confirmed spectroscopic redshifts, this sample will be used to investigate other questions about the size evolution of quiescent systems that have recently emerged. One inconsistency found in several recent studies is the connection between galaxy compactness and age (see § 4.5.3 for details). We will employ the stellar population modelling code used by Glazebrook et al. (2004) to measure masses of the GDDS sample (presented in Chapters 3 and 4) to test the proposed connection between compactness and age, with the goal of better understanding the role that adiabatic expansion plays in the size growth of these systems.

Ellipticities are measured for a subset of our data. Recent results reported by van der Wel et al. (2011), based on a sample of 14 high redshift quiescent galaxies, claim that a significant fraction ($\gtrsim 50\%$) of those objects are disk dominated. These authors conclude

that the most plausible scenario for the evolution of these objects from $z \sim 2$ to $z = 0$ is the one that combines major dry merging with accretion of low mass density stellar material (minor mergers). The subset of our sample which can be compared to the small number of $z \sim 2$ galaxies in van der Wel et al. (2011) is at least an order of magnitude larger and spans a range of redshifts. We plan to test the van der Wel et al. (2011) results with our data and map out the change in fraction of disks among quiescent galaxies with redshift.

6.2.2 Environment of compact ellipticals

Some theoretical considerations suggest that minor mergers or accretions cannot efficiently enlarge galactic radius unless the rates and mass-ratios of mergers are very finely tuned (e.g., Shankar et al., 2010). One can envision that this idea can be tested by investigating galaxy sizes in rich environments. For example, it is conceivable that a higher number of ‘fly-by’ events in clusters could help galaxies grow in size by adding (small amounts of) stellar material to their outskirts during each encounter. We will use the existing GDDS photometric catalog (Abraham et al., 2004), augmented with photometry in medium-band NIR filters (van Dokkum et al., 2009b), to determine more precise photometric redshifts for hundreds of objects in the four GDDS fields (total area 120 arcmin²) and find distances to the nearest neighbours for compact and normal ellipticals. The medium-band NIR filters, now available for the FourStar NIR Camera on the Magellan Baade Telescope, will help us to achieve much more accurate photometric redshifts at $z > 1.5$. The augmented photometric redshift will also be used to select targets for a planned spectroscopic study of compact quiescent galaxies with GMOS on Gemini North Telescope.

6.2.3 Velocity dispersions and chemical composition of compact ellipticals at high redshifts

Our team has been granted guaranteed science-verification commissioning time on the (long-delayed) red-sensitive Hamamatsu CCD devices that are coming on-line at the Gemini North Telescope. (Commissioning of these is now scheduled for 2012). We will use this time to measure velocity dispersions and chemical abundances for a subset of compact and normal quiescent ellipticals with confirmed spectroscopic redshifts $z \lesssim 1.2$

in one GDDS field. We will be targeting age indicators, such as $H\gamma$ λ 4341 Å and $H\delta$ λ 4102 Å absorption lines, that are tracers of recent star formation. This data set will put tighter constraints on the stellar age distributions in two galaxy populations and determine the time scales of their mass assembly. Based on the results of this pilot program, this deep spectroscopic survey may be extended to all four GDDS fields and include hundreds of objects from our photo- z catalog.

6.2.4 Spatially resolved chemical and dynamical properties of the most compact ellipticals in the local Universe

As described in § 1.2, in order to better understand how compact quiescent galaxies assemble their stellar masses we require spatially resolved information. High resolution HST imaging using combinations of ACS and WFC3 filters will be able to provide more insight into the spatial distribution of young and old stellar populations in these objects. However, spatially resolved chemical abundances and velocity dispersion maps for quiescent high- z galaxies will only become available when (if?) JWST, carrying the NIRSPEC IFU, and/or 30m-class telescopes come on-line. In the meantime, ground based IFUs can be used to probe resolved dynamical and chemical characteristics of a small sample of compact elliptical galaxies that has been reported recently at redshifts $z \sim 0.05$ (Valentinuzzi et al., 2010a) and $z \sim 0.1$ (Trujillo et al., 2009). These systems are the closest match to the high- z compact early-type objects in both parameters of the size-mass phase space: they are massive ($M_* > 10^{10} M_\odot$) and have small effective radii ($R_e \gtrsim 1$ kpc). The combination of high stellar masses and small physical sizes of these objects boosts their surface brightness and makes them the perfect targets for IFU follow-up observations. It has been reported that some of these local objects have extended low surface brightness envelopes (Shih & Stockton, 2011). They can be produced by re-distribution of existing stars from the central regions of the galaxy during a major merger event, or by the smooth and steady accretion of low surface brightness material after the formation of a compact core. In the former scenario, spatially resolved spectroscopy should reveal positive age and negative metallicity gradient from the core to the galaxy outskirts. In the latter case, we expect negative gradients for the age of stellar populations and positive gradients for their metallicity. The results of an IFU survey targeting these objects will provide an interesting local comparison/calibration

sample for spatially resolved high- z observations.

6.2.5 The development of the Adaptive Optics Deep Field

Our exploration of the AODF (described in Chapter 5) will start in December 2011 with imaging in five bands covering the visible wavelength range, $Ugriz$, using the Wide Field Camera on the 2.5m Isaac Newton Telescope on La Palma (PI: J. Brinchmann). In order to obtain accurate photometric redshifts and galaxy parameters for a large sample of objects, we will also need to conduct deep NIR imaging and to augmented these data with spectroscopic follow up studies using a multi-object spectrograph. The full data set will allow us to construct a sample of thousands of high-redshift galaxies, with known stellar masses, ages, extinctions, and star-formation rates. Essentially all of these objects will be available for follow-up AO-based high resolution imaging or IFU spectroscopy, since almost every galaxy will have several suitable natural guide stars nearby.

Bibliography

Abazajian, K. N., Adelman-McCarthy, J. K., Agüeros, M. A., Allam, S. S., Prieto, C. A., An, D., Anderson, K. S. J., Anderson, S. F., Annis, J., Bahcall, N. A., Bailer-Jones, C. A. L., Barentine, J. C., Bassett, B. A., Becker, A. C., Beers, T. C., Bell, E. F., Belokurov, V., Berlind, A. A., Berman, E. F., Bernardi, M., Bickerton, S. J., Bizyaev, D., Blakeslee, J. P., Blanton, M. R., Bochanski, J. J., Boroski, W. N., Brewington, H. J., Brinchmann, J., Brinkmann, J., Brunner, R. J., Budavári, T., Carey, L. N., Carliles, S., Carr, M. A., Castander, F. J., Cinabro, D., Connolly, A. J., Csabai, I., Cunha, C. E., Czarapata, P. C., Davenport, J. R. A., de Haas, E., Dilday, B., Doi, M., Eisenstein, D. J., Evans, M. L., Evans, N. W., Fan, X., Friedman, S. D., Frieman, J. A., Fukugita, M., Gänsicke, B. T., Gates, E., Gillespie, B., Gilmore, G., Gonzalez, B., Gonzalez, C. F., Grebel, E. K., Gunn, J. E., Györy, Z., Hall, P. B., Harding, P., Harris, F. H., Harvanek, M., Hawley, S. L., Hayes, J. J. E., Heckman, T. M., Hendry, J. S., Hennessy, G. S., Hindsley, R. B., Hoblitt, J., Hogan, C. J., Hogg, D. W., Holtzman, J. A., Hyde, J. B., Ichikawa, S.-i., Ichikawa, T., Im, M., Ivezić, v., Jester, S., Jiang, L., Johnson, J. A., Jorgensen, A. M., Jurić, M., Kent, S. M., Kessler, R., Kleinman, S. J., Knapp, G. R., Konishi, K., Kron, R. G., Krzesinski, J., Kuropatkin, N., Lampeitl, H., Lebedeva, S., Lee, M. G., Lee, Y. S., Leger, R. F., Lépine, S., Li, N., Lima, M., Lin, H., Long, D. C., Loomis, C. P., Loveday, J., Lupton, R. H., Magnier, E., Malanushenko, O., Malanushenko, V., Mandelbaum, R., Margon, B., Marriner, J. P., Martínez-Delgado, D., Matsubara, T., McGehee, P. M., McKay, T. A., Meiksin, A., Morrison, H. L., Mullally, F., Munn, J. A., Murphy, T., Nash, T., Nebot, A., Neilsen, E. H., Newberg, H. J., Newman, P. R., Nichol, R. C., Nicinski, T., Nieto-Santisteban, M., Nitta, A., Okamura, S., Oravetz, D. J., Ostriker, J. P., Owen, R., Padmanabhan, N., Pan, K., Park, C., Pauls, G., Peoples, J., Percival, W. J., Pier, J. R., Pope, A. C., Pourbaix, D., Price, P. A., Purger, N., Quinn, T., Raddick, M. J., Fiorentin, P. R., Richards, G. T., Richmond, M. W., Riess, A. G., Rix, H.-W., Rockosi, C. M., Sako, M., Schlegel, D. J.,

- Schneider, D. P., Scholz, R.-D., Schreiber, M. R., Schwobe, A. D., Seljak, U., Sesar, B., Sheldon, E., Shimasaku, K., Sibley, V. C., Simmons, A. E., Sivarani, T., Smith, J. A., Smith, M. C., Smolčić, V., Snedden, S. A., Stebbins, A., Steinmetz, M., Stoughton, C., Strauss, M. A., SubbaRao, M., Suto, Y., Szalay, A. S., Szapudi, I., Szkody, P., Tanaka, M., Tegmark, M., Teodoro, L. F. A., Thakar, A. R., Tremonti, C. A., Tucker, D. L., Uomoto, A., Vanden Berk, D. E., Vandenberg, J., Vidrih, S., Vogeley, M. S., Voges, W., Vogt, N. P., Wadadekar, Y., Watters, S., Weinberg, D. H., West, A. A., White, S. D. M., Wilhite, B. C., Wonders, A. C., Yanny, B., Yocum, D. R., York, D. G., Zehavi, I., Zibetti, S., & Zucker, D. B. 2009, *The Astrophysical Journal Supplement Series*, 182, 543
- Abraham, R. G., Glazebrook, K., McCarthy, P. J., Crampton, D., Murowinski, R., Jørgensen, I., Roth, K., Hook, I. M., Savaglio, S., Chen, H.-W., Marzke, R. O., & Carlberg, R. G. 2004, *The Astronomical Journal*, 127, 2455
- Abraham, R. G., Nair, P., McCarthy, P. J., Glazebrook, K., Mentuch, E., Yan, H., Savaglio, S., Crampton, D., Murowinski, R., Juneau, S., Le Borgne, D., Carlberg, R. G., J, I., Roth, K., Chen, H., & Marzke, R. O. 2007, *The Astrophysical Journal*, 669, 184
- Alcal, J. M., Pannella, M., Puddu, E., Radovich, M., Silvotti, R., Arnaboldi, M., Cappacioli, M., Covone, G., Dall’Ora, M., De Lucia, G., Grado, A., Longo, G., Mercurio, A., Musella, I., Napolitano, N., Pavlov, M., Rifatto, A., Ripepi, V., & Scaramella, R. 2004, *Astronomy and Astrophysics*, 428, 339
- Arnouts, S., Walcher, C. J., Le Fèvre, O., Zamorani, G., Ilbert, O., Le Brun, V., Pozzetti, L., Bardelli, S., Tresse, L., Zucca, E., Charlot, S., Lamareille, F., McCracken, H. J., Bolzonella, M., Iovino, A., Lonsdale, C., Polletta, M., Surace, J., Bottini, D., Garilli, B., Maccagni, D., Picat, J. P., Scaramella, R., Scodreggio, M., Vettolani, G., Zanichelli, A., Adami, C., Cappi, A., Ciliegi, P., Contini, T., de la Torre, S., Foucaud, S., Franzetti, P., Gavignaud, I., Guzzo, L., Marano, B., Marinoni, C., Mazure, A., Meneux, B., Merighi, R., Paltani, S., Pellò, R., Pollo, A., Radovich, M., Tempurin, S., & Vergani, D. 2007, *Astronomy and Astrophysics*, 476, 137
- Assémat, F., Gendron, E., & Hammer, F. 2007, *Monthly Notices of the Royal Astronomical Society*, 376, 287

- Baldry, I. K. & Glazebrook, K. 2003, *The Astrophysical Journal*, 593, 258
- Baldry, I. K., Glazebrook, K., Brinkmann, J., Ivezić, v., Lupton, R. H., Nichol, R. C., & Szalay, A. S. 2004, *The Astrophysical Journal*, 600, 681
- Baldry, I. K., Glazebrook, K., & Driver, S. P. 2008, *Monthly Notices of the Royal Astronomical Society*, 388, 945
- Baumgardt, H. & Kroupa, P. 2007, *Monthly Notices of the Royal Astronomical Society*, 380, 1589
- Bell, E., McIntosh, D., Barden, M., Wolf, C., Caldwell, J., Rix, H., Beckwith, S., Borch, A., Häussler, B., Jahnke, K., & Others. 2004a, *The Astrophysical Journal Letters*, 600, L11
- Bell, E., Naab, T., McIntosh, D., Somerville, R., Caldwell, J., Barden, M., Wolf, C., Rix, H., Beckwith, S., Borch, A., & Others. 2006a, *The Astrophysical Journal*, 640, 241
- Bell, E. F., Phleps, S., Somerville, R. S., Wolf, C., Borch, A., & Meisenheimer, K. 2006b, *The Astrophysical Journal*, 652, 270
- Bell, E. F., Wolf, C., Meisenheimer, K., Rix, H., Borch, A., Dye, S., Kleinheinrich, M., Wisotzki, L., & McIntosh, D. H. 2004b, *The Astrophysical Journal*, 608, 752
- Bernardi, M., Nichol, R. C., Sheth, R. K., Miller, C. J., & Brinkmann, J. 2006, *The Astronomical Journal*, 131, 1288
- Bernardi, M., Sheth, R., Annis, J., Burles, S., Eisenstein, D., Finkbeiner, D., Hogg, D., Lupton, R., Schlegel, D., SubbaRao, M., & Others. 2003a, *The Astronomical Journal*, 125, 1849
- Bernardi, M., Sheth, R. K., Annis, J., Burles, S., Eisenstein, D. J., Finkbeiner, D. P., Hogg, D. W., Lupton, R. H., Schlegel, D. J., SubbaRao, M., Bahcall, N. A., Blakeslee, J. P., Brinkmann, J., Castander, F. J., Connolly, A. J., Csabai, I., Doi, M., Fukugita, M., Frieman, J., Heckman, T., Hennessy, G. S., Ivezić, v., Knapp, G. R., Lamb, D. Q., McKay, T., Munn, J. A., Nichol, R., Okamura, S., Schneider, D. P., Thakar, A. R., & York, D. G. 2003b, *The Astronomical Journal*, 125, 1817
- Bertin, E., Mellier, Y., Radovich, M., Missonnier, G., Didelon, P., & Morin, B. 2002, *Astronomical Data Analysis Software and Systems XI*, 281

- Bessell, M. S. 1979, *Publications of the Astronomical Society of the Pacific*, 91, 589
- Bezanson, R., van Dokkum, P. G., Tal, T., Marchesini, D., Kriek, M., Franx, M., & Coppi, P. 2009, *The Astrophysical Journal*, 697, 1290
- Blumenthal, G. R., Faber, S. M., Primack, J. R., & Rees, M. J. 1984, *Nature*, 311, 517
- Bonaccini, D., Hackenberg, W., Cullum, M., Quattri, M., Brunetto, E., Quentin, J., Koch, F., Allaert, E., & van Kesteren, A. 1999, *The Messenger*, 98, 8
- Bournaud, F., Elmegreen, B. G., & Elmegreen, D. M. 2007, *The Astrophysical Journal*, 670, 237
- Bouwens, R. J., Illingworth, G. D., Franx, M., Chary, R.-R., Meurer, G. R., Conselice, C. J., Ford, H., Giavalisco, M., & van Dokkum, P. 2009, *The Astrophysical Journal*, 705, 936
- Bouwens, R. J., Illingworth, G. D., González, V., Labbé, I., Franx, M., Conselice, C. J., Blakeslee, J., van Dokkum, P., Holden, B., Magee, D., Marchesini, D., & Zheng, W. 2010, *The Astrophysical Journal*, 725, 1587
- Bower, R., Benson, A., Malbon, R., Helly, J., Frenk, C., Baugh, C., Cole, S., & Lacey, C. 2006, *Monthly Notices of the Royal Astronomical Society*, 370, 645
- Boylan-Kolchin, M., Ma, C., & Quataert, E. 2005, *Monthly Notices of the Royal Astronomical Society*, 362, 184
- Boylan-Kolchin, M., Ma, C.-P., & Quataert, E. 2006, *Monthly Notices of the Royal Astronomical Society*, 369, 1081
- Brammer, G., Whitaker, K., van Dokkum, P., Marchesini, D., Franx, M., Kriek, M., Labbe, I., Lee, K., Muzzin, A., Quadri, R., & Others. 2011, Arxiv preprint arXiv:1104.2595
- Brown, M., Dey, A., Jannuzi, B., Brand, K., Benson, A., Brodwin, M., Croton, D., & Eisenhardt, P. 2007, *The Astrophysical Journal*, 654, 858
- Brown, M., Dey, A., Jannuzi, B., Lauer, T., Tiede, G., & Mikles, V. 2003, *The Astrophysical Journal*, 597, 225

- Buitrago, F., Trujillo, I., Conselice, C. J., Bouwens, R. J., Dickinson, M., & Yan, H. 2008, *The Astrophysical Journal*, 687, L61
- Bundy, K., Fukugita, M., Ellis, R. S., Targett, T. a., Belli, S., & Kodama, T. 2009, *The Astrophysical Journal*, 697, 1369
- Bundy, K., Treu, T., & Ellis, R. S. 2007, *The Astrophysical Journal*, 665, L5
- Cappellari, M., di Serego Alighieri, S., Cimatti, a., Daddi, E., Renzini, a., Kurk, J. D., Cassata, P., Dickinson, M., Franceschini, a., Mignoli, M., Pozzetti, L., Rodighiero, G., Rosati, P., & Zamorani, G. 2009, *The Astrophysical Journal*, 704, L34
- Carrasco, E. R., Conselice, C. J., & Trujillo, I. 2010, *Monthly Notices of the Royal Astronomical Society*, 405, 2253
- Cassata, P., Cimatti, A., Kurk, J., Rodighiero, G., Pozzetti, L., Bolzonella, M., Daddi, E., Mignoli, M., Berta, S., Dickinson, M., Franceschini, A., Halliday, C., Renzini, A., Rosati, P., & Zamorani, G. 2008, *Astronomy and Astrophysics*, 483, L39
- Cassata, P., Giavalisco, M., Guo, Y., Ferguson, H., Koekemoer, A. M., Renzini, A., Fontana, A., Salimbeni, S., Dickinson, M., Casertano, S., Conselice, C. J., Grogin, N., Lotz, J. M., Papovich, C., Lucas, R. A., Straughn, A., Gardner, J. P., & Moustakas, L. 2010, *The Astrophysical Journal*, 714, L79
- Cassata, P., Giavalisco, M., Guo, Y., Renzini, A., Ferguson, H., Koekemoer, A., Salimbeni, S., Scarlata, C., Grogin, N., Conselice, C., & Others. 2011, *Arxiv preprint arXiv:1106.4308*
- Chen, H., Marzke, R., McCarthy, P., Martini, P., Carlberg, R., Persson, S., Bunker, A., Bridge, C., & Abraham, R. 2003, *The Astrophysical Journal*, 586, 745
- Cimatti, A., Cassata, P., Pozzetti, L., Kurk, J., Mignoli, M., Renzini, A., Daddi, E., Bolzonella, M., Brusa, M., Rodighiero, G., Dickinson, M., Franceschini, A., Zamorani, G., Berta, S., Rosati, P., & Halliday, C. 2008, *Astronomy and Astrophysics*, 482, 21
- Cimatti, A., Daddi, E., Mignoli, M., Pozzetti, L., Renzini, A., Zamorani, G., Broadhurst, T., Fontana, A., Saracco, P., Poli, F., Cristiani, S., D'Odorico, S., Giallongo, E., Gilmozzi, R., & Menci, N. 2002, *Astronomy and Astrophysics*, 381, L68

- Cimatti, A., Daddi, E., Renzini, A., Cassata, P., Vanzella, E., Pozzetti, L., Cristiani, S., Fontana, A., Rodighiero, G., Mignoli, M., & Zamorani, G. 2004, *Nature*, 430, 184
- Ciotti, L. & Bertin, G. 1999, *Astronomy and Astrophysics*, 352, 447
- Cooper, M. C., Newman, J. A., Weiner, B. J., Yan, R., Willmer, C. N. A., Bundy, K., Coil, A. L., Conselice, C. J., Davis, M., Faber, S. M., Gerke, B. F., Guhathakurta, P., Koo, D. C., & Noeske, K. G. 2007, *Monthly Notices of the Royal Astronomical Society*, 383, 1058
- Coupon, J., Ilbert, O., Kilbinger, M., McCracken, H. J., Mellier, Y., Arnouts, S., Bertin, E., Hudelot, P., Schultheis, M., Le Fèvre, O., Le Brun, V., Guzzo, L., Bardelli, S., Zucca, E., Bolzonella, M., Garilli, B., Zamorani, G., Zanichelli, A., Tresse, L., & Aussel, H. 2009, *Astronomy and Astrophysics*, 500, 981
- Cowie, L., Hu, E., & Songaila, A. 1995, *Astronomical Journal*, 110, 1576
- Cowie, L. L., Songaila, A., Hu, E. M., & Cohen, J. G. 1996, *The Astronomical Journal*, 112, 839
- Daddi, E., Cimatti, A., Renzini, A., Vernet, J., Conselice, C., Pozzetti, L., Mignoli, M., Tozzi, P., Broadhurst, T., di Serego Alighieri, S., & Others. 2004, *The Astrophysical Journal Letters*, 600, L127
- Daddi, E., Dickinson, M., Chary, R., Pope, A., Morrison, G., Alexander, D., Bauer, F., Brandt, W., Giavalisco, M., Ferguson, H., & Others. 2005a, *The Astrophysical Journal Letters*, 631, L13
- Daddi, E., Renzini, a., Pirzkal, N., Cimatti, a., Malhotra, S., Stiavelli, M., Xu, C., Pasquali, a., Rhoads, J. E., Brusa, M., di Serego Alighieri, S., Ferguson, H. C., Koekoemoer, a. M., Moustakas, L. a., Panagia, N., & Windhorst, R. a. 2005b, *The Astrophysical Journal*, 626, 680
- Damjanov, I., Abraham, R. G., Glazebrook, K., Mccarthy, P. J., Carlberg, R. G., Chen, H.-w., Crampton, D., Green, A. W., Jørgensen, I., Juneau, S., Le Borgne, D., Marzke, R. O., Mentuch, E., Murowinski, R., Roth, K., Savaglio, S., & Yan, H. 2011a, *Arxiv preprint arXiv:1108.0656*

- Damjanov, I., Abraham, R. G., Glazebrook, K., McGregor, P., Rigaut, F., McCarthy, P. J., Brinchmann, J., Cuillandre, J.-C., Mellier, Y., McCracken, H. J., Hudelot, P., & Monet, D. 2011b, *Publications of the Astronomical Society of the Pacific*, 123, 348
- Damjanov, I., McCarthy, P. J., Abraham, R. G., Glazebrook, K., Yan, H., Mentuch, E., Le Borgne, D., Savaglio, S., Crampton, D., Murowinski, R., Juneau, S., Carlberg, R. G., Jørgensen, I., Roth, K., Chen, H.-W., & Marzke, R. O. 2009, *The Astrophysical Journal*, 695, 101
- Davies, R., Rabien, S., Lidman, C., Louarn, M., Kasper, M., Schreiber, N., Roccatagliata, V., Ageorges, N., Amico, P., Dumas, C., & Others. 2008, *The Messenger*, 131, 7
- Davis, M., Guhathakurta, P., Konidaris, N., Newman, J., Ashby, M., Biggs, A., Barmby, P., Bundy, K., Chapman, S., Coil, A., & Others. 2007, *The Astrophysical Journal Letters*, 660, L1
- De Lucia, G. & Blaizot, J. 2007, *Monthly Notices of the Royal Astronomical Society*, 375, 2
- De Propris, R., Driver, S. P., Colless, M., Drinkwater, M. J., Loveday, J., Ross, N. P., Bland-Hawthorn, J., York, D. G., & Pimblet, K. 2010, *The Astronomical Journal*, 139, 794
- de Vaucouleurs, G. 1948, *Annales d'Astrophysique*, 11
- de Vaucouleurs, G., de Vaucouleurs, A., & Corwin, H. G. 1976, *University of Texas Monographs in Astronomy*
- Desroches, L.-B., Quataert, E., Ma, C.-P., & West, A. A. 2007, *Monthly Notices of the Royal Astronomical Society*, 377, 402
- di Serego Alighieri, S., Vernet, J., Cimatti, A., Lanzoni, B., Cassata, P., Ciotti, L., Daddi, E., Mignoli, M., Pignatelli, E., Pozzetti, L., Renzini, A., Rettura, A., & Zamorani, G. 2005, *Astronomy and Astrophysics*, 442, 125
- Dickinson, M., Giavalisco, M., & Team, T. 2003a, *ESO/USM Workshop "The Mass of Galaxies at Low and High Redshift"* (Venice, Italy, October 2001), eds. R. Bender and A. Renzini, 324

- Dickinson, M., Papovich, C., Ferguson, H., & Budavari, T. 2003b, *The Astrophysical Journal*, 587, 25
- Djorgovski, S. & Davis, M. 1987, *The Astrophysical Journal*, 313, 59
- Dressler, A., Lynden-Bell, D., Burstein, D., Davies, R., Faber, S., Terlevich, R., & Wegner, G. 1987, *The Astrophysical Journal*, 313, 42
- Driver, S. & Robotham, A. 2010, *Monthly Notices of the Royal Astronomical Society*, 407, 2131
- Drory, N., Feulner, G., Bender, R., Botzler, C., Hopp, U., Maraston, C., Mendes de Oliveira, C., & Snigula, J. 2001, *Monthly Notices of the Royal Astronomical Society*, 325, 550
- Efstathiou, G. & Silk, J. 1983, *Fundamentals of Cosmic Physics* (ISSN 0094-5846), 9, 1
- Egami, E., Dole, H., Huang, J., PerezGonzalez, P., Le Floch, E., Papovich, C., Barmby, P., Ivison, R. J., Serjeant, S., Mortier, A., Frayer, D. T., Rigopoulou, D., Lagache, G., Rieke, G. H., Willner, S. P., AlonsoHerrero, A., Bai, L., Engelbracht, C. W., Fazio, G. G., Gordon, K. D., Hines, D. C., Misselt, K. A., Miyazaki, S., Morrison, J. E., Rieke, M. J., Rigby, J. R., & Wilson, G. 2004, *The Astrophysical Journal Supplement Series*, 154, 130
- Eggen, O., Lynden-Bell, D., & Sandage, A. 1962, *The Astrophysical Journal*, 136, 748
- Eikenberry, S. S. 2004, *FLAMINGOS-2: the facility near-infrared wide-field imager and multi-object spectrograph for Gemini*, Vol. 5492 (SPIE), 1196–1207
- Eisenstein, D., Hogg, D., Fukugita, M., Nakamura, O., Bernardi, M., Finkbeiner, D., Schlegel, D., Brinkmann, J., Connolly, A., Csabai, I., & Others. 2003, *The Astrophysical Journal*, 585, 694
- Ellerbroek, B. & Tyler, D. 1998, *Publications of the Astronomical Society of the Pacific*, 110, 165
- Ellerbroek, B. L. 2003, *MCAO for Gemini South*, Vol. 4839 (SPIE), 55–66
- Ellis, R. S. 1997, *Annual Review of Astronomy and Astrophysics*, 35, 389

- Epinat, B., Contini, T., Le Fèvre, O., Vergani, D., Garilli, B., Amram, P., Queyrel, J., Tasca, L., & Tresse, L. 2009, *Astronomy and Astrophysics*, 504, 789
- Erb, D. K., Steidel, C. C., Shapley, A. E., Pettini, M., Reddy, N. a., & Adelberger, K. L. 2006, *The Astrophysical Journal*, 646, 107
- Faber, S. M. & Jackson, R. E. 1976, *The Astrophysical Journal*, 204, 668
- Faber, S. M., Willmer, C. N. a., Wolf, C., Koo, D. C., Weiner, B. J., Newman, J. a., Im, M., Coil, a. L., Conroy, C., Cooper, M. C., Davis, M., Finkbeiner, D. P., Gerke, B. F., Gebhardt, K., Groth, E. J., Guhathakurta, P., Harker, J., Kaiser, N., Kassin, S., Kleinheinrich, M., Konidaris, N. P., Kron, R. G., Lin, L., Luppino, G., Madgwick, D. S., Meisenheimer, K., Noeske, K. G., Phillips, a. C., Sarajedini, V. L., Schiavon, R. P., Simard, L., Szalay, a. S., Vogt, N. P., & Yan, R. 2007, *The Astrophysical Journal*, 665, 265
- Fan, L., Lapi, A., Bressan, A., Bernardi, M., De Zotti, G., & Danese, L. 2010, *The Astrophysical Journal*, 718, 1460
- Fan, L., Lapi, A., De Zotti, G., & Danese, L. 2008, *The Astrophysical Journal Letters*, 689, L101
- Fasano, G., Cristiani, S., Arnouts, S., & Filippi, M. 1998, *The Astronomical Journal*, 115, 1400
- Fernández Lorenzo, M., Cepa, J., Bongiovanni, A., Pérez García, A. M., Ederoclite, A., Lara-López, M. A., Pović, M., & Sánchez-Portal, M. 2011, *Astronomy and Astrophysics*, 526, A72
- Ferreras, I., Lisker, T., Pasquali, A., & Kaviraj, S. 2009, *Monthly Notices of the Royal Astronomical Society*, 395, 554
- Flicker, R. & Rigaut, F. 2002, in *European Southern Observatory Conference and Workshop Proceedings*, Vol. 58, 377
- Flores, H., Hammer, F., Puech, M., Amram, P., & Balkowski, C. 2006, *Astronomy and Astrophysics*, 455, 107

- Fontana, A., Pozzetti, L., Donnarumma, I., Renzini, A., Cimatti, A., Zamorani, G., Menci, N., Daddi, E., Giallongo, E., Mignoli, M., Perna, C., Salimbeni, S., Saracco, P., Broadhurst, T., Cristiani, S., D'Odorico, S., & Gilmozzi, R. 2004, *Astronomy and Astrophysics*, 424, 23
- Fontana, A., Salimbeni, S., & Grazian, A. 2006, *Astronomy and Astrophysics*, 459, 745
- Förster Schreiber, N. M., Genzel, R., Bouché, N., Cresci, G., Davies, R., Buschkamp, P., Shapiro, K., Tacconi, L. J., Hicks, E. K. S., Genel, S., Shapley, a. E., Erb, D. K., Steidel, C. C., Lutz, D., Eisenhauer, F., Gillessen, S., Sternberg, a., Renzini, a., Cimatti, a., Daddi, E., Kurk, J., Lilly, S., Kong, X., Lehnert, M. D., Nesvadba, N., Verma, a., McCracken, H., Arimoto, N., Mignoli, M., & Onodera, M. 2009, *The Astrophysical Journal*, 706, 1364
- Fruchter, A. & Hook, R. 2002, *Publications of the Astronomical Society of the Pacific*, 114, 144
- Fukugita, M., Hogan, C. J., & Peebles, P. J. E. 1998, *The Astrophysical Journal*, 503, 518
- Fukugita, M., Yasuda, N., Brinkmann, J., Gunn, J. E., Ivezić, v., Knapp, G. R., Lupton, R., & Schneider, D. P. 2004, *The Astronomical Journal*, 127, 3155
- Gallagher III, J., Hunter, D., & Tutukov, A. 1984, *The Astrophysical Journal*, 284, 544
- Gardner, J. P., Mather, J. C., Clampin, M., Doyon, R., Greenhouse, M. A., Hammel, H. B., Hutchings, J. B., Jakobsen, P., Lilly, S. J., Long, K. S., Lunine, J. I., Mccaughrean, M. J., Mountain, M., Nella, J., Rieke, G. H., Rieke, M. J., Rix, H.-W., Smith, E. P., Sonneborn, G., Stiavelli, M., Stockman, H. S., Windhorst, R. A., & Wright, G. S. 2006, *Space Science Reviews*, 123, 485
- Gargiulo, A., Saracco, P., & Longhetti, M. 2011, *Monthly Notices of the Royal Astronomical Society*, 412, 1084
- Gebhardt, K., Faber, S., Koo, D., Im, M., Simard, L., Illingworth, G., Phillips, A., Sarajedini, V., Vogt, N., Weiner, B., & Others. 2003, *The Astrophysical Journal*, 597, 239

- Glazebrook, K., Abraham, R. G., McCarthy, P. J., Savaglio, S., Chen, H.-W., Crampton, D., Murowinski, R., Jørgensen, I., Roth, K., Hook, I., Marzke, R. O., & Carlberg, R. G. 2004, *Nature*, 430, 181
- González-García, A. & Van Albada, T. 2003, *Monthly Notices of the Royal Astronomical Society*, 342, L36
- Gorski, K. M., Hivon, E., Banday, a. J., Wandelt, B. D., Hansen, F. K., Reinecke, M., & Bartelmann, M. 2005, *The Astrophysical Journal*, 622, 759
- Graves, G. J., Faber, S. M., & Schiavon, R. P. 2009, *The Astrophysical Journal*, 693, 486
- Green, A., Glazebrook, K., McGregor, P., Abraham, R., Poole, G., Damjanov, I., McCarthy, P., Colless, M., & Sharp, R. 2010, *Nature*, 467, 684
- Guo, Y., Giavalisco, M., Cassata, P., Ferguson, H. C., Dickinson, M., Renzini, A., Koekoemoer, A., Grogin, N. a., Papovich, C., Tundo, E., Fontana, A., Lotz, J. M., & Salimbeni, S. 2011, *The Astrophysical Journal*, 735, 18
- Guo, Y., McIntosh, D. H., Mo, H. J., Katz, N., van den Bosch, F. C., Weinberg, M., Weinmann, S. M., Pasquali, A., & Yang, X. 2009, *Monthly Notices of the Royal Astronomical Society*, 398, 1129
- Hills, J. 1980, *The Astrophysical Journal*, 235, 986
- Hopkins, P. F., Bundy, K., Croton, D., Hernquist, L., Keres, D., Khochfar, S., Stewart, K., Wetzel, A., & Younger, J. D. 2010a, *The Astrophysical Journal*, 715, 202
- Hopkins, P. F., Bundy, K., Hernquist, L., Wuyts, S., & Cox, T. J. 2010b, *Monthly Notices of the Royal Astronomical Society*, 401, 1099
- Hopkins, P. F., Bundy, K., Murray, N., Quataert, E., Lauer, T. R., & Ma, C.-P. 2009, *Monthly Notices of the Royal Astronomical Society*, 398, 898
- Hubble, E. 1926, *The Astrophysical Journal*, 64, 321
- Hubble, E. P. 1936, *Realm of the Nebulae*
- Hyde, J. & Bernardi, M. 2009, *Monthly Notices of the Royal Astronomical Society*, 394, 1978

- Javier Cenarro, A. & Trujillo, I. 2009, *The Astrophysical Journal*, 696, L43
- Jedrzejewski, R. 1987, *Monthly Notices of the Royal Astronomical Society*, 226, 747
- Jørgensen, I., Franx, M., & Kjaergaard, P. 1995, *Monthly Notices of the Royal Astronomical Society*, 273, 1097
- . 1996, *Monthly Notices of the Royal Astronomical Society*, 280, 167
- Kang, X., Jing, Y., & Silk, J. 2006, *The Astrophysical Journal*, 648, 820
- Kauffmann, G., Heckman, T., White, S., Charlot, S., Tremonti, C., Brinchmann, J., Bruzual, G., Peng, E., Seibert, M., Bernardi, M., & Others. 2003, *Monthly Notices of the Royal Astronomical Society*, 341, 33
- Khochfar, S. & Silk, J. 2006, *The Astrophysical Journal Letters*, 648, 21
- Kormendy, J. 1977, *The Astrophysical Journal*, 218, 333
- Kriek, M., Van Dokkum, P., Franx, M., Quadri, R., Gawiser, E., Herrera, D., Illingworth, G., Labbé, I., Lira, P., Marchesini, D., & Others. 2006, *The Astrophysical Journal Letters*, 649, L71
- Kriek, M., van Dokkum, P. G., Franx, M., Illingworth, G. D., & Magee, D. K. 2009, *The Astrophysical Journal*, 705, L71
- La Barbera, F., De Carvalho, R., De La Rosa, I., & Lopes, P. 2010, *Monthly Notices of the Royal Astronomical Society*, 408, 1335
- Labbé, I., Franx, M., Rudnick, G., Schreiber, N., Rix, H., Moorwood, A., van Dokkum, P., van der Werf, P., Röttgering, H., van Starckenburg, L., & Others. 2003, *The Astronomical Journal*, 125, 1107
- Labbé, I., Huang, J., Franx, M., Rudnick, G., Barmby, P., Daddi, E., Van Dokkum, P., Fazio, G., Schreiber, N., Moorwood, A., & Others. 2005, *The Astrophysical Journal Letters*, 624, L81
- Lai, O., Chun, M., Cuillandre, J. C., Carlberg, R., Richer, H., Andersen, D., Pazder, J., Tonry, J., Doyon, R., Thibault, S., Dunlop, J., Pritchet, C., Veran, J. P., Ftaclas, C., Onaka, P., Hodapp, K. W., McLaren, R. A., Bertin, E., Mellier, Y., Astier, P., & Pain,

- R. 2008, IMAKA: imaging from Mauna KeA with an atmosphere corrected 1 square degree optical imager, Vol. 7015 (SPIE), 70154H–70154H–12
- Law, D. R., Steidel, C. C., Erb, D. K., Larkin, J. E., Pettini, M., Shapley, A. E., & Wright, S. a. 2009, *The Astrophysical Journal*, 697, 2057
- Le Borgne, D., Rocca-Volmerange, B., Prugniel, P., Lançon, A., Fioc, M., & Soubiran, C. 2004, *Astronomy and astrophysics*, 425, 881
- Lilly, S., Fevre, O., Crampton, D., Hammer, F., & Tresse, L. 1995, *The Astrophysical Journal*, 455, 50
- Longhetti, M., Saracco, P., Severgnini, P., Della Ceca, R., Braitto, V., Mannucci, F., Bender, R., Drory, N., Feulner, G., & Hopp, U. 2005, *Monthly Notices of the Royal Astronomical Society*, 361, 897
- Longhetti, M., Saracco, P., Severgnini, P., Della Ceca, R., Mannucci, F., Bender, R., Drory, N., Feulner, G., & Hopp, U. 2007, *Monthly Notices of the Royal Astronomical Society*, 374, 614
- Maier, C., Lilly, S. J., Zamorani, G., Scodreggio, M., Lamareille, F., Contini, T., Sargent, M. T., Scarlata, C., Oesch, P., Carollo, C. M., Le Fèvre, O., Renzini, a., Kneib, J.-P., Mainieri, V., Bardelli, S., Bolzonella, M., Bongiorno, a., Caputi, K., Coppa, G., Cucciati, O., de la Torre, S., de Ravel, L., Franzetti, P., Garilli, B., Iovino, a., Kampczyk, P., Knobel, C., Kovač, K., Le Borgne, J.-F., Le Brun, V., Mignoli, M., Pello, R., Peng, Y., Montero, E. P., Ricciardelli, E., Silverman, J. D., Tanaka, M., Tasca, L., Tresse, L., Vergani, D., Zucca, E., Abbas, U., Bottini, D., Cappi, a., Cassata, P., Cimatti, a., Fumana, M., Guzzo, L., Halliday, C., Koekemoer, a. M., Leauthaud, a., Maccagni, D., Marinoni, C., McCracken, H. J., Memeo, P., Meneux, B., Porciani, C., Pozzetti, L., & Scaramella, R. 2009, *The Astrophysical Journal*, 694, 1099
- Mancini, C., Daddi, E., Renzini, A., Salmi, F., McCracken, H. J., Cimatti, A., Onodera, M., Salvato, M., Koekemoer, A. M., Aussel, H., Floc'h, E. L., Willott, C., & Capak, P. 2010, *Monthly Notices of the Royal Astronomical Society*, 401, 933
- Mannucci, F. 2007, Ringberg Workshop on Astronomy with Laser Guide Star Adaptive Optics: 29 Oct. - 2 Nov.

- Maraston, C., Daddi, E., Renzini, a., Cimatti, a., Dickinson, M., Papovich, C., Pasquali, a., & Pirzkal, N. 2006, *The Astrophysical Journal*, 652, 85
- McCarthy, P., Carlberg, R., Chen, H., Marzke, R., Firth, A., Ellis, R., Persson, S., McMahon, R., Lahav, O., Wilson, J., & Others. 2001, *The Astrophysical Journal Letters*, 560, L131
- McCarthy, P., Le Borgne, D., Crampton, D., Chen, H., Abraham, R., Glazebrook, K., Savaglio, S., Carlberg, R., Marzke, R., Roth, K., & Others. 2004, *The Astrophysical Journal Letters*, 614, L9
- McCarthy, P., Yan, H., Abraham, R., Mentuch, E., Glazebrook, K., Yan, L., Chen, H., Persson, S., Nair, P., Savaglio, S., & Others. 2007, *The Astrophysical Journal Letters*, 664, L17
- McGrath, E., Stockton, A., Canalizo, G., Iye, M., & Maihara, T. 2008, *The Astrophysical Journal*, 682, 303
- McGrath, E. J., Stockton, A., & Canalizo, G. 2007, *The Astrophysical Journal*, 669, 241
- McGregor, P. 2004, *Gemini South Adaptive Optics Imager (GSAOI)*, Vol. 5492 (SPIE), 1033–1044
- Monet, D., Levine, S., Canzian, B., Ables, H., Bird, A., Dahn, C., Guetter, H., Harris, H., Henden, A., Leggett, S., & Others. 2003, *The Astronomical Journal*, 125, 984
- Morgan, W. 1971, *The Astronomical Journal*, 76, 1000
- Moriondo, G., Cimatti, A., & Daddi, E. 2000, *Astronomy and Astrophysics*, 364, 26
- Mosleh, M., Williams, R. J., Franx, M., & Kriek, M. 2011, *The Astrophysical Journal*, 727, 5
- Moustakas, L. a., Casertano, S., Conselice, C. J., Dickinson, M. E., Eisenhardt, P., Ferguson, H. C., Giavalisco, M., Grogin, N. a., Koekemoer, A. M., Lucas, R. a., Mobasher, B., Papovich, C., Renzini, A., Somerville, R. S., & Stern, D. 2004, *The Astrophysical Journal*, 600, L131
- Moustakas, L. a. & Somerville, R. S. 2002, *The Astrophysical Journal*, 577, 1

- Murray, N., Quataert, E., & Thompson, T. a. 2010, *The Astrophysical Journal*, 709, 191
- Naab, T., Johansson, P. H., & Ostriker, J. P. 2009, *The Astrophysical Journal*, 699, L178
- Naab, T., Johansson, P. H., Ostriker, J. P., & Efstathiou, G. 2007, *The Astrophysical Journal*, 658, 710
- Nair, P., van den Bergh, S., & Abraham, R. 2010, *The Astrophysical Journal*, 715, 606
- . 2011, *The Astrophysical Journal Letters*, 734, L31
- Newman, A. B., Ellis, R. S., Treu, T., & Bundy, K. 2010, *The Astrophysical Journal*, 717, L103
- Nigoche-Netro, A., Aguerri, J. A. L., Lagos, P., Ruelas-Mayorga, A., Sánchez, L. J., & Machado, A. 2010, *Astronomy and Astrophysics*, 516, A96
- Nigoche-Netro, A., Ruelas-Mayorga, A., & Franco-Balderas, A. 2008, *Astronomy and Astrophysics*, 491, 731
- Nipoti, C., Treu, T., Auger, M., & Bolton, A. 2009, *The Astrophysical Journal Letters*, 706, L86
- Ono, Y., Ouchi, M., Shimasaku, K., Akiyama, M., Dunlop, J., Farrah, D., Lee, J. C., McLure, R., Okamura, S., & Yoshida, M. 2010, *Monthly Notices of the Royal Astronomical Society*, 402, 1580
- Oser, L., Naab, T., Ostriker, J., & Johansson, P. 2011, Arxiv preprint arXiv:1106.5490
- Pahre, M., Djorgovski, S., & De Carvalho, R. 1998, *The Astronomical Journal*, 116, 1591
- Peng, C. Y., Ho, L. C., Impey, C. D., & Rix, H.-W. 2002, *The Astronomical Journal*, 124, 266
- Pipino, A. & Matteucci, F. 2008, *Astronomy and Astrophysics*, 486, 763
- Queyrel, J., Contini, T., Pérez-Montero, E., Garilli, B., Le Fèvre, O., Kissler-Patig, M., Epinat, B., Vergani, D., Tresse, L., Amram, P., & Lemoine-Busserolle, M. 2009, *Astronomy and Astrophysics*, 506, 681
- Ragazzoni, R., Marchetti, E., & Valente, G. 2000, *Nature*, 403, 54

- Ragone-Figueroa, C. & Granato, G. L. 2011, *Monthly Notices of the Royal Astronomical Society*, 414, 3690
- Raichoor, A., Mei, S., Nakata, F., Stanford, S. a., Holden, B. P., Rettura, A., Huertas-Company, M., Postman, M., Rosati, P., Blakeslee, J. P., Demarco, R., Eisenhardt, P., Illingworth, G., Jee, M. J., Kodama, T., Tanaka, M., & White, R. L. 2011, *The Astrophysical Journal*, 732, 12
- Rettura, A., Rosati, P., Nonino, M., Fosbury, R. a. E., Gobat, R., Menci, N., Strazzullo, V., Mei, S., Demarco, R., & Ford, H. C. 2010, *The Astrophysical Journal*, 709, 512
- Rigaut, F. & Gendron, E. 1992, *Astronomy and Astrophysics*, 261, 677
- Rigaut, F. J., Ellerbroek, B. L., & Flicker, R. 2000, *Proc. SPIE Vol. 4007*, 4007, 1022
- Rix, H., Barden, M., Beckwith, S. V. W., Bell, E. F., Borch, A., Caldwell, J. a. R., Haussler, B., Jahnke, K., Joglee, S., McIntosh, D. H., Meisenheimer, K., Peng, C. Y., Sanchez, S. F., Somerville, R. S., Wisotzki, L., & Wolf, C. 2004, *The Astrophysical Journal Supplement Series*, 152, 163
- Rix, H.-W., Guhathakurta, P., Colless, M., & Ing, K. 1997, *Monthly Notices of the Royal Astronomical Society*, 285, 779
- Roberts, M. S. & Haynes, M. P. 1994, *Annual Review of Astronomy and Astrophysics*, 32, 115
- Roggemann, M. C. & Welsh, B. 1996, *Imaging through turbulence* (CRC Press), 320
- Rousset, G., Fusco, T., Assemat, F., Morris, T., Gendron, E., Myers, R., Brangier, M., Cohen, M., Dipper, N., Evans, C., Gratadour, D., Jagourel, P., Laporte, P., Le Mignant, D., Puech, M., Robert, C., Schnetler, H., Taylor, W., Vidal, F., Cuby, J.-G., Lehnert, M., Morris, S., & Parr-Burmann, P. 2010, 1st AO4ELT conference - Adaptive Optics for Extremely Large Telescopes
- Rudnick, G., Labbe, I., Forster Schreiber, N. M., Wuyts, S., Franx, M., Finlator, K., Kriek, M., Moorwood, A., Rix, H., Rottgering, H., Trujillo, I., van der Wel, A., van der Werf, P., & van Dokkum, P. G. 2006, *The Astrophysical Journal*, 650, 624

- Rudnick, G., Rix, H., Franx, M., Labbé, I., Blanton, M., Daddi, E., Foerster Schreiber, N., Moorwood, A., Röttgering, H., Trujillo, I., & Others. 2003, *The Astrophysical Journal*, 599, 847
- Ryan, R. E., McCarthy, P. J., Cohen, S. H., Yan, H., Hathi, N. P., Koekemoer, A. M., Rutkowski, M. J., Mechtley, M. R., Windhorst, R. A., O'Connell, R. W., Balick, B., Bond, H. E., Bushouse, H., Calzetti, D., Crockett, R. M., Disney, M., Dopita, M. A., Frogel, J. A., Hall, D. N. B., Holtzman, J. A., Kaviraj, S., Kimble, R. A., MacKenty, J., Mutchler, M., Paresce, F., Saha, A., Silk, J. I., Trauger, J., Walker, A. R., Whitmore, B. C., & Young, E. 2011, *The Astrophysical Journal*, submitted, arXiv: 1007.1460
- Saglia, R. P., Sánchez-Blázquez, P., Bender, R., Simard, L., Desai, V., Aragón-Salamanca, a., Milvang-Jensen, B., Halliday, C., Jablonka, P., Noll, S., Poggianti, B., Clowe, D. I., De Lucia, G., Pelló, R., Rudnick, G., Valentinuzzi, T., White, S. D. M., & Zaritsky, D. 2010, *Astronomy and Astrophysics*, 524, A6
- Saracco, P., Longhetti, M., & Andreon, S. 2009, *Monthly Notices of the Royal Astronomical Society*, 392, 718
- Saracco, P., Longhetti, M., & Gargiulo, A. 2010, *Monthly Notices of the Royal Astronomical Society: Letters*, 408, L21
- . 2011, *Monthly Notices of the Royal Astronomical Society*, 412, 2707
- Schade, D., Lilly, S. J., Crampton, D., Ellis, R. S., Le Fèvre, O., Hammer, F., Brinchmann, J., Abraham, R., Colless, M., Glazebrook, K., Tresse, L., & Broadhurst, T. 1999, *The Astrophysical Journal*, 525, 31
- Schlegel, D., Finkbeiner, D., & Davis, M. 1998, *The Astrophysical Journal*, 500, 525
- Schombert, J. 1986, *The Astrophysical Journal Supplement Series*, 60, 603
- Schweizer, F. 1986, *Science (New York, N.Y.)*, 231, 227
- Scoville, N., Aussel, H., Brusa, M., Capak, P., Carollo, C. M., Elvis, M., Giavalisco, M., Guzzo, L., Hasinger, G., Impey, C., Kneib, J., LeFevre, O., Lilly, S. J., Mobasher, B., Renzini, a., Rich, R. M., Sanders, D. B., Schinnerer, E., Schminovich, D., Shopbell, P., Taniguchi, Y., & Tyson, N. D. 2007, *The Astrophysical Journal Supplement Series*, 172, 1

- Searle, L. & Zinn, R. 1978, *The Astrophysical Journal*, 225, 357
- Sersic, J. L. 1968, *Atlas de galaxias australes*
- Shankar, F., Marulli, F., Bernardi, M., Dai, X., Hyde, J., & Sheth, R. 2010, *Monthly Notices of the Royal Astronomical Society*, 403, 117
- Shankar, F., Marulli, F., Bernardi, M., Mei, S., Meert, A., & Vikram, V. 2011, Arxiv preprint arXiv:1105.6043
- Shih, H. & Stockton, A. 2011, *The Astrophysical Journal*, 733, 45
- Shim, H., Colbert, J., Teplitz, H., Henry, A., Malkan, M., McCarthy, P., & Yan, L. 2009, *The Astrophysical Journal*, 696, 785
- Simard, L., Willmer, C., Vogt, N., Sarajedini, V., Phillips, A., Weiner, B., Koo, D., Im, M., Illingworth, G., & Faber, S. 2002, *The Astrophysical Journal Supplement Series*, 142, 1
- Stockton, A., Canalizo, G., & Maihara, T. 2004, *The Astrophysical Journal*, 605, 37
- Szapudi, I. & Colombi, S. 1996, *The Astrophysical Journal*, 470, 131
- Szomoru, D., Franx, M., Bouwens, R. J., van Dokkum, P. G., Labbé, I., Illingworth, G. D., & Trenti, M. 2011, *The Astrophysical Journal*, 735, L22
- Szomoru, D., Franx, M., van Dokkum, P. G., Trenti, M., Illingworth, G. D., Labbé, I., Bouwens, R. J., Oesch, P. A., & Carollo, C. M. 2010, *The Astrophysical Journal*, 714, L244
- Targett, T., Dunlop, J., McLure, R., Best, P., Cirasuolo, M., & Almaini, O. 2011, *Monthly Notices of the Royal Astronomical Society*, 412, 295
- Taylor, E. N., Franx, M., Glazebrook, K., Brinchmann, J., van der Wel, A., & van Dokkum, P. G. 2010, *The Astrophysical Journal*, 720, 723
- Terlevich, A., Caldwell, N., & Bower, R. 2001, *Monthly Notices of the Royal Astronomical Society*, 326, 1547
- Tody, D. 1993, in *Astronomical Data Analysis Software and Systems II*, Vol. 52, 173

- Toft, S., Franx, M., van Dokkum, P., Förster Schreiber, N. M., Labbe, I., Wuyts, S., & Marchesini, D. 2009, *The Astrophysical Journal*, 705, 255
- Toft, S., van Dokkum, P., Franx, M., Labbe, I., Forster Schreiber, N. M., Wuyts, S., Webb, T., Rudnick, G., Zirm, A., Kriek, M., van der Werf, P., Blakeslee, J. P., Illingworth, G., Rix, H., Papovich, C., & Moorwood, A. 2007, *The Astrophysical Journal*, 671, 285
- Toomre, A. & Toomre, J. 1972, *The Astrophysical Journal*, 178, 623
- Tortora, C., Napolitano, N., & Romanowsky, A. 2011, Arxiv preprint arXiv: 1107.2918
- Trenti, M. & Stiavelli, M. 2008, *The Astrophysical Journal*, 676, 767
- Treu, T., Ellis, R., Liao, T., & van Dokkum, P. 2005a, *The Astrophysical Journal Letters*, 622, L5
- Treu, T., Ellis, R. S., Liao, T. X., van Dokkum, P. G., Tozzi, P., Coil, A., Newman, J., Cooper, M. C., & Davis, M. 2005b, *The Astrophysical Journal*, 633, 174
- Treu, T., Stiavelli, M., Casertano, S., Møller, P., & Bertin, G. 2002, *The Astrophysical Journal Letters*, 564, L13
- Trujillo, I., Cenarro, a. J., de Lorenzo-Cáceres, A., Vazdekis, A., de la Rosa, I. G., & Cava, A. 2009, *The Astrophysical Journal*, 692, L118
- Trujillo, I., Conselice, C. J., Bundy, K., Cooper, M. C., Eisenhardt, P., & Ellis, R. S. 2007, *Monthly Notices of the Royal Astronomical Society*, 382, 109
- Trujillo, I., Ferreras, I., & de la Rosa, I. G. 2011, Arxiv preprint arXiv:1102.3398
- Trujillo, I., Feulner, G., Goranova, Y., Hopp, U., Longhetti, M., Saracco, P., Bender, R., Braito, V., Della Ceca, R., Drory, N., Mannucci, F., & Severgnini, P. 2006, *Monthly Notices of the Royal Astronomical Society: Letters*, 373, L36
- Valentinuzzi, T., Fritz, J., Poggianti, B. M., Cava, a., Bettoni, D., Fasano, G., D'Onofrio, M., Couch, W. J., Dressler, a., Moles, M., Moretti, a., Omizzolo, a., Kjærgaard, P., Vanzella, E., & Varela, J. 2010a, *The Astrophysical Journal*, 712, 226

- Valentinuzzi, T., Poggianti, B. M., Saglia, R. P., Aragón-Salamanca, A., Simard, L., Sánchez-Blázquez, P., D'onofrio, M., Cava, A., Couch, W. J., Fritz, J., Moretti, A., & Vulcani, B. 2010b, *The Astrophysical Journal*, 721, L19
- van de Sande, J., Kriek, M., Franx, M., van Dokkum, P. G., Bezanson, R., Whitaker, K. E., Brammer, G., Labbé, I., Groot, P. J., & Kaper, L. 2011, Arxiv preprint arXiv:1104.3860
- van de Ven, G., van Dokkum, P. G., & Franx, M. 2003, *Monthly Notices of the Royal Astronomical Society*, 344, 924
- van den Bergh, S. 1999, *Astronomy and Astrophysics Review*, 9, 273
- van der Wel, A., Bell, E. F., van den Bosch, F. C., Gallazzi, A., & Rix, H.-W. 2009, *The Astrophysical Journal*, 698, 1232
- van der Wel, A., Franx, M., van Dokkum, P., & Rix, H. 2004, *The Astrophysical Journal Letters*, 601, L5
- van der Wel, a., Franx, M., van Dokkum, P. G., Rix, H., Illingworth, G. D., & Rosati, P. 2005, *The Astrophysical Journal*, 631, 145
- van der Wel, A., Holden, B. P., Zirm, A. W., Franx, M., Rettura, A., Illingworth, G. D., & Ford, H. C. 2008, *The Astrophysical Journal*, 688, 48
- van der Wel, A., Rix, H., Wuyts, S., McGrath, E., Koekemoer, A., Bell, E., Holden, B., Robaina, A., & McIntosh, D. 2011, *The Astrophysical Journal*, 730, 38
- van Dokkum, P. G. 2005, *The Astronomical Journal*, 130, 2647
- van Dokkum, P. G., Franx, M., Forster Schreiber, N. M., Illingworth, G. D., Daddi, E., Knudsen, K. K., Labbe, I., Moorwood, A., Rix, H., Rottgering, H., Rudnick, G., Trujillo, I., van der Werf, P., van der Wel, A., van Starckenburg, L., & Wuyts, S. 2004, *The Astrophysical Journal*, 611, 703
- van Dokkum, P. G., Franx, M., Kelson, D. D., & Illingworth, G. D. 1998, *The Astrophysical Journal*, 504, L17

- van Dokkum, P. G., Franx, M., Kriek, M., Holden, B., Illingworth, G. D., Magee, D., Bouwens, R., Marchesini, D., Quadri, R., Rudnick, G., Taylor, E. N., & Toft, S. 2008, *The Astrophysical Journal*, 677, L5
- van Dokkum, P. G., Kriek, M., & Franx, M. 2009a, *Nature*, 460, 717
- van Dokkum, P. G., Labbe, I., Marchesini, D., Quadri, R., Brammer, G., Whitaker, K. E., Kriek, M., Franx, M., Rudnick, G., Illingworth, G., Lee, K.-S., & Muzzin, A. 2009b, *Publications of the Astronomical Society of the Pacific*, 121, 2
- van Dokkum, P. G., Whitaker, K. E., Brammer, G., Franx, M., Kriek, M., Labbé, I., Marchesini, D., Quadri, R., Bezanson, R., Illingworth, G. D., Muzzin, A., Rudnick, G., Tal, T., & Wake, D. 2010, *The Astrophysical Journal*, 709, 1018
- Villar, V., Gallego, J., Pérez-González, P., Pascual, S., Noeske, K., Koo, D., Barro, G., & Zamorano, J. 2008, *The Astrophysical Journal*, 677, 169
- Wang, L., Ellerbroek, B., Veran, J.-P., & Siquin, J.-C. 2008, *Evaluating sky coverage for the NFIRAOS tip/tilt control architecture*, Vol. 7015 (SPIE), 70155X–70155X–9
- Weiner, B., Phillips, A., Faber, S., Willmer, C., Vogt, N., Simard, L., Gebhardt, K., Im, M., Koo, D., Sarajedini, V., & Others. 2005, *The Astrophysical Journal*, 620, 595
- Williams, R., Quadri, R., & Franx, M. 2011, *Arxiv preprint arXiv:1106.6054*
- Williams, R. J., Quadri, R. F., Franx, M., van Dokkum, P., Toft, S., Kriek, M., & Labbé, I. 2010, *The Astrophysical Journal*, 713, 738
- Wolf, C., Meisenheimer, K., Rix, H.-W., Borch, A., Dye, S., & Kleinheinrich, M. 2003, *Astronomy and Astrophysics*, 401, 73
- Wuyts, S., van Dokkum, P. G., Kelson, D. D., Franx, M., & Illingworth, G. D. 2004, *The Astrophysical Journal*, 605, 677
- Yan, L. & Thompson, D. 2003, *The Astrophysical Journal*, 586, 765
- Yasuda, N., Fukugita, M., & Schneider, D. P. 2007, *The Astronomical Journal*, 134, 698
- Yee, H., Morris, S., Lin, H., Carlberg, R., Hall, P., Sawicki, M., Patton, D., Wirth, G., Ellingson, E., & Shepherd, C. 2000, *The Astrophysical Journal Supplement Series*, 129, 475

Zacharias, N., Urban, S. E., Zacharias, M. I., Wycoff, G. L., Hall, D. M., Monet, D. G., & Rafferty, T. J. 2004, *The Astronomical Journal*, 127, 3043

Zhao, H. 2002, *Monthly Notices of the Royal Astronomical Society*, 336, 159

Zirm, A. W., Dickinson, M., & Dey, A. 2003, *The Astrophysical Journal*, 585, 90

Zirm, A. W., van der Wel, A., Franx, M., Labbe, I., Trujillo, I., van Dokkum, P., Toft, S., Daddi, E., Rudnick, G., Rix, H., Rottgering, H. J. A., & van der Werf, P. 2007, *The Astrophysical Journal*, 656, 66